24 December 2004

Science

Vol. 306 No. 5705
Pages 2149–2292 $10

AAAS

Science

COVER A brightly colored male American redstart (*Setophaga ruticilla*) feeding its young. In this species, males that provide high levels of parental care late in the season molt during migration to the tropics and so produce less colorful feathers than those grown on the breeding grounds. See page 2249. [Image: J. P. O'Neill]

Volume 306
24 December 2004
Number 5705

DEPARTMENTS

NEWS OF THE WEEK

NEWS FOCUS

2174

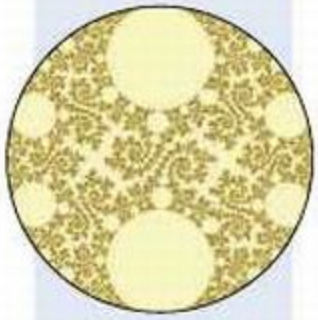

2182

2192

LETTERS

BOOKS *ET AL.*

POLICY FORUM

PERSPECTIVES

REVIEW

Contents continued

Science

Science Express www.sciencexpress.org

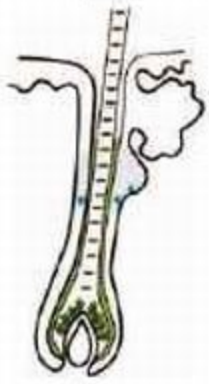

Technical Comment Abstracts

Brevia

Research Article

Reports

2215

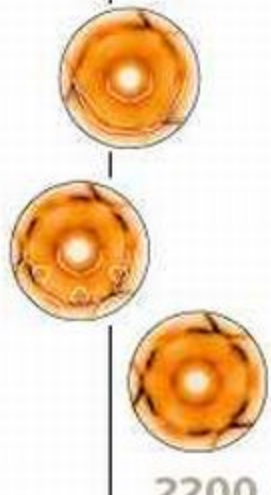

2200 & 2221

Contents continued

Science

REPORTS CONTINUED

2251

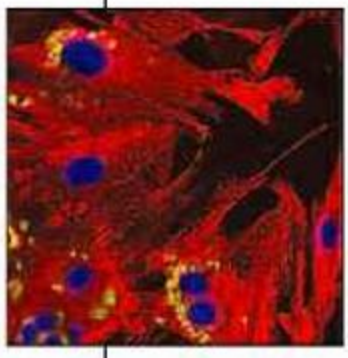

2261

AAAS
ADVANCING SCIENCE, SERVING SOCIETY

SCIENCE (ISSN 0036-8075) is published weekly on Friday, except the last week in December, by the American Association for the Advancement of Science, 1200 New York Avenue, NW, Washington, DC 20005. Periodicals Mail postage (publication No. 484460) paid at Washington, DC, and additional mailing offices. Copyright © 2004 by the American Association for the Advancement of Science. The title SCIENCE is a registered trademark of the AAAS. Domestic individual membership and subscription (51 issues): $139 ($74 allocated to subscription). Domestic institutional subscription (51 issues): $500. Foreign postage extra: Mexico, Caribbean (surface mail) $55; other countries (air assist delivery) $80. First class, airmail, student, and retired rates on request. Canadian rates with GST available upon request, GST # 125488122. Publications Mail Agreement Number 1069624. Printed in the U.S.A.

Change of address allow 4 weeks, giving old and new addresses and 8-digit account number. Postmaster: Send change of address to Science, P.O. Box 1811, Danbury, CT 06813–1811. Single copy sales: $10.00 per issue prepaid includes surface postage; bulk rates on request. Authorization to photocopy material for internal or personal use under circumstances not falling within the fair use provisions of the Copyright Act is granted by AAAS to libraries and other users registered with the Copyright Clearance Center (CCC) Transactional Reporting Service, provided that $15.00 per article is paid directly to CCC, 222 Rosewood Drive, Danvers, MA 01923. The identification code for Science is 0036-8075/03 $15.00. Science is indexed in the Reader's Guide to Periodical Literature and in several specialized indexes.

Contents continued

Science
www.scienceonline.org

sciencenow www.sciencenow.org Daily News Coverage

A Century of Melting Ice
Photos document stunning changes in the Alaskan landscape as glaciers retreat.

Eyeing the Fear Factor
The whites of our eyes are a powerful signal for communicating fear.

Too Tired to Be Sexy
Genetically modified glowing fish may lack the energy to lure a mate in the wild.

Resources for entrepreneurs.

science's next wave www.nextwave.org Career Resources for Young Scientists

MiSciNet: Exploring Scientific Entrepreneurship *S. Clemmons*
Learn about helpful resources and strategies for scientists interested in forming their own companies.

Global/US: The Ride of Your Life *R. Arnette*
Many would scream for a job as senior roller coaster engineer at Great Coasters International Inc.

US: Educated Woman, Chapter 34, Hoop Number 314,159—Choosing Your Committee *M. P. DeWhyse*
There is pain and pleasure in choosing the torturers for your Ph.D. thesis committee.

Canada: A Maple Leaf on Mars—Interview with Canada's Space Exploration Lead *A. Fazekas*
Dr. Berinstain of the Canadian Space Agency discusses Canada's plans for exploring Mars and beyond.

GrantsNet: Funding News for December 2004 *Edited by S. Martin*
Find out about opportunities from private and U.S. government funding sources for postdocs and students.

US: Careers in Science Web Log *J. Austin*
Breaking news and observations related to science careers are updated throughout the week.

science's sage ke www.sageke.org Science of Aging Knowledge Environment

Perspective: Telomeres and Human Aging—Facts and Fibs *A. Aviv*
The jury is still out on whether telomere dynamics is a surrogate for or a key determinant of human aging.

News Focus: Once More, with Feeling *R. J. Davenport*
Hobbling glycation-detecting protein restores feeling in diabetic mice.

News Focus: Trashing Vision *M. Leslie*
Cell receptor helps prevent garbage pileups in the eye.

News Focus: Natural Foods *R. J. Davenport*
Wildlike pattern of feast and famine extends Medfly life span.

News Focus: Telltale Text *M. Leslie*
Novelist's final work reveals early signs of Alzheimer's disease.

News Focus: Gray Matters *M. Beckman*
Hair pigment stem cells malfunction in old age.

Telomere shortening—ringing out the old?

A whirlwind of acronyms.

science's stke www.stke.org Signal Transduction Knowledge Environment

Glossary
Updates to the Glossary define acronyms and abbreviations used in cell signaling.

ST on the Web
See the Bioinformatics Resources section for information on mark-up languages used to describe cell signaling and biochemistry.

Events
Find out which meetings and conferences are coming up in 2005.

Separate individual or institutional subscriptions to these products may be required for full-text access.

edited by Stella Hurtley and Phil Szuromi

Melting Metal Monolayers

Detailed information on the electronic properties of liquids and amorphous metals is difficult to come by because the lack of long-range order in these materials limits the usefulness of most usual experimental probes. **Baumberger *et al.*** (p. 2221, published online 25 November 2004; see the Perspective by **Petroff**) get around the lack of long-range order by looking at a monolayer of lead deposited on a copper substrate. As the temperature is raised through the melting point of the lead layer, the underlying order of the copper substrate provides a surrogate for the energy and momentum information lost in the liquid lead thin film and allows the changes in the electronic density of states to be followed as the metal melts.

Microbial Activities of the Deep

Although deep subterranean bacterial biota have very low metabolic rates, their metabolism is highly significant on a global scale. Submarine sediment depth-profile data from the Ocean Drilling Project have provided insight into electron acceptors for bacterial respiration, including sulfate, nitrate, and oxidized iron, as well as their metabolic end products, such as sulfide and methane. **D'Hondt *et al.*** (p. 2216; see the Perspective by **DeLong**) used these data to estimate microbial activities deep in the sediments. The expected stratifications were upset by intrusions of oxidized compounds, such as nitrate and sulfate from the basaltic aquifer.

Seek, Sense, and Destroy

Highly virulent enterococcal strains possess a pathogenicity island within their genome that encodes, among other traits, a cytolytic toxin that uses a quorum-sensing mechanism to affect autoinduction. **Coburn *et al.*** (p. 2270; see the Perspective by **Garsin**) show that the bacterium actively secretes two components, an autoinducer and an anti-autoinducer. In the absence of target cells, these two interact and prevent the autoinducer from feeding back to induce high-level expression of the cytolysin. In the presence of the target cell, however, the anti-autoinducer binds to the target cell and allows the autoinducer to accumulate to the threshold level required for quorum induction of the cytolysin operon. The anti-autoinducer is itself a toxin component and effectively tags the target for destruction.

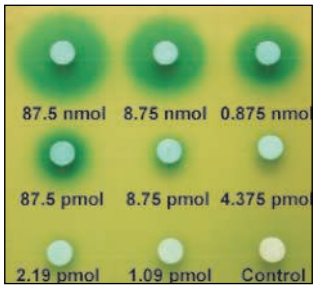

Diversity with Less Competition

Species diversity has recovered from some mass extinctions rapidly, within 1 million years or so. However, mass extinctions may also greatly effect ecosystems by altering interactions among species, and these effects may be more long lasting and cryptic. **Dietl *et al.*** (p. 2229) examined the effects of a late Pliocene extinction (about 3 million years ago) on the feeding behavior of marine snails. In an experiment, they show that snails, when competing with other snails or facing predation themselves, attack bivalves on their shell edge. When isolated, however, they attack through the cell wall—a slower but safer feeding approach. The fossil record records many edge attacks prior to the extinction, but exclusively shell-wall feeding afterward, a pattern that continues to today. Although diversity recovered promptly, the level of competition did not.

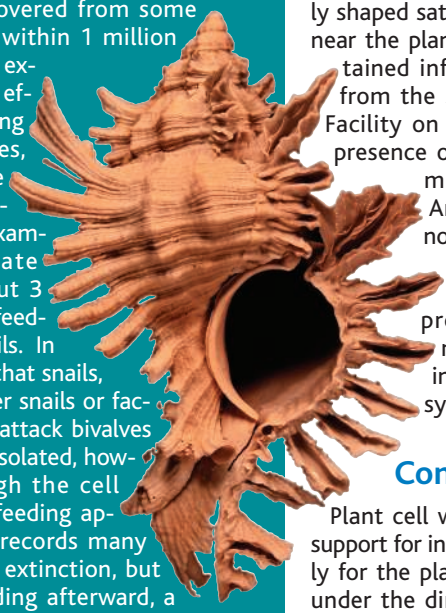

Organics on Jovian Orbiters

Amalthea and Thebe are small and irregularly shaped satellites of Jupiter that orbit very near the planet. **Takato *et al.*** (p. 2224) obtained infrared spectra of the satellites from the Subaru and Infrared Telescope Facility on Hawaii. The spectra show the presence of hydrous minerals or organic materials on the surface of Amalthea. Such materials could not have survived if the satellites formed from the circumjovian nebula, so these satellites probably are leftovers or remnants of the organic-rich building blocks from which the jovian system was formed.

Complex Cell Walls

Plant cell walls, which serve as structural support for individual plant cells and ultimately for the plant as a whole, are constructed under the direction of perhaps as many as 1000 different genes. However, these cell walls have many other functions. Analysis from a systems approach, reviewed by **Somerville *et al.*** (p. 2206), promises new insight into the complex functions of cell walls, which include regulating growth, development, responses to pathogens, and signaling.

The Proteins Came in Three by Three

Maps of protein interaction networks provide a kind of blueprint of cellular functions. Comparing the presence or absence of a pair of proteins in various species can provide clues to functional associations in such networks. **Bowers *et al.*** (p. 2246) take such logic a step further and examine the presence of groups of three proteins in 67 sequenced genomes. A search for logical relationships between the three (for example, A is present only if B and C are also present) revealed 750,000 new relationships between protein family members. These and higher-order logic relationships may be useful in modeling, engineering, and understanding biological systems.

Of Migrations and Moltings

Greater insights into the details of bird migration requires following and sampling individual birds. Using stable isotopes from feather samples, **Norris *et al.*** (p. 2249; see the cover and the Perspective by **Hill**) show that American redstarts migrating from Canada to the tropics adopt a strategy of molting during migration, which results in the overlap of two energetically costly activities of the annual cycle.

CREDITS: (TOP TO BOTTOM) DIETL *ET AL.*; COBURN *ET AL.*

Published by AAAS

A tradeoff was observed between molting during migration versus the timing and amount of parental care adults provide during the previous breeding season. Thus, events during a short period of the annual cycle can produce lasting effects on a migratory animal.

Phosphoryl Moiety Closes the Hatch

The calcium-dependent adenosine triphosphatase (ATPase) of the sarcoplasmic reticulum is one of the best studied ion pumps, and the structural description of two of the intermediate states in the reaction cycle helped to define the calcium ion binding sites within the transmembrane region of the enzyme. A recent series of crystal structures of the enzyme trapped at other stages in the reaction cycle is now capped by **Olesen *et al.*** (p. 2251), who identify the binding sites for the counter-transported protons. They also found that phosphoryl transfer from ATP to the enzyme closes the entry hatch to the calcium-binding site and that the release of adenosine diphosphate opens the exit hatch and allows the exchange of calcium for protons. Phosphoryl transfer from the enzyme to water and closes the exit hatch. Finally, release of phosphate opens the entry hatch and allows the exchange of protons for calcium.

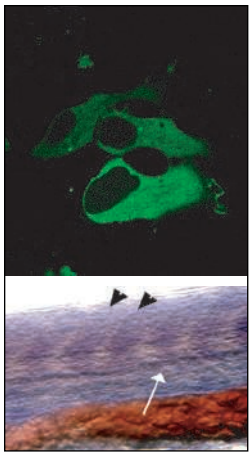

Hedgehog, Smoothened, and β-Arrestin

Hedgehog (Hh) proteins carry signals that are essential for pattern formation during vertebrate embryogenesis. Extracellular Hh molecules bind to a receptor on the cell surface and activate Smoothened, a membrane-spanning protein, which transmits signals to the cell interior. β-arrestin proteins are inhibitors of G protein–coupled receptor (GPCR) signaling and also promote internalization and signaling by GPCRs. **Chen *et al.*** (p. 2257) find that in mammalian cells, activated Smoothened molecules preferentially associate with β-arrestin 2. Reducing levels of β-arrestin 2 inhibited internalization of Smoothened. Furthermore, **Wilbanks *et al.*** (p. 2264) find that loss of β-arrestin 2 in zebrafish causes developmental abnormalities similar to those of mutants in the Hh signaling pathway. Overexpression of β-arrestin 2 could partially rescue some defects in embryos with deficient Hh signaling, and loss of β-arrestin 2 decreased expression of Hh-responsive genes. Together, the findings provide insight into the roles of β-arrestin 2 during development and the mechanisms by which Hh signaling influences developmental processes from embryogenesis to cancer.

Role of Transcription Factors in Neural Development

Neural development is often thought to be a matter of axons finding the right connections. **Gray *et al.*** (p. 2255) highlight the importance of transcription in regulating neural development. Analysis of the mouse genome revealed more than 1000 genes that encode transcription factors. In situ hybridization studies further revealed that more than 300 transcription factors were differentially expressed in the central nervous system during development.

Regenerating Beta Cells in Vitro

The islets of Langerhans contain the insulin-producing β cells that must be replenished throughout life. **Gershengorn *et al.*** (p. 2261, published online 25 November 2004) show that in vitro mature β cells proliferate poorly. However, given the right circumstances, they can dedifferentiate into a mesenchymal cell type that can proliferate better but fail to produce insulin. These proliferating cells can then be induced to redifferentiate into insulin-producing β cells, which would be useful in β-cell replacement therapies for diabetes.

A Human Transcriptome

Elucidating the transcribed regions of the genome constitutes a fundamental aspect of human biology. **Bertone *et al.*** (p. 2242, published online 11 November 2004) designed and used a genome-wide high-resolution tiling array to develop a transcription map for human liver. The approach validated many known and putative genes, and in addition, more than 10,000 novel transcribed regions were identified across the genome.

CREDITS: (TOP TO BOTTOM) CHEN *ET AL.*; WILBANKS *ET AL.*

A Dangerous Signal to Science

When you rush, you make mistakes. The recently passed U.S. budget for fiscal year (FY) 2005, finalized in a scurry to complete the congressional lame duck session, did more than just shortchange science. Perhaps worse, it sent a dangerous message that will reverberate throughout the global science and technology enterprise for a long time to come. Although homeland security and defense did receive notable increases in funding, the National Science Foundation (NSF) and the Environmental Protection Agency actually had their funding reduced from FY 2004 levels (*Science*, 3 December 2004, p. 1662). Other agencies received flat budgets or increases below the level of inflation. This is the third decrease for NSF research funding in its over-50-year history, a decrease that comes, embarrassingly, in the wake of a resolution passed in 2001 to double the NSF budget over the next 5 years. What was Congress thinking?

Lest we think this is a one-year alarming incident, analysis by the American Association for the Advancement of Science (AAAS) of the Bush administration's budget projections show the purchasing power of R&D investments declining over the next 5 years in all areas except homeland security, defense, and space (http://www.aaas.org/spp/rd/guioutyr.htm).

CREDIT: JOE SUTLIFF

This bad news comes at a time when science, already deeply embedded in modern life, will become increasingly vital to America's future prosperity and its competitive position in the world. Moreover, because science is increasingly global in character, decreased NSF support, so critical to much international collaboration, has implications for science that reach well beyond the United States.

The decrease in NSF funding will not only hurt basic science research programs but will seriously hamper efforts to improve science education, in which NSF plays a key role. Decreased science education funding is coming at a time when young people need greater science literacy to live full lives and when the United States increasingly needs a well-educated technical workforce to keep its industries onshore and competitive.

NIH-supported biomedical scientists may experience temporary relief, but their increase is below the rate of inflation. Moreover, the NSF cut leaves the increasingly interdisciplinary life sciences portfolio seriously unbalanced through its reduced support for mathematics, physics, and chemistry.

What to do? At a recent postelection forum sponsored by AAAS and Research! America, former Congressmen John Porter and Paul Rogers both emphasized the need for the research community to build stronger partnerships with its beneficiaries and patrons in the public. They particularly urged alliances with leaders in industry. Making the case for the support of science in partnership with those who will use our products to advance the public welfare strengthens it. Scientifically sympathetic members of Congress advise us again and again that messages from constituents about the importance of science have more political leverage than the occasional scientists who come to testify.

Reaching out to the public is not a strong tradition for the science community, perhaps because we may think that nonscientists cannot understand our work. We're wrong about that. As evidenced by the extent and high quality of science coverage in many national and local newspapers, the general public is excited when we share the thrill of scientific discovery.

Congressmen Vernon Ehlers (R-MI) and Rush Holt (D-NJ), two scientists currently in the U.S. Congress, frequently remind us that we really need grassroots support. Many of us have given talks to local clubs and lodges about scientific work and what it means. When we visit local schools, students and their parents can get a sense of the excitement of what we do. Alliances with leaders in local industry have a special kind of leverage, and science/industry partnerships can convince government representatives of the need to support science and its use for the benefit of society at large. Some 50 new members of the U.S. House and Senate give us a great opportunity to educate the national leaders of the future. Rather than lamenting our fate, we can mobilize our natural allies—the people we serve—to convince our policymakers not to make the same mistakes again.

Alan I. Leshner
Chief Executive Officer, AAAS
Executive Publisher, Science

10.1126/science.1108749

edited by Stella Hurtley

NEUROSCIENCE

Limits to Growth

Plasticity in neurons is regulated, in part, by the degradation of specific proteins at synapses. Actively dividing cells rely on ubiquitin-dependent degradation to regulate the transitions through the phases of the cell cycle. Van Roessel *et al*. find that a key enzyme involved in the latter process, the anaphase-promoting complex (APC), plays a role in controlling synaptic size and plasticity. [APC has also been linked to axonal growth and patterning (Konishi *et al*. Reports, 13 February 2004, p. 1026).] In *Drosophila*, APC subunits are found at neuromuscular synapses, and when APC levels were reduced, the synaptic boutons of motor neurons increased in size because of the action of the protein Liprin-α, which is a substrate for APC-stimulated ubiquitinylation and degradation. Furthermore, muscles lacking APC displayed altered synaptic transmission, and the postsynaptic levels of glutamate receptor were increased. These pre- and postsynaptic functions of APC may explain why a cell cycle regulator is expressed in differentiated postmitotic cells. — SMH

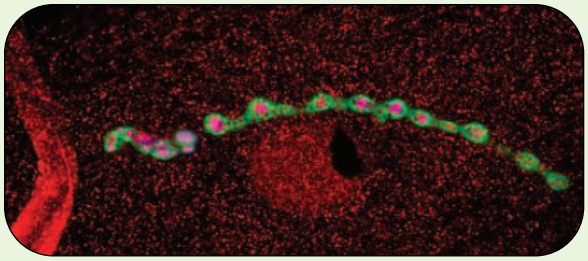

APC (red) localizes to neuromuscular synapses (green and blue).

Cell **119**, 707 (2004).

EVOLUTION

Of Mice . . .

Murid rodents are only one of the approximately 146 families of mammals, yet comprise nearly one-third of all mammalian species. A robust phylogeny would provide the framework for understanding their evolutionary success as well as their roles as model organisms in biomedical research and as hosts and vectors of human pathogens. Steppan *et al*. present analyses based on sequences from 53 genera of four nuclear genes (*GHR*, *BRCA1*, *RAG1*, and *c-myc*), which yield nearly identical phylogenies. Taken together, these resolve most relationships among the 16 subfamilies and identify four distinct explosive radiations. One occurred when the ancestor of most Sigmodontinae colonized South America; another as the Murinae (Old World mice and rats) expanded their range from Southeast Asia across Asia and Africa. The results also suggest that—through the attribution of fossil calibrations to the wrong nodes and the neglect of rate heterogeneity—nearly all past applications of a molecular clock calibrated using the mouse/rat divergence have overestimated dates (that is, placed them too far back in time) by 20 to 50%. — SJS

Syst. Biol. **53**, 533 (2004).

NANOTECHNOLOGY

Ingesting Nanotubes

One concern in nanotechnology is that the uptake and fate of nanomaterials in cells may differ from those of larger micrometer-scale particles. Two groups have imaged the uptake of carbon nanotubes into mammalian cells. Cherukuri *et al*. incubated single-walled carbon nanotubes (SWNTs, about 1 nm in diameter and 1 μm in length) solubilized in Pluronic surfactant with cultured mouse peritoneal macrophage-like cells. Using near-infrared fluorescence imaging, they found that the macrophages ingested the SWNTs and apparently localized them in phagocytic compartments, without signs of acute toxicity. Monteiro-Riviere *et al*. looked at the uptake of multiwalled carbon nanotubes (MWNTs) by cultured human epidermal keratinocytes. Although most of the MWNTs, which were not modified after growth on silicon wafers, did not interact with the cells, enough did that 84% of the cells took up MWNTs after 48 hours of exposure at 0.4 mg/ml. After 24 hours at this concentration, the percentage of viable cells decreased by 30%, and transmission electron microscopy revealed MWNTs (some almost 4 mm in length) within cytoplasmic vacuoles in 60% of the cells. Although these cultured keratinocytes lack the protective stratum corneum of human skin, these results indicate that further studies of carbon nanotube exposure risks are in order. — PDS

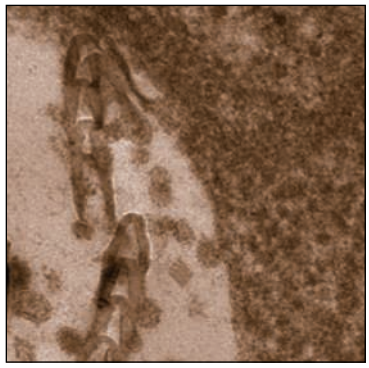

Micrograph of MWNT within a keratinocyte vacuole.

J. Am. Chem. Soc. **126**, 15638 (2004); *Toxicol. Lett.* 10.1016/j.toxlet.2004.11.004

PSYCHOLOGY

Individual Differences

Neuroimaging has begun to map specific patterns of brain activity associated with cognitive functions. The usual statistical analysis of these rather large data sets relies on having about a dozen subjects and looking for consistent neuronal activations, but an increasing interest in how personality traits and mood states might influence responses has led to looking at activations across subjects.

Canli *et al*. used the emotional Stroop interference task to show that negative words elicited greater activation of the anterior cingulate region, which is known to be involved in processing cognitive/emotional stimuli, with greater negative mood of the subject; whereas activation due to positive words correlated with higher scores for the trait of extraversion. This dissociation might plausibly be interpreted as reflecting a greater susceptibility to being distracted by negative interfering stimuli while in a negative frame of mind and, conversely, being more receptive to positive stimuli if one is inherently an outgoing sort. Kumari *et al*. have used the n-back task to show that with increasing cognitive

CREDITS: (TOP) VAN ROESSEL *ET AL., CELL* **119**, 707 (2004); (BOTTOM) MONTEIRO-RIVIERE *ET AL., TOXICOL LETT.* 10.1016/J.TOXLET.2004.11.004

demands, activation in the anterior cingulate increased in all subjects, but much more so for the ones who scored as extroverts, consistent with them being less aroused or anxious at rest and hence having to mobilize more cognitive resources to perform at the same level. — GJC

Behav. Neurosci. **118**, 897 (2004); *J. Neurosci.* **24**, 10636 (2004).

CHEMISTRY

Salting in Nanotubes

Single-walled carbon nanotubes (SWNTs) are of interest because of their outstanding mechanical and electrical properties, and the tendency of SWNTs to aggregate into bundles has been overcome by modifying them chemically, dissolving them in superacids, or by sonicating them with the addition of surfactants or polymers. Unfortunately, all of these methods are based on an intercalating mediator that prevents the strong sidewall van der Waals forces from reaggregating the tubes, and many of these methods cut or damage the tubes.

Pénicaud *et al.* show that SWNTs can be reduced using alkali metals to form polyelectrolyte salts that dissolve in aprotic polar organic solvents such as dimethyl sulfoxide. Elemental analysis indicated that the metals removed one negative charge for every 10 carbon atoms; however, only one of five charges was dissociated, whereas the others were balanced by the condensation of alkali cations. The nanotube polyelectrolyte solutions appear to be stable indefinitely, although they need to be kept under an inert atmosphere because the reduced SWNTs are sensitive to air. — MSL

J. Am. Chem. Soc. 10.1021/ja0443373 (2004).

MOLECULAR BIOLOGY

Making a Copy of a Copy

MicroRNAs (miRNAs) are small noncoding RNAs that are complementary to their targets and are encoded in the genomes of most plants and animals as self-complementary fold-back precursors, which undergo processing into ~21-nucleotide (nt) effector species. The fold-back structure of miRNA precursors suggests that miRNA genes may have evolved from inverted duplications of their target genes, and Allen *et al.* explore this possibility in *Arabidopsis*. If miRNAs arose in this manner, they should have regions of homology extending beyond the ~21-nt complementary core. Of the 91 miRNA loci used to search the *Arabidopsis* genome, only miR161 and miR163 showed extended sequence similarity to their target genes and to closely related family members. Unlike other miRNA multigene families, miR161 and miR163 are represented by single genes and are not found outside *Arabidopsis*, supporting the idea that they might be evolutionarily recent additions. Potential evolutionary intermediates of miRNAs were also identified; one of these loci is located close to its putative targets, as are miR161 and miR163, and phlyogenetic analysis indicates that all three are related to their targets. — GR

Nature Genet. **36**, 1282 (2004).

EVOLUTION

. . . and Men

Fossil and molecular evidence have hitherto suggested that the cercopithecoids (Old-World monkeys) and hominoid (ape and human) lineages diverged around the Oligocene/Miocene boundary, 23 to 25 million years ago (Ma). In a challenge to the recentness of this estimate, Steiper *et al.* adopt a molecular approach called quartet analysis, which uses sequence data from two pairs of species from two clades to assess divergence dates with greater precision. For the hominoid branch, chimpanzee and human were chosen, and for the cercopithecoids, baboon and macaque; the divergence dates between the members of each pair were calibrated from fossil data. The resulting model suggests that the hominoid/cercopithecoid divergence took place in the Early Oligocene, 29 to 34.5 Ma. The implication of this result is that several million years of early hominoid history have yet to be sampled paleontologically and that *Proconsul*—hitherto considered the earliest of all hominoids—may have had earlier hominoid ancestors. — AMS

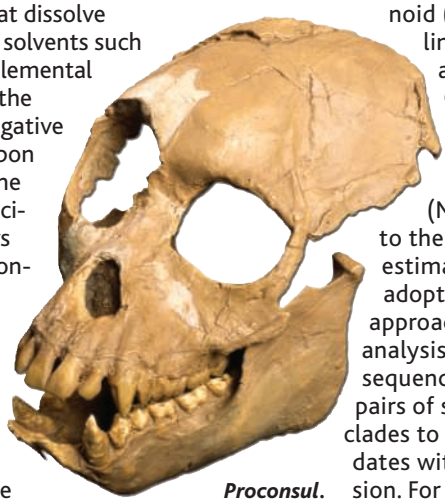

Proconsul.

Proc. Natl. Acad. Sci. U.S.A. **101**, 17021 (2004).

CREDITS: PASCAL GOETGHELUCK/PHOTO RESEARCHERS, INC.

NetWatch

edited by Mitch Leslie

WEB LOGS

Sifting for Truth About Global Warming

Frustrated by Web sites claiming to debunk global warming, several scientists this month launched their own blog on the evidence that humans are heating up the planet. Realclimate.org is hosted by a public relations firm called Environmental Media Services, but nine academic and government scientists write the content, says co-organizer Gavin Schmidt of NASA (speaking in a personal capacity). They hope to counter industry-supported sites such as www.CO2science.org and www.junkscience.com, where so-called experts "have a habit of seriously misquoting, distorting, and outright manipulating data," says Schmidt.

So far, the site has addressed topics such as why the heat generated by large cities (above, an infrared image of Atlanta) makes only a minuscule contribution to surface warming and the flaws in Michael Crichton's latest novel, *State of Fear*, which dismisses global warming as hype. Visitors can chime in, but comments are screened before they're posted.

www.realclimate.org

NET NEWS

HapMap Lifts Data Restrictions

A global project to map human genetic variation has fully opened its data to the public. The International HapMap Consortium is sequencing the DNA of 270 people from four populations to map common patterns of mutations (*Science*, 21 November 2003, p. 1305). Because of concerns that someone might try to patent the data, the project had required users downloading results on individuals to sign a nonexclusive license agreement. But enough human variation information is now publicly available that patenting is no longer a worry, organizers say. The removal of restrictions now means other genome databases, such as Ensembl, can fold HapMap findings into their sites.

www.hapmap.org

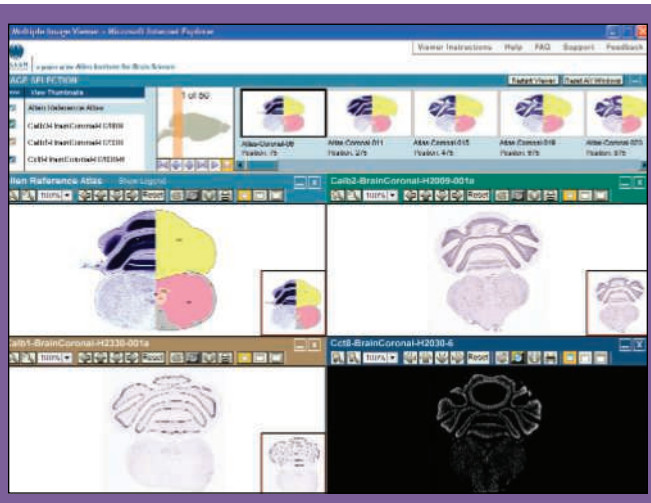

DATABASE

Genes on the Brain

Researchers are just beginning to decipher how differences in gene activity allow different parts of the brain to recall memories, sense pain, move limbs, and carry out other jobs. A new atlas aims to provide a picture of gene expression throughout the brain for the most common lab mouse strain. The ambitious project—aimed at neuroscientists, drug designers, behavioral geneticists, and other experts—is one of the first fruits of the Seattle, Washington–based Allen Institute for Brain Science, launched last year with seed money from Microsoft co-founder Paul Allen (*Science*, 19 September 2003, p. 1642). This month's initial data release consists of brain slices stained to indicate activity levels of 2000 genes. Users can voyage through the brain slice by slice, zooming in on particular cells and superimposing slices from different structures to compare expression patterns. The institute plans to post results for the remaining 18,000 or so mouse genes by the end of 2006.

www.brainatlas.org

TOOLS

Cartography of Pollution

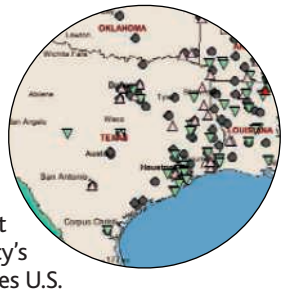

Wondering which factories have trimmed their emissions of lead the most over the last decade? Want to find out how much benzene has been escaping from the refinery down the road? Visit TOXMAP, a new site from the National Library of Medicine that lets you chart values from the Environmental Protection Agency's Toxics Release Inventory. The annual report tallies U.S. emissions of some 650 hazardous chemicals into the air, water, and soil. Using TOXMAP, you can pinpoint pollution sources or map up to 15 years of data to identify emission trends. For example, this map (above) indicates release of formaldehyde in 2002, compared to the average for the years 1987–2001. The red triangles denote sources whose output climbed the most.

toxmap.nlm.nih.gov/toxmap/main/index.jsp

SOFTWARE

Genome Speed-Reading

A free program from the Broad Institute in Cambridge, Massachusetts, can help researchers locate genes and determine their functions in freshly sequenced genomes. Known as Argo, the new software makes it easy to compare notations about DNA landmarks, such as segments that might code for a piece of a protein, identified by automated genome-parsing programs. Argo-nauts can zoom in on these features and craft hypotheses about how they mesh to form a working gene. Another feature lets visitors analyze sequences from different species side by side.

www.broad.mit.edu/annotation/argo

Send site suggestions to netwatch@aaas.org. Archive: www.sciencemag.org/netwatch

CREDITS (TOP TO BOTTOM): NASA; ALLEN INSTITUTE FOR BRAIN SCIENCE; NATIONAL LIBRARY OF MEDICINE

Published by AAAS

This Week

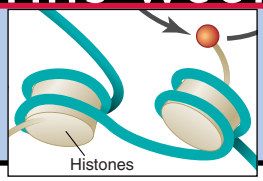

PAGE 2171
A long-sought genetic switch

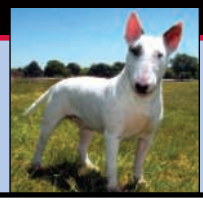

2172
A driver for dog evolution?

HIV TRANSMISSION

Allegations Raise Fears of Backlash Against AIDS Prevention Strategy

Much to the dismay of AIDS researchers and clinicians around the world, the Associated Press (AP) ran a series last week that has reignited debate about the safety of one of the most heralded interventions in AIDS prevention: use of the drug nevirapine to prevent HIV transmission from an infected mother to her infant. This treatment likely has spared tens of thousands of children from the disease. Experts insist that, although the drug is not problem-free and some irregularities occurred during one clinical trial, nevirapine's benefit far outweighs the risks.

The AP stories focus on a study in Uganda, which revealed in September 1999 that a single dose of nevirapine given to an HIV-infected mother in labor and to her infant could halve transmission rates. The finding, later confirmed by other studies, led to the widespread use of this cheap, simple intervention in poor countries. The AP series alleges that officials at the National Institute of Allergy and Infectious Diseases (NIAID), which funded the so-called HIVNET 012 study, downplayed problems that surfaced in 2002, did not promptly communicate them to the Food and Drug Administration (FDA) and the White House, and steamrolled over concerns of its staff, one of whom has gone to Congress with charges of an alleged "cover-up."

The study had "irregularities with record keeping" at its headquarters in Kampala, Uganda, acknowledges Clifford Lane, NIAID's deputy director. But he stresses that "there has been nothing to refute the claims of safety and efficacy with regard to single dose nevirapine treatment to prevent the transmission from mother to infant." And he worries that "this particular news story may cause people to stop using nevirapine, and infants could be infected and die needlessly."

In the wake of the story, Rev. Jesse Jackson, a former U.S. Presidential candidate, decried NIAID's actions as "a crime against humanity" and called for Congress to investigate "this catastrophe." In South Africa, where President Thabo Mbeki's government has been criticized for its slow adoption of nevirapine to prevent mother-to-child transmission (MTCT), the political online publication *ANC Today* said the AP stories proved the hesitation was "fully justified," and it assailed NIAID for using Africans as "guinea pigs."

Nonprofit organizations that provide nevirapine to prevent maternal-infant transmission in developing countries have struck back on their websites. The Elizabeth Glaser Pediatric AIDS Foundation in Los Angeles notes that the drug has been used hundreds of thousands times "without any significant toxicities for mothers or babies." A statement from Global Strategies for HIV Intervention, based in San Rafael, California, says six other MTCT studies confirm the safety and efficacy of nevirapine and stresses that the problems at the Ugandan site have been known for years. "This is not new news," says the statement.

Center of controversy. A shack on the grounds of Kampala's Mulago Hospital served as the HIVNET 012 trial site.

In fact, Boehringer Ingelheim, the drug's manufacturer, first uncovered problems with HIVNET 012, which involved 645 mother-infant pairs. Nevirapine is an FDA approved drug to treat HIV infection, but the Uganda results led Boehringer to seek FDA endorsement for its use in preventing MTCT, explains principal investigator J. Brooks Jackson of Johns Hopkins University, which collaborated with researchers from Makerere University in Kampala. As part of the process, Boehringer audited the Uganda site in January 2002 and discovered discrepancies in the records. A Boehringer representative said the audit turned up "a lot of pin pricks but no show stoppers,'" recalls Jackson.

When advised of the problems later that month, NIAID's Division of AIDS should have informed FDA within 3 days but did not. "That was an error," concedes Edmund Tramont, who heads NIAID's Division of AIDS and who did not learn about the discrepancies until March 2002. At that point NIAID informed FDA, shut down the site for new studies, and notified the public, triggering a flurry of press coverage. NIAID also hired a contractor to audit the site. That second audit revealed serious unreported incidents, including deaths and "thousands" of less serious "adverse events." Tramont's worries were assuaged when he learned that the unreported deaths, which were not related to the drug, had in fact been recorded, and that the unreported adverse events were also unrelated to the drug and involved diseases like malaria and tuberculosis.

Because an initial review of the discrepancies uncovered no safety issues, NIAID officials say they saw no reason to give the White House a detailed briefing about their concerns. That June, President George W. Bush announced a $500 million program to prevent MTCT in developing countries that would rely heavily on nevirapine. The AP alleges that NIAID "chose not to inform the White House" about its internal concerns for fear of "scuttling the use of nevirapine in Africa."

Tramont sent over yet another audit team. This third audit compared the hospital records of 80 mother-infant pairs to the information in the database—-a statistically significant sample. It found discrepancies, but they were relatively infrequent. In early April 2003, when NIAID was wrestling with whether to reopen the Ugandan site for research, NIAID's Betsy Smith wrote a report for FDA that sharply criticized the study's adverse event reporting. "Subject records on site were of poor quality and below expected standards of clinical research considered at the forefront of medical research," Smith concluded. Tramont edited the report and removed that detail and other critical aspects, a move the AP reported led to "disbelief" among some staffers. Tramont says he made the changes because he felt Smith relied too heavily on the misleading second audit.

CREDIT: MALCOLM LINTON

Published by AAAS

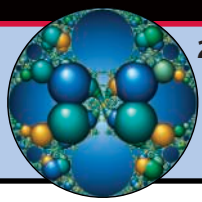

Jonathan Fishbein, the NIAID staffer who has gone public with his concerns, became embroiled in what was then a backroom dispute in July 2003, shortly after he was hired by the Division of AIDS to improve clinical trials. Fishbein wanted more time to review the issues before allowing the Ugandan site to reopen for new clinical studies, but Tramont was impatient. "I want this restriction lifted ASAP because the site is now the best in Africa run by black Africans," Tramont e-mailed Fishbein. "The site was shut down for 15 months," says Tramont. "It was stupid and bureaucratic not to reopen it."

In February 2004, with office tensions mounting, Fishbein received notice that he was being terminated for "non-performance." He took complaints of what he viewed as his mistreatment and the scientific cover up to many officials, including the head of the National Institutes of Health (NIH). He also sought whistleblower status. Although NIH will not discuss Fishbein by name, deputy director Raynard Kington says a research integrity officer reviewed what he called allegations of "scientific misconduct" and determined they were "erroneous." NIH did ask the Institute of Medicine to review the scientific issues surrounding HIVNET 012, and that panel plans to issue a report in March 2005. Meanwhile, Fishbein says he is "not is disagreement" that nevirapine saves lives. "My issue is not nevirapine, but the process." –JON COHEN

HIGH-ENERGY PHYSICS

Report Slams SLAC's Safety Practices

Management at the Stanford Linear Accelerator Center (SLAC) routinely disregarded safety regulations in order to keep the scientific results coming. That's the conclusion of a Department of Energy (DOE) investigation into a serious electrical accident this fall at DOE's high-energy physics facility in Menlo Park, California (*Science*, 29 October, p. 788). The accident has led to the indefinite shutdown of the lab's accelerators, causing SLAC to lose ground to a Japanese laboratory engaged in the same type of research.

Released on 15 December, the DOE accident report blasts SLAC management for fostering a culture in which "unsafe conditions have become a part of the everyday way of doing business." SLAC spokesperson Neil Calder says the lab will take its comeuppance and do what's needed to fix the problems. "The report is the report," says Calder. "We respect that, and now we can use [the report] as a means of going ahead" to improve safety.

The 11 October accident occurred when an electrician tried to install a circuit breaker in a 480-volt power panel without shutting off the electricity, a practice known as hot work. The action presumably was a timesaving step. A short caused an explosion that set the electrician's clothes on fire. He suffered severe burns over 50% of his body and was hospitalized for several weeks. The accident automatically triggered the inquiry by DOE's Office of Environment, Safety, and Health. The lab's flagship PEP-II particle collider and other accelerators had been taken down for repairs and improvements in July but were scheduled to resume operations in mid-October.

Investigators found plenty of blame to go around. There was no justification for installing the breaker with the power on, they concluded, and the SLAC field supervisor who ordered the work had not obtained the required hot work permit. The electrician, a contractor, lacked the face shield, hood, fire-resistant clothing, and insulated tools that would have protected him. Moreover, according to the report, local DOE officials had not been pressing the lab to follow its own safety regulations.

But investigators directed their harshest criticism at laboratory management. "It appears that SLAC has consistently placed operations ahead of safety," the report says. Investigators found that hot work was routinely performed without permits, and that management allowed such breaches of protocol in order to keep the lab's accelerators running and the data flowing. "SLAC's emphasis on the scientific mission as a means to secure funding from the [DOE] Office of Science and compete with other laboratories reached [the field supervisor's] level as direction to 'just get the job done,' " the report states.

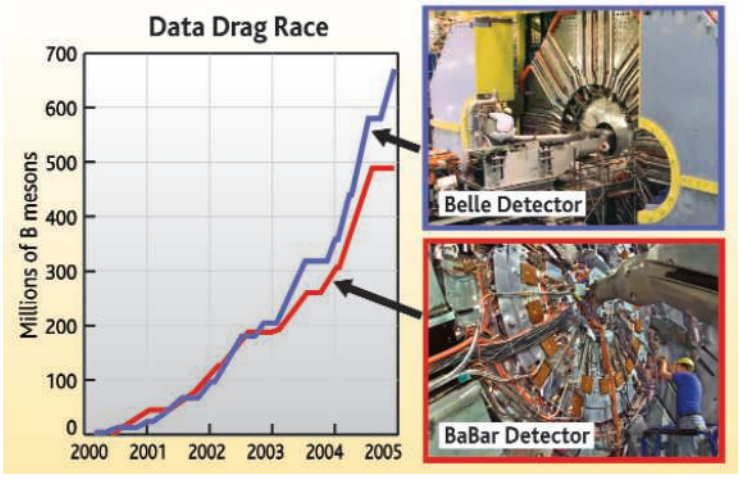

Busy as Bs. SLAC's BaBar detector is falling behind its Japanese counterpart in spotting B mesons.

SLAC's main competitor is the Japanese particle physics laboratory KEK in Tsukuba. Like SLAC, KEK has a collider designed to produce fleeting particles called B mesons, which may hold the key to understanding the subtle differences between matter and antimatter. In recent years KEK's collider has pumped out significantly more B mesons than SLAC's (see graph). SLAC researchers are still competitive, says Sheldon Stone, a physicist at Syracuse University in New York, but "it certainly doesn't help that they're shut down."

SLAC and local DOE officials must draw up a corrective action plan, to be submitted to DOE by early February. The lab's accelerators won't start up until DOE is sure that the lab can operate safely, says Milton Johnson, chief operating officer for DOE's Office of Science. "We'll take whatever time is necessary to assure that the employees and workers are safe," he says. In the meantime, Stanford University, which runs the lab for DOE, has convened its own panel of experts to examine lab safety.

–ADRIAN CHO

CREDITS: PHOTOS (TOP TO BOTTOM) COURTESY OF KEK; COURTESY OF LAWRENCE BERKELEY NATIONAL LABORATORY; GRAPH SOURCE: SLAC AND KEK

Published by AAAS

CLINICAL TRIALS

Halt of Celebrex Study Threatens Drug's Future, Other Trials

Another COX-2 inhibitor is on the ropes. On 17 December, the National Cancer Institute (NCI) halted a 2000-person clinical trial testing whether Celebrex could inhibit colon polyps. Hours later, two more cancer trials and an Alzheimer's trial testing Celebrex and Naproxen were suspended by the scientists overseeing them. In addition, dozens of other trials involving the drug were undergoing careful review amid a flurry of conference calls. As *Science* went to press, the National Institutes of Health (NIH) was trying to decide whether to halt its Celebrex trials—roughly 40 in all—and the Food and Drug Administration (FDA) was weighing whether to pull Celebrex off the U.S. market.

Heart-stopper. Celebrex's side effects led to suspended studies.

The scenario was strikingly similar to what happened this fall to Vioxx, a COX-2 inhibitor manufactured by Merck. The company withdrew the drug on 30 September after a study of Vioxx's effect on colon polyps revealed a doubling of heart attacks and strokes from the drug after 18 months of use. That action triggered a painstaking review of cardiac events in the NCI study called Adenoma Prevention with Celecoxib (APC). Experts found a 2.5-fold increase in heart attacks and strokes for those taking a moderate dose of Celebrex, and a 3.4-fold increase for those taking a high dose. As with Vioxx, extended use of the drug seemed to correlate with cardiac hazards: Volunteers were taking Celebrex for an average of 33 months.

Pfizer, the drug's maker, is so far hesitant to withdraw Celebrex. "The cardiovascular findings ... are unexpected and not consistent" with a comparable colon polyp study that Pfizer is running, said Hank McKinnell, the company's chairman and chief executive officer, in a statement. Pfizer has stopped advertising Celebrex to consumers, however.

NIH director Elias Zerhouni said in a hastily called press conference last week that for now, the agency is leaving decisions about trial suspension up to individual investigators. But Zerhouni ordered a review of all NIH-funded studies of COX-2 inhibitors and requested that researchers send out revised informed consent forms to participants. In addition to cancer studies, NIH was funding a 2500-person trial of whether Celebrex can prevent Alzheimer's.

"It may not be possible to get these trials done," says Charles Geyer, director of medical affairs for the National Surgical Adjuvant Breast and Bowel Project (NSABP), a cooperative group funded by the NCI that runs multi-center trials. NSABP has suspended its two Celebrex studies while it reviews the APC data. One study, slated to enroll 1200 people, is testing whether Celebrex can prevent colon polyps; a second, slated to enroll 2700 women, is testing Celebrex as a treatment for breast cancer.

"This is going to put a brick wall in the field," says Richard Goldberg of the University of North Carolina, Chapel Hill, and the lead investigator on the NSABP colon polyp trial. "The COX-2 inhibitors have been an important therapeutic approach." In addition to its use for arthritis pain, Celebrex is already approved to reduce intestinal polyps in patients with familial adenomatous polyposis, a hereditary condition that leads to colon cancer.

Although no published Celebrex study is as extensive as the APC trial, many researchers were taken aback by the APC results. Historically, Celebrex has displayed fewer problems than Vioxx, perhaps because it targets the COX-2 enzyme less selectively. "We were dismayed" by the APC findings, says John Breitner, a psychiatrist at the VA Puget Sound and the University of Washington in Seattle and the lead investigator on the Alzheimer's prevention trial.

Another COX-2 inhibitor made by Pfizer, Bextra, was also recently shown to cause cardiovascular problems in high-risk patients. That has added to concern about the whole class of drugs, although it's not clear if selective blocking of COX-2 explains everything. Scientists may need to reconsider other mechanisms, and whether long-term use of non-steroidal anti-inflammatory drugs in general can cause blood clotting. —JENNIFER COUZIN

SCIENTIFIC PUBLISHING

Editing No Longer Infringes U.S. Trade Sanctions

Pushed into a legal corner, the U.S. Treasury Department last week removed all restrictions on editing manuscripts from authors in three countries under a U.S. trade embargo. Publishers hailed the step by the department's Office of Foreign Assets Control (OFAC). But some wondered why the same freedoms were not extended to music, films, and other forms of artistic expression, and others questioned whether the government should be exerting any control at all.

Under the new ruling, U.S. citizens are no longer required to seek a license from OFAC for any transactions with individuals in Iran, Cuba, and Sudan that "directly support the publishing and marketing of manuscripts, books, journals, and newspapers." It overturns two recent OFAC pronouncements that had sparked intense protests from publishers and led to a suit this fall by a coalition of organizations (*Science*, 1 October, p. 30). Iranian human-rights activist and 2003 Nobel Peace Prize winner Shirin Ebadi joined the lawsuit, claiming suppression of her memoirs.

"This is a true victory for the freedom of the press," says Marc Brodsky, executive director of the American Institute of Physics, which publishes 11 journals. "It's unfortunate that the bureaucracy couldn't get itself organized to change the rules until we went to court." The plaintiffs have not yet decided whether to drop the suit.

OFAC denies that the ruling, which applies to "academic and research institutions and their personnel," was a response to the legal challenge. "OFAC's previous guidance was interpreted by some as discouraging the publication of dissident speech from within these oppressive regimes. This is the opposite of what we want," says the Treasury's Stuart Levey.

The 16 December statement may not be enough to end the controversy, however. Observers note that the new ruling retains OFAC's jurisdiction over publishing and also prohibits U.S. citizens from collaborating on manuscripts from government officials in the embargoed countries. Representative Howard Berman (D–CA), author of a 1988 amendment to the trade sanctions law that exempts informational materials, is unhappy that the new ruling exempts only publishing. "Why should it be OK for a publisher to commission a book from an Iranian dissident but not for a film studio to work with a Sudanese filmmaker?" he says. "The [decision] reflects the fact that these regulations were a desperate attempt to head off mounting legal and political pressure."

–YUDHIJIT BHATTACHARJEE

CREDIT: MARY ALTAFFER/AP PHOTO

MOLECULAR BIOLOGY

Long-Sought Enzyme Found, Revealing New Gene Switch on Histones

In the molecular biology equivalent of stubbing one's toe on King Tut's undiscovered tomb, a team of scientists, to its great surprise, has identified a genetic switch hunted by biologists for decades. The switch, buried deep inside a cell's nucleus, is an enzyme that chemically alters the protein spools around which a cell's DNA wraps. The enzyme's discovery, reported online last week in *Cell* and in the 29 December issue—along with related finds published this fall—has scientists racing to find more switches like it. The switches could reveal much about how cells control gene activity and illuminate cancer, multiple sclerosis, and other diseases that may be spurred by gene expression gone awry.

"It's the sort of thing that everybody wanted to find," says Tony Kouzarides, a molecular biologist at the University of Cambridge, U.K. In the last couple of years, though, hope had faded. "The feeling," says Kouzarides, "was … that they didn't exist."

The newly discovered enzyme acts upon histones, the specialized proteins that

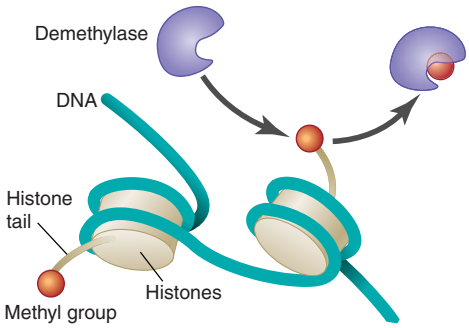

Mission Accomplished. Scientists have finally found an enzyme acting as a histone demethylase.

strands of DNA loop around in order for a cell to condense its genetic material inside a nucleus. Rather than inert spools, histones are increasingly seen as active cogs in a cell's gene-regulation machinery. For example, certain enzymes can add methyl groups to tails that protrude from histones, which turns genes either on or off. But biologists couldn't find enzymes that did the opposite, leaving them wondering whether methylation was permanent.

Although many biologists had searched for these so-called histone demethylases, Harvard molecular biologist Yang Shi wasn't one of them. Rather, his group had become entranced by an unusual protein complex that performs a dizzying array of functions in cells. One component of the complex, an enzyme found in species from yeast to people, had an ability to quash gene expression on its own. Trying to discern how it acted, Shi and his colleagues spent a year ruling out every viable option but histone demethylation, which they left for last in part because few believed it existed.

Eventually, the team conducted biochemistry experiments showing that the enzyme demethylated a specific amino acid, a lysine, on the tail of one kind of histone. Shi's group then used the technique of RNA interference to reduce levels of the enzyme in human cells. That led to methylation of various histones and increased the expression of nearby genes. This, says Shi, drove home that the enzyme, dubbed lysine specific demethylase 1 (LSD1), represses specific genes by maintaining unmethylated histones.

Other scientists are struck by the work. "It opens up a whole new horizon," says David Allis, a molecular biologist at Rockefeller University in New York City who has argued for the existence of a "histone code" in which methylation and other histone tail modifications control gene expression. A report published this fall in *Science* by Allis and Scott Coonrod at Cornell's Weill Medical College in New York City, and a separate paper published at the same time in *Cell* by Kouzarides's team, offered the first hints that cells could perform demethylation. The two teams independently found that part of a human protein could chemically transform amino acids on a histone, demethylating them in the process. But in those studies, demethylation took place amid other chemical reactions. Shi's paper describes "true demethylation," says Kouzarides.

Questions to be explored now include how demethylation is controlled and what role it might play in diseases. "We just have to understand what signals trigger this regulation," says Stéphane Richard, a molecular biologist at McGill University in Montreal. Kouzarides and others predict that additional histone demethylases will be found. Some may activate genes instead of repressing them as LSD1 does, the researchers say.

Several diseases, in particular certain leukemias and colon cancer, have been tentatively linked to faulty methylation, so histone demethylases could represent inviting drug targets. Indeed, Shi has already filed for a patent on LSD1, and Allis and a company with which Kouzarides is affiliated have done the same for their enzyme.

—JENNIFER COUZIN

CREDIT: K. SUTLIFF

ScienceScope

Bush Dives into Oceans

Responding to calls from two blue-ribbon panels for better coordination and more resources, the White House last week created a Cabinet-level committee to oversee the management of U.S. marine resources.

The new committee is part of a 40-page action plan that addresses some of the 200 recommendations from a congressionally mandated commission, headed by retired Adm. James Watkins, that reported this fall (oceancommission.gov) and an earlier report by the Pew Oceans Commission (http://www.pewoceans.org/oceans/downloads/oceans_report.pdf). The multiagency body, coordinated by the White House Council of Environmental Quality (CEQ), has been asked to design a plan to set ocean-related research priorities, expand ocean buoy monitoring, fund new research vessels, deal with depleted fish stocks, protect coral reefs, and assess oil and gas resources.

The plan is a step in the right direction, says Lisa Speer of the Natural Resources Defense Council in New York. "But it's not clear what they are going to be doing or how quickly."

—ELIZABETH PENNISI

Italy Hosts a Climate Research Center

TRIESTE, ITALY— Italy will host a new Euro-Mediterranean Center for Climate Change Study (CMCC) to operate from the National Institute for Geophysics and Vulcanology (INGV) in Bologna, with headquarters and a dedicated supercomputer at the University of Lecce. Officials made the announcement during last week's meeting in Buenos Aires to review the Kyoto Protocol, a global pact to reduce carbon dioxide emissions.

The four Italian ministries that created the center have pledged $36 million through 2007. CMCC will coordinate research on climate change and disaster planning, complementing work in the United States, the U.K., Germany, and Japan. INGV currently concentrates on climate simulations based on models of the atmosphere's circulation, the oceans, the Mediterranean Sea, and marine ice. "We aim to take this a step further," explains new CMCC head Antonio Navarra, by coupling these models with models of the earth's biosphere, marine ecosystems, and chemistry of the atmosphere to allow "simulations that are more reliable and have higher resolution."

—SUSAN BIGGIN

Published by AAAS

GENETICS

A Ruff Theory of Evolution: Gene Stutters Drive Dog Shape

Evolutionary biologists like to go to exotic places for their studies. For his graduate work in evolutionary biology at the University of Texas Southwestern Medical Center in Dallas, John Fondon III simply headed to the local dog park. He wanted to sniff out DNA changes that enabled canines to evolve quickly into more than 100 breeds, and dog parks were a good source for the DNA of purebreds.

Armed with DNA from more than 100 dogs, including their own, Fondon and his adviser Harold Garner have now shown that slight differences in the lengths of certain genes involved in development can transform a collie nose into a puglike one and even change the number of toes in one breed. Furthermore, their study, reported in the 28 December *Proceedings of the National Academy of Sciences*, drives home the potential evolutionary importance of repetitive DNA sequences called tandem repeats. Changes in the size of a tandem repeat within a gene can alter the gene's protein, making it work more or less efficiently. "We think the value and impact of these [repeats] on genetics and on phenotype is very much underestimated," says Garner, a physicist. "They are resources in the genome for things to rapidly evolve," not just in dogs but in other species as well.

Less DNA, more toes. The sixth toe (x-ray) in Great Pyrenees seemed to arise when a key gene lost some bases.

That provocative proposal has received mixed reviews so far. Fondon and Garner have yet to prove that differences in the lengths of tandem repeats matter, says Robert Wayne, an evolutionary biologist at the University of California, Los Angeles, but the concept intrigues him. "Tandem repeats, generally regarded as junk DNA, offer a novel mechanism for evolutionary change," agrees Wayne.

Fondon began to chase down tandem repeats after a stint on the Human Genome Project. These genetic stutters are sequences of three or so DNA bases that are repeated over and over again. No one knows for sure what causes a particular stutter to double or triple in number. But once multiple copies exist, enzymes copying DNA can drop off repeats or add extra copies.

With Garner, Fondon had come up with a program to identify tandem repeats in the human genome. "I was really dumbfounded [at] the number and types of repeats coded in the genes," particularly developmental ones, Fondon recalls. Intrigued by the role these repeats might have in evolution, he turned to dogs. Most researchers assume that the DNA variation underlying evolutionary adaptations comes about by single base changes in a gene's sequence. But modern dogs have changed much faster than can be explained by these so-called point mutations.

So, using human and mouse genes known to be involved in development as probes, Fondon and Garner tracked down 37 related canine genes and sequenced the repetitive regions in each one in 92 dog breeds. They initially tapped their own pets for blood samples: Fondon's Labrador retriever, and Garner's Weimaraner and Dalmatian. Next, Fondon headed to dog parks. He also tracked down canine DNA samples from kennel clubs and breeders he solicited on the Internet. Garner even persuaded one of the university's key donors to make an unusual gift: blood from her three dogs.

The 142 dogs tested diverged significantly in the number of repeats in the various development genes. To determine if these tandem repeat variations translated into physical differences, i.e., altered phenotypes, Fondon and Garner used a high-resolution laser scanner that generated three-dimensional images of dog skulls. A program that morphed one breed's skull into another's helped quantify differences between breeds. The researchers then correlated the degree of change with variations in repeat length and in the ratios of different repeats.

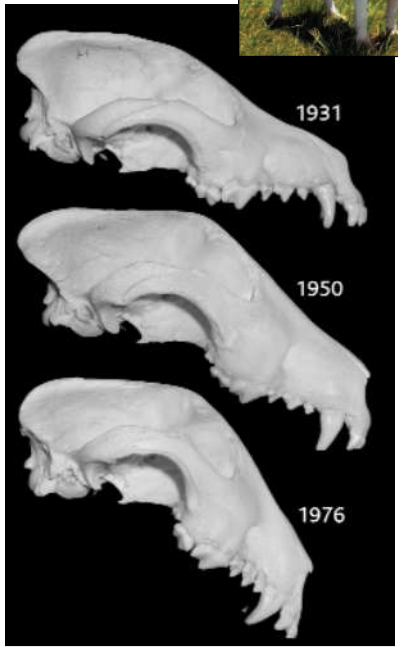

Snout slip. In 65 years, changes in repetitive DNA may have caused the bull terrier's nose to point ever more downward.

For example, the length of a breed's snout correlated directly with the number of repeats in a gene called *Runx-2*. But there was a twist, Garner notes. *Runx-2*'s tandem repeat consists of two different three-base sequences, randomly ordered along the length of the repeat. If there's more of one threesome relative to the other, that breed's muzzle tends to be longer and straighter.

The researchers found an intriguing connection with another gene, *Alx-4*. Most dogs have five toes on their hind legs, but members of the Great Pyrenees breed tend to have six. Knowing that *Alx-4* causes mutant mice to have an extra toe, Fondon checked that gene in dogs. The tandem-repeat region of the six-toed Great Pyrenees was 51 bases shorter than in other breeds. In contrast, a five-toed Great Pyrenees had the full complement of bases.

By comparing DNA and skulls of bull terriers from the 1930s and now, Fondon and Garner may have seen evolution in action. The older skull was less droopy, and DNA extracted from it also had one more repeat in the *Runx-2* gene than did the modern terrier's gene.

Sean Carroll from the University of Wisconsin, Madison, worries that Fondon and Garner overestimate the importance of tandem repeats in typical evolution, noting that dog owners have bypassed natural selection by breeding for physical characteristics without thought to how the resulting changes would impact a dog's survival in the wild. Intensive breeding may have prompted the rampant changes in tandem repeats, more so than would occur under natural conditions. But David King, an evolutionary biologist at Southern Illinois University in Carbondale, argues that it doesn't matter whether natural selection or artificial breeding is at work—the role of tandem repeats is now clearly important: "[Fondon and Garner] have shown that tandem repeats are effective for fine-tuning evolution."

—ELIZABETH PENNISI

CREDITS (TOP TO BOTTOM): JOHN FONDON; JOHN FONDON AND MARC NUSSBAUMER; (INSETS) ©AKC. PHOTOS BY MARY BLOOM

Published by AAAS

EDUCATION

Singapore Leads, U.S. Lags in Science, Math Student Achievement

Singaporean students lead the world in math and science, according to the latest international comparison of student performance. Educators say that the top ranking, among elementary and middle school students from as many as 49 countries, also demonstrates how a nation's commitment to excellence can pay off fairly quickly.

The findings come from the 2003 Trends in Mathematics and Science Study (TIMSS) released last week by the International Association for the Evaluation of Educational Achievement (timss.bc.edu). Singapore had excelled in two previous studies, but this time its fourth graders rose from fifth to first place in science after education officials revamped the small island nation's curriculum and strengthened teacher training. "The lesson here is that when you focus on a goal, you can produce measurable results within a short period of time," says Patrick Gonzales, an analyst with the U.S. National Center for Education Statistics in Washington, D.C.

More than 360,000 fourth- and eighth-grade students participated in the 2003 study, taking math and science tests designed to assess both knowledge and understanding and based on common elements of the various curricula (see box). The survey's top tier has a decidedly Asian flavor, with students from Japan, Chinese Taipei, and Hong Kong ranking among the top five countries in both math and science at both grade levels (see tables). Most European countries fall somewhere in the middle, whereas most Middle Eastern and North African nations lag. And although boys and girls have similar scores in math at both levels in most countries, boys show significantly higher achievement than girls in eighth-grade science.

For U.S. students, the results send a mixed message. Eighth-graders did better in both subjects, rising from 28th (of 41 countries) to 15th (of 46) in math and from 17th in 1995 to 9th in science. But fourth-grade students stayed in the middle of the pack in math—12th out of 26 and 25 countries, respectively, and lost ground in science, slipping from 3rd to 6th place.

The decline in fourth-grade science is a result of less time spent on the subject, argues the National Science Teachers' Association (NSTA). "We have been hearing from many elementary teachers that they are not teaching science because of the increased emphasis on literacy," says NSTA executive director Gerald Wheeler. "Science is essentially being squeezed out of the elementary classroom."

One piece of good news for U.S. educators is a shrinking achievement gap between white and minority students in eighth-grade science. But the survey highlights the continued disparity in achievement along economic lines. Eighth-graders in schools with 75% or more students eligible for free or reduced-price lunch, a measure of poverty, scored 110 points below their peers in schools at which fewer than 10% of the students receive a subsidy, for example.

"Poor kids are held to lower standards than more affluent kids," says Jack Jennings, director of the Center on Education Policy in Washington, D.C. "We must bring higher quality teaching and resources to the poorer school districts."

The next TIMSS will be held in 2007.

–YUDHIJIT BHATTACHARJEE

Does your 8th grader know this?

The burning of fossil fuels has increased the carbon dioxide content of the atmosphere. What is a possible effect that the increased amount of carbon dioxide is likely to have on our planet?

- ● A warmer climate (correct answer)
- ○ A cooler climate
- ○ Lower relative humidity
- ○ More ozone in the atmosphere

Correct answers (selected countries):

Singapore: 83% United States: 56%
Japan: 80% Int'l average: 44%

Science Ranking for Selected Nations

Country	Average Score	
GRADE 8		
Singapore	578	(-3)*
Chinese Taipei	571	--------
Korea	558	(+13)
Hong Kong	556	(+46)
Estonia	552	-------
Japan	552	(-2)
Hungary	543	(+6)
Netherlands	536	(-6)
United States	527	(+15)
Australia	527	(+13)
GRADE 4		
Singapore	565	(+42)
Chinese Taipei	551	-------
Japan	543	(-10)
Hong Kong	542	(+35)
England	540	(+13)
United States	536	(-6)
Latvia	532	(+43)
Hungary	530	(+22)
Russian Federation	526	------
Netherlands	525	(-5)

*change from 1995 score.

SOURCE: TIMSS, 2003

ScienceScope

"Risky" Task Force Set

The oversight body of the National Science Foundation (NSF) wants to help the agency hit scientific home runs as well as singles.

Last week the National Science Board (NSB) approved creation of a Task Force on Transformative Research to recommend better ways for the $5.5 billion agency to take a flier on high-risk but potentially high-reward research. Its target is the inherently conservative bent of NSF's peer review process (*Science*, 8 October, p.220).

Nina Federoff, an NSB member and plant biologist at Pennsylvania State University in State College, is expected to chair the task force, which will include outside scientists. Federoff foresees holding several workshops to obtain additional community input.

—JEFFREY MERVIS

Tauzin Takes Drug Industry Post

A battle with intestinal cancer has convinced a retiring U.S. lawmaker to take a lucrative job as a drug industry lobbyist that he was up for earlier this year.

Representative Billy Tauzin (R-LA) was rumored to be in line for the job as president and CEO of the Pharmaceutical Research and Manufacturers of America (PhRMA) before critics said his role in negotiating a new Medicare prescription law posed a conflict of interest (*Science*, 6 February, 2004, p. 761). Tauzin, 61, said he did not negotiate with PhRMA while handling the drug bill, but that being a patient for most of the year inspired him to take the PhRMA job. He assumes the post on 3 January.

–JOCELYN KAISER

Klein Heads Stem Cell Panel

The wealthy California real estate financier behind the $3 billion state stem cell initiative has been appointed chairman of the board that will administer the state's bold new research program.

Robert Klein II, who has a diabetic son, is a great choice, says stem cell researcher Evan Snyder of the Burnham Institute in La Jolla. "He's an enormously efficient organizer [and] knows the ins and outs of stem cell research," he says.

The panel met for 2 days this month at the west-coast offices of the National Academy of Sciences to begin sketching out the research institute created by the passage of Proposition 71. The panel plans four community forums next month.

—CONSTANCE HOLDEN

Published by AAAS

Scientists and ethicists are taking a closer look at ways to create pluripotent human stem cells without involving embryos. But how close are such ideas to reality?

A Technical Fix For an Ethical Bind?

"There are a lot of ways to skin the cat here," says Robert Lanza of Advanced Cell Technologies (ACT). In this case, the "cat" is the challenge of devising new and genetically tailor-made human stem cell lines while bypassing the creation of an embryo. Such an achievement would enable scientists to sidestep the ethical debate that has polarized the United States and triggered governments around the world to become involved to an unprecedented degree in regulating research.

Last month, the President's Council on Bioethics heard two such proposals. One would allow scientists to determine that an embryo is nonviable before any cells are taken from it; the second was a way to jinx DNA before it is transferred into an egg so that it could never develop into a viable organism. Out of the political limelight, other researchers are working on additional methods that might ease some of the controversy over whether embryos can be used to further potentially lifesaving medicine.

Although public opinion polls show wide support for human embryonic stem (ES) cell research, it's likely that for some time stem cell researchers will be confronted with a patchwork of standards ranging from the permissive policies in some Asian countries to outright bans in Catholic countries such as Ireland and Austria.

Many scientists feel that the possible benefits from human ES cells for understanding and curing disease far outweigh any ethical concerns about destroying a week-old embryo. But some are deeply conflicted. And even those who are not hope for new techniques that will be more effective as well as less ethically problematic. To find those, scientists are exploring various ways to derive ES-like cells from an abundance of early cell types. Ultimately, everyone agrees, the Holy Grail of ES cell generation resides in finding a way to coax mature body cells to "dedifferentiate"—make the journey back to earlier, more plastic stages—with no use of eggs or embryos.

But progress is slow. The ideas presented last month are theoretical and have not yet been tested in the lab. Although other approaches have been tested, they have not yet proven as efficient as the standard methods for deriving ES cells. And some of the new ideas raise troubling ethical questions of their own. Most important, some scientists say, the field has a lot of work to do to figure out exactly what ES cells are capable of, and they worry that the new proposals will divert attention or resources from that effort. "Suggesting experiments for political ends … is in itself simply another obstruction," says Stanford University stem cell researcher Irving Weissman.

Idea man. Ethicist William Hurlbut is promoting a worry-free way to clone.

Not-quite-cloning

Physician and ethicist William Hurlbut of Stanford is touting the jinxed DNA idea, which he calls "altered nuclear transfer," as a comprehensive solution to the challenge of creating new human embryonic cell lines with specific genetic properties—the goal of human nuclear transfer or research cloning. By knocking out a key developmental gene before transferring the nucleus of a donor cell into an enucleated egg cell, he says, one could create a reprogrammed cell capable of forming ES cells but lacking the signals needed to form an organized embryo. No embryo created, he says, no embryo destroyed.

But not everyone agrees, and Hurlbut's proposal is not, in fact, new. "These ideas have been floating around for years," he acknowledges, although he takes credit for "reframing the moral argument." Cloning and stem cell researcher José Cibelli, now at Michigan State University in East Lansing, filed for a patent on the technique in 2002, when he still worked for ACT in Worcester, Massachusetts. And developmental biologist Hans Schöler of the Max Planck Institute for Molecular Biomedicine in Münster, Germany, says he proposed the technique independently in 2002 as a way around Germany's embryo protection law. In a slight variation, Schöler has suggested injecting a snippet of RNA into the recipient oocyte to block expression of key developmental genes.

> "These ideas [for alternative nuclear transfer] have been floating around for years. … I've reframed the moral argument."
>
> –William Hurlbut, Stanford University

In the method patented by ACT and proposed by Hurlbut, scientists would genetically alter the donor nucleus to block the expression of a gene required for the proper organization of the early embryo. The

CREDITS (TOP TO BOTTOM): YORGOS NIKAS/PHOTO RESEARCHERS INC.; COURTESY OF W. HURLBUT

Published by AAAS

The prize. Researchers hope pluripotent stem cells will help cure disease.

resulting cell would lack the key organizational cues essential to form a fetus and would likely differentiate into a random assortment of cell types, not an embryo, Hurlbut argues.

To date, the discussions have remained theoretical. Weissman thinks the idea is reasonable, but he has advised Hurlbut—who is not a researcher—"on how hard it is to make even reasonable ideas work." Until someone spends long hours in the lab testing the idea, he says, he cannot take it seriously.

But if Hurlbut or someone else could develop an efficient method, Weissman says, "he would be doing the medical and scientific world a great favor." The president's bioethics group seemed to agree. And Hurlbut says he got a thumbs-up from the Archbishop of San Francisco, William J. Levada, who wrote President George W. Bush last summer commending the idea.

Many seem to have doubts about it. If the knockout gene allows for several days of relatively normal development, then it would not solve the problem, says Richard Doerflinger of the National Council of Catholic Bishops in Washington, D.C. "A short-lived embryo is still an embryo." "I think this is an abuse of cloning technology," says Lanza of ACT—more troubling than nuclear transfer itself. "It will be a sad day when scientists use genetic manipulation to deliberately create crippled embryos to please the Church." Cibelli concedes that his team "debated about whether we should file for a patent. We thought some would see this as creating a defective human for purposes of exploitation."

Eggs alone?

Some researchers think that a type of disordered embryo created solely from an unfertilized egg cell is a better option. Researchers can trick an egg into dividing with either chemical or electrical signals that set off the same cascade as the penetration of a sperm does. The result is called a parthenote. In some insects and reptiles, parthenogenesis occurs naturally and can produce live offspring. In mammals, however, the lack of genes from the father invariably causes defects that kill the fetus before birth.

A parthenote "is obviously not an embryo," says developmental biologist Ann Kiessling of the Bedford Stem Cell Research Foundation in Somerville, Massachusetts, who with her colleagues has been working to derive pluripotent stem cells from human parthenotes. The only mammalian parthenote—a mouse—that has made it to term was the product of heavy genetic intervention by her creators, she notes (*Science*, 23 April, p. 501).

Kiessling and others also argue that parthenogenesis may be more efficient than nuclear transfer because "primate eggs seem to activate pretty readily," with roughly 25% of them surviving to the blastocyst stage—more than twice the success rate reported this year by a Chinese group using nuclear transfer (*Science*, 12 March, p. 1669). So this approach could provide a simpler way to get genetically tailored cell lines both for studying and treating genetic diseases—at least for women with viable oocytes, she says.

Reproductive biologist Karl Swann of the University of Cardiff says he and his colleagues have found a chemical trigger that seems especially powerful at sparking division in oocytes—even those that have failed to fertilize when exposed to sperm. This could greatly add to egg availability, he says, because fertility clinics discard many thousands after they fail a second attempt at fertilization. Swann says he and his team have achieved reliable development to the blastocyst stage, but they have not yet derived any cell lines.

If cell lines from parthenotes can be developed, says ACT's Lanza, they would offer another enormous benefit. They have only one set of genes, he says, which reduces the complexity of surface proteins responsible for immune rejection. Thus, he says, they would be ideal for stem cell banking: "With a few hundred lines, you could match the genetics of most of the population"—a practical goal that could never be reached with nuclear transfer because "you would need millions and millions of eggs" to treat individual patients.

But Cibelli says that, contrary to Lanza's claims, the immunity issue has by no means been resolved: "The big question now is, will [cells from parthenotes] be recognized as cells or foreign tissue?" He and his colleagues are trying to find out with the ES-like cell line he derived at ACT in 2002 from a rhesus monkey parthenote—the only primate line created that way so far (*Science*, 1 February 2002, p. 779). George Daley of Harvard University is also intrigued but skeptical. He is using mice to check on the "engraftability" of cells from parthenotes, but he warns that the cells might trigger rejection by the immune system, which "not only recognizes foreign [cells] but absence of self."

Hurlbut says many scientists are unenthusiastic about parthenogenesis. It "is of limited value because the genotypes would be restricted to those of fertile females, and it is hard to be certain that these cells would not carry genetic abnormalities," he says. "Most of the scientists I talk to really want nuclear transfer."

Nor does this solution completely satisfy Catholic critics. "If [parthenotes] are organized enough to make a blastocyst, my concerns would still be there," says Doerflinger. "The jury is out on what exactly a parthenote is, but I don't think it's been shown that it isn't an embryo."

Getting Around the Controversy

Ideas for embryo-free ways to derive human ES cells

- Nuclear transfer with "jinxed" genes
- Cell lines from "organismically dead" embryos
- Cell lines from parthenotes
- Cell lines from single cells from early embryos
- Egg-free reprogramming of adult cells

No daddy. Five-day-old human parthenote.

CREDITS (TOP TO BOTTOM): PETER MACDIARMID/CORBIS; J. CIBELLI/ACT

Exploiting defunct embryos

Donald Landry and Howard Zucker of Columbia University in New York City floated another proposal at the bioethics meeting: using cells from more or less defunct embryos. Up to 60% of the embryos created for in vitro fertilization (IVF) treatments are considered "nonviable," meaning development has been arrested, but individual cells are still functioning. Drawing an analogy to brain death in human organ donors, Landry and Zucker propose that markers could be developed to determine "organismic death" in embryos.

To test that idea, he and Zucker plan to monitor several hundred embryos that have stopped dividing. They will then characterize the chemical and genetic signatures of embryos that haven't shown any signs of development for 24 hours. Such signals could be used to declare embryos nonviable. "My expectation is that the analogy to brain death and the harvesting of organs will be so directly applicable … that this will be seen properly as falling within the guidelines of current federal policy," says Landry.

But Daley and others question whether such embryos could really yield cell lines. "We know the more intact the blastocyst, the better the cells," he says. Cibelli also cautions that it will be "very hard to determine" an embryo's status—"we don't have an EEG machine we can plug into the embryo." What's more, some ethicists are skeptical about this one too. Tadeusz Pacholczyk of the National Catholic Bioethics Center in Philadelphia, Pennsylvania, says: "I'm not convinced that an arrested embryo is the same as a dead embryo," given the ability of single cells from early embryos to form entire organisms.

Snatching the single cell

Lanza, for one, is much more enthusiastic about another potential method for getting cells without destroying embryos: growing new ES cell lines from single cells that have been detached from embryos without damaging them. The procedure is already used for preimplantation genetic diagnosis, so the main trick would be to get the extracted cell to start dividing. ES cells are herd animals, and they often die when alone in culture. But Lanza says ACT expects to be able to cultivate new cell lines from single cells taken from either blastocysts or earlier-stage embryos called morulas without harming their development.

But possibilities also breed perils. At the morula stage, a cell may still be totipotent, which means it has the potential to develop into a full embryo. So in some eyes, destroying it to make an ES cell line is akin to destroying a complete embryo, observes Peter Braude, a stem cell researcher at Guy's, King's and St. Thomas' School of Medicine in London. Braude points out that scientists are now in a position to dream up countless unprecedented scenarios. For example, he says, what if you take an eight-cell embryo and separate it into two four-cell clumps? If one clump develops into a blastocyst, is implanted, and becomes a baby, and the other is used to start a cell line, no embryo was destroyed—but "there are those that would argue that a twin life has been destroyed."

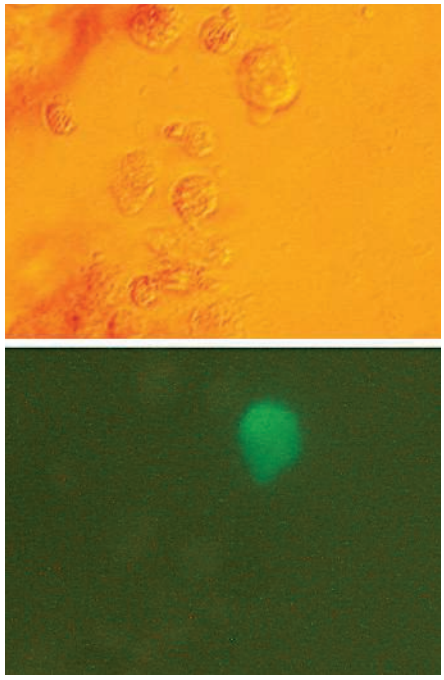

Reprogrammed? Fusion with an ES cell nucleus prompts a nervous system cell to glow green—a sign a pluripotent gene has turned on.

CREDIT: H. SCHÖLER/MAX PLANCK INSTITUTE FOR MOLECULAR BIOMEDICINE

The Holy Grail

The best chance to circumvent the ethical dilemmas may be to find a way to reprogram mature cells into pluripotent stem cells while bypassing both egg cells and embryos. That would not only satisfy critics, it would also eliminate headaches involved in obtaining donated eggs and embryos. Technically as well, it would fulfill the promise offered by so-called therapeutic cloning: cell lines tailored to an individual's genes that would enable doctors to study complex diseases in the lab and provide potential donor cells that avoid the problems of immune incompatibility. And nothing would be created that could potentially be implanted and become a baby.

That goal is many years away, however. Scientists must first figure out what really happens in the process of reprogramming during nuclear transfer. Researchers have yet to nail down exactly what factors in the egg cytoplasm manage to turn a differentiated nucleus back into one that can direct the development of a whole organism. Some clues about where not to look have come from experiments in which scientists sought to see if an ES cell could be used instead of an egg to reprogram the nucleus of a somatic cell. But ES cell cytoplasm does not seem to contain the magic ingredient.

However, a new paper from Schöler and his colleagues suggests that the key ingredients may lie in ES cell nuclei. In the November issue of *Stem Cells*, the team reports on work that grew out of the observation that ES cells can fuse with mature cells in culture and apparently prompt them to turn on genes key to ES cells' plasticity. To track down the source of that reprogramming power, the team fused mouse neural cells with either ES cell cytoplasm or ES cell nuclei. The cytoplasm didn't seem to have any effect. But the neural cells that fused with ES cell nuclei turned on their own embryonic genes and formed ES cell–like colonies.

The resulting cells have twice the normal number of chromosomes and therefore are not the kind of reprogrammed cell line scientists are aiming for. But the experiments home in on factors that apparently reside in the nucleus, Schöler says.

Another approach to finding the magic ingredients has been taken by chemists Peter Schultz and Sheng Ding at the Scripps Research Institute in La Jolla, California, who are screening small molecules in a hunt for those that can turn the clock forward or back in a cell's development. They are on the trail of a small molecule they call "reversin" that will cause a muscle cell to dedifferentiate into a multipotent progenitor cell. "This really does open up the possibility that you could use your own cells to dedifferentiate to some kind of multipotent cell type" that could be used, say, to treat a heart patient, says Schultz.

The entire subject has become so sensitive that someone undoubtedly will find ethical issues in any new technique. Some scientists are impatient with the philosophizing and want to get on with the work. As Daley says, "Doing a scientific experiment not for a scientific reason but to quell an ethical debate" is not his idea of science. Some say this is analogous to other early panics about new technologies, such as IVF, that have now become widely accepted. But as Braude notes, ES cell technology, more than any biological manipulation that has preceded it, "is challenging the very foundations of some ethical and religious beliefs" about what it is to be human.

–CONSTANCE HOLDEN AND GRETCHEN VOGEL

Heightened Security or Neocolonial Science?

New restrictions on federally funded research involving the world's most dangerous pathogens are hampering foreign collaborations

ALMATY, KAZAKHSTAN—Scott Weaver thought he had a green light for a great research partnership. After an expensive security upgrade of his labs and hours of paperwork, the director for tropical and emerging infectious disease research at the University of Texas Medical Branch (UTMB) in Galveston was ready to resume research on the Venezuelan equine encephalitis (VEE) virus in Colombia, Peru, and Venezuela. The mosquito-borne disease, endemic in all three countries, is not the worst of its kind: The alphavirus kills less than 1% of its human victims. But VEE's potential to incapacitate has landed it on a list of "select agents": several dozen of the nastiest sorts of pathogens that the U.S. government fears could be turned into biological weapons. That designation has thrown up new hurdles for Weaver and his collaborators in South America—and for many other U.S. scientists working overseas.

In August, the U.S. National Institute of Allergy and Infectious Diseases (NIAID) informed Weaver that under the terms of his two VEE grants, the laboratories of his foreign colleagues must have procedures in place for handling select agents that are equivalent to tough U.S. regulations* imposed last year. "I seriously doubt whether my collaborators in Caracas or Bogotá could ever meet U.S. standards for select-agent security," says Weaver. "These developing countries cannot afford the kinds of elaborate systems that labs in the U.S. have been required to install," such as sophisticated security and inventory systems and background checks on employees. He's since had to alter his projects to avoid isolating the VEE virus in the labs south of the border. Because the new policy may force some foreign partners to serve as mere sample exporters, it resurrects "the stereotype of the ugly American: arrogant, demanding, and insensitive," Weaver charges: "American collaborations will be unwelcome in many developing countries of the world."

Although his case may be one of the first, Weaver is not the only researcher feeling the chill. According to a prominent U.S. specialist on select agents, researchers with the U.S. Centers for Disease Control and Prevention (CDC) have seen a curtailment of foreign collaborations on avian flu and viral hemorrhagic fevers. (CDC officials declined to comment.) Scientists at the U.S. Army Medical Research Institute of Infectious Diseases (USAMRIID) in Frederick, Maryland, are experiencing similar constraints on projects involving Congo-Crimean hemorrhagic fever and related diseases. "The important work we need to do will get done," says USAMRIID public affairs officer Caree Vander Linden, although the details have not been worked out.

No picnic. Venezuelan scientists draw blood from rodents to isolate VEE virus. New NIH rules have crimped projects on this and other select agents.

CREDIT: JUAN CARLOS NAVARRO

U.S. inspectors will soon be heading out to assess lab standards overseas, scientists learned at a closed-door meeting last month. Paula Strickland, acting director of NIAID's Office of International Extramural Activities, told a group at the annual meeting of the American Society of Tropical Medicine and Hygiene (ASTMH) in Miami, Florida, that security teams will include senior microbiologists from CDC's select-agents program. An interagency committee chaired by Strickland with representatives from the U.S. State and Justice departments will determine whether foreign labs "meet minimum biosafety and biosecurity requirements."

The stepped-up regulations are the latest example of the clash between scientists' cherished ways of doing business and the urgent need to reduce the potential for bioterrorism, and some researchers say the rules make sense. "It would be very embarrassing for a U.S. collaborator and a U.S. agency to be funding a facility that had a major accident, or one that was involved in a bioterrorism event," says Paul Keim, an anthrax specialist at Northern Arizona University in Flagstaff.

But others fear that the tightened security could stifle cooperation. "One doesn't develop productive collaborative relationships with foreign counterparts by announcing upon arrival that 'from now on we must do things the American way,' " says UTMB arbovirus specialist Robert Tesh. "Each country has its security priorities. The U.S. cannot demand that they conform to ours." Adds Weaver: "By inhibiting research on the ecology and epidemiology of potential biological weapons in their natural settings overseas, we will be less prepared to respond optimally to the introduction of these agents by a terrorist."

Clampdown

After letters containing powdered anthrax were mailed to members of Congress and others in the fall of 2001, the U.S. government crafted tough requirements for scientists it funds to study dangerous pathogens. In addition to tightening security at facilities in which the microbes are kept and studied, U.S. regulations now demand rigorous protocols covering security assessments, emergency response plans, training, transfers of materials, and inspections.

Under the new NIAID rules, which the institute began developing in 2003, U.S. grantees must submit a dossier on a foreign collaborating institution detailing its "policies and procedures for the possession, use, and transport of select agents." For what NIAID calls "security risk assessments," grantees "must be willing to provide the names of all individuals who will have access to the select agents."

Weaver says the new rules prompted him to drop his original plan to process field samples potentially infected with VEE virus in South America. Now, he says, he will have all the samples shipped to Galveston. "This seems to have gotten me off the hook for the time being," he says, in that his colleagues at the National Institute of Health in Bogotá and the Central University of Venezuela and the National Institute of Hygiene in Caracas now won't have to adhere to the select-agent

* www.cdc.gov/od/sap/docs/42cfr73.pdf

Published by AAAS

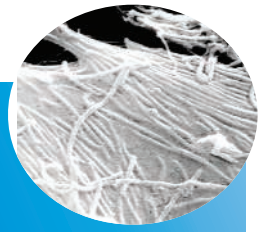

A Selection of Select Agents

Smallpox virus
Crimean-Congo hemorrhagic fever virus
Lassa fever viruses
Central European tick-borne encephalitis
Yersinia pestis (plague)
Foot-and-mouth disease virus
Ebola viruses ▶
Ricin
Tetrodotoxin
Bacillus anthracis (anthrax)
Venezuelan equine encephalitis virus
Botulinum neurotoxin

terms. But the change will reduce efficiency and timeliness, he says.

"Basically, the NIH [U.S. National Institutes of Health] left me with little choice," because it would have taken "months or years" to bring overseas labs into compliance, Weaver says. Already, the labs in Colombia and Venezuela store many VEE virus isolates in their freezers: Preventing the isolation of a few more strains, he says, will not deny the virus to a potential terrorist.

Although security at foreign facilities working with select agents generally has been strengthened since the 9-11 attacks, most labs would still run afoul of the new U.S. rules. Many outside the United States appear to be unaware of the regulations. "I haven't heard much," says Lev Sandakhchiev, director general of the State Research Center of Virology and Biotechnology, a former bioweapons lab near Novosibirsk, Russia, that collaborates with the United States on smallpox research.

Foreign researchers say they hope to find a way to continue working with U.S. counterparts because it would bolster security in their home countries. "If collaborations will continue, that will inevitably bring the standards up," says Bakyt Atshabar, director of the Kazakh Science Center for Quarantine and Zoonotic Diseases in Almaty, Kazakhstan, which specializes in studying endemic plague with Pentagon funding (*Science*, 17 December, p. 2021).

ASTMH and other societies intend to lobby for a relaxation of the rules. "The approach to this will not be easy," says Peter Weller, an immunologist at Harvard Medical School in Boston and ASTMH's most recent past president. For one, many agencies will want to weigh in on any change of policy. Second, Weller says, "the facile reply is that you scientists gave the Pakistanis nuclear secrets; how do we trust you on these issues?" In an e-mail response to questions from *Science*, NIAID officials say they expect no change to the select-agent terms "in the immediate future."

But some experts such as Keim say raising global security levels to U.S. standards makes sense. "We should not allow U.S. researchers to avoid regulatory oversight by going abroad. This would certainly apply to human subjects in clinical trials and animal-care standards in animal protocols. Why not security of dangerous pathogens?"

Critics of the policy say they are not opposed to strengthened security overseas. Rather, they decry how the U.S. government is going about it. NIH "seems to be hell-bent on enforcing the regulations," says Thomas Monath, chief scientific officer at Acambis in Cambridge, Massachusetts, and president of ASTMH. He wonders whether his company's research on Japanese encephalitis, a select agent, with colleagues in Thailand and Australia will be subject to such oversight. Monath fears that U.S. researchers might be held criminally responsible for violations by collaborators. When he raised this issue with Strickland at the ASTMH meeting, he says, it was apparent that "NIH had neither thought about this nor had any clear response."

NIAID officials say they are simply in step with the times; later they plan to adopt standards being developed by the World Health Organization. "We will do what we can to ensure that every possible avenue has been pursued that will allow our NIH-funded researchers to be able to conduct their research safely and securely," the officials say. Much of that work, it appears, may well have to be done inside U.S. borders.

–RICHARD STONE

Earthquake Preparedness

Some Countries Are Betting That A Few Seconds Can Save Lives

Japan, Mexico, and Taiwan are investing in early warning systems that can offer precious seconds of warning before a major tremor

TOKYO—What would you do with 5 to 50 seconds' warning of a major earthquake?

It's not an academic question. Systems that can detect earthquakes near their source and issue warnings before the shaking starts are in place or being deployed in Mexico, Taiwan, and Japan and are being studied for locales from southern California to Istanbul. Enthusiasts are convinced that short-term warnings can save lives by stopping trains before they pass over damaged track, emptying out elevators, and alerting rescue units. "It is an epochmaking" advance in earthquake safety, says Masato Motosaka, a Japanese earthquake engineer at Tohoku University in Sendai.

On alert. Nowcast stations are being installed across Japan.

Not everyone agrees, however. Skeptics note that warning systems don't provide enough time to reduce casualties close to the epicenter of an earthquake. They also worry that such systems could divert spending from earthquake preparedness, which they say has the potential to do much greater good. "Warnings only help in some cases," says Robert Olshansky, an urban planner at the University of Illinois, Urbana-Champaign. "Investing too much of one's money and hopes in a short-term warning system is a distraction from the hard and less sexy work, such as upgrading older structures, that is really needed to improve seismic safety."

Faster than a speeding S wave

Early warning systems are not forecasts. Instead, they detect actual quakes near their source and issue warnings to automated systems and humans up to several hundred kilometers away. They work because electronic signals transmitted through wires or air travel faster than seismic waves moving through the earth. Warning schemes also take advantage of the two types of seismic waves that are generated when a fault ruptures. The first—and faster moving—primary (P) waves radiate directly outward from the epicenter. The secondary (S) waves, which cause the oscillating motions responsible for the most damage, lag by tens of seconds over a distance of a few hundred kilometers. "The P waves carry information; the S waves carry energy," explains Hiroo Kanamori, a seismologist at the California Institute of Technology (Caltech) in Pasadena. Unfortunately,

CREDITS (TOP TO BOTTOM): C. GOLDSMITH/CDC; JAPAN METEOROLOGICAL AGENCY

Published by AAAS

P waves and S waves would arrive almost simultaneously near the epicenter, making warning impossible where shaking is most intense.

Farther away from the epicenter, there is time to analyze the signals and automatically generate warnings. After the October 1989 Loma Prieta earthquake in California, the U.S. Geological Survey (USGS) deployed a temporary array of three seismometers that warned workers demolishing a collapsed highway viaduct in Oakland about aftershocks. The system gave workers 23 seconds' notice of S waves from 12 aftershocks stronger than magnitude 3.7.

Two permanent early warning systems were put in place in the early 1990s in Mexico and Japan. In 1991 the Centro de Instrumentacion y Registro Sismico (CIRES), a private Mexican nonprofit organization, set up a network of 12 instruments along the country's Pacific coast near Acapulco, where seismologists think a magnitude 8 earthquake is overdue. If the system works as intended, residents of the capital city, 280 km away, could get 70 seconds' warning. Schools and some government offices are serviced by dedicated transmission lines, and citizens have access to automated radio broadcasts. Two years ago, a similar system was set up for the city of Oaxaca, in southern Mexico.

Likewise in Japan, the country's early warning systems are likely to prove most useful for the most devastating earthquakes, those that occur off the Pacific coast where the North American plate is being forced under the Philippine plate. For example, Motosaka says that the Sendai area would receive 15 seconds' warning that the effects of a magnitude 7 to 8 offshore earthquake were about to hit; seismologists give such an earthquake a 40% chance of occurring in the next 10 years.

In 1992, railway operators started deploying the Urgent Earthquake Detection and Alarm System (UrEDAS) along the country's bullet train lines. After detecting P waves, UrEDAS cuts power to trains in nearby sectors if the anticipated shaking will exceed a given threshold. In February, the Japan Meteorological Agency began deploying what will be the world's most comprehensive early warning system, featuring more than 200 stations throughout the four main islands. Installation of the $90 million network, called Nowcast, began in 2003 and could be completed in 2 years if the money keeps flowing. In December 2000, Taiwan's Central Weather Bureau switched on an islandwide network of 86 seismic stations that alerts the bureau's central office and a hospital, both in Taipei.

Authorities are still trying to figure out the best way to use early warning systems. Officials at Taiwan's weather bureau receive warnings on their computer screens, "allowing staff to move to disaster response stations a few seconds quicker than if they wait for the shaking to start," says Yih-Min Wu, a seismologist at the National University of Taiwan involved in setting up the system. Taiwan's high-speed rail line will likely be added to the system once train service begins next fall.

Japan's system, partially operational, sends warnings to a select group of regional disaster response centers, private companies, an elementary school, and a university hospital in the Tohoku region northeast of Tokyo. Tohoku University's Motosaka, who is leading a government study of potential warning uses, says earthquake education and drills can be worked into the school curriculum, as is now being done at the Nakamachi Elementary School in Sendai. Pupils have been taught to duck under their desks to avoid falling ceiling tiles and lighting fixtures, and teachers to open doors so they don't jam shut and hinder a postquake evacuation. In a hospital, the warnings could allow surgeons to pause during delicate procedures and give rescue teams extra seconds to prepare.

Three Warning Systems

TAIWAN

Early Warning System (completed 2000) works for the entire island. Cost: $930,000

MEXICO

Seismic Alert System (completed 1991) warns Mexico City of a major quake near Alcapulco. Cost: $1.2 million

JAPAN

Urgent Earthquake and Detection Alarm System (completed 1992) was established to slow or halt bullet trains after an earthquake. Cost: Not available

Nowcast (partial operation in 2004) was developed as a general seismic warning system. Cost: $90 million

Call ahead. Early warning systems could save lives in elevators and operating rooms.

CREDITS (TOP TO BOTTOM): GARETH BROWN/CORBIS; JUPITER IMAGES

The list of possible applications is endless, says Thomas Heaton, a Caltech earthquake engineer and longtime proponent of early warning systems. It includes switching all traffic lights to red, closing valves in oil and gas pipelines, shutting down nuclear power plants, and preparing tsunami warnings. "I don't think anybody knows right now what all the potential applications will be," says Heaton.

One unresolved issue is whether to broadcast warnings to the general public. The Mexican system has generated 11 warnings of strong (magnitude 6 or greater) earthquakes in 14 years without a hitch, according to Juan Espinosa-Aranda, director general of Mexico's CIRES. "Contrary to what many expected, we have never had any indications that the warnings resulted in panic," he says. Part of the reason, says Heaton, may be their benign content: "Ninety percent of the time, the message will be 'This will be light shaking, relax and enjoy it.'"

Without warning

To date, the payoff from early warning systems is scant, proponents admit. In 12 years, operators of Japan's UrEDAS can cite only one case in which the warning headed off a potentially dangerous situation. That occurred in May 2003, when a magnitude 8 earthquake struck northeast of Tokyo: The system halted two trains headed toward a viaduct that had suffered cracks in 23 columns.

In contrast, a bullet train derailed during the country's most recent severe earthquake, on 23 October in Niigata Prefecture, because the train was too close to the epicenter for a warning to arrive in time. Likewise, no early warning system would have mitigated the devastating 1995 Kobe earthquake, which claimed 5000 lives, because the fault that ruptured runs right under the city. "Warnings don't work" in such cases, admits Motosaka.

That fact of life, say scientists, means early warning systems should never replace seismic preparedness. "We need to spend money on mitigation and preparedness," says the University of Illinois's Olshanky. "Making promises of prediction or warnings distracts from this task."

Skepticism about earthquake warnings seems greatest in the United States, in part because the most dangerous faults are close to urban areas. Caltech's Heaton says that federal agencies have rejected several of his proposals to test a prototype early warning system for southern California after they received mixed reviews. "Half the reviewers said it was a great idea, and the other half said it's not very useful," he says.

To find out who's right, seismologists need hard data. Although they don't wish for misfortune, they know that earthquakes are inevitable. And they are counting on Mexico, Taiwan, and Japan to serve as test beds.

–DENNIS NORMILE

A Plasma Too Far? Researchers Hunt for Early State of Matter

Brookhaven scientists think they've seen evidence of the long-sought quark-gluon plasma. But something's not quite right

In 2000, scientists at CERN, Europe's high-energy physics lab near Geneva, Switzerland, thought they were on the brink of creating a state of matter not seen since a few fractions of a second after the universe was born. Their colleagues at Brookhaven National Laboratory in Upton, New York, working on a new and more powerful accelerator, were even more confident of success. But nearly 5 years later, no one has claimed credit for making a quark-gluon plasma, an extremely high-energy state in which the fundamental components of protons and neutrons roam free.

Something interesting is certainly happening within the giant detectors that record the high-energy collisions of heavy particles that scientists hope will lead them to their goal. But what? Researchers confess that they don't understand their prey well enough to know if they've snared it. And what they have captured doesn't behave as it should. Such is life on the frontiers of the quark-gluon plasma. "I'm a little baffled and not sure exactly what to do," says Thomas Kirk, Brookhaven's associate laboratory director for high-energy and nuclear physics. "If it sounds like I'm frustrated, it's because I am."

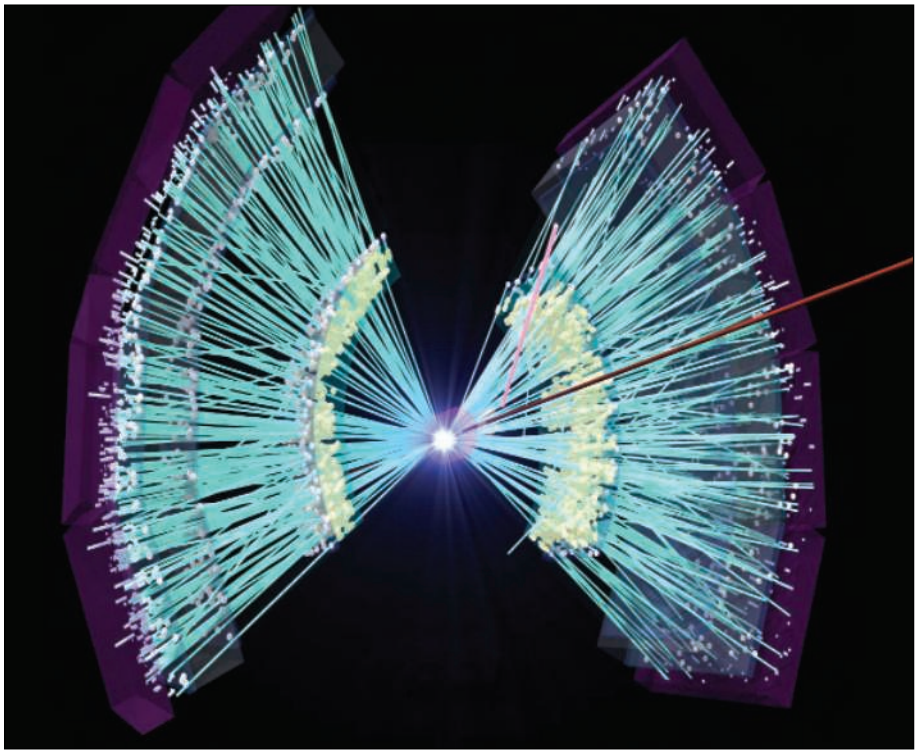

Little bang. The particle tracks from a high-speed collision of two gold atoms provide clues about whether quarks and gluons had roamed free.

A near meltdown

In our frigid universe, quarks, which make up most known matter, are frozen inside hadrons. They are never seen alone, unbound, or roaming free. But in the very, very hot early universe, scientists believe that quarks and gluons, which bind quarks together, swirled and danced for a brief moment before they "froze out" and formed hadrons. Researchers have been trying to recreate that brief moment—the era of the quark-gluon plasma—for years.

A particle collider is like a time machine; the higher its energy, the further back in time it can see. At CERN's Super Proton Synchrotron (SPS), the 3.5-TeV collisions brought scientists to within a few millionths of a second after the big bang. Using enormous magnets, SPS, buried under farmland outside Geneva, smashed lead atoms together at such speeds that the nuclear components—protons and neutrons—cracked open and their contents spilled out. Scientists analyzed the resulting spray of particles, some of which were born out of the quarks and gluons of the lead nuclei, others of which sprang forth from the enormous vacuum-searing energy of the collision itself, looking for signs that quarks and gluons had melted once more and roamed free of their usual constraints.

The evidence was suggestive, if not conclusive. One promising indicator was a striking lack of a particular type of particle known as the J/Ψ, which is made up of a relatively rare quark known as charm and its antimatter counterpart. The dearth might be a sign of free-roaming quarks, scientists argued. Here's why: The charm quark and antiquark are born near each other, out of energy rather than nuclear matter. (Protons and neutrons don't contain any charm quarks or antiquarks.) Neighboring quarks are quite likely to bind to each other during freezing, creating J/Ψs. But quarks that roam about before freeze-out will in all likelihood bind to more common quarks, such as ups and downs, and create particles such as D mesons rather than J/Ψs.

Sure enough, the SPS team saw many fewer J/Ψs in high-energy collisions than expected. For some physicists, that was a signal that they might have created a quark-gluon plasma. But SPS fell by the wayside in 2000 as CERN shifted its attention to building a much more powerful particle-physics accelerator, the Large Hadron Collider. Until LHC starts up, CERN is pretty much out of the quark-gluon plasma game.

Luckily, an even higher-energy collider was coming online: the Relativistic Heavy Ion Collider (RHIC) at Brookhaven. RHIC can slam together nuclei of atoms at roughly five times the energy levels of SPS, and early results seemed to confirm that scientists were close to creating the elusive plasma. Although RHIC's four detectors didn't yet have the capability to spot a lack of J/Ψ particles, scientists were seeing other favorable signs. According to Brookhaven physicist Miklos Gyulassy, these signs are "striking" evidence that quarks had been liberated from their shackles. "The data are in for me," he says.

One piece of supporting evidence is a phenomenon known as "jet quenching." When two nuclei collide, scads of particles fly out from the center of the collision, where the temperature is highest. In a low-temperature collision, these particles would carom off one another like billiard balls and spray away from the nucleus in jets. The RHIC collisions

CREDIT: PHENIX/BROOKHAVEN NATIONAL LABORATORY

Published by AAAS

created fewer jets than expected. Physicists argued that this "jet quenching" happened because the particles were behaving more like melted clumps of sticky wax than solid billiard balls. By clinging and transferring energy to each other before shooting away with diminished vigor, the objects' nuclei were behaving like a liquid or a gas rather than a solid. And that behavior is exactly what scientists had forecast when protons and neutrons melt, setting their quarks and gluons free.

The manner in which particles flew away from the collision in the nucleus also was characteristic of a liquid. Instead of acting like hard billiard balls and scattering in all directions after a collision, the particles behaved as if they were in one large, expanding puddle. This effect, which is quantified with a parameter known as "elliptic flow," showed that the postcollision matter was closer to a collection of melted objects than a clump of solid ones.

More recent experiments involving the collision of deuterium and gold atoms point in the same direction. Physicists predicted that the effects stemming from a quark-gluon plasma, such as jet quenching, would disappear because the lesser mass of the deuterium doesn't impart enough energy into the smashup to make the nucleons melt. And, indeed, the strange effects disappeared as predicted. In gold-gold collisions, says Gyulassy, there was a marked decrease in the number of twinned jets from the collisions, but with "deuteron on gold, [the twin jets] came back to life again."

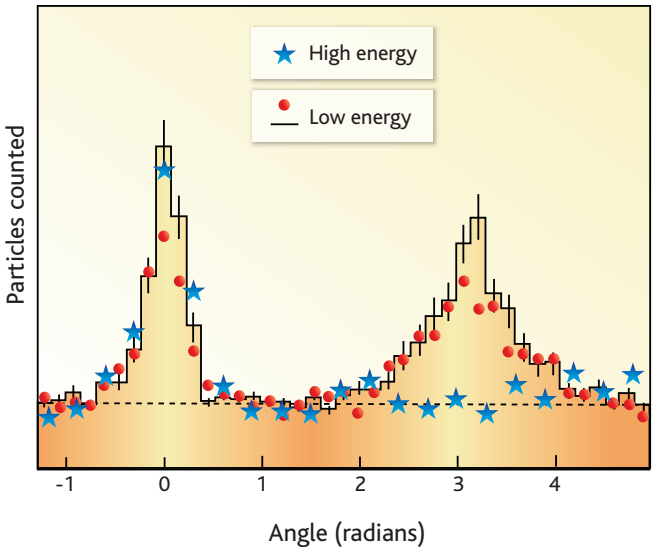

Liquid center. At low energies, particles often stream off collisions in two back-to-back jets, represented by two peaks in this graph (red dots). The disappearance at high energies of one of those jets (blue stars) could represent passage through a liquidlike quark-gluon plasma.

Frozen out?

The conclusion seemed obvious: Scientists had created a quark-gluon plasma. So why hasn't RHIC announced the discovery? The answer is that the quark-gluon plasma isn't behaving at all the way physicists expected it would.

For one, there's no nice, neat phase transition as quarks and gluons change from their ordinary condensed state into some kind of quark-gluon plasma. If you add heat to a chunk of ice near zero degrees Celsius, its temperature rises for a while. Then, all of a sudden, its temperature stops climbing as the ice changes phase from solid to liquid. It resumes its climb once all the ice has melted.

Not all phase transitions are so nice and neat. "But there was an expectation that we could observe a direct signal of the phase transition that the system would undergo as it cools," says Jean-Paul Blaizot, a physicist at France's Center for Atomic Energy in Saclay. No such luck. Instead, scientists are left with a handful of phenomena—jet quenching, elliptic flow, and a handful of other atypical observations—that indicate something new is happening but fail to constitute a smoking gun. "None by itself show a completely new state of matter," he says.

At the same time, theorists have been shocked by what is spewing forth from RHIC's collisions of two heavy nuclei at high energies. They had expected that the nucleons would evaporate into something resembling a gas. That would give the quarks and gluons a chance to roam about for a few moments before recondensing when the temperature dropped.

This isn't at all what has happened, however. The observations of elliptic flow—the very data that helped convince scientists that the nucleus was no longer behaving like a solid—show that the nucleus isn't behaving like a gas, either. Instead of streaming past each other without interacting much, quarks and gluons feel one another's presence quite strongly. As a result, the melted material at the heart of a gold-gold collision behaves like one collective object, like a drop of water, rather than a collection of individual quarks and gluons. In fact, physicists have concluded that the stuff at the center of a gold-gold collision is the most perfectly fluidlike fluid ever discovered.

This finding undermines one of the original lines of evidence for a quark-gluon plasma. The models that accounted for the lack of J/Ψ particles implicitly assumed that quarks and gluons weren't strongly interacting with each other and that the barely interacting charm quarks would fly away from each other rapidly and recondense with other noncharm quarks. But in a collectively moving liquid—and one that behaves like a liquid very shortly after the collision—the charm quarks don't have the same chance to zoom apart. In other words, if the goop at the center of a collision is behaving like a strongly interacting liquid rather than a weakly interacting gas, the lack of J/Ψ particles is a quandary.

So although it's clear that something new is happening at the center of the high-energy collisions at RHIC, it's not at all the gas that scientists expected. "Have we created a weakly interacting gas of quarks and gluons? The answer to that question is an emphatic no. We have not," says Jamie Nagle, a physicist at the University of Colorado, Boulder, and member of one of the RHIC collaborations. However, Nagle says that the data show that the quarks and gluons melt into a strongly interacting liquid whose properties are not yet understood: "That is the reason why I would say that we have not made a discovery yet."

Enormous microscope. The PHENIX detector, one of four that adorn Brookhaven's RHIC accelerator ring, explores phenomena on the tiniest scales accessible to humans.

Is this liquid the fabled quark-gluon plasma? Blaizot argues that it's difficult to answer the question, "Are we there yet?" when you don't yet know where "there" is. "When you have a not-well-defined problem, it's hard to give a well-defined answer," he says.

That's also the dilemma facing officials at Brookhaven, who for half a decade have been poised to proclaim a major discovery. "We can't march people to the lectern and force them to make an announcement," says Kirk. "Maybe we have a really nice discovery that will just dribble out."

–CHARLES SEIFE

CREDITS (TOP TO BOTTOM): SOURCE: ADAPTED FROM STAR COLLABORATION; PHENIX/BROOKHAVEN NATIONAL LABORATORY

Published by AAAS

Taming the Hyperbolic Jungle by Pruning Its Unruly Edges

Answering decades-old questions, two new theorems set limits on how wild some universes can get

For mathematicians, one of the joys of three-dimensional topology is the chance to study not only the shape of our universe but also the shape of all the universes that might have been. This requires some radical shifts in perspective, because geometric rules familiar in our universe won't hold in universes where the "shape" of space is different. To explore these alien territories, mathematicians study manifolds—abstract spaces that resemble our universe on a small scale but may connect up differently in the large. This has been a banner year for manifolds, thanks to the proof of two major conjectures that date from the 1970s. "The combination of [the two proofs] is indeed a fantastic piece of news," says Francis Bonahon, a topologist at the University of Southern California in Los Angeles.

In 1973, a Yale University mathematician named George Mostow proved that many three-dimensional manifolds, or 3-manifolds, can take only one possible shape, provided that every part of the universe is equally "curved." Measure the curvature of space in your back yard, and you know the shape of the universe. "It was the most influential piece of mathematics in geometry in the last 35 years," says Howard Masur, a geometer at the University of Illinois, Chicago. But Mostow's theorem applied only to manifolds of finite size. Topologists have struggled ever since to come up with a similar principle for a much more interesting class of manifolds in which, as Frank Sinatra sang about clear days, "you can see forever."

Now they have succeeded. Two groups—Ian Agol of the University of Illinois, Chicago, and (jointly) Danny Calegari of Caltech and David Gabai of Princeton University—have shown that a major category of 3-manifolds always have orderly edges, or "tame ends." A third group, consisting of Yair Minsky of Yale, Jeffrey Brock of Brown University, and Richard Canary of the University of Michigan, Ann Arbor, has shown how to classify the shapes of those tame ends and proved that once you know the shape of the end, you know the shape of the manifold. (The proofs are posted at xxx.lanl.gov/pdf/math.GT/0405568, 0407161, and 0412006.) The two theorems fit together like a mortise and tenon and resolve several other conjectures from the 1960s and 1970s. Minsky orchestrated the proof of the so-called Ending Lamination Conjecture over a period of 13 years, with major contributions from Masur as well as Canary and Brock. By contrast, the Tame Ends Conjecture began to appear solvable only last year, when Agol, Calegari, and Gabai began working on it.

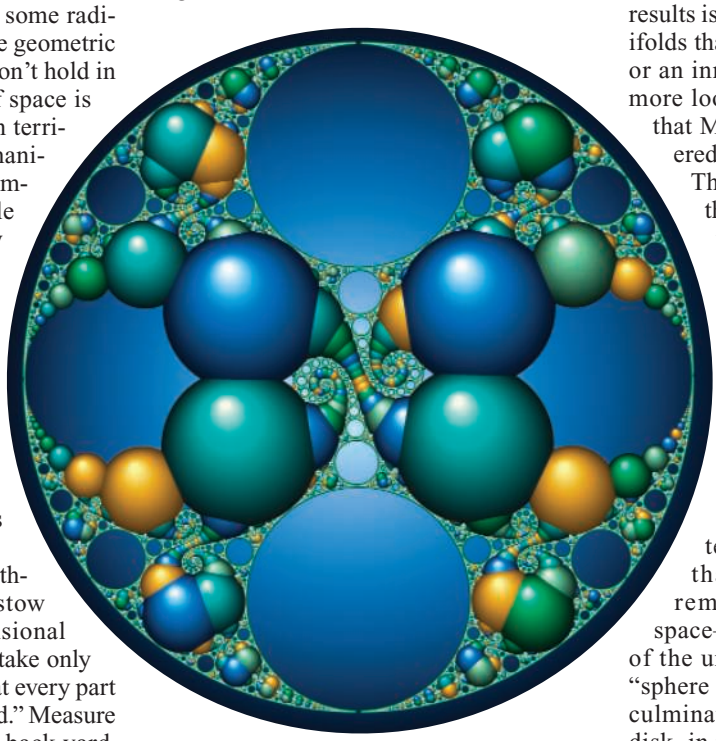

Mirror World. A "hall of mirrors" in hyperbolic space produces a fantastically filigreed fractal.

"In my mind, the real achievement is Brock-Canary-Minsky, and Agol-Calegari-Gabai puts a cherry on top—although a very impressive cherry," says Bonahon.

Both conjectures—now promoted to theorems, assuming that the proofs check out—pertain to a class of universes known as hyperbolic manifolds. Their geometry is unlike the familiar Euclidean or "flat" geometry, which has been known since ancient Greece. Euclidean geometry is characterized by a property called zero curvature: Parallel lines stay a constant distance apart. In spherical geometry, which has positive curvature, lines that start out in parallel converge, like meridians on a sphere. Hyperbolic geometry has negative curvature; in it, parallel rays splay apart like the flowers in a bouquet. Hyperbolic manifolds, which are the most common type, also tend to be by far the most unruly and mathematically interesting ones, which makes their taming even more remarkable.

The central question in both of the new results is how to describe the shape of manifolds that don't close up nicely, like a ball or an inner tube, but instead have one or more loose ends. (Most of the manifolds that Minsky and his colleagues considered have two ends, just like a string.) These ends come in various shapes—they can be narrow like a tunnel, or they can flare outward like the bell of a trumpet. Usually geometers prefer to think of the loose ends, or tunnels or arms, as being infinitely long. Thus, someone living in such a universe would never reach the end of the universe but would always see more space stretching out in front of him. It may seem bizarre that mathematicians have chosen the term "end" to describe something that is literally endless. Yet one remarkable feature of hyperbolic space—reminiscent of medieval views of the universe—is that it comes with a "sphere at infinity." Here the infinite end culminates in a specific shape, such as a disk, in much the way the infinitely long decimal fraction 0.33333… culminates in the number 1/3. Although an inhabitant of the manifold could not see or reach the sphere at infinity, its culminating shape nevertheless has a profound influence on his space.

The story behind these universes begins more than 100 years ago, when the German geometer Felix Klein began pondering questions like this one: Suppose you stand in a room with perfectly reflecting mirrors—what would you see? Of course, with flat mirrors you would expect a "hall of mirrors" effect, with infinitely many copies of yourself as far as the eye could see. But now imagine that the mirrors are cylindrical (or convex). You would still see infinitely many copies of yourself, but the convex mirrors would make your reflections skinnier and skinnier. After enough reflections, the images of your head would shrink to point-sized dots. Now imagine somehow reaching *through* the mirrors and connecting all the

CREDIT: JOS LEYS

Published by AAAS

dots. With just three cylindrical mirrors, you would get a circle, with the real you standing in the middle. With four mirrors, depending on their size and arrangement, you might get a circle, or you might get a jagged, contorted figure that defied Klein's attempts to draw it. Klein was born a century too early to see such figures—now called fractals—become an icon of pop art, thanks to computer graphics. You can think of these fractals as being drawn on the "sphere at infinity," the canvas at the end of the universe.

In 1881, Henri Poincaré discovered a far-from-obvious connection between Klein's fractals and hyperbolic geometry. Each fractal corresponds to a particular manifold, and each open-ended manifold has a particular Kleinian fractal at each of its infinite ends. Nearly a century later, William Thurston (then at Princeton University, now at Cornell) showed that the Kleinian fractal defines a geometric structure on the ends of its corresponding manifold. He called that structure an "ending lamination." Perhaps, he suggested, a manifold's ending lamination would in fact determine the geometry of the whole manifold—in effect, rigidifying it or crystallizing it from the outside in.

Minsky sneaked up on the Ending Laminations Conjecture in stages. He started with a special case, in which the manifold's ends culminate in an inner tube with a puncture through it. Inner-tube shapes, or tori, are as basic to topologists as quarks are to physicists or cells to biologists. He chose this punctured torus because it was the first case complicated enough to be interesting but simple enough to be solvable.

Minsky discovered a way to organize all the possible Kleinian fractals for the manifolds that have this punctured-torus-shaped end (see figure, below). You can think of this picture as a sort of dictionary or map of all the possible Kleinian fractals in question. Each point in the map corresponds to a fractal with a different shape. In the colored region, the relatively simple fractals, such as the two at left in the figure below, correspond to geometries in which the punctured-inner-tube-shaped end grows exponentially fast as it moves out to infinity. The boundary of the colored region in the figure looks like a scalloped coastline. Each "inlet" corresponds to cusped fractals like the four shown on the right in the figure. In these cases, the inner tube shrinks to a point in some places as it moves out to infinity. Likewise, the fractals themselves pinch down simultaneously in infinitely many places and fragment the "sphere at infinity" into infinitely many pieces. Each cusped fractal can also be assigned its own address, a simple fraction, with the 3/5 cusp lying between 1/2 and 2/3, 5/8 between 2/3 and 3/5, and so on.

But amazingly, even irrational numbers like $(\sqrt{5} - 1)/2 = 0.618033985\ldots$, which cannot be expressed as a fraction and therefore lie "between" all the inlets, also correspond to Kleinian fractals. These most monstrous fractals are ferociously difficult even for a computer to draw. (See the bottom box in the figure.) In the corresponding geometry, the punctured-torus end neither grows nor shrinks but oscillates in a perpetual state of indecision as it moves out toward infinity. With his collaborators Brock and Canary, Minsky showed that Thurston's ending laminations play the same role as the irrational "addresses" in the above description. But the numbers are more than mere addresses: They are a genetic code. Two ending laminations provide all the information needed to assemble a perfect replica of a two-ended manifold.

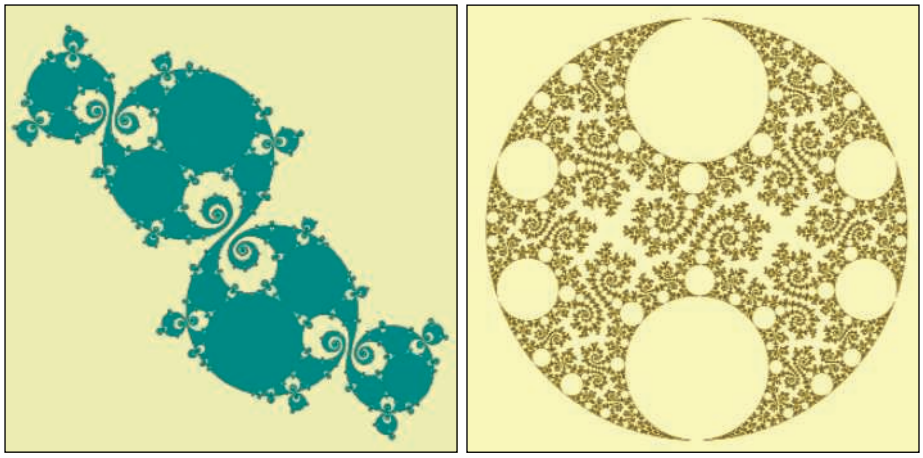

Infinite fascination. Spiralling (left) and cusped (right) Kleinian fractals bound hyperbolic universes.

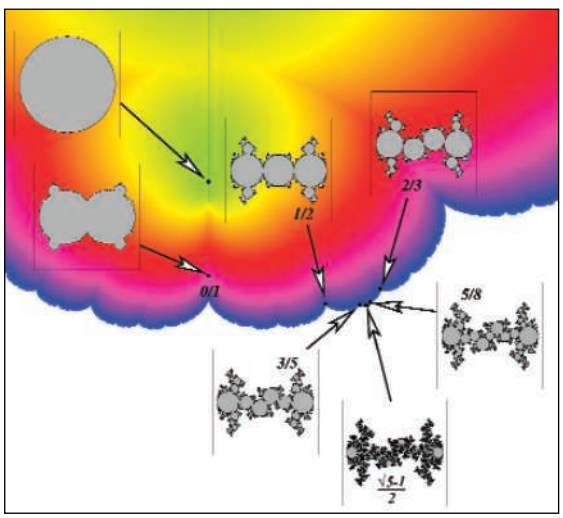

Organizing principle. In this "map" of Kleinian fractals, cusped fractals lie on the "coastline."

CREDITS (TOP TO BOTTOM): JOS LEYS; DAVID WRIGHT/OKLAHOMA STATE UNIVERSITY

One problem was left to be cleared up. The Ending Lamination Theorem works only for certain hyperbolic manifolds: the ones with "tame ends." It assumes that each end of the manifold keeps the same general shape as it stretches out toward infinity. A tame end can be visualized as a tunnel that can grow or shrink in width but cannot split into separate tubes or have tubes that merge together. But "wild ends" can change their shape or split into pieces as they go. Agol and Calegari and Gabai found a way to eliminate even the trickiest of these wild ends from consideration, as long as the manifold in question is hyperbolic.

According to Alfred Marden of the University of Minnesota, who proposed the Tame Ends Conjecture in 1974, "it was just pie in the sky. No one had the vaguest idea how to prove it. If you ever questioned whether there is linear progress in mathematics, this is a very clear example. This proof could not have been done 30 years ago."

Together, the two theorems resolve several other problems that had been open for decades. For instance, one consequence is that Kleinian fractals, if drawn with an infinitely thin line, are either invisible or solid black, in the same mysterious way that all the points in a line color the line black, even though each point is infinitely small. Agol and Minsky believe that the taming of the hyperbolic ocean will lead to progress on other problems as well. Calegari, on the other hand, is afraid that three-dimensional topology will fragment. "The key conjectures tied together people who didn't have a lot in common—specialists in Kleinian groups, hyperbolic geometry, knot theory, foliations, and quantum invariants," he says. "Now there's less incentive for them to be in the same field."

– DANA MACKENZIE

Dana Mackenzie is a freelance writer based in Santa Cruz, California.

Random Samples

Edited by Constance Holden

Tooth Fight

How many paleoanthropologists does it take to locate a molar on the correct side of a fossil jawbone? The short answer to this joke, which was winging around the Internet this month, is 28. That's the number of paleoanthropologists who, in the current issue of the *South African Journal of Science*, declare that a fossilized wisdom tooth belonged in the right rather than the left lower jaw of a famous fossil of a putative human ancestor from Chad.

In 2002, *Sahelanthropus tchadensis* was proposed as the earliest known hominid by paleontologist Michel Brunet of the University of Poitiers, France, and colleagues (*Science*, 12 July 2002, p. 171). But earlier this year, University of Paris X geographer Alain Beauvilain, a former member of Brunet's team, and orthodontist Yves Le Guellec questioned Brunet's placement of the isolated molar in the right lower jawbone and questioned why other fossils found at the same site have not yet been not published. Their challenge in last spring's issue of the South African journal, reported widely by the French media, did not cast doubt on the fossil's status, but it did cast a cloud over Brunet's methods.

In the current issue, Brunet presents computed tomography scans showing what he calls an "unambiguous match" between the molar and roots in the right side of the jawbone. The 28 paleoanthropologists signing the letter back up that conclusion. One of the letter's organizers, Tim White of the University of California, Berkeley, notes that Beauvilain's report was translated by College de France geologist Martin Pickford, who discovered a rival fossil candidate for oldest hominid.

But Beauvilain and Pickford—who has now rescinded an earlier apology to Brunet—are fighting back tooth and nail. In the same journal issue, Beauvilain responds to Brunet's defense by insisting that the molar that was found separately from the jaw was glued into the wrong side. Interviewed by *Science*, Pickford called the multiauthor letter an intimidation tactic designed to squelch scientific debate on published fossils.

Beauvilain also seems intent on forcing Brunet to reveal other fossils by raising the tantalizing possibility that leg bones of *Sahelanthropus* may be included in 52 unpublished mammalian fossils from the Chadian site. A leg bone could shed light on whether *Sahelanthropus* was an upright-walking ancestor of humans or a quadrupedal ape. Brunet declines to comment, saying that the fossils are still under study.

SARS War Memorial

China has no animal-rights movement to speak of. But its scientists still think about the sacrifices made by their research animals. The latest memorial sits on the lawn at the Animal Research Institute of the Chinese Academy of Medical Sciences in Beijing, a tribute to the animals that gave their lives to develop a vaccine against severe acute respiratory syndrome (SARS).

The "Soul-Consoling Stone," as it is named in Chinese, was installed in spring 2003, not long after SARS swept through Asia. Qin Chuan, a pathologist and head of the institute, says the monument is only now being publicized because of promising early vaccine trials (*Science*, 17 December, p. 2021). Qin says she hopes the stone will remind people of the contribution of mice, guinea pigs, rabbits, and monkeys to human health. "After all," she says, "human beings or animals, we are all Nature's creatures."

New Primate Discovered in India

Scientists surveying biodiversity in remote mountain forests along India's northeastern border with China have stumbled upon a new monkey species: the *Macaca munzala*, or Arunachal macaque.

The first new macaque species discovered anywhere since 1903, the primate is the 21st known macaque species and the eighth in India. The last primate found in India was the golden langur, discovered in 1955.

The Arunachal macaque is "stockily built and has an unusually dark face," according to its discoverers, Anindya Sinha, Aparajita Dutta, M. D. Madhusudan, and Charudutt Mishra, who work with the Nature Conservation Foundation in Mysore. The animal largely keeps to the forests and lives at altitudes up to 3500 meters, making it one of the highest-dwelling primates in the world.

The animal appears to be thriving even though its habitat is under immense threat from logging and human settlements. The scientists found "a fairly large population" in 14 troops spread over 1200 square kilometers. The team is urging the Indian government to designate the primate's habitat as a "protected area." A paper describing the new macaque will appear in the August 2005 *International Journal of Primatology*.

CREDITS (TOP TO BOTTOM): *CHINA FEATURES*; ALAIN BEAUVILAIN/*SOUTH AFRICAN JOURNAL OF SCIENCE*; M. D. MADHUSUDAN

Published by AAAS

Edited by Yudhijit Bhattacharjee

NONPROFIT WORLD

Graduate lobbyist. Patricia McAllister hopes to give U.S. graduate education a higher profile in Washington, D.C., policy circles as the first-ever director of government relations at the Council of Graduate Schools. McAllister, 52, moves over from a similar post at the Educational Testing Service.

JOBS

Sunnier climes. An electrical engineer who became the first woman to lead an engineering school at a major research university has been named chancellor of the University of California (UC), Santa Cruz. Denice Denton, currently dean of engineering at the University of Washington (UW), Seattle, will take up her new job in February as successor to M.R.C. Greenwood, who was appointed UC provost in February 2004.

Denton, 45, is known for her efforts to improve mathematics and science education from kindergarten through college and for helping increase the diversity of the undergraduate engineering population. In May, she was among nine scholars who received a Presidential Award for Excellence in Science, Mathematics, and Engineering Mentoring.

Denton, who has been at UW since 1996, says she was drawn to UCSC by "its tradition of pioneering, interdisciplinary research" and plans to support the "innovative spirit" of its faculty. She will receive an annual salary of $275,000.

PIONEERS

Flying high. Aviation medicine was a fallback career for Padma Bandopadhyay after less-than-perfect eyesight prevented her from becoming a pilot. But after 37 years, she's gone where no woman has gone before, becoming the first female Air Marshal in the history of the Indian Air Force (IAF).

The 59-year-old Bandopadhyay has flown thousands of kilometers in the course of her research on human physiology at high altitudes. She's also co-led a joint expedition with Soviet scientists to the Arctic Circle to understand how long it takes people from the tropics to acclimatize to the extreme cold.

A mother of two, Bandopadhyay says her IAF colleagues, who are predominantly male, have been extremely supportive. "I am not a feminist of any sort," she says.

Isolated behavior? The National Institutes of Health (NIH) has appointed Brown University psychologist David Abrams to oversee behavioral and social science research, a post vacant for nearly 2 years. But the new hire is lukewarm to the community's plea to give basic research a home in one institute.

Abrams, 53, takes over next month as director of the Office of Behavioral and Social Sciences Research, which leads cross-agency initiatives and collaborations. The previous head, Raynard Kington, was promoted to NIH deputy director in February 2003.

The South Africa–born Abrams, whose expertise is in behavioral and preventive medicine, says he thinks social and behavioral research "can play a much greater role" in translating findings into treatments. But he questions the recent recommendation of an NIH-appointed working group to locate basic behavioral and social research within a single, existing institute (*Science*, 10 December, p. 1878). "We're better off not having it in one place," he says. That view disappoints advocates such as Alan Kraut, executive director of the American Psychological Society. "My fear is that David's appointment, as good as he is, does not mark any change in how behavioral science will be treated by NIH higher-ups,"

Got any tips for this page? E-mail people@aaas.org

SIDELINES

Heady stuff. Three Boston-area sisters with more than 2 meters of hair among them have been named Women of the Year by the Luxuriant Flowing Hair Club for Scientists. Johanna Bobrow, a staff scientist at the Massachusetts Institute of Technology (MIT) in Cambridge, Elizabeth Bobrow, an electrical engineer with BAE Systems, and Laurel Bobrow, an MIT undergraduate majoring in cognitive science, were chosen through a consensus among the 100-odd club members. The club was started in 2001 with Harvard psychologist Steven Pinker inducted as the first member.

CREDITS (TOP TO BOTTOM): PALLAVA BAGLA; BROWN UNIVERSITY; LFHCFS

Published by AAAS

Letters to the Editor

Letters (~300 words) discuss material published in *Science* in the previous 6 months or issues of general interest. They can be submitted through the Web (www.submit2science.org) or by regular mail (1200 New York Ave., NW, Washington, DC 20005, USA). Letters are not acknowledged upon receipt, nor are authors generally consulted before publication. Whether published in full or in part, letters are subject to editing for clarity and space.

Debate Over Open Access in the U.K.

DANIEL CLERY'S ARTICLE ABOUT OPEN ACCESS IN the United Kingdom ("Mixed week for open access in the U.K.," News of the Week, 12 Nov., p. 1115) seems to be carrying on a tradition on this topic of drubbing Peter to pox Paul! Clery reports that the U.K. government rejected recommendations on open access from the House of Commons Science and Technology Committee.

The only major recommendation of the committee was to mandate open access self-archiving (i.e., that U.K. researchers must make their published journal articles publicly accessible to all would-be users on their institution's Web sites). Yet no one—members of Parliament, press, publishers, or librarians—seems to be able to stop going on and on about open access publishing (where the author-institution pays for publication per outgoing article instead of the reader-institution paying for subscription per incoming journal), which was not what the committee recommended mandating.

All three committee recommendations—the one major one, to mandate open access self-archiving, plus the two minor ones [(i) to encourage "experimenting" with open access publishing and (ii) to provide some funds for authors who wish to publish in open access journals]—were turned down by the government (mainly via Department of Trades and Industry), all on the basis of arguments against open access publishing.

Let the next parliamentary recommendation be shorter and clearer and make no mention whatsoever of Paul (open access publishing), and then maybe Peter will stand a fair chance!

Or can we just not resist provoking a good fight with publishers every time and having a good moan about library budgets and a royal go at economic reform? Can we, in other words, not keep in mind that access is what this is all about, and that even affordability would become a minor matter if only the access needs were fully taken care of—as they would be if all articles were made open access through self-archiving?

STEVAN HARNAD
Centre de Neuroscience de la Cognition, Université du Québec à Montréal, Case postale 8888, succursale Centre-ville, Montréal, QC H3C 3P8, Canada.

Breast Cancer Risks for *BRCA1/2* Carriers

THE REPORT BY M.-C. KING *ET AL.* ESTIMATES breast cancer risks in carriers of the Ashkenazi Jewish founder mutations in *BRCA1* and *BRCA2* ("Breast and ovarian cancer risks due to inherited mutations in *BRCA1* and *BRCA2*," 24 Oct. 2003, p. 643). The analysis was based on data from relatives of identified mutation-carrying breast cancer cases unselected for family history. Only those relatives for whom a DNA sample was available were analyzed, a total of 84 of the 104 cases. The authors estimate the breast cancer risk by age 70 to be 71%, irrespective of mutation, and claim that "the results are likely to be generalizable to women with any pathogenic *BRCA1* and *BRCA2* mutations…" Their estimate is, however, higher than the estimates from a combined analysis of 22 similar studies from a variety of populations, based on the relatives of 500 unselected mutation-carrying cases: 65% for *BRCA1* and 45% for *BRCA2* (*1*). Another study of Ashkenazi Jews estimated the risks in ancestral mutation carriers to be 46% and 26%, respectively (*2*). We are concerned about inconsistencies within the data of King *et al.* and suggest that their results may be subject to a form of selection bias that does not affect previous reports.

The high lifetime risk of breast cancer that they report appears to be inconsistent with the prevalence of mutations among unselected cases in the same study [10.3%, almost identical to the 10.1% reported in (*2*)]. If the age-specific risk estimates reported by King *et al.* were to apply to all carriers, then given the known population prevalences of AJ founder mutation carriers, they should have observed a prevalence of 21.2%, i.e., more than 200 case carriers, rather than the 104 actually observed (see table). This inconsistency calls into question the general applicability of the risk estimates and of the modifying effects reported by King *et al*. It also illustrates the notion that there is not a single quantity known as "the penetrance." Rather, what is usually called penetrance is actually an average effect of the particular mutations in the population in which they have been sampled (*3*). In addition to variation among risk factors, individuals' "penetrance" may be modified by a host of unknown factors, some of which may aggregate in families and, if not properly allowed for, bias estimates of penetrance (*4*).

A possible explanation for their high risk estimates for both genes is that restriction of the analysis to known mutation carriers could have introduced bias if the detection of carriers in relatives was not independent of disease status. Among deceased relatives, DNA was sometimes available from archival tissue of affected women, but it was not available for unaffected women. Among living relatives, affected women may have been more willing to participate.

OBSERVED AGE-SPECIFIC PREVALENCE OF *BRCA1* AND *BRCA2* MUTATIONS IN ASHKENAZI JEWISH WOMEN WITH BREAST CANCER AND PREDICTED NUMBERS BASED ON THE PENETRANCE ESTIMATES OF KING *ET AL.*

Age-group	Risk in carriers (%)*		Risk in noncarriers (%)†	Predicted prevalence (%)‡; number in parentheses		Observed prevalence (%)§	
	BRCA1	*BRCA2*		*BRCA1*	*BRCA2*	*BRCA1*	*BRCA2*
<40	21	17	0.44	34.7 (36.5)	21.1 (22.1)	24	10
40–44	9.6	9	0.56	19.1 (25.7)	13.4 (18.1)	9	7
45–49	8.4	8	0.95	11.6 (21.8)	8.3 (15.6)	6	2
50–59	19	14	2.70	9.8 (29.9)	5.4 (16.5)	5	2
60–79	23	37	7.31	4.5 (12.5)	5.4 (15.1)	0.8	2
All ages	–	–	–	12.5 (126.4)	8.7 (87.4)	6.7 (67)	3.7 (37)

*Risk of becoming affected within the age interval, based on Table 2 of King *et al.* Incidence rates for the age groups 40 to 44 and 45 to 49 have been assumed to be equal. †Risk of becoming affected within the age interval, based on rates for U.S. white females reported by the SEER program (1993–97). ‡Predicted prevalence of *BRCA1* 185delAG or 5382insC carriers combined, and of *BRCA2* 6174delT carriers, in women with breast cancer diagnosed within the age interval, based on risk in Table 2 of King *et al.* [assuming the prevalence at birth was 1.6% and 1.2% for *BRCA1* and *BRCA2*, as given by the prevalences in the youngest age group by (*2*); other studies give similar estimates]. §Observed prevalence of *BRCA1* 185delAG or 5382insC carriers combined, and of *BRCA2* 6174delT carriers, in women with breast cancer diagnosed within the age interval, based on Table 1 of King *et al.*

Published by AAAS

The advantage of the likelihood-based approach used in other studies is that it incorporates the phenotypes of all subjects, irrespective of whether their genotypes are known, properly allowing for uncertainty about the genotypes of untyped subjects (*1*). Perhaps the cancer and genotyping data on all 104 families, including individuals for whom DNA was not available, could be presented in a format that permits independent analysis [see, e.g., Table 1 from (*5*)].

DOUGLAS F. EASTON,[1] JOHN L. HOPPER,[2] DUNCAN C. THOMAS,[3] ANTONIS ANTONIOU,[1] PAUL D. P. PHAROAH,[1] ALICE S. WHITTEMORE,[4] ROBERT W. HAILE[5]

[1]Department of Public Health and Primary Care, University of Cambridge, Strangeways Research Laboratory, Cambridge CB1 8RN, UK. [2]Centre for Genetic Epidemiology, University of Melbourne, Carlton, Victoria 3053, Australia. [3]Department of Preventive Medicine, University of Southern California, CHP-220, Los Angeles, CA 90089, USA. [4]Department of Health Research and Policy, Stanford University School of Medicine, Stanford, CA 94305, USA. [5]Department of Preventive Medicine, University of Southern California, NOR 4455A, Los Angeles, CA 90033, USA.

References
1. A. Antoniou *et al.*, *Am. J. Hum. Genet.* **72**, 1117 (2003).
2. J. M. Satagopan *et al.*, *Cancer Epidemiol. Biomark. Prev.* **10**, 467 (2001).
3. J. L. Hopper, *Semin. Cancer Biol.* **11**, 367 (2001).
4. C. B. Begg, *J. Natl. Cancer Inst.* **94**, 1221 (2002).
5. J. L. Hopper *et al.*, *Cancer Epidemiol. Biomark. Prev.* **8**, 741 (1999).

THE NEW YORK BREAST CANCER STUDY (NYBCS) Group Report ("Breast and ovarian cancer risks due to inherited mutations in *BRCA1* and *BRCA2*," M.-C. King *et al.*, 24 Oct. 2003, p. 643) states that their results "indicate that breast and ovarian cancer risks among *BRCA1* or *BRCA2* mutation carriers who are ascertained through a single affected relative are as high as risks observed in multiply affected families." We disagree. The design, implementation, and analysis of the NYBCS could have led to serious overestimation of penetrance because of ascertainment bias. Their attempts to rule out overestimation are not convincing. Family members must be enrolled irrespective of disease status to achieve unbiased penetrance estimates. That is, a carrier relative who dies from heart disease and one who dies from breast cancer must be equally available for genotyping and subsequent inclusion in the analysis.

1) When only confirmed carriers are included, availability of tumor blocks as a source of DNA for genotyping could influence who is included.

2) Relatives with breast or ovarian cancer, particularly distant relatives, might be more likely to be reported by probands and enrolled by investigators.

3) The authors excluded the entire sibship when one female sibship member could not be genotyped directly or by reconstruction. This strategy could increase net bias because one refuser can exclude the entire sibship; this may be more likely to occur when there are no affected women in the sibship and in older sibships. Also, this strategy gives no protection from bias in a one-female sibship. Presentation of numbers of relatives according to relationship to proband, cancer status, and method of determining carrier status (blood, blocks, or inferred) would help the reader evaluate the importance of ascertainment bias.

4) A study based on relatives of cancer patients is not optimal for assessing heterogeneity of risk for carriers in different families (*1*–*5*) because relatives in higher-risk families, if any, will be overrepresented. In the extreme, women in families segregating a mutation but having no breast cancer in the pedigree are excluded from all analyses because only breast cancer cases can be probands. Moreover, if carrier relatives from the 52 low-incidence families constitute half of all carrier women, the difference between penetrance in high-incidence and low-incidence families would be double the difference between entries in tables S2C and S2A; for example, at age 70, the difference would be 18 percentage points (62% versus 80%).

5) Probands were ascertained from 12 "major cancer centers" and affiliated private practitioners. Patients from "low-incidence" families may be more likely to be treated at community hospitals and be missed by this study. Similarity of mutation prevalence at each cancer center does not address this concern.

6) Probands were Jewish breast cancer patients referred to the study team by clinicians. Women of uncertain ethnicity but with a strong family history may have been referred more often than women with no family history. Although the NYBCS provides data comparing family history of refusers and participants, they cannot investigate family history of carriers not referred by participating physicians, and the pool of individuals from which referred cases were drawn is not known.

Penetrance estimates from truly population-based designs (*2*, *4*, *6*) and a large survey of a Jewish community (*1*, *3*) are lower than those from multiplex consortium families (*7*) and the NYBCS. If families segregating *BRCA* mutations have wide variation in risk, differences in penetrance estimates among studies may reflect differences in the proportion of carriers enrolled from higher or lower risk families (*1*, *2*, *4*, *5*). Because the NYBCS does not show convincingly that carriers with no or modest family history have nearly the same penetrance as carriers with extensive family history, it does not provide new support for recommendations of broader screening given in the accompanying Perspective ("A risky business—assessing breast cancer risk," E. Levy-Lahad, S. E. Plon, 24 Oct. 2003, p. 574).

We agree that environmental and genetic factors can lead to heterogeneity of risk among individual carriers (*8*, *9*). However, the design and analysis of the New York study do not reliably investigate them. With additional consideration of the methodologic issues raised here, results about penetrance and cofactors from the NYBCS can be better integrated with the extensive body of published evidence.

SHOLOM WACHOLDER, JEFFERY P. STRUEWING, PATRICIA HARTGE, MARK H. GREENE, MARGARET A. TUCKER

Division of Cancer Epidemiology and Genetics, National Cancer Institute, M/S 7244, Bethesda, MD 20892–7244, USA. E-mail: Wacholder@NIH.gov

References
1. J. P. Struewing *et al.*, *N. Engl. J. Med.* **336**, 1401 (1997).
2. S. Wacholder *et al.*, *Am. J. Epidemiol.* **148**, 623 (1998).
3. J. L. Hopper *et al.*, *Cancer Epidemiol. Biomark. Prev.* **8**, 741 (1999).
4. A. Antoniou *et al.*, *Am. J. Hum. Genet.* **72**, 1117 (2003).
5. C. B. Begg, *J. Natl. Cancer Inst.* **94**, 1221 (2002).
6. S. Thorlacius *et al.*, *Lancet* **352**, 1337 (1998).
7. D. Ford *et al.*, *Am. J. Hum. Genet.* **62**, 676 (1998).
8. B. Modan *et al.*, *N. Engl. J. Med.* **345**, 235 (2001).
9. P. Hartge *et al.*, *Epidemiology* **13**, 255 (2002).

Response

RESULTS OF THE NEW YORK BREAST CANCER Study (NYBCS) (*1*) were that lifetime risks of breast cancer associated with inherited mutations in *BRCA1* and *BRCA2* in the present-day American Ashkenazi Jewish population exceed 80%, that these risks apply to mutation carriers regardless of their family history of breast or ovarian cancer, and that breast cancer risks to mutation carriers have changed over time due to influences of nongenetic factors. The premise of the Letters of Easton *et al*. and Wacholder *et al*. is that NYBCS estimates of breast cancer risk among carriers of *BRCA1* and *BRCA2* mutations are substantially higher at all ages than are penetrance estimates from previous analyses. The Letters' authors then suggest various biases to which they believe the NYBCS could have been subject, leading to these putatively high penetrance estimates.

We disagree with this premise. The first table (p. 1289) compares penetrance estimates for carriers of mutations in *BRCA1* or *BRCA2* from several studies (*1*–*5*). These studies, from four groups, are those most frequently cited in the literature, involve most of the authors of the two critiques, are the largest collections of original data on this topic, and represent four different study designs [see Supporting Online Material (SOM) for more details] (*6*).

As indicated in the first table, estimates of breast cancer risk for mutation carriers for ages up to 60 years are similar in all the studies. Such close concordance is striking,

particularly given the very different study designs employed. In contrast, penetrance estimates for risks by age 70 and by age 80 differ among studies. Estimates from the NYBCS fall in the middle of those previously reported. The divergent penetrance estimates at older ages may be caused by smaller sample sizes and hence wider confidence intervals for estimates and/or less accurate reporting of breast cancer for older relatives, particularly in studies that relied completely on reported family history by the proband. The latter problem may particularly pertain to (*5*), for which risk estimates after age 60 are remarkably flat.

Therefore, we do not think that penetrance estimates are too high in the NYBCS, because, at least for penetrance estimates up to age 60, they agree with results from numerous other studies.

Easton *et al.* use NYBCS risk data to estimate the proportion of breast cancer probands expected to carry *BRCA1* or *BRCA2* mutations. Their estimates predict 213 mutation carriers among the 1008 NYBCS probands. The NYBCS identified 104 mutation carriers among the 1008 probands, a frequency of 10.3%, consistent with other studies of this population and not in dispute. Easton *et al.* thus conclude that NYBCS risks must be overestimated.

We disagree. The discrepancy between predicted and observed numbers of carriers among probands noted by Easton *et al.* is in part the result of their use of incorrect values for "risks in noncarriers" (second table, p. 1290, columns 2, 5, 9, 13). When correct values from SEER age-specific breast cancer rates are used (columns 3, 6, 10, 14), the difference between expected and observed numbers of *BRCA1* and *BRCA2* mutation carriers is reduced (second table, columns 3, 6, 10, 14). But some difference remains. Why?

The resolution lies in identifying the population offering the most accurate breast cancer risk estimates for Ashkenazi Jewish women who do not carry mutations in *BRCA1/2*. Do risks from the SEER registry for U.S. white females accurately reflect breast cancer risks to Ashkenazi Jewish "noncarriers"? Quite apart from genetic predisposition, the population of Ashkenazi Jewish women in the United States may carry a high prevalence of important breast cancer risk factors, including late age at first pregnancy, fewer pregnancies, and (until very recently) frequent use of hormone replacement therapy. Is there a source of breast cancer risk data specifically for Ashkenazi Jewish noncarrier women?

ESTIMATED PENETRANCES OF BREAST CANCER GENES FROM FOUR STUDIES

Risk of breast cancer by age	Cancer and Steroid Hormones Study (*2*)	Breast Cancer Linkage Consortium (*3*, *4*)	Washington, DC Ashkenazi Jewish families (*9*)	New York Breast Cancer Study (*1*)
40	0.14	0.16	0.15	0.20
50	0.38	0.43	0.35	0.37
60	0.55	0.52	0.54	0.55
70	0.67	0.85	0.56	0.71
80	0.92	–	0.62	0.82

Published by AAAS

The Washington, D.C., study of breast cancer among Ashkenazi Jewish women estimated the risks to noncarriers of *BRCA1/2* mutations [fig. 1B of (*5*)]. We reconstructed the calculations of the critique using these estimates, reading data from this figure as accurately as possible (second table, column 4). When the analysis incorporates age-specific breast cancer risk estimates for U.S. Ashkenazi Jewish noncarrier women, rather than for all U.S. Caucasian noncarrier women, the result is striking. The expected number of *BRCA1/2* carriers among 1008 probands is 107 (column 15), very similar to the 104 carriers observed in the NYBCS (column 16). It is reasonable to conclude that the observed frequencies of *BRCA1* and *BRCA2* mutation carriers among NYBCS probands are consistent with the penetrance estimates from the NYBCS.

Easton *et al.* comment that "there is not a single quantity known as 'the penetrance.'" We agree and showed this to be true in the NYBCS. In particular, the highly significant effect of birth cohort on breast cancer risk in the NYBCS demonstrated that penetrance depends on nongenetic factors. We also agree that modifiers (either genetic or nongenetic) may cluster in families, leading to biased estimates of penetrance (*7*). However, results of three analyses demonstrated that this was not the case in the families of the NYBCS. As indicated in our Report, the effect of birth cohort did not cluster within families, but rather transcended families. Furthermore, the 11 women with mutations who reached age 65 without developing breast or ovarian cancer (i.e., potentially "low risk" carriers) were members of 11 different families, clearly not evidence of clustering of modifiers in some lineages. Finally, risk in low-incidence families was the same as risk in high-incidence families, an observation not consistent with familial clustering of modifiers of penetrance.

Wacholder *et al.* contend that various biases in the NYBCS led to inflated estimates of penetrance of *BRCA1* and *BRCA2* mutations. We address each point, following the numbering used in their Letter.

1) In principle, availability of pathology specimens would enable genotyping of deceased cancer patients more easily than genotyping of deceased individuals who never underwent biopsy. To avoid this bias, the NYBCS only included deceased sisters, aunts, or cousins with cancer in the analysis if all their affected and unaffected sisters could be genotyped as well, either directly or through their surviving children.

2) It is not clear whether breast and ovarian cancer in relatives is more likely to be overreported or underreported. A recent analysis (*8*) suggests that underreporting is a greater problem than overreporting, with accuracy decreasing with distance of relationship. We minimized reporting problems by obtaining information from multiple relatives. That is, after a mutation was identified in a proband, multiple relatives were enrolled and sampled, and family histories were obtained from each.

3) Wacholder *et al.* express concern about biases that would be introduced by including distant relatives in the analysis. We were very much aware of this problem and addressed it in the following way. Grandmothers could be included in our analysis even if their sisters were not available. However, a sister-ship of great aunts was included or excluded as a unit. As one would expect, our analysis therefore included very few great aunts: Among more than 700 relatives genotyped, only four were great aunts of a proband.

4) It is correct that each family in the NYBCS was ascertained through a single breast cancer case. Whether such an ascertainment scheme leads to overrepresentation of multiply affected families can be evaluated by knowing the proportion of families ascertained more than once. In the NYBCS, one of 1008 families was ascertained twice, through a mother and daughter both diagnosed at participating hospitals during the ascertainment period. This mother and daughter were wild-type for *BRCA1* and *BRCA2*.

Wacholder *et al.* state that "carrier relatives from the 52 low-incidence families constitute half of all carrier women." This is not correct; half of all carrier probands (52 of 104), not half of all relatives, were from low-incidence families.

5) The 12 cancer centers participating in the NYBCS differ from one another in that some are tertiary referral centers and others community hospitals; some are urban and some suburban. Income levels of patients and the proportions of patients who are Jewish differ among centers as well. The tertiary referral centers did not have a higher frequency of mutation carriers than did other centers.

6) We addressed the problem of an unknowable pool of potentially eligible patients by comparing risks in families of patients drawn from NYBCS collaborators with the most different referral patterns. We were particularly concerned that patients referred by private physicians would be from higher-risk families. We hypothesized both that privately referred patients would be more likely to carry *BRCA1* or *BRCA2* mutations and that the families would be more severely affected. Our rationale for including a private partnership of physicians in the NYBCS collaborative group was to include a probable

PREDICTED AND OBSERVED NUMBERS OF *BRCA1* AND *BRCA2* MUTATION CARRIERS AMONG NYBCS PROBANDS

		Breast cancer risk to white females in age interval			Predicted number of *BRCA1* carriers among NYBCS probands				Predicted number of *BRCA2* carriers among NYBCS probands				Predicted *BRCA1* and *BRCA2* carriers among NYBCS probands			
Column:	1	2	3	4	5	6	7	8	9	10	11	12	13	14	15	16
Age group		Easton *et al.*	Corrected values from SEER public database (*9*)	Ashkenazi Jewish non-carriers (*5*)	Easton *et al.*	Corrected values from SEER public database (*9*)	Ashkenazi Jewish non-carriers (*5*)	*BRCA1* probands observed	Easton *et al.*	Corrected values from SEER public database (*9*)	Ashkenazi Jewish non-carriers (*5*)	*BRCA2* probands observed	Easton *et al.*	Corrected values from SEER public database (*9*)	Ashkenazi Jewish non-carriers (*5*)	*BRCA1/2* probands observed
<40		0.0044	0.0043	0.005	36.4	37.2	32	26	22.2	22.7	20	11	58.6	59.9	52	37
40–44		0.0056	0.0057	0.01	25.8	25.3	14	12	16.2	15.9	9	11	42.0	41.2	23	23
45–49		0.0095	0.0092	0.03	21.3	22.0	7	11	17.2	17.8	5	4	38.5	39.8	12	15
50–59		0.0143	0.0290	0.05	29.6	14.6	8	15	16.5	8.1	5	5	46.1	22.7	13	20
60–79		0.0204	0.0805	0.08	12.7	3.2	3	3	15.2	3.9	4	6	27.9	7.1	7	9
All ages		–	–	–	125.8	102.3	64	67	87.3	68.4	43	37	213.1	170.7	107	104

"outlier" group. To our surprise, however, of the 25 probands referred by private practitioners, all were wild-type for the three ancient mutations in *BRCA1* and *BRCA2*.

As we demonstrated in the NYBCS, women with *BRCA1* and *BRCA2* mutations are at very high risks of breast and ovarian cancer. We hope this reality will not be lost in the discussion of optimal statistical approaches.

MARY-CLAIRE KING, ON BEHALF OF THE NEW YORK BREAST CANCER STUDY GROUP

Departments of Medicine and Genome Sciences, University of Washington, Seattle, WA 98195, USA.

References and Notes

1. M.-C. King, J. H. Marks, J. B. Mandell, New York Breast Cancer Study Group, *Science* **302**, 643 (2003).
2. E. B. Claus, N. Risch, W. D. Thompson, *Cancer* **73**, 643 (1994).
3. D. F. Easton, D. Ford, D. T. Bishop, Breast Cancer Linkage Consortium, *Am. J. Hum. Genet*. **56**, 265 (1995).
4. D. Ford *et al.*, *Am. J. Hum. Genet*. **62**, 676 (1998).
5. J. P. Struewing *et al.*, *N. Engl. J. Med*. **336**, 1401 (1997).
6. SOM is available on Science Online at www.sciencemag.org/cgi/content/full/306/5705/2187c/DC1/
7. C. B. Begg, *J. Natl. Cancer Inst*. **94**, 1221 (2002).
8. A. Ziogas, H. Anton-Culver, *Am. J. Prev. Med*. **24**, 190 (2003).
9. See www.seer.cancer.gov.

Research Ethics and the EPA

IN MANY WAYS, E. SILBERGELD *ET AL.*, IN THEIR Policy Forum "Human health research ethics" (13 Aug., p. 949), agree with the recommendations put forth in our report, *Intentional Human Dosing Studies for EPA Regulatory Purposes: Scientific and Ethical Issues* (*1*), which recommends that the U.S. Environmental Protection Agency (EPA) require that all human research conducted for use by the agency, regardless of who is conducting or supporting the research, be "approved in advance by an appropriately constituted Institutional Review Board (IRB) or an acceptable foreign equivalent" (p. 133). We further suggest that the EPA "may wish to use FDA's implementation of its equivalent of the Common Rule as a guide for its adoption of such a requirement" (p. 133). Although we believe that IRBs are a crucial part of the system of protection for research participants, we also conclude that in some special cases, additional review is needed. Consider, for example, the National Institutes of Health's Recombinant DNA Advisory Committee, which reviews gene transfer protocols. Because of the unique risk-benefit calculus of human dosing studies conducted for EPA regulatory purposes, we believe that a similarly centralized and elevated review is called for, and we thus recommend that the EPA establish a Human Studies Review Board (HSRB) to evaluate intentional dosing studies both before they are conducted and after they have been completed (p. 135).

The HSRB would supplement the work of the IRB, and its recommendations would be advisory. Its principal function would be to help ensure that the EPA considers only intentional human dosing studies that meet the rigorous scientific and ethical standards specified in our report. The post-review is intended to provide advice to the EPA on "whether, and to what extent, the results should be considered" (p. 135) by the EPA, something an IRB does not do. We recommend that the HSRB's review be made public, and we call for an assessment of the HSRB after 5 years (p. 142). We believe that implementation of the recommendations in our report will ensure the most protective system for intentional human dosing studies.

JAMES F. CHILDRESS[1] AND MICHAEL R. TAYLOR[2]

[1]Institute for Practical Ethics and Public Life, University of Virginia, Post Office Box 400800, Charlottesville, VA 22904, USA. [2]Risk, Resource, and Environmental Management Division, Resources for the Future, 1616 P Street, NW, Washington, DC 20036, USA.

*Co-chairs, NRC Committee on the Use of Third Party Toxicity Research with Human Research Participants

Reference

1. National Research Council, *Intentional Human Dosing Studies for EPA Regulatory Purposes: Scientific and Ethical Issues* (National Academies Press, Washington, DC, 2004).

Response

AS CHILDRESS AND TAYLOR NOTE, WE ARE IN agreement with the National Research Council recommendation (*1*) that the EPA should ensure that all research it uses is reviewed by an appropriately constituted Institutional Review Board (IRB) before initiation, regardless of the source of funding. However, the recommendation for an EPA-sponsored Human Study Review Board (HSRB) is based on the arguable assumption that there is a "unique risk-benefit calculus" for intentional human dosing studies used by the EPA. In fact, the same ethical issues arise in human toxicity testing prior to a clinical trial of a therapeutic agent.

Childress and Taylor do not address the resolution of a situation where the EPA's proposed HSRB disagrees with the IRB of the investigator. Obviously, the situation is untenable if the institutional IRB does not approve the study, and the investigator appeals to the EPA and gets a countervening approval.

When a regulatory issue arises, how would existing literature be handled? A study that was conducted without intent to submit to the EPA would not have been presented to the HSRB. Would that exclude it from future consideration by the EPA?

We fail to see how a review after a study is completed provides any meaningful protection of the subjects. On the basis of the EPA's Advanced Notice of Proposed Rulemaking (*2*), we are concerned that inappropriate considerations, such as provenance or the potential impact of a study on a regulation, would be applied in this retrospective assessment.

In short, we continue to believe that application of the Common Rule to all research considered by the EPA is both necessary and sufficient to protect human research subjects.

ELLEN SILBERGELD,[1] STEVEN E. LERMAN,[2] LESLIE J. HUSHKA[3]

[1]Johns Hopkins University, Bloomberg School of Public Health, Baltimore, MD 21205, USA. [2]ExxonMobil Biomedical Sciences Inc., Annandale, NJ 08801, USA. [3]Exxon Mobil Corporation, Houston, TX 77079, USA.

References

1. National Research Council, *Intentional Human Dosing Studies for EPA Regulatory Purposes: Scientific and Ethical Issues* (National Academies Press, Washington, DC, 2004).
2. EPA, Human testing: Advance notice of proposed rulemaking, Docket no. OPP-2003-0132, *Fed. Regist*. **68**, 24410 (2003).

TECHNICAL COMMENT ABSTRACTS

COMMENT ON "The Evolution of Modern Eukaryotic Phytoplankton"

Patrick J. Keeling, John M. Archibald, Naomi M. Fast, Jeffrey D. Palmer

The portable plastid hypothesis for the evolution of eukaryotic phytoplankton (Review, Falkowski *et al.*, 16 July, 2004, p. 354) is based on two assumptions: Endosymbiont-to-host nuclear gene transfer is rare and secondary plastids arise most often from red algal endosymbionts. Available evidence contradicts both claims, and so the hypothesis is unlikely to explain algal evolution.

Full text at www.sciencemag.org/cgi/content/full/306/5705/2191b

RESPONSE TO COMMENT ON "The Evolution of Modern Eukaryotic Phytoplankton"

Daniel Grzebyk, Miriam E. Katz, Andrew H. Knoll, Antonietta Quigg, John A. Raven, Oscar Schofield, F. J. R. Taylor, Paul G. Falkowski

Based on a comparison of plastid, nuclear, and mitochondrial genomes, the portable plastid hypothesis suggests that a diverse group of extant eukaryotic host cells obtained their plastids from independent endosymbiotic events with eukaryotic photosynthetic organisms. We maintain that because they retain more genes in their genome, red plastids were more likely to be successfully acquired than green plastids.

Full text at www.sciencemag.org/cgi/content/full/306/5705/2191c

TECHNICAL COMMENT

Comment on "The Evolution of Modern Eukaryotic Phytoplankton"

Falkowski *et al*. (*1*) reviewed the evidence that three disparate groups of algae—dinoflagellates, diatoms, and coccolithophores, each with plastids derived from red algae by secondary endosymbiosis—have come to dominate the oceans' flora over the past 250 million years and speculated about the forces responsible for this domination. Central to this speculation is the "portable plastid hypothesis" (*1*, *2*), which posits that the likelihood with which plastids will be transferred between eukaryotes by secondary endosymbiosis is directly related to the number of genes in their genomes. The more genes, the argument contends, the more portable the plastid. This hypothesis rests on three claims: (i) red algal plastids retain more genes than do green algal plastids; (ii) gene transfer from the (primary) endosymbiont nucleus to the (secondary) host nucleus is rare; and (iii) red algae have been acquired by secondary endosymbiosis more often than have green algae. Although the limited number of red algal plastids examined to date do have more genes (*3*), claims (ii) and (iii) are not consistent with the available data, thus rendering the hypothesis effectively unsupported.

Although red algal plastids may contain more genes than those of green algae, this difference pales against the nuclear contribution to plastid function. All plastid genomes encode only a small fraction of the proteins needed for plastid function—at most ~10 to 20%, and only ~1% in the case of dinoflagellates. The vast majority of plastid proteins are encoded by nuclear genes; most of these genes are derived from the plastid but have been transferred to the nuclear

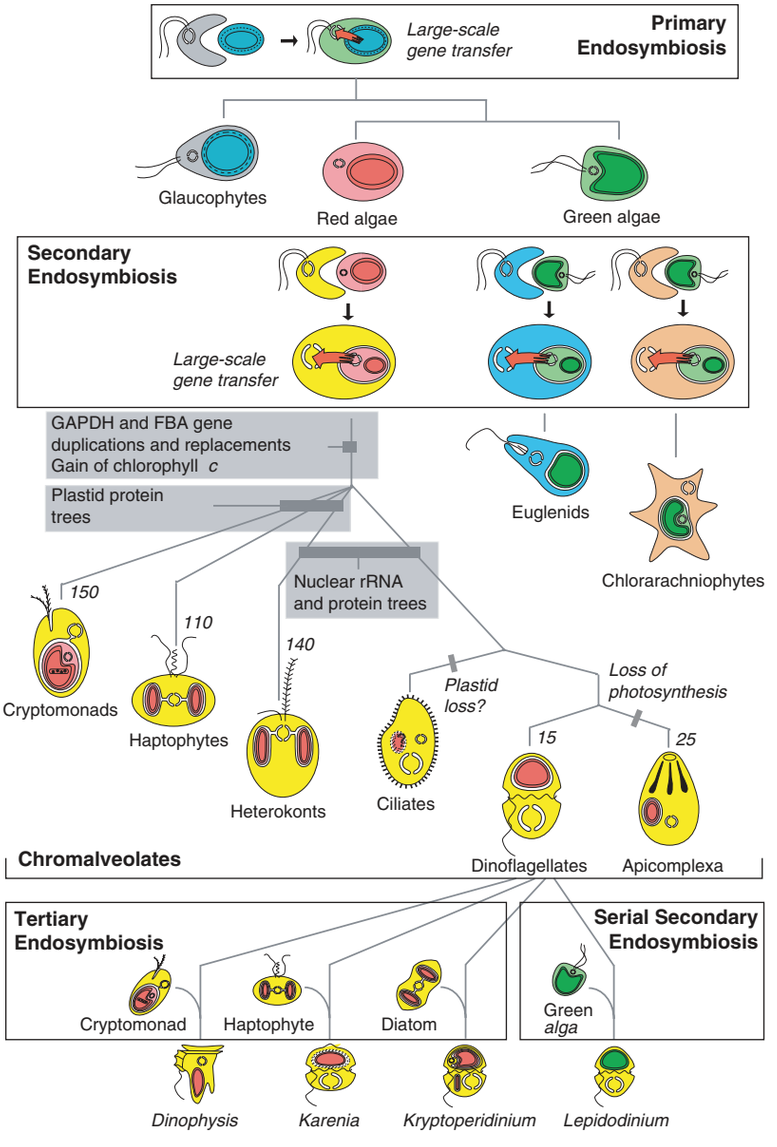

Fig. 1. Algal evolution and the origin and spread of plastids by endosymbiosis. At the top is the single origin of plastids by primary endosymbiosis between a cyanobacterium and a eukaryotic host. This endosymbiont was reduced and integrated, and part of this process involved the transfer of hundreds of genes from the cyanobacterium/plastid to the eukaryotic host nucleus (red arrow). Glaucophytes, red algae, and green algae all descended from this fully integrated partnership. Next, plastids spread to other eukaryotic groups by secondary endosymbiosis (middle). Green algae were most likely involved in two independent events, giving rise to euglenids (turquoise) and chlorarachniophytes (orange). A single endosymbiosis involving a red alga probably gave rise to the chromalveolates (yellow); this group is supported by several molecular characters and gene trees (plotted on the figure). Plastids have apparently been lost in ciliates and *Cryptosporidium* (and perhaps other lineages), and photosynthesis has been lost in apicomplexa and many other individual lineages. Numbers indicate the approximate number of protein genes in the plastid genomes of the various lineages with secondary red plastids. Finally, dinoflagellates have substituted their ancestral plastid several times, most notably by tertiary endosymbioses involving other chromalveolates (a cryptomonad, a haptophyte, and a diatom) and by serial secondary endosymbiosis involving a green alga (*24*).

genome over time, and their protein products are now targeted back to the plastid (*4*, *5*). Indeed, most algae with secondary plastids have entirely lost their endosymbiont nucleus and, even where retained, this nucleus is largely vestigial and encodes only a few plastid-targeted proteins (*6*). Therefore, in all known cases of secondary endosymbiosis, the host nucleus must have acquired hundreds of genes encoding plastid-targeted proteins from the endosymbiont nucleus (Fig. 1). Falkowski *et al*. (*1*) state that such gene transfer "seldom occurs," but all studies based on single genes, genome surveys, or complete genomes show this to be clearly wrong (*7*–*11*). In the face of such massive nucleus-to-nucleus gene transfer, it is very unlikely that the presence, in green algae, of a small proportion of additional nuclear genes encoding plastid-targeted proteins would substantially hinder the portability of their plastids.

What about the claim that red algae have been involved in secondary endosymbiosis twice as often as have green algae? Current evidence suggests that the opposite is true. The "chromalveolate hypothesis" (*12*)—which posits that all algae believed to possess secondary red plastids [dinoflagellates, heterokonts (including diatoms), haptophytes (including coccolithophores), cryptomonads, and apicomplexa] acquired them by a single common endosymbiosis—is now supported by considerable data. First, there are a number of morphological and biochemical characters that unite some or all chromalveolates, including plastid membrane topology, storage carbohydrates, flagellar structure, and accessory pigments. Most important, all photosynthetic chromalveolates contain chlorophyll *c*, which is absent from red algae and best interpreted as a shared derived character (*12*). Second, two plastid-targeted proteins—glyceraldehyde-3-phosphate dehydrogenase (GAPDH) and fructose-1,6-bisphosphate aldolase (FBA)—have unusual evolutionary histories that are unique to chromalveolates, which also indicates a common origin of their plastids (*13*–*15*). Third, phylogenies of concatenated plastid genes support a clade comprising cryptomonads, heterokonts, and haptophytes, which suggests that their plastids are derived from a single secondary endosymbiotic event (*16*, *17*). Fourth, phylogenies of individual and concatenated cytosolic proteins and rRNAs indicate a sister-group relationship of alveolates (dinoflagellates, apicomplexans, and ciliates) and heterokonts but do not yet resolve the position of haptophytes and cryptomonads (*18*–*21*). Taken together, there is increasingly strong evidence for a single, common origin for these organisms and their plastids, but no strong evidence for any alternative.

We agree with Falkowski *et al*. (*1*) that there have probably been three independent secondary endosymbioses of green algae. Therefore, red algae have most likely been involved in fewer, not more, secondary endosymbiotic events than have green algae (Fig. 1). Does this mean that green plastids are somehow more portable? The answer is almost certainly no, because the total number of secondary endosymbioses is so low and the differences between these small numbers (four versus two, or one versus three) are insubstantial.

The foundations of the portable plastid hypothesis do not hold up to scrutiny. This is broadly important because the emerging view that "red" secondary plastids probably originated only once has obvious implications for how we interpret not only the process of endosymbiosis but also the fossil record, the evolutionary history of marine algae and their plastids, and their role in shaping today's oceans.

Patrick J. Keeling
Department of Botany
University of British Columbia
Vancouver, British Columbia V6T 1Z4, Canada
E-mail: pkeeling@interchange.ubc.ca

John M. Archibald
Department of Biochemistry and Molecular Biology
Dalhousie University
Halifax, Nova Scotia, B3H 1X5, Canada
E-mail: jmarchib@dal.ca

Naomi M. Fast
Department of Botany
University of British Columbia
Vancouver, British Columbia, V6T 1Z4, Canada
E-mail: nfast@interchange.ubc.ca

Jeffrey D. Palmer
Department of Biology
Indiana University
Bloomington, IN 47405, USA
E-mail: jpalmer@bio.indiana.edu

References and Notes

1. P. G. Falkowski *et al.*, *Science* **305**, 354 (2004).
2. D. Grzebyk, O. Schofield, C. Vetriani, P. G. Falkowski, *J. Phycol.* **39**, 259 (2003).
3. The claim that red algal plastids contain more protein genes (~200) than do green algal plastids (at most ~100) is consistent with existing data, but only three red algal plastid genomes have been sequenced. The ancestor of red algae must have had at least this many genes, but this does not necessarily mean that the genome of the ancestor (or ancestors) of secondary red algal plastids retained all of these genes. If, as Falkowski *et al*. (*1*, *2*) postulate, there have been multiple red plastid secondary endosymbioses, one must identify the donor red lineage for each endosymbiosis and show that it contained ~200 plastid protein genes to infer that red plastids are in general twice as portable, with respect to plastid gene content, as are green plastids. Indeed, this is a premature claim, given that the few sequenced plastid genomes from cryptomonads, heterokonts, haptophytes, and dinoflagellates contain only about 150, 140, 110 (*22*, *23*), and 15 protein genes, respectively. Therefore, under the hypothesis of multiple red secondary endosymbioses, it is entirely possible that the red algal progenitors of some or even all of these plastids had many fewer than 200 plastid protein genes.
4. G. I. McFadden, *J. Eukaryot. Microbiol.* **46**, 339 (1999).
5. W. Martin *et al.*, *Nature* **393**, 162 (1998).
6. S. Douglas *et al.*, *Nature* **410**, 1091 (2001).
7. J. M. Archibald, M. B. Rogers, M. Toop, K. Ishida, P. J. Keeling, *Proc. Natl. Acad. Sci. U.S.A.* **100**, 7678 (2003).
8. T. R. Bachvaroff, G. T. Concepcion, C. R. Rodgers, E. M. Herman, C. F. Delwiche, *Protist*, in press.
9. J. D. Hackett *et al.*, *Curr. Biol.* **14**, 213 (2004).
10. S. A. Ralph *et al.*, *Nature Rev. Microbiol.* **2**, 203 (2004).
11. E. V. Armbrust *et al.*, *Science* **306**, 79 (2004).
12. T. Cavalier-Smith, *J. Eukaryot. Microbiol.* **46**, 347 (1999).
13. N. J. Patron, M. B. Rogers, P. J. Keeling, *Eukaryot. Cell* **3**, 1169 (2004).
14. N. M. Fast, J. C. Kissinger, D. S. Roos, P. J. Keeling, *Mol. Biol. Evol.* **18**, 418 (2001).
15. J. T. Harper, P. J. Keeling, *Mol. Biol. Evol.* **20**, 1730 (2003).
16. H. S. Yoon, J. D. Hackett, G. Pinto, D. Bhattacharya, *Proc. Natl. Acad. Sci. U.S.A.* **99**, 15507 (2002).
17. H. S. Yoon, J. D. Hackett, C. Ciniglia, G. Pinto, D. Bhattacharya, *Mol. Biol. Evol.* **21**, 809 (2004).
18. J. T. Harper, E. Waanders, P. J. Keeling, *Int. J. Sys. Evol. Microbiol.* **55**, 487 (2005).
19. S. L. Baldauf, A. J. Roger, I. Wenk-Siefert, W. F. Doolittle, *Science* **290**, 972 (2000).
20. A. Ben Ali, R. De Baere, G. Van der Auwera, R. De Wachter, Y. Van de Peer, *Int. J. Syst. Evol. Microbiol.* **51**, 737 (2001).
21. Y. Van de Peer, R. De Wachter, *J. Mol. Evol.* **45**, 619 (1997).
22. V. Sanchez Puerta, C. Delwiche, personal communication.
23. M. Turmel, F. Lang, C. Lemieux, personal communication.
24. This depiction of plastid evolution differs from figure 4 in (*1*) in several ways. This scheme takes into account evidence for a single origin of chromalveolate plastids and includes plastid-bearing groups not considered in (*1*). The most important of these groups is the apicomplexa, but we also show that tertiary endosymbiosis has occurred between dinoflagellates and diatoms (*Kryptoperidinium*) as well as cryptomonads and haptophytes. Falkowski *et al*. show the green alga-containing dinoflagellates arising from an ancestral "alveolate" in a secondary endosymbiotic event at the same level as that which gave rise to peridinin-containing dinoflagellate plastids. However, there are only two closely related genera of dinoflagellates with green algal plastids, and it is widely accepted that they originated relatively recently from a peridinin-containing dinoflagellate host, not from an ancestral alveolate. Falkowski *et al*. show all plastids to be morphologically identical and, most important, show all secondary and tertiary plastids as having two membranes. In reality, secondary plastids have four membranes, except those of euglenids and peridinin-containing dinoflagellates, which are bound by three membranes. Membrane structure of tertiary plastids varies. Falkowski *et al*. also omitted the relict nuclei (nucleomorphs) found in the secondary endosymbionts of chlorarachniophytes and cryptomonads (as well as the relict diatom nucleus in the tertiary plastid of *Kryptoperidinium*).

10 August 2004; accepted 2 December 2004
10.1126/science.1103879

TECHNICAL COMMENT

Response to Comment on "The Evolution of Modern Eukaryotic Phytoplankton"

Falkowski *et al*. (*1*) examined when, why, and how a diverse group of eukaryotic phytoplankton, which overwhelmingly contain red plastids, rose to ecological prominence in Mesozoic time and continue to dominate the contemporary oceans. Our analysis included the fossil record of thecate dinoflagellates, coccolithophores, and diatoms; biochemical composition of extant taxa and their phylogenetic relationships; geochemical reconstructions of ocean paleochemistry; eustatic changes in sea level; and ecosystem interactions. One facet in our analysis was the portable plastid hypothesis (*2*), which was included to accommodate the observation that several distinct clades of eukaryotic algae (e.g., heterokonts, haptophytes, cryptophytes, and dinoflagellates) contain secondary plastids derived from a common ancestral red alga.

A comparative analysis of plastid genomes led Grzebyk *et al*. (*2*) to conclude that not only are more genes retained in red plastids than in green plastids but also many of the retained genes play critical roles in photosynthetic electron transport and carbon fixation. For example, genes that encode key components of both photosystems, ferredoxin, the ATP synthase and, perhaps most important, the small subunit of ribulose 1,5-bisphosphate carboxylase/oxygenase are present in extant red, but not green, plastids. Although originally based on a small number of plastid genomes, the hypothesis subsequently has been supported by analyses of other chromophytes (*3*, *4*). Based on phylogenetic analyses of nuclear and mitochondrial genomes, the hypothesis assumes that the cells serving as hosts to secondary red plastids do not share a recent common ancestor and, hence, that the plastids in each clade were obtained from independent endosymbiotic events (*5*, *6*). As such, the portable plastid hypothesis implicitly conflicts with the "chromalveolate hypothesis" (*7*), which proposes that all algae believed to possess secondary red plastids acquired them by a single common endosymbiosis.

There is some evidence that secondary red plastids are derived from different taxa within the red algae (*8*, *9*). However, most analyses that consider the phylogeny of plastid-encoded genes, as well as plastid-targeted genes encoded in the nucleus, indicate that all secondary red plastids are derived from a common ancestral algal clade (*10*–*12*). In contrast, however, phylogenetic analyses of nuclear-encoded genes that are not plastid targeted (e.g., 18S rRNA and cytosolic GAPDH) do not support the proposition that cryptophytes, haptophytes, heterokonts, and alveolates (including dinoflagellates) recently diverged from a common ancestor (*5*, *13*–*16*). Similarly, mitochondrial genome analyses and ultrastructural features do not comport with a recent common ancestor of chromophyte host cells (*17*, *18*). Paradoxically, there is evidence that the ancestor of heterokonts and alveolates was not photosynthetic. Thus, while the chromalveolate hypothesis is consistent with current phylogenetic data that support a common origin of all secondary red plastids, it is not strongly supported by phylogenetic analyses of the host cells.

A major problem with the chromalveolate hypothesis is that it requires multiple plastid losses in the evolution of alveolates and heterokonts. If the basal groups of alveolates and heterokonts contained a plastid, how and why did nonphotosynthetic alveolates, such as Ciliates, Colpodellids, and Perkinsids (*19*), and several basal groups of dinoflagellates, lose their plastids? Plastid losses must also be invoked to account for basal heterotrophic heterokonts (*20*). Plastid losses are not explained by the chromalveolate hypothesis but are not required by the portable plastid hypothesis. Hence, while the chromalveolate hypothesis aims at making a single red plastid acquisition the most parsimonious event in the evolution of secondary symbionts, it is hardly the most parsimonious hypothesis.

Plastid portability is not limited to secondary endosymbiosis of red plastids, but also holds for tertiary endosymbioses and kleptoplastidy. Tertiary red plastids were acquired on at least three occasions in dinoflagellates: from cryptophytes, diatoms, or haptophytes. There are no known tertiary green plastids. Kleptoplastidy (the capability for heterotrophic organisms to temporarily retain functional photosynthetic plastids from algal prey) occurs in dinoflagellates, ciliates, foraminifera, and mollusks. The vast majority of the retained plastids are obtained from chromophytes (*21*, *22*).

Although the vast majority of plastid-targeted genes present in the primary algal cell nucleus were clearly transferred to the secondary host as part of the endosymbiotic process, secondary plastid associations are relatively rare. Assuming that all secondary red plastids originated from a single endosymbiotic event (as the chromalveolate hypothesis proposes) would give even more support to this claim. Although Keeling *et al*. (*23*) claim that red plastids are no more portable than green plastids, secondary green plastid-containing algae are rare in the contemporary oceans. If green plastids were as portable as red plastids, why is the eukaryotic phytoplankton community in the contemporary ocean dominated by such a diverse group of secondary symbionts that contain red plastids?

Although we believe that current genomic data support the portable plastid hypothesis, the explosion of genomic information expected in the next several years will provide the opportunity to test this hypothesis and the competing chromalveolate alternative.

Daniel Grzebyk
Environmental Biophysics and Molecular Ecology Program
Institute of Marine and Coastal Sciences
Rutgers, The State University of New Jersey
71 Dudley Road
New Brunswick, NJ 08901, USA

Miriam E. Katz
Department of Geological Sciences
Rutgers, The State University of New Jersey
Piscataway, NJ 08854, USA

Andrew H. Knoll
Department of Organismal and Evolutionary Biology
Harvard University
Cambridge, MA 02138, USA

Antonietta Quigg*
Environmental Biophysics and Molecular Ecology Program
Institute of Marine and Coastal Sciences
Rutgers, The State University of New Jersey
New Brunswick, NJ

John A. Raven
Division of Environmental and Applied Biology
University of Dundee at SCRI
Scottish Crop Research Institute
Inergowrie, Dundee DD2 5DA, UK

Oscar Schofield
Environmental Biophysics and Molecular Ecology Program
Institute of Marine and Coastal Sciences
Rutgers, The State University of New Jersey
New Brunswick, NJ

F. J. R. Taylor
Department of Earth and Ocean Science
and Department of Botany
University of British Columbia
270 University Boulevard
Vancouver, BC, Canada V6T 1Z4

Paul G. Falkowski†
Environmental Biophysics and
Molecular Ecology Program
Institute of Marine and Coastal Sciences
Rutgers, The State University of New Jersey
New Brunswick, NJ
and
Department of Geological Sciences
Rutgers, The State University of New Jersey
Piscataway, NJ

**Present address: Department of*
Marine Biology
Texas A&M University
Galveston, TX 77551, USA

†To whom correspondence should be addressed.
E-mail: falko@imcs.rutgers.edu

References and Notes

1. P. G. Falkowski *et al.*, *Science* **305**, 354 (2004).
2. D. Grzebyk, O. Schofield, C. Vetriani, P. G. Falkowski, *J. Phycol.* **39**, 259 (2003).
3. J. R. Manhart, personal communication.
4. M. V. Sanchez Puerta, T. R. Bachvaroff, C. F. Delwiche, *58th Annual Meeting of the Phycological Society of America, Williamsburg VA, 6–12 August 2004*, poster communication (2004).
5. D. Bhattacharya, L. Medlin, *Plant Physiol.* **116**, 9 (1998).
6. C. F. Delwiche, *Am. Nat.* **154**, S164 (1999).
7. T. Cavalier-Smith, *J. Eukaryot. Microbiol.* **46**, 347 (1999).
8. K. M. Müller, M. C. Oliveira, R. G. Sheath, D. Bhattacharya, *Am. J. Bot.* **88**, 1390 (2001).
9. H. S. Yoon, J. D. Hackett, D. Bhattacharya, *Proc. Natl. Acad. Sci. U.S.A.* **99**, 11724 (2002).
10. K.-i. Ishida, B. R. Green, *Proc. Natl. Acad. Sci. U.S.A.* **99**, 9294 (2002).
11. H. S. Yoon, J. D. Hackett, C. Ciniglia, G. Pinto, D. Bhattacharya, *Mol. Biol. Evol.* **21**, 809 (2004).
12. K. Takishita, K.-i. Ishida, T. Maruyama, *Protist* **154**, 443 (2003).
13. N. M. Fast, J. C. Kissinger, D. S. Roos, P. J. Keeling, *Mol. Biol. Evol.* **18**, 418 (2001).
14. J. T. Harper, P. J. Keeling, *Mol. Biol. Evol.* **20**, 1730 (2003).
15. M. E. Katz, Z. V. Finkel, D. Grzebyk, A. H. Knoll, P. G. Falkowski, *Annu. Rev. Ecol. Evol. Syst.* **35**, 523 (2004).
16. K. Takishita, K.-i. Ishida, T. Maruyama, *Protist* **155**, 447 (2004).
17. M. W. Gray *et al.*, *Nucleic Acids Res.* **26**, 865 (1998).
18. M. V. Sanchez Puerta, T. Bachvaroff, C. F. Delwiche, *DNA Res.* **11**, 1 (2004).
19. B. S. Leander, P. J. Keeling, *Trends Ecol. Evol.* **18**, 395 (2003).
20. S. A. Karpov, M. L. Sogin, J. D. Silberman, *Protistology* **2**, 34 (2001).
21. F. J. R. Taylor, D. J. Blackbourn, J. Blackbourn, *J. Fish. Res. Bd. Can.* **28**, 391 (1969).
22. M. Schweikert, M. Elbrächter, *Phycologia* **43**, 614 (2004).
23. P. J. Keeling, J. M. Archibald, N. M. Fast, J. D. Palmer, *Science* **306**, 2191 (2004); www.sciencemag.org/cgi/content/full/306/5705/2191b.
24. Our research is supported by NSF through the Biocomplexity program.

16 September 2004; accepted 29 November 2004
10.1126/science.1105297

HEALTH CARE

Toward Better Drugs for Less

Daniel Philip Kessler

The Truth About the Drug Companies
How They Deceive Us and What To Do About It
by Marcia Angell
Random House, New York, 2004. 325 pp. $24.95, C$34.95. ISBN 0-375-50846-5.

Powerful Medicines
The Benefits, Risks, and Costs of Prescription Drugs
by Jerry Avorn
Knopf, New York, 2004. 457 pp. $27.50, C$39.95. ISBN 0-375-41483-5.

What was the cost of your last prescription? Did it work as intended, have no effect, or actually make you sicker? Would something that cost half as much have worked just as well? The fact that most patients—and doctors—in the United States don't know the answers to these questions means that we are probably not getting good value for the money that we spend on prescription drugs. Because spending for prescription drugs has been the fastest-growing component of health spending for the past 5 years (increasing at rates from 13.4% to 19.7% per year) and is forecast to be $205 billion in 2004 (or 11.5% of total health spending), our collective ignorance about the costs, risks, and benefits of prescription drugs is an important social problem.

Two recent books offer very different views of this problem and its solutions. The titles of the books say a lot about their tone and content. In *The Truth About the Drug Companies: How They Deceive Us and What To Do About It*, Marcia Angell (a former editor-in-chief of the *New England Journal of Medicine*) contends that the root of the problem is the pharmaceutical industry. In *Powerful Medicines: The Benefits, Risks, and Costs of Prescription Drugs*, Jerry Avorn (a professor at Harvard Medical School) sees the problem as stemming from a failure of public policy to confront a handful of unavoidable trade-offs. For example, reducing intellectual property protection for new drugs leads to lower drug prices but weakens incentives for research, development, production, and distribution. More stringent regulation of drug approval decreases the chance that a harmful drug will reach consumers but increases the chance that a beneficial one will be kept off the market. Limitations on advertising and promotion diminish the opportunities to mislead doctors and patients but also reduce the opportunities to inform people about promising new therapies.

Both books have something to offer, but *Powerful Medicines* characterizes the problem more accurately—and provides suggestions for policy reform that are more likely to succeed.

The strongest aspect of *The Truth About the Drug Companies* is Angell's effort to raise public awareness about the extensive conflicts of interest in the current system. To pick three that she discusses: (i) Many studies of drugs' effectiveness are financed by their manufacturers. Even if each study is conducted impartially, the fact that a manufacturer is more likely to publish studies that are favorable to its product—there is no legal requirement that companies publicize negative results—may lead doctors and the public to believe that new drugs are better than they actually are. (ii) The majority of the costs—over 60% in 2001—of the continuing medical education that doctors must receive in order to maintain their licenses is financed by pharmaceutical firms. (iii) Although it is illegal to pay a physician to prescribe a specific drug, pharmaceutical firms can purchase data on doctors' prescribing habits in order to "target" their marketing and promotional activities.

The weakest aspect of Angell's account is its economic and policy analysis. For example, the book claims that "it is very hard to make a case that lower prices would reduce R&D [research and development] spending. In fact, whether price regulation would cut into R&D would depend entirely on whether the industry wanted it to." Because pharmaceutical firms (like all firms) want to maximize their profits, the question is how price regulation affects the relationship between R&D spending and profit. An extensive economic literature (with its own strengths and weaknesses) has generally found that price regulation reduces research and development, but this finding is hardly discussed in the book. Angell's analysis of pharmacy benefits management firms (PBMs)—administrators of prescription drug benefits for large buyers of health services—also falls short: "Whether on balance PBMs lower costs for their customers is impossible to say, since their transactions are anything but transparent. My guess is that they add to costs, since they are just one more hand in the till." These firms may be another hand in the till, but if they ultimately lead to higher costs, why do so many large employers (which can hardly be characterized as unaware of or unconcerned with the costs of prescription drugs) voluntarily enlist them to manage their employees' health care? Angell's book does not say.

Powerful Medicines offers an engaging combination of clinical case studies; a comprehensive review of the medical literature on the costs, risks, and benefits of prescription drugs; and practical policy analysis. The book is divided into five parts: benefits, risks, costs, information, and policy. The first three parts explain the trade-offs that we must confront. "Benefits" uses the case of hormone-replacement therapy as a parable to illustrate why randomized controlled trials are the gold standard for evaluating the safety and effectiveness of prescription drugs. (Until the 1990s, postmenopausal women were routinely prescribed synthetic estrogens at least in part to prevent heart disease; in 1998, a randomized controlled trial showed that estrogens actually increased the risk of heart attack.) "Risks" provides the most readable narrative explanation of medical risk-benefit analysis that I have encountered. "Costs" does the same for cost-effectiveness analysis—for a more technical explanation, see Alan Garber's article "Advances in Cost-Effectiveness Analysis" (*1*). The book's last two parts

The reviewer is at the Graduate School of Business and Hoover Institution, Stanford University, Stanford, CA 94305, USA. E-mail: fkessler@stanford.edu

Published by AAAS

provide some ideas for grappling with these trade-offs. Two of these suggestions stand out:

First, Avorn advocates a more subtle approach to drug approval. At present, the U.S. Food and Drug Administration (FDA) approves drugs as long as they are shown to be "safe and effective." In other words, to gain approval, a drug need not be safer or more effective than existing therapies and need not be cost-effective at all. Why must drug evaluation be limited to a binary designation? As *Powerful Medicines* points out, the FDA currently puts the most promising new-drug applications on a fast track for evaluation. Why not expand this distinction to the final approval itself, allowing or requiring the FDA to categorize approved drugs more finely? The book suggests one possible mechanism for doing so.

Second, Avorn proposes a public-private partnership to inform practicing doctors about the costs, risks, and benefits of prescription drugs. Pharmaceutical firms currently employ vast sales forces of "detailers," who visit individual doctors to promote the use of particular prescription drugs. Detailers are obviously an effective marketing tool; if they were not, for-profit firms would not employ them. Why shouldn't patients—perhaps through a series of partnerships between the government and large private purchasers of prescription drugs—adopt the same strategy in order to pursue our collective interest in the appropriate, cost-effective use of prescription medicines? Avorn provides some evidence—based on randomized controlled trials he has carried out and the experience of the Australian National Prescribing Service—that provision of information on prescription drugs by neutral, noncommercial detailers effectively improves doctors' prescribing habits. Indeed, as the author points out, large managed-care organizations have already begun to do this.

Both books, however, neglect what (to an economist) is an obvious and essential part of the solution: reform the federal tax code to reduce or eliminate the powerful impetus it presently provides for patients to remain unconscious of the true cost of health care. Under current law, the employer-paid portion of health insurance costs is generally deductible to the employer and excludable from the calculation of both income and payroll taxes by the employee; in contrast, out-of-pocket expenditures must be made from after-tax income. This policy makes people insensitive to the true cost of health care in two ways: First, the exclusion from taxable income of compensation paid in the form of health insurance makes buying health care look less expensive than it really is. Second, the exclusion makes buying health care through insurance in general—and low-deductible, low-copayment insurance in particular—look less expensive than health care bought with out-of-pocket dollars.

As a consequence, individual patients and physicians have weak incentives to contain or even learn about costs, which leads them to use health services in unproductive ways [for empirical evidence, see (*2*)]. Avorn is not unaware of this problem; he observes that "participants in frontline drug purchasing decisions have until recently been about as cost-conscious as players in a late-night game of Monopoly after a few beers." Taken together, tax reform and the two principal recommendations made in *Powerful Medicines* hold significant promise to improve the U.S. health care system.

References

1. A. Garber, in *Handbook of Health Economics*, A. J. Culyer, J. P. Newhouse, Eds. (North-Holland, Amsterdam, 2000), vol. 1, pp. 181–221.
2. J. P. Newhouse *et al., Free for All? Lessons from the RAND Health Insurance Experiment* (Harvard Univ. Press, Cambridge, MA, 1993).

DOI: 10.1126/science.1108287

BEHAVIOR

Murder They Wrote

Richard A. Posner

To begin, *A Cultural History of Causality* is mistitled. It is not, as one might think, a book about the history of concepts of causation: Hume, Kant, necessary versus sufficient conditions, covering laws, and the like. That would be a very interesting account. Stephen Kern's is a less interesting book—though thoughtful and carefully done, the fruit of considerable research by a cultural historian—about how, since the Victorian era, the changes in views concerning the causes of murder have been reflected in crime novels (also movies), both highbrow and lowbrow.

A Cultural History of Causality
Science, Murder Novels, and Systems of Thought
by Stephen Kern

Princeton University Press, Princeton, NJ, 2004. 447 pp. $29.95, £18.95. ISBN 0-691-11523-0.

In the 19th century, under the influence of Darwin, causes of murder were often sought in an ancestral trait, human or animal. With the rise of Freud, the causes of crime were often searched for in some childhood trauma or fantasy. Then came modern neuroscience, and more precise biological causes were posited. This is a vast oversimplification of a very long, dense book, but it will give you the basic idea. From his history, Kern concludes that the causes of murder—as they are understood by natural scientists, social scientists, and philosophers and then picked up in literature—are ever more numerous, specific, and precise, but by the same token more uncertain because more complex.

The science deployed in the book is, so far as I can judge, accurate; and it is lucidly expounded. There is an odd detour, though, into quantum theory. It is odd because, as Kern acknowledges, no one has thought to seek the causes of crime in behavior at the atomic or subatomic level. What is true, but would be relevant only to a very different kind of book—the kind I suggested would be more interesting than Kern's—is that quantum theory's apparent violation of the laws of causality provides food for thought about concepts of causation. But that is not Kern's subject.

It should be, in the following sense: without some notion of the social or human function of ascriptions of causality, it is difficult to talk intelligently about the "causes" of crime. Every event has multiple causes, as Kern insists. But society, or observers, usually are interested in just one cause and call that "the" cause to mark their interest. From the standpoint of a neuroscientist, the cause of a murder might be neuronal activity in the brain; from the standpoint of an abortion-rights activist, it might be the failure of the murderer's mother to have aborted an unwanted child; from the standpoint

The reviewer is at the U.S. Court of Appeals for the Seventh Circuit, 219 South Dearborn, Chicago, IL 60604, USA. E-mail: Richard_Posner@ca7.uscourts.gov

Multiple motives. In Dostoevski's *Crime and Punishment*, Raskolnikov (here, Peter Lorre in Josef von Sternberg's 1935 film) is drawn to murder by his theory of the "exceptional man" and his needs for cash.

PUBLIC HEALTH

Will Vaccines Be Available for the Next Influenza Pandemic?

Klaus Stöhr and Marja Esveld

Twenty per cent of the world's population falls ill. One in every hundred of those ill is hospitalized (if enough beds are available). Seven million deaths occur in a few months and 28 million are hospitalized. This is how the next influenza pandemic might look, according to optimistic estimates (*1*, *2*) (see the figure, this page). Estimates from other models are far more frightening, but even this best-case scenario is cause for considerable concern.

Enhanced online at www.sciencemag.org/cgi/content/full/306/5705/2195

The events leading to influenza pandemics are recurring biological phenomena and cannot be prevented. Influenza pandemics are caused by sudden emergence of a new influenza subtype in humans. New subtypes most probably derive from the vast animal influenza reservoir, where 15 different influenza A subtypes freely circulate, mainly in aquatic migratory birds. Only two subtypes (H3 and H1) are presently circulating in humans. If a subtype extends its host range to include humans, it will ignite the next pandemic. A pandemic virus will cause moving waves of outbreaks in humans lasting 1 to 2 months in a given region and complete its global spread in less than 8 to 12 months. During this time, it will cause a global health emergency. It would probably, as a strong competitor, replace the currently circulating subtypes. Finally, the pandemic virus will settle down to cause much milder seasonal epidemics, until the next pandemic virus takes over. Three to four influenza pandemics have occurred each century, and there is no reason to believe this century will be spared.

With the unprecedented outbreak of avian influenza in Asia (caused by H5N1), the world has come closer than ever to the first pandemic since 1968. The currently very widely circulating avian H5N1 strain has already caused disease in at least 44 persons and killed 32 of them. It is not easily transmissible between humans. However, it is feared that this would quickly change if, for example, it picks up a few genes from a human influenza virus during a coinfection; this change would ignite a new influenza pandemic.

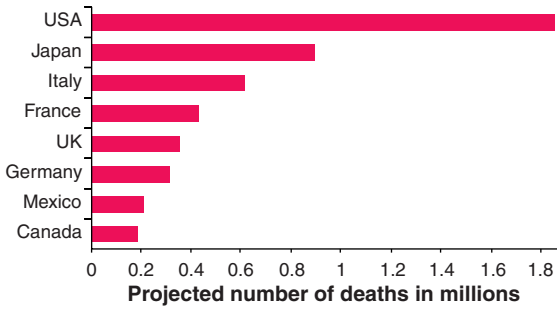

Projections of numbers of deaths during the next influenza pandemic for selected countries based on statistics from the 1918–1919 pandemic (*4*).

All existing data suggest that vaccines would be the best line of defense against the high morbidity and mortality invariably associated with influenza pandemics. However, vaccines have never been used to any large degree during a pandemic, including the last two, in 1957 and 1968, when vaccination against seasonal influenza was fully established. There are several reasons, all associated with sudden emergence of the pandemic virus and the small window for interventions (6 to 10 months) before the virus had completed global spread.

Delayed recognition may have arisen from inadequate surveillance systems and/or from an increase in human transmissibility so gradual it escaped early detection. Preparing a prototype seed virus for vaccine manufacturing took much too long. Preclinical and clinical vaccine testing was difficult and an optimal formulation (content of vaccine virus, number of doses, etc.) could not be established. Vaccine production capacity was extremely limited, and strategies for antigen sparing (using less vaccine virus per dose to achieve equivalent vaccine efficacy) remained unexplored. Finally, the regulatory pathways were not fixed by licensing agencies, which created uncertainty about requirements for testing and manufacturing of a safe and effective pandemic vaccine.

Most of the technical obstacles that precluded availability of a vaccine at the start of a pandemic have now been overcome. Human disease surveillance systems, although far from perfect, have become more sensitive, and case reporting is now more reliable. Laboratories in the WHO Global Influenza Surveillance Network can rapidly assess emerging field strains and provide prototype strains for vaccine production. Although new avenues for rapid influenza vaccine production during pandemics are being pursued (e.g., cell culture vaccines and recombinant antigen production), they are not yet available. A major breakthrough has been development of laboratory methods to design pandemic vaccine prototype strains rapidly and with predictable characteristics, such as the absence of avian pathogenicity. This allows vaccine manufacturing in eggs and compliance with biosafety requirements for production plants. Furthermore, annual influenza vaccine production capacity, although still insufficient to meet an explosive global demand, has doubled during the last 10 years alone, reaching almost 0.9 billion doses of a monovalent vaccine.

Finally, major national and international licensing agencies have published safety and efficacy requirements for pandemic vaccine registration, thus providing a predictable regulatory environment in which companies can plan vaccine testing and development. Such registration, which can be done with any influenza subtype of pandemic potential, is the condition that every manufacturer must fulfill to receive market authorization for making a pandemic vaccine, regardless of when the next pandemic occurs and which strain causes it.

Currently, manufacturers would need an estimated 6 to 8 months to advance a pandemic influenza vaccine to obtain registration and begin commercial production (excluding ~2 months for vaccine prototype development). If this development process only begins once the pandemic virus has started to spread, the virus will probably cover the world before large-scale manufacturing can be initiated.

Unfortunately, that would be the current reality. No "template" influenza pandemic vaccine has been licensed by any company. The formulation of an efficient H5N1 pandemic vaccine has not been established by clinical trials, nor are antigen-sparing for-

The authors are in the World Health Organization Influenza Programme, Geneva, Switzerland.

mulations known. Should a pandemic virus emerge at the end of 2004, most manufacturers would need to start the groundwork of pandemic vaccine testing and registration: upgrading production facilities to fulfill biosafety requirements; preparation of master and production seed; and initiation of laboratory, animal, and clinical trials. Pandemic vaccine production would not begin before mid-2005, and significant amounts would not be available until several months later.

Slow progress of influenza pandemic vaccine development is no longer caused by insurmountable technical hurdles. The hurdles are political and economic in nature. Uncertainty over a viable market prevents companies from investing in pandemic vaccine development, and many governments see no reason to step in, as availability of pandemic vaccines is not considered a public health good. This is surprising in view of the expected benefits of influenza vaccination during a pandemic. If only 10% of the world population were vaccinated, the death toll, hospitalizations, and disease would likely be cut at about the same rate.

For the first time in history, the virus subtype of a possibly looming pandemic is known, and a vaccine against it could be stored for immediate use at the start of efficient human-to-human transmission. WHO is therefore recommending creation of national and international stockpiles of H5N1 vaccine, for emergency use in affected areas and as a defense strategy for slowing international spread. This might allow more time to increase vaccine supplies, especially if it acts as an incentive to vaccine companies.

Of the nearly 10 companies that represent about 90% of the global production capacity, five have begun or finished with seed development for H2, H5, H7, or H9 influenza A subtypes. Only three have taken the next steps and are preparing small batches of an H5N1 pandemic vaccine for clinical testing, scheduled for early 2005. One other company has completed trials with an H2 virus and will request licensing shortly. Many of the remaining companies have plans to consider seed development, after mid- to end-2005, and clinical testing, pending external funding.

A recent WHO meeting (*3*) has outlined several avenues to overcome the key hurdle, the lack of market forces, and to save time in pandemic vaccine development. It is hoped that governments will create incentives. The National Institutes of Health support clinical trials with H5N1 influenza vaccines for companies with seasonal influenza vaccines licensed in the United States. In addition, government purchase of 2 million doses of an H5N1 vaccine certainly facilitated the manufacturers' decision to invest in vaccine seed development. The Japanese Ministry of Health will spend US$ 1.2 million in 2005 to assist with pandemic vaccine development by the country's four influenza vaccine manufacturers and is considering additional support in 2006. The French government is negotiating a national stockpile of an H5N1 vaccine with a domestic company that is already investing in pandemic vaccine development.

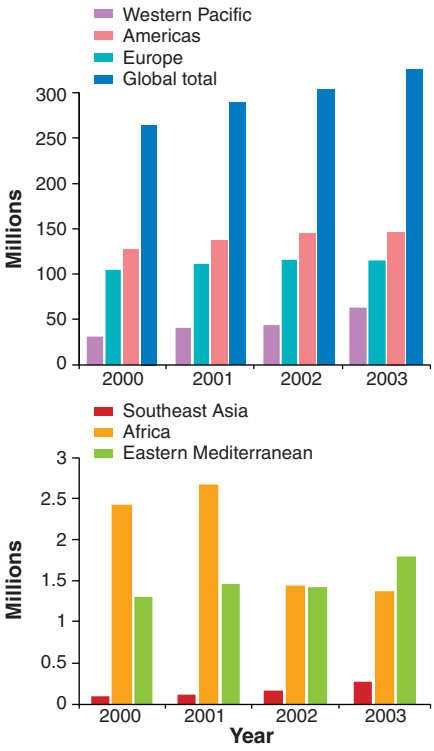

Global distribution of influenza vaccine by WHO region. Data compiled by the Influenza Vaccine Supply International Task Force of the International Federation of Pharmaceutical Manufacturers Associations; it covers >95% of the total annual worldwide distribution. [Source (*5*)]

International coordination to facilitate simultaneous clinical trials for vaccine licensing and studies on antigen-sparing strategies is also essential. Coordination will include rapid exchange of preclinical and clinical study results to avoid duplication. Regulatory coordination would facilitate defining expectations for immunogenicity studies and clinical trials and support standardization.

Influenza vaccine manufacturers should develop contingency plans to expedite the rapid switch from epidemic to pandemic vaccine production, considering the need for reallocation of intracompany vaccine production, filling, packaging, and distribution resources. Furthermore, governmental agencies of countries that plan vaccine use during pandemics need to address the liability issues that will arise during mass immunization campaigns.

If these measures were implemented, the time between the start of a pandemic and the start of commercial-scale production could be reduced by at least 6 to 8 months. Each day of manufacturing gained could represent at least 5 million additional doses, if global influenza vaccine manufacturing is operating at its full potential.

In the long term, manufacturing capacity can only be increased sustainably through augmented use of vaccines for seasonal epidemics of influenza. Capacity to manufacture a pandemic vaccine is dependent on existing production capacity, which is driven by the annual demand for vaccines for seasonal influenza.

Almost all manufacturing capacity for influenza vaccines is concentrated in the industrialized world (~65% in Europe alone), and almost all seasonal influenza vaccine is used there (see the figure, this page). Affluent countries also have the means to support domestic manufacturers, if they consider pandemic vaccines a public good. Furthermore, the attention these countries attach to pandemic vaccine development will also influence how much, if any, influenza vaccine will be left for nonproducing countries, as governments have historically nationalized production of vital medicines only until domestic demand was satisfied.

Will vaccines be available for the next influenza pandemic? Yes, but there is no doubt that current production capacity is insufficient to meet, within a few months, world need for vaccine during an influenza pandemic. The better we prepare now, the more vaccine will eventually be available hopefully also for nonproducing countries. The window of opportunity for coordinated and rapid action is still open. It can only be hoped that the national and international public health communities will live up to the expectations of the population at risk for the next influenza pandemic: everybody.

References and Notes

1. M. I. Meltzer, N. J. Cox, K. Fukuda, *Emerg. Infect. Dis. 5*, 659 (1999).
2. M. I. Meltzer, presentation at the WHO consultation on priority public health interventions before and during an influenza pandemic, Geneva, 16 to 18 March 2004; see www.who.int/csr/disease/avian_influenza/consultation/en/
3. Report of an informal WHO meeting on influenza pandemic vaccines, Geneva, Switzerland, 11 to 12 November 2004 (WHO/CDS/CSR/GIP/2004.3); see www.who.int/csr/disease/influenza/.
4. N. P. A. S. Johnson, J. Mueller, *Bull. Hist. Med.* **76**, 105 (2002).
5. "Global distribution of influenza vaccines, 2000–2003," *WHO Wkly Epidemiol Rec.* **79** (40), 366 (2004); available at www.who.int/wer/2004/en/wer7940.pdf.

10.1126/science.1108165

ATMOSPHERE

Ecological Versus Climatic Thresholds

Mark Maslin

One of the most pressing questions concerning future climate change is how it will affect the terrestrial vegetation (*1*). Nowhere is this more hotly debated than in the tropics, where the future of the Amazon rainforest (*2*) and the continued viability of current agricultural practices (*3*) are at stake. Studies of past climates may elucidate how quickly vegetation can respond to climate change. Recently, Hughen *et al.* (*4*) reported that tropical vegetation in Venezuela has in the past responded to climate change within less than 50 years. In contrast, Jennerjahn *et al.* report a vegetation response time of 1000 to 2000 years in northeast Brazil [see page 2236 (*5*)].

Does this difference mean that there is a conflict in our understanding of the effect of climate change on tropical vegetation? On the contrary: The difference between the estimated ecological response times in (*4*, *5*) may provide valuable insight into how different parts of the tropics respond to rapid climate changes. As the study by Jennerjahn *et al.* (*5*) shows, climate thresholds and ecological or vegetation thresholds are not always the same.

Usually, comparison between past land and ocean records is difficult, because the errors in dating each record can be larger than the lead and lag times that are being studied. This problem is solved by Jennerjahn *et al.* (*5*) who, like Hughen *et al.* (*4*), look at vegetation and climate records in the same marine sediment core. As long as there are no delays in the transport of either the continental or oceanic signal to the marine sediment, the lead and lag times between climate and vegetation can be looked at in detail.

Jennerjahn *et al.* (*5*) study a marine sediment core from the continental margin off the northeast coast of Brazil. They focus on the last "Heinrich event," a cool period accompanied by ice rafting in the North Atlantic that lasted from about 17,500 to 15,500 years ago. At the beginning of the event, they observe a substantial increase in the amount of iron deposited in their marine core, suggesting a sharp increase in continental erosion from enhanced rainfall (*5*). This increased rainfall is accompanied by an increase in pioneer vegetation, as indicated by moss fern spores. A major increase in tree pollen and tree fern spores, showing the development of gallery and montane forest, does not occur until 1000 years later.

Today, northeast Brazil has a semiarid climate. A dry period of 8 months per year prevents the development of rainforest, which cannot survive dry periods of more than 4 months. Jennerjahn *et al.* (*5*) suggest that there may have been a substantial increase in the amount of rainfall and the duration of the wet season at the start of the Heinrich event, but that the dry season still lasted more than 4 months, preventing the development of forest. Only later in the Heinrich event was this ecological threshold of four dry months crossed, allowing the development of forest in northeast Brazil (see the figure, middle panel). Different dry season lengths may thus produce a more sensitive and direct relationship between climate and vegetation in Venezuela (*4*) than in northeast Brazil (*5*).

Ecological thresholds are not unique to the tropics. On page 2231 of today's issue, Tzedakis *et al.* (*6*) study pollen records in a marine core from southwest Europe. They show that the duration of tree cover can be shorter than the length of interglacial periods (as defined by periods of low global ice volume). This observed shortened period of tree cover seems to be caused by millennial-scale climate deteriorations during each interglacial. These short, cold dry events trigger an ecological threshold, causing tree

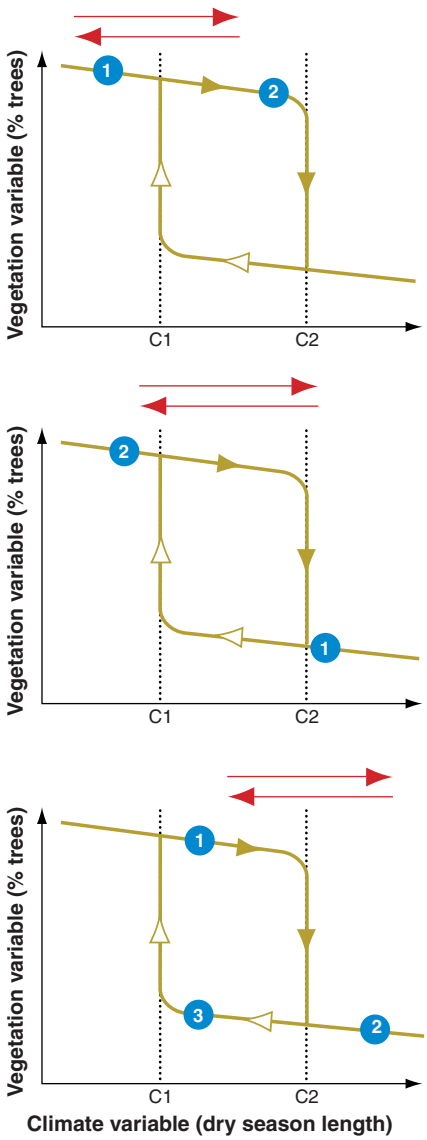

The vegetation–climate relationship. Here, the climate and vegetation variables are exemplified by the tropical dry season length and percentage of land cover by trees, respectively. (**Top**) The vegetation does not vary greatly between points 1 and 2 despite large changes in climate (*9*). (**Middle**) When the controlling climate variable drops beneath the critical threshold point C1 (for example, a 4-month dry season), there is a major change in the vegetation [such as a significant increase in tree cover (*5*)]. When the climate variable returns to its original state, the vegetation at first resists the climatic change (the rainforest recycles moisture, allowing it to survive longer dry seasons), but eventually returns to its original level (point 1) and is thus reversible. (**Bottom**) The controlling climate variable crosses the second critical threshold C2; however, returning the climate variable to its original state does not reverse the vegetation change and the vegetation remains at point 3 [see, for example, (*2*, *6*)]. An additional change to the climate variable is required to overcome the bifurcation and return the vegetation to its original level at point 1. If this additional change is not possible within the system, the threshold crossing becomes irreversible.

The author is at the Environment Change Research Centre, Department of Geography, University College London, London WC1H 0AP, UK. E-mail: mmaslin@geog.ucl.ac.uk

CREDIT: ADAPTED FROM (*8*)

Published by AAAS

populations to crash; the vegetation does not necessarily recover when the climate returns to normal interglacial conditions. The pollen records are mirrored by variations in the Antarctic atmospheric methane record (*6*), suggesting a more global vegetation response to these events and subsequent lack of recovery.

The results of Tzedakis *et al.* (*6*) imply that in some areas, the relationship between climate change and vegetation is not reversible. This observation has important implications for future climate change, because it suggests that once an ecological threshold has been crossed, a return to the previous climatic conditions does not guarantee a similar reversal in vegetation (see the figure, bottom panel). This sort of bifurcation has previously been suggested for the relationship between surface ocean salinity and the rate of deep-ocean circulation (*7*), but it may be more prevalent in the climate system than previously thought (*8*).

Why are climatic and ecological thresholds so different? The distribution of different vegetation types, or biomes, is controlled by a number of different climatic factors, such as annual and seasonal temperature, annual and seasonal precipitation, and the atmospheric carbon dioxide concentration (*9*). Jennerjahn *et al.* (*5*) provide an excellent example of a tropical ecological threshold that is primarily controlled by the duration of the dry seasonal and not the total annual rainfall. But it is also important how these climatic factors interact. For example, until recently it was assumed that large parts of the Amazon rainforest could not survive glacial climates. There is, however, growing evidence that the majority of the Amazon rainforest survived the climatic threshold of the last ice age (*10*). Modeling suggests that the colder glacial temperatures counterbalanced the worst effects of the drier conditions and lower atmospheric carbon dioxide concentrations by reducing water and carbon loss (*9*). In the case of the Amazon, the combination of two different climatic thresholds—aridity and cooling—did not produce a significant ecological threshold (see the figure, top panel).

Given the right set of climatic changes, vegetation distributions can vary on time scales of less than 50 years (*4*). However, the reports of Jennerjahn *et al.* (*5*) and Tzedakis *et al.* (*6*) illustrate that unless we understand ecological thresholds and their relationship to climate change, we cannot predict how or when vegetation will change as a result of global warming. Moreover, we do not know whether these changes will be reversible.

References

1. M. A. Maslin, *Global Warming, a Very Short Introduction* (Oxford Univ. Press, Oxford, 2004), p. 162.
2. P. M. Cox, R. A. Betts, C. D. Jones, *Nature* **408**, 184 (2000).
3. J. J. McCarthy *et al.*, Eds., *Climate Change 2001: Impacts, Adaptation, and Vulnerability, Contribution of Working Group II to the Third Assessment Report of the Intergovernmental Panel on Climate Change (IPCC)* (Cambridge Univ. Press, Cambridge, 2001).
4. K. Hughen *et al.*, *Science* **304**, 1955 (2004).
5. T. C. Jennerjahn *et al.*, *Science* **306**, 2236 (2004); published online 2 December 2004 (10.1126/science.1102490).
6. P. C. Tzedakis, K. H. Roucoux, L. de Abreu, N. J. Shackleton, *Science* **306**, 2231 (2004); published online 2 December 2004 (10.1126/science.1102398).
7. S. Rahmstorf, *Nature* **378**, 145 (1995).
8. M. A. Maslin *et al.*, in *The Oceans and Rapid Climate Change: Past, Present and Future*, D. Seidov, B. J. Haupt, M. A. Maslin, Eds. (American Geophysical Union, Washington, DC, 2001), p. 9.
9. S. Cowling *et al.*, *Quat. Res.* **55**, 140 (2001).
10. F. Mayle *et al.*, *Philos. Trans. R. Soc. London Ser. B* **359**, 499 (2004).

Published online 2 December 2004;
10.1126/science.1107481
Include this information when citing this paper.

MICROBIOLOGY

Microbial Life Breathes Deep

Edward F. DeLong

The apparent paucity of deep-sea biota led the 19th-century biologist Edward Forbes to question the very existence of life at depths greater than 550 m. Subsequent oceanographic expeditions soon laid Forbes' "azoic theory" to rest, with discoveries of a diverse and abundant marine fauna flourishing in the greatest depths of the oceans. In parallel ways, contemporary microbial surveys are expanding the range of known habitats where microbial life thrives. On page 2216 of this issue, D'Hondt and colleagues (*1*) now report evidence for metabolically diverse and active microbial communities buried deep within marine sediments nearly 0.5 km below the seafloor (see the figure). Using chemical clues hidden deep within marine sediment cores, these investigators infer how subseafloor microbes eat and breathe (*1*). They suggest that certain microbial activities deviate substantially from standard models (*2*) of microbial metabolism in subseafloor sediments.

How important are the microbial communities buried deep within the marine sediments that overlay two-thirds of Earth's surface? Counting microbes under the microscope (which does not distinguish living from dead organisms) reveals that substantial numbers of microbes must exist in deep seafloor sediments (*3*). Quantitative estimates indicate that the vast majority of these sediment-associated microbes (97% or so) reside in the upper 600 m of sediment (*3*, *4*). Microbial cell numbers range from 10^8 cells per gram of sediment just below the seafloor, to about 10^4 cells per gram of sediment 0.5 km deep in the subsurface (*3*). This substantial subsurface microbial biomass raises a number of interesting questions. Do these microbes represent well-preserved remnants of a microbial burial at sea? Alternatively, do these organisms thrive actively in the subsurface and, if so, what do they eat and how do they breathe? Does microbial activity vary with the depth and geochemical gradients found deep within the sediments? D'Hondt *et al.* (*1*) begin to answer these questions with their analyses of deep-sea sediment cores recovered from the equatorial Pacific Ocean off the coast of Peru. Some of their conclusions are rather unexpected.

Comparative analyses of the geochemistry of subseafloor sediment cores is providing new insights into subsurface microbial life. The sediment cores collected by D'Hondt *et al.* were sampled to depths of 420 m. Samples include those from the Peruvian shelf, the Peru Trench, and further offshore from open-ocean sediments. Similar to previous studies (*3*), D'Hondt *et al.* discovered remarkable numbers of microbes in sediment samples, which decreased with increasing sediment depth. These investigators also measured potential respiratory electron acceptors (oxidants), including sulfate and nitrate. The flux of these oxidants can serve as markers of specific microbial activities, because certain microbes use them to respire in the absence of oxygen. The occurrence and distribution of other microbial metabolic by-products—carbon dioxide, ammonia, sulfide, methane, manganese, and iron—also provide metrics of microbial activity. Profiles of these biologically processed compounds paint a picture of how microbial activities may be partitioned in the deep sediment, and serve as indicators of which metabolic pathways are crucial.

Throughout their sediment cores, D'Hondt and co-workers found abundant

The author is in the Department of Civil and Environmental Engineering and Division of Biological Engineering, Massachusetts Institute of Technology, Cambridge, MA 02139, USA. E-mail: delong@mit.edu

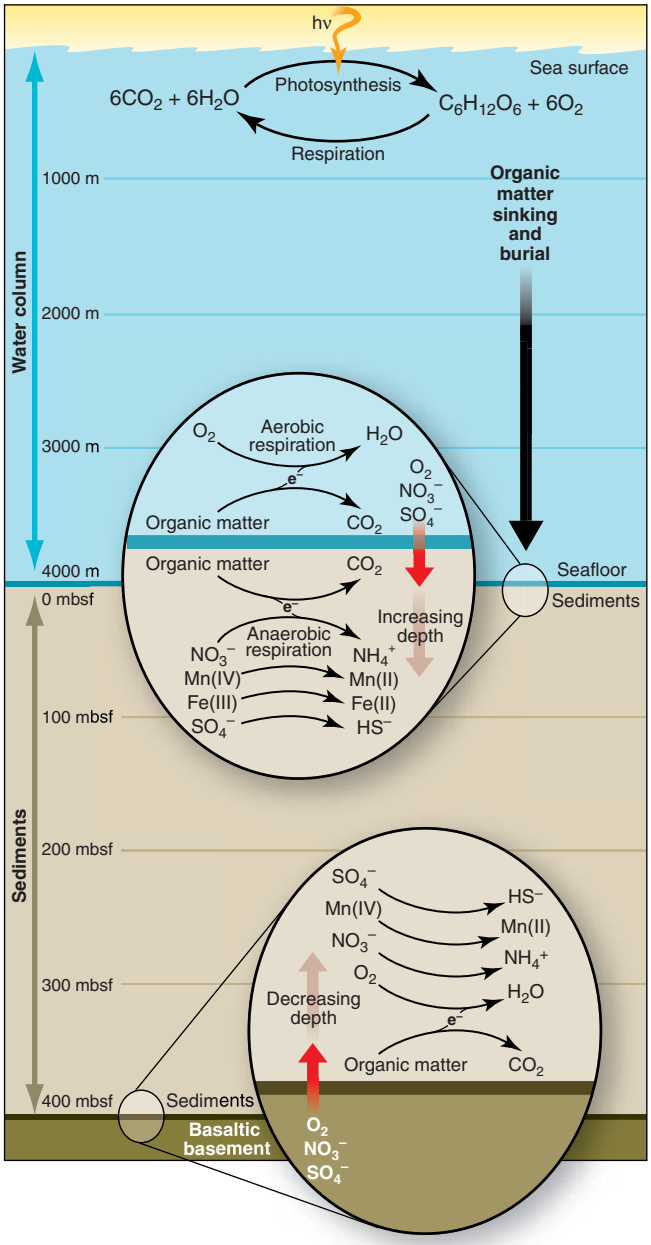

The ups and downs of organic matter. Microbial respiration at the ocean's surface and in the sediments of the subseafloor. At the sea surface, photosynthesis captures light energy in the ocean's photic zone, driving subsequent transformations of energy and organic matter that propagate as far down as 400 m below the seafloor (mbsf). In the aerobic water column, respiratory processes use oxygen to oxidize organic matter to carbon dioxide (CO_2). (**Top inset**) In the upper sediments of the seafloor, oxygen is rapidly depleted and alternative electron acceptors, such as nitrate (NO_3) and sulfate (SO_4), that diffuse downward from the water column are commandeered by certain Archaea and bacteria for respiration. These electron acceptors are used in a predictable sequential series, according to the free energy yielded by their reduction. (**Bottom inset**) D'Hondt *et al.* (*1*) observe that oxygen, NO_3, and SO_4 also diffuse upward from the deep basaltic basement of the sediment, resulting in an "upside down" electron acceptor consumption series. This series somewhat mirrors that seen in near-surface sediments. All of these processes rely ultimately on the oxygen and organic matter produced by photosynthesis in the ocean's photic zone.

CREDIT: KATHARINE SUTLIFF/*SCIENCE*

evidence for the "usual suspects"—that is, previously identified biochemical activities of sediment-associated microbes. These processes include carbon oxidation, methane production and consumption, and reduction of sulfate, nitrate, and manganese. The existence of these processes deep within marine sediments may be no big surprise, but their location was in some cases unexpected. Normally, electron acceptors (oxidants such as oxygen, sulfate, and nitrate) diffuse into sediments from the overlying seawater and are then consumed sequentially in a predictable series of metabolic reactions (see the figure). This produces a microbially catalyzed oxidant-depletion profile in which oxygen is reduced first, then nitrate, manganese, iron, sulfate, and finally carbon dioxide. Such profiles are thought to reflect competitive processes that deplete available oxidants, with those yielding the greatest free energy being the first to be consumed (*2*). The profiles of electron acceptors and metabolic by-products in the marine sediment cores typically conform to this predicted series.

There are important ways, however, in which the profiles of electron acceptors in deep sediments observed by D'Hondt *et al*. deviate substantially from the norm. This discovery suggests unsuspected sources of microbial metabolites within subseafloor sediments. In several instances, D'Hondt and colleagues report that oxidants that normally diffuse downward from overlying seawater appear to have entered the sediments from subseafloor sources (see the figure). Several cores provide evidence for sulfates originating from brines below the sediment base, as well as for nitrate and oxygen entering from deep basaltic aquifers underneath the sediment column. This situation produces "upside-down" redox profiles, with atypical sources from beneath sediments providing oxidants such as sulfate and nitrate that enable microbes to respire anaerobically (see the figure). Such microbial respiratory activities may drive cycling of manganese and iron in a sort of "bucket brigade" of cascading respiratory electron shuttles that pass electrons through various sources and sinks. Thus, these new observations imply the presence of a physiologically diverse and active deep-sediment microbiota that operates somewhat differently from model predictions.

The rates of microbial metabolic activities, estimated from the flux of electron acceptors, varied predictably in cores from the different sites. Microbial respiration of sulfate was much greater in sample cores from the continental margin than in those from open-ocean sites. Unexpectedly, respiration rates for subsurface manganese and nitrate were greater at the open-ocean site and were driven entirely by the upward flux of nitrate from the basaltic aquifer beneath the sediments. Also unexpected is the co-occurrence of deep sediment methanogenesis, as well as manganese and iron reduction, within zones of high sulfate. According to the standard hierarchy of energy processing and substrate competition, sulfate-reducing microbes are expected to "win" in zones of high sulfate concentration. The D'Hondt *et al*. work reveals that microorganisms in the deep subsurface (and their energetics) may differ substantially from well-studied model microorganisms in shallow near-surface sediments.

Exactly which microbes are responsible for the subsurface energy cycling revealed by D'Hondt *et al*. remains uncertain. Although viable sediment-associated microbes were recovered by the investigators, the relevance of these microbes to subsurface metabolism is questionable. Many of the recovered bacterial isolates form spores or are close relatives of surface-dwelling bacteria. It seems unlikely that these represent authentic deep subsurface inhabitants. Indeed, microbial survey methods that don't depend on cultivation (*5*) suggest that a quite different suite of indigenous subsurface archaea and bacteria may predominate deep within sediments (*6*–*8*). Such microbes may represent the indigenous, active members of deep-sea microbial communities.

The new observations by D'Hondt *et al*. confirm that subsurface microbes living

Published by AAAS

deep in marine sediments ultimately rely on energy sources and oxidants produced from sunlight, rather than subsisting on geochemicals emanating from Earth's interior. Although microbial metabolites seem to wend their way into deep sediments in unexpected and interesting ways, the energy sources and electron sinks produced by photosynthesis still appear to rule the roost, even 0.5 km below the ocean's abyssal plains. Even so, D'Hondt *et al.*'s analyses demonstrate that important, diverse, and qualitatively unique microbial processes occur in the deep, dark environs far below the seafloor.

References

1. S. D'Hondt *et al.*, *Science* **306**, 2216 (2004).
2. D. E. Canfield *et al.*, *Mar. Geol.* **113**, 27 (1993).
3. R. J. Parkes *et al.*, *Nature* **371**, 410 (1994).
4. W. B. Whitman, D. C. Coleman, W. J. Wiebe, *Proc. Natl. Acad. Sci. U.S.A.* **95**, 6578 (1998).
5. N. R. Pace, *Science* **276**, 734 (1997).
6. C. J. Newberry *et al.*, *Environ. Microbiol.* **6**, 274 (2004).
7. H. Sturt, R. Summons, K. Smith, M. Elvert, K. Hinrichs, *Rapid Commun. Mass Spectrom.* **18**, 617 (2004).
8. F. Inagaki *et al.*, *Appl. Environ. Microbiol.* **69**, 7224 (2003).

10.1126/science.1107241

PHYSICS

The Electronic Structure of Liquid Lead

Yves Petroff

Crystalline metals have been studied intensively over the past 40 years. Sophisticated theoretical models and experimental tools have resulted in a generally very good understanding of these materials. In contrast, the atomic and electronic structure of liquid metals is poorly understood. In a liquid metal, the atomic structure varies in both time and space, and the only information that can be obtained is averaged. The lack of periodicity makes it also very difficult to determine whether the electrons are bound to individual atoms or delocalized over the entire liquid, because the band structure (which determines the electronic properties) can no longer be measured.

On page 2221 of this issue, Baumberger *et al.* (*1*) report the first direct measurements of the band structure of liquid lead at the lead/copper interface. They use angular resolved photoemission to show that the Fermi surface (which separates the occupied electronic states from the empty ones) persists in the liquid phase and that the localization of the electronic wave function depends strongly on the symmetry of the two $p_{x,y}$ bands of lead.

Four years ago, Reichart *et al.* (*2*) introduced a trick to enable them to study the atomic structure of liquid lead. It has been predicted (*3*, *4*) that in monatomic three-dimensional liquids such as lead, atoms should cluster to form icosahedrons. Reichart *et al.* argued that at the interface of liquid lead with a silicon (001) surface, the potential of the silicon surface cannot cause any long-range ordering in the lead, but that it can break the icosahedrons into pentagonal halves, which can be captured at the silicon surface in a preferred orientation. They therefore measured the scattering of totally reflected (evanescent) x-rays, which are sensitive only to the liquid structure at the interface, from a liquid lead layer supported on Si(001). They detected a five-fold local symmetry and obtained experimental evidence for the predicted icosahedral fragments.

Baumberger *et al.* (*1*) now study the electronic properties of a liquid lead film on a copper surface. They perform angular resolved photoemission spectroscopy to obtain the band structure $E(\mathbf{k})$ of liquid lead. To do so, they investigate a lead monolayer supported on a copper (111) surface as the temperature is raised through the melting transition (at 568 K) of the film. Lead films on Cu(111) grow layer by layer with a defined orientation (they form "epitaxial films") (*5*). Because of the proximity of the Cu(111) substrate, information about the momentum of the electronic states of the liquid phase can be retrieved.

Before discussing the results, we have to introduce a few definitions. A three-dimensional crystal can be described with three noncoplanar vectors, which define a unit cell. Associated with each crystal lattice is the reciprocal lattice, which is also defined by three vectors. A very simple relationship exists between the vectors of the direct space and the reciprocal (or momentum) space. The Brillouin zone is a subsection of the reciprocal lattice that includes all the important symmetry points. For three-dimensional crystals, the Brillouin zone is a polyhedron.

The results are summarized in the figure, which shows the experimentally observed band structure of the lead monolayer along the symmetry direction $\bar{\Gamma}\bar{M}$ for the solid (top panel) and for the liquid (bottom panel). The authors observed an inner and an outer Fermi surface (see the figure). These two Fermi surfaces persist in the liquid phase. Around the $\bar{M}$ point, three bands are observed in both phases. Bands **1** and **3** are due to the $p_{x,y}$ states of lead, and band **2** results from the *sp* band of copper. The

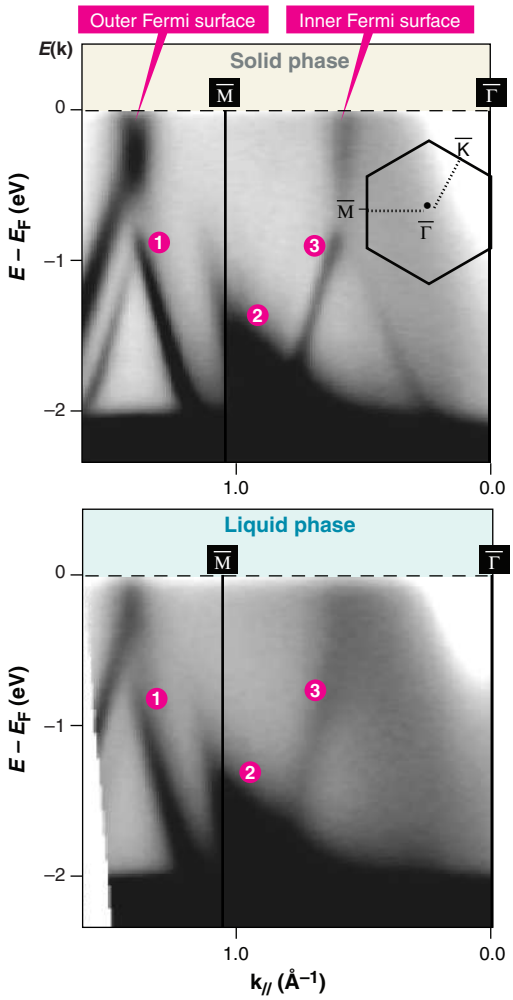

From solid to liquid. Experimental band structure $E(\mathbf{k})$ along the $\bar{\Gamma}\bar{M}$ direction for a lead monolayer on a copper (111) surface, obtained by angular-resolved photoemission. (**Top**) Solid layer at room temperature. Small hexagon: two-dimensional Brillouin zone of the lead layer. E_F is the Fermi energy, and $k_{//}$ is the momentum of the photoelectron. (**Bottom**) Same for the liquid layer at 585 K.

CREDIT: ADAPTED FROM (*1*)

The author is at the Ministry of Research, 1 rue Descartes, 75231 Paris cedex 05, France. E-mail: petroff@esrf.fr

strong dark line at –2.2 eV corresponds to the 3*d* band of copper.

Comparison between the bands of the liquid and the solid phase reveals strong similarities but also large differences. Band **1** broadens only slightly, indicating that the electronic states conserve their character through the solid-to-liquid transition. For band **3**, the states change from extended states in the solid to highly localized ones in the liquid, as seen by the large broadening of this band and the decrease in intensity. As discussed in (*1*), the states of band **3** no longer fulfill the basic condition for a delocalized state (*6*). Rotenberg *et al.* have reported a similar observation in quasicrystalline materials (*7*).

Why do bands **1** and **3** behave so differently in the liquid phase? The reason may lie either in the symmetry or in the wavelength of the wave function. Baumberger *et al.* attribute the difference to the symmetry of the atomic wave functions. The bands of the inner Fermi surface have a negative group velocity (that is, the band energy decreases with increasing electronic wave vector); a behavior that is characteristic of *p*-type wave functions, which change their phase at the site of the atomic nucleus. In the solid, the band minimum lies at the Brillouin zone boundary, but in the liquid, this zone boundary no longer exists.

The results reported by Baumberger *et al.* (*1*) open up new possibilities for studying liquid metals and show that angular resolved photoemission can be a powerful tool for that. However, more experiments are needed. In particular, it will be interesting to study in detail the importance of the wavelength and the symmetry of the wave function by analyzing different liquid/solid interfaces. The effect of the substrate should also be carefully studied. Finally, experiments on quasicrystals should also be pursued, because they present some similarities with a liquid at an interface: The electronic states show a dispersion relation (*7*) that corresponds to the potential distribution of the local environment, but with strongly damped amplitudes.

References

1. F. Baumberger, W. Auwärter, T. Greber, J. Osterwalder, *Science* **306**, 2221 (2004); published online 25 November 2004 (10.1126/science.1103984).
2. H. Reichart *et al.*, *Nature* **408**, 839 (2000).
3. F. C. Frank, *Proc. R. Soc. London A* **215**, 43 (1952).
4. J. D. Bernal, *Proc. R. Soc. London A* **280**, 299 (1952).
5. F. Baumberger *et al.*, *Surf. Sci* **532**, 82 (2003).
6. N. F. Mott, *Adv. Phys.* **16**, 49 (1967).
7. E. Rotenberg *et al.*, *Nature* **406**, 602 (2000).

10.1126/science.1106676

ECOLOGY

A Head Start for Some Redstarts

Geoffrey E. Hill

For the past 50 years, most field ornithologists studying migratory birds that breed in North America and Europe have concentrated on analyzing their breeding ecology. Molt and migration have received scant attention, as has the time these migratory birds spend at their wintering grounds, even though this period may occupy 8 months of a bird's annual cycle (*1*). It is easy to understand why ornithologists, most of whom live in the United States, Canada, and Europe, have concentrated on the breeding biology of migratory birds. Not only are there many interesting questions that can be addressed through breeding studies, but also migratory birds are accessible in the spring and summer, are predictable in their movements, and conspicuous in song. After breeding, territories are abandoned, home ranges expand greatly, and birds begin their nocturnal southward movement, making it impossible to track individuals of most species. However, as Norris *et al.* (*2*) demonstrate on page 2249 of this issue, new technologies are helping ornithologists to overcome these obstacles, bringing studies of molt and migration to the fore. Norris and co-workers analyze the ratio of stable-hydrogen isotopes in the feathers (*3*) of individual American redstarts (*Setophaga ruticilla*) of known reproductive history to determine when and where molting takes place.

The author is in the Department of Biological Science, Auburn University, Auburn, AL 36849, USA. E-mail: ghill@acesag.auburn.edu

Redstarts are typical Neotropical migratory birds that breed in the eastern United States and Canada and winter in Central America and the Caribbean (see the figure). Norris *et al*. observed that the stable-hydrogen isotope signature of feathers grown while male birds reside at their breeding grounds in Ontario differs from that of feathers grown by birds on the migratory pathway much farther south. Thus, by analyzing feathers for their isotope content, Norris *et al*. could tell the latitude at which individual redstarts molted. They found that some redstarts completed their fall molt on the breeding grounds after they had finished nesting, thereby temporally separating the three most energetically costly activities of the year: breeding, molt, and migration. Other redstarts molted as they migrated. Most significantly, these investigators found evidence for a trade-off between energy investment in current reproduction, timing of the molt (a critical aspect of self-maintenance), and sexual signaling by males through feather color (a key determinant of future reproduction). Male redstarts that invested more energy in reproduction, including breeding later into the summer, completed their molt farther south on the migratory route, with greater overlap of molt and migration, and these males grew less colorful nuptial plumage. Analysis of stable-hydrogen isotopes in feathers is the only technique by which this striking pattern could have been revealed—there is essentially no chance of finding and accessing individual study birds during migration, even with radio telemetry.

Being forced to molt while migrating sounds like an energetically costly endeavor compared to molting on the breeding grounds before migration, but is there evidence for such a cost? Norris *et al*. looked at the carotenoid-based coloration of tail feathers. Male redstarts have a striking orange and black nuptial plumage, and individual tail feathers have a black tip with an orange base (see the figure). The authors found a negative correlation between plumage coloration and molting latitude—birds that grew their feathers while they migrated had less saturated orange coloration than birds that molted on the breeding grounds. Carotenoid pigments must be ingested by birds to be used in color displays (*4*). In other species of songbirds, expression of carotenoid-based plumage coloration signals a male's condition that is used by females in choosing mates or by rival males in assessing fighting ability (*4*). A reduction in ornamental coloration could have a direct negative impact on future reproductive success.

Loss of red coloration is a striking cost of reproduction, but there are likely to be other, more-difficult-to-detect costs of delaying molting into the migratory period. Most redstarts arrive in their wintering areas by flying over the Gulf of Mexico, a feat that requires substantial fat reserves (*5*). If the energetic demands of molting compete with premigratory fattening, then late-molting birds may have to attempt trans-Gulf migration with lower fat reserves. Molting during migration may also slow males, causing them to arrive later and get less preferred wintering sites. These speculations underscore a problem with the Norris *et al*. data: All of the males in the study were necessarily survivors. Males had to return to the same breeding grounds 1 year after breeding to have their

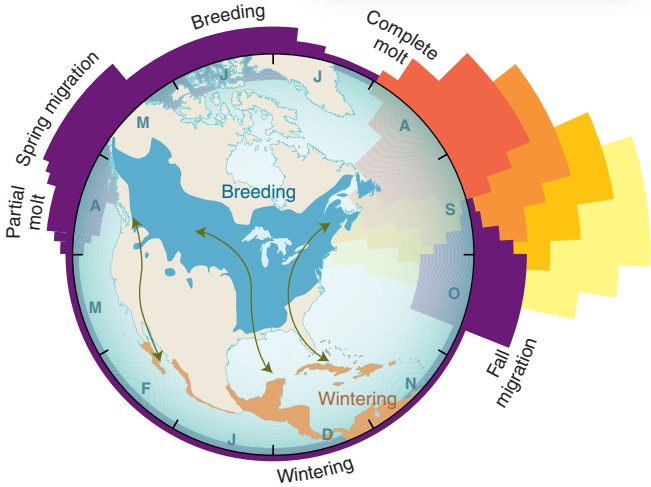

There is a season—turn, turn, turn. The annual life cycle of the American redstart, which breeds in the deciduous forests of temperate North America and Canada and winters in the Caribbean and Central America. Height of the colored bars indicates approximate relative daily energy expenditures during the major events in the redstart's annual life cycle: breeding, molt, migration, and wintering. The true energy costs of these activities are not known. Male redstarts that invest more energy in reproduction during the breeding season molt later, often during their southward migration. As a result, there is a greater overlap of molting with migration, and the energy cost results in these males growing drabber nuptial feathers (illustrated in the off-set histograms by decreased redness and color saturation with increasing overlap between molting and migration). Reduction in nuptial coloration may affect the reproductive success of these males during the next breeding season.

tails plucked for their molt location and coloration to be determined. Any birds that died as a result of reproductive effort were eliminated from the study. It seems unlikely that eliminating birds that died would have created the patterns that make this study so interesting, but eliminating such birds from the analysis might dilute the estimated cost of reproduction.

The Norris *et al*. study is not the first high-profile study of American redstarts using stable isotopes. Marra *et al*. (*6*) examined stable-isotope ratios in muscle tissue to show that the quality of wintering habitat affects timing of arrival at breeding grounds and hence reproductive success. The studies by Marra *et al*. and Norris *et al*. fit together like missing pieces of a complex life-history puzzle. Winter habitat affects spring arrival, territory quality, and date of nesting initiation. Timing of breeding affects timing of the fall molt and migration, and likely the arrival date of migrating birds at their wintering grounds. Birds are squeezed at both ends of their life cycle, as well as during their movements in between. What happens on one side of the continent has a direct and important impact on what happens on the other side. The implications of these studies for the conservation and management of migratory birds are inescapable—if we focus exclusively on the breeding biology of migratory birds we are missing at least half of the picture.

On the island of Jamaica, redstarts are called Christmas Birds because they are conspicuous during the Christmas season. For most ornithologists working in temperate climes, the redstart is a distant memory at Christmas—out of sight and out of mind. But for the growing number of ornithologists using tools like stable isotopes to take a more comprehensive approach to the study of migratory birds, it is becoming clear that what happens in the winter in the tropics and on the way there and back has a large impact on individual migratory birds and the populations in which they reside.

References

1. J. Terborgh, *Where Have All the Birds Gone? Essays on the Biology and Conservation of Birds That Migrate to the American Tropics* (Princeton Univ. Press, Princeton, NJ, 1989).
2. D. R. Norris, P. P. Marra, R. Montgomerie, T. K. Kyser, L. M. Ratcliffe, *Science* **306**, 2249 (2004).
3. K. A. Hobson, L. I. Wassenaar, *Oecologia* **120**, 312 (1999).
4. G. E. Hill, *A Red Bird in a Brown Bag: The Function and Evolution of Ornamental Plumage Coloration in the House Finch* (Oxford Univ. Press, New York, 2002).
5. D. E. Loria, F. R. Moore, *Behav. Ecol.* **1**, 24 (1990).
6. P. P. Marra, K. A. Hobson, R. T. Holmes, *Science* **282**, 1884 (1998).

10.1126/science.1107749

MICROBIOLOGY

Peptide Signals Sense and Destroy Target Cells

Danielle A. Garsin

Bacteria are not isolated solitary organisms, but actively "speak" to one another by sending and receiving transmissions in the form of chemical signals. In a process called "quorum sensing," bacteria measure the concentration of these signaling molecules in order to assess the size of the bacterial population. Once a "quorum" is reached, certain biological programs—such as sporulation, or the production of light, biofilms or virulence factors, depending on the species and context—are activated synchronously throughout the population (*1*, *2*). There are also examples where the chemical transmissions of one species can be detected by another, suggesting that these signals may be used for intraspecies as well as interspecies communication (*3*). On page 2270 of this issue, Coburn *et al.* (*4*) reveal a remarkable example of a bacterial quorum-sensing molecule that is used not only for bacterial communication but also for direct detection of eukaryotic target cells.

The author is in the Department of Microbiology and Molecular Genetics, University of Texas Health Science Center, Houston, TX 77030, USA. E-mail: danielle.a.garsin@uth.tmc.edu

In Gram-positive bacteria such as the enterococci, small peptides are the quorum-sensing signals of choice (*1*). Some of these peptides have additional biological activities such as the ability to lyse target cells. Cytolysin produced by the human pathogen *Enterococcus faecalis* is one of these special peptides (*5*) and has been designated a virulence factor because it enhances virulence in a variety of animal models (*6*–*9*) and is associated with increased mortality among infected humans (*10*). When the activity was first discovered 70 years ago, the cytolysin of *E. faecalis* was termed a "pseudohaemolysin" because it seemed only to lyse blood cells when the bacteria were grown on blood agar plates. Intriguingly, this "blood-bashing" activity could not be detected in the supernatants of *E. faecalis* liquid broth cultures (*11*). As Coburn and colleagues now argue in their new study (*4*), the cytolysin of *E. faecalis* should be called a "smart-

haemolysin" instead, because target cells must be present before the cytolysin upregulates its own synthesis and lyses them. This cytolysin therefore acts not only as a quorum-sensing molecule and an agent of cytolysis, but also as a "sonarlike" signal projected into the environment to detect target cells. Coburn and colleagues elegantly demonstrate that bacterial quorum-sensing molecules can detect and react to not only other bacteria but also eukaryotic cells from afar.

The *E. faecalis* cytolysin is composed of two subunits, $CylL_L''$ and $CylL_S''$, which together form a complex that creates pores in the membranes of target cells (see the figure). These two peptides are modified and secreted into the extracellular environment with the help of several other proteins encoded by the same cytolysin (*cyl*) operon. Although $CylL_L''$ and $CylL_S''$ work together to promote target cell lysis, they have opposing regulatory effects on the transcription of the *cyl* operon. It is well established that the exogenous addition of purified $CylL_S''$ to *E. faecalis* greatly increases transcription from the *cyl* operon (*12*). Coburn *et al*. now show that the $CylL_L''$ peptide blocks $CylL_S''$-mediated derepression of the *cyl* operon. Presumably this occurs by direct complex formation between the two subunits because stable complexes form when the two peptides are mixed together in vitro (*4*).

Coburn and co-workers hypothesized that preferential adsorption of $CylL_L''$ by target cells should lower the concentration of $CylL_L''$ in solution available to block $CylL_S''$. To test this idea, they incubated red blood cells with $CylL_L''$, washed the cells to get rid of any excess, and then added $CylL_S''$: They observed rapid lysis of the erythrocytes. However, the red blood cells did not lyse as quickly when the order of addition was reversed—$CylL_S''$ before $CylL_L''$—suggesting that $CylL_S''$ binds less readily to red blood cells than does $CylL_L''$. By measuring the dissociation constants, the authors observed that $CylL_L''$ did indeed have a higher affinity for cell membranes than did $CylL_S''$.

To show that these differences in target cell affinity account for the autoinduction of the bacterial *cyl* operon by free $CylL_S''$, the authors tested whether or not the presence of erythrocytes affected induction. When they added equimolar quantities of purified $CylL_S''$ to $CylL_L''$, no induction was observed, presumably owing to the creation of inactive $CylL_L''$–$CylL_S''$ complexes. However, when erythrocytes were added to $CylL_L''$ before addition of $CylL_S''$, there was induction of the *cyl* operon suggesting that target cells soaked up enough $CylL_L''$ to allow free $CylL_S''$ to induce expression of the *cyl* operon in *E. faecalis*.

Based on this experimental information, Coburn *et al*. propose the following model (see the figure). In the absence of target cells, basal levels of $CylL_L''$ and $CylL_S''$ are secreted by *E. faecalis* bacteria into the extracellular environment where they form an inactive oligomeric complex. In the presence of target cells, $CylL_L''$ preferentially binds to the target cell membrane, freeing up enough $CylL_S''$ to activate transcription of the *cyl* operon, thus creating more of the components necessary for lysis of target cells. The resulting increase in $CylL_S''$ concentration favors binding to the target cell membrane where, together with $CylL_L''$, a pore is formed. One fascinating feature of this mechanism is that once processed, $CylL_L''$ and $CylL_S''$ are only 38 and 21 amino acids in length, respectively. Yet despite their small size these peptides are capable of several different interactions. They form an oligomeric inactive complex in solution, and a pore complex in target cell membranes. Additionally, $CylL_S''$ induces transcription of the *cyl* operon by interacting with its repressor (thought to be a complex of CylR1 and CylR2). Elucidation of the structure/function relationships of these peptides should prove informative.

The virulence mechanism described by Coburn *et al.* is new in that *E. faecalis* senses host cells and then targets their destruction without coming into contact with them. Specifically, *E. faecalis* sends out a transmission and then responds to the feedback, like a bat that sends out a sonar signal, and then locates its prey based on the echo. In contrast, other types of virulence mechanisms commonly found in bacteria, such as Type III secretion systems, are activated only upon contact with host cells (*13*). Although it has long been suspected that the chemical signals used by bacteria to sense members of their own species could also be used to detect other types of cells, this is the first example of quorum-sensing molecules directly detecting eukaryotic target cells. It is highly probable that similar mechanisms are involved not only in other pathogenic interactions but also in symbiotic associations, where bacteria must also locate and interact appropriately with their hosts.

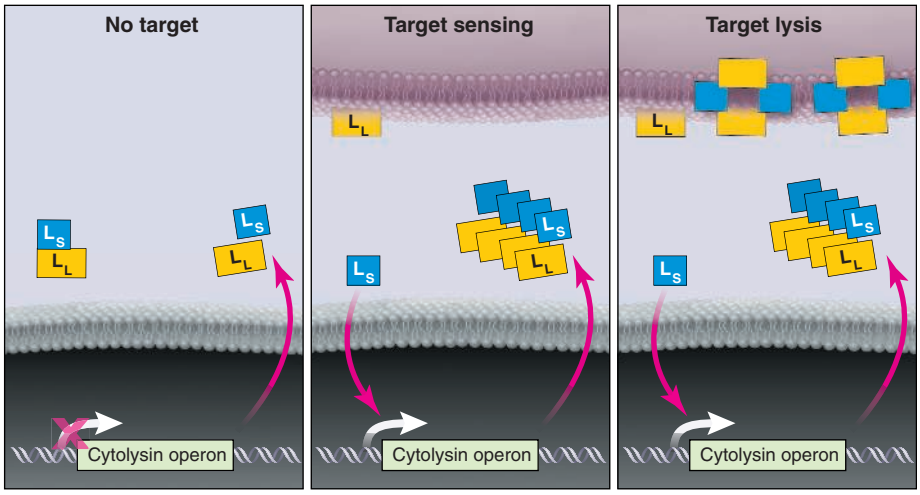

CREDIT: KATHARINE SUTLIFF/*SCIENCE*

Quorum sensing of eukaryotic cells. The cytolysin peptides of the enterococcal bacterium *E. faecalis*, $CylL_L''$ and $CylL_S''$, regulate expression of the cytolysin operon (*4*). (**Left**) In the absence of target cells, $CylL_L''$ and $CylL_S''$ are secreted by *E. faecalis* bacteria into the extracellular environment where they form an inactive oligomeric complex. (**Middle**) In the presence of target cells, $CylL_L''$ preferentially binds to the target cell membrane, freeing up sufficient $CylL_S''$ to activate transcription of the bacterial *cyl* operon. (**Right**) This leads to an increase in the production of $CylL_S''$ and $CylL_L''$, and other components that the bacteria need to lyse target cells of the host.

References and Notes

1. M. H. Sturme *et al.*, *Antonie Leeuwenhoek* **81**, 233 (2002).
2. N. A. Whitehead, A. M. Barnard, H. Slater, N. J. Simpson, G. P. Salmond, *FEMS Microbiol. Rev.* **25**, 365 (2001).
3. J. M. Henke, B. L. Bassler, *Trends Cell Biol.* **14**, 648 (2004).
4. P. S. Coburn, C. M. Pillar, B. D. Jett, W. Haas, M. S. Gilmore, *Science* **306**, 2270 (2004).
5. P. S. Coburn, M. S. Gilmore, *Cell Microbiol.* **5**, 661 (2003).
6. J. W. Chow *et al.*, *Antimicrob. Agents Chemother.* **37**, 2474 (1993).
7. Y. Ike, H. Hashimoto, D. B. Clewell, *Infect. Immun.* **45**, 528 (1984).
8. B. D. Jett, H. G. Jensen, R. E. Nordquist, M. S. Gilmore, *Infect. Immun.* **60**, 2445 (1992).
9. D. A. Garsin *et al.*, *Proc. Natl. Acad. Sci. U.S.A.* **98**, 10892 (2001).
10. M. M. Huycke, C. A. Spiegel, M. S. Gilmore, *Antimicrob. Agents Chemother.* **35**, 1626 (1991).
11. E. W. Todd, *J. Pathol. Bacteriol.* **39**, 299 (1934).
12. W. Haas, B. D. Shepard, M. S. Gilmore, *Nature* **415**, 84 (2002).
13. S. Y. He, *Annu. Rev. Phytopathol.* **36**, 363 (1998).

14. I thank H. Kaplan for helpful comments. This work was supported by a New Scholar Award in Global Infectious Disease from the Ellison Medical Foundation.

10.1126/science.1107236

Toward a Systems Approach to Understanding Plant Cell Walls

Chris Somerville,[1,2]* Stefan Bauer,[1] Ginger Brininstool,[1] Michelle Facette,[1,2] Thorsten Hamann,[1] Jennifer Milne,[1] Erin Osborne,[1] Alex Paredez,[1,2] Staffan Persson,[1] Ted Raab,[1] Sonja Vorwerk,[1] Heather Youngs[1,2]

One of the defining features of plants is a body plan based on the physical properties of cell walls. Structural analyses of the polysaccharide components, combined with high-resolution imaging, have provided the basis for much of the current understanding of cell walls. The application of genetic methods has begun to provide new insights into how walls are made, how they are controlled, and how they function. However, progress in integrating biophysical, developmental, and genetic information into a useful model will require a system-based approach.

Plant cell walls are complex and dynamic structures composed mostly of polysaccharides with high molecular weights (*1*–*4*), highly glycosylated proteins, and lignin. As a measure of the complexity, the *Arabidopsis* genome contains more than 730 genes encoding putative glycosyltransferases or glycosyl hydrolases (*5*) and several hundred additional genes encoding other types of proteins implicated in wall biosynthesis or function. Although their general catalytic activity can often be inferred from sequence, the precise enzymatic function and biological role of most of these proteins are unknown (*2*). For example, genetic analysis has identified the specific biological role for only two of the more than 170 gene products with similarity to pectin-degrading enzymes (*6*, *7*).

Faced with the prospect of analyzing the function of 1000 or more genes that may contribute to the synthesis and remodeling of cell walls, we explored the idea that a systems approach may provide a useful framework for defining the hierarchy of essential questions. The concept of systems biology has recently emerged as a way of envisioning how multifactorial biological processes operate as a whole (*8*). The concept is usually applied to understanding networks of genes or gene products but is more broadly applicable. Kitano (*8*) defines four key elements in a system: the design principles, system structure, the control method, and the system dynamics. Here, we attempted to evaluate the current state of knowledge about the polysaccharide components of dicotyledonous plant cell walls in the context of these elements. Not surprisingly, our analysis highlights many major gaps in our knowledge. However, the application of genomics, molecular genetics, and new analytical methods should provide many opportunities to close some gaps in the foreseeable future.

Design Principles

The body plan of a higher plant is essentially like a building made of ''osmotic bricks.'' Each cell is osmotically pressurized to between 0.1 and 3.0 MPa (1 MPa ~ 145 pounds per square inch). The pressure rigidifies the cells by creating tension in the cell walls. Each cell is glued to adjacent cells by pectic polysaccharides that normally prevent sliding of the cells under large strains. However, cell walls are also capable of controlled modifications that allow cells to expand in a polarized fashion during growth. Because each cell wall is attached to adjoining cell walls, coordinated expansion is necessary. It has been proposed that the role of the brassinosteroid hormones is to coordinate cell expansion (*9*).

Plant cell division involves the biogenesis and integration of new walls at the plane of division. In this process, two opposing walls form within the mother cell, and then the new walls integrate with the existing wall, and the plasma membrane repositions to form the daughter cells (*10*, *11*). Certain cell types, such as the fiber cells in wood, are subject to mechanical stress and undergo additional cell wall synthesis after the cells have finished dividing and are fully expanded. This ''secondary cell wall'' is deposited interior to the ''primary cell wall.'' Thus, the fundamental design principles include strength, expandability, and modularity.

Cell walls also provide a barrier to infection by pathogens. Exogenous application of cell wall fragments to uninfected plants triggers defensive reactions, indicating the existence of glycan-activated signal transduction chains. It has been proposed that some of the structural complexity in plant cell wall composition reflects the presence of latent signal molecules, which trigger defensive responses when they are released during the cell wall degradation that accompanies pathogenesis (*12*). Several lines of evidence have also implicated cell wall polysaccharide fragments and proteoglycans in developmental processes (*13*–*15*). For example, deglycosylation inactivated a proteoglycan named xylogen that mediates intercellular interactions required for xylem differentiation in cultured Zinnia cells (*14*). Thus, the design principles of cell walls cannot be understood solely in the context of mechanical properties.

System Structure

When viewed by electron microscopy (EM) (Fig. 1), cell walls appear to be a network of extended polysaccharides with high molecular weights (*16*, *17*). In higher plants, the visually dominant structural features are cellulose microfibrils with diameters of ~3 nm, which appear to wrap around the cells and are cross-linked by single-chain polysaccharides such as xyloglucans.

Structural analysis of cell wall polysaccharides has resulted in the compilation of ''average'' structures for the major cell wall polysaccharides (*4*, *18*). These are illustrated in figs. S1 to S6. In brief, the leaf cell walls of a dicot species such as *Arabidopsis* contain three major classes of polysaccharides: cellulose, hemicelluloses, and pectins. Cellulose is present as long unbranched fibrils composed of approximately 30 to 36 hydrogen-bonded chains of β-1,4-glucose. The length of the fibrils is unknown but single glucans containing up to 14,000 glucose units have been observed, corresponding to a fibril length of about 7 μm. Hemicelluloses are branched polysaccharides containing backbones of neutral sugars that can form hydrogen bonds to the surface of cellulose fibrils. Pectins are defined by the presence of uronic acids as

[1]Carnegie Institution, Department of Plant Biology, 260 Panama Street, Stanford, CA 94305, USA. [2]Department of Biological Sciences, Stanford University, Stanford, CA 94305, USA.

*To whom correspondence should be addressed. E-mail: crs@stanford.edu

major components. The simplest of these is homogalacturonan (HG), an unbranched polymer of (1→4)α-D-galacturonic acid. Rhamnogalacturonan I (RGI) has a backbone composed of alternating (1→2)α-L-rhamnose-(1→4)α-D-galacturonic acid decorated primarily with arabinan and galactan side chains. It has recently been suggested that RGI functions as a scaffold to which other pectins, such as rhamnogalacturonan II (RGII) and HG, are covalently attached as side chains (*18*).

A representative structure for an *Arabidopsis* leaf primary cell wall that is broadly consistent with more specialized models (*18*) and with views from EM (*16*, *17*) is presented in Fig. 2. The complexity of the image underscores the challenge associated with understanding the structure, function, and synthesis of plant cell walls. The cellulose microfibrils, which are made at the plasma membrane, are insoluble because the glucan chains aggregate laterally by means of hydrogen bonding and van der Walls forces to produce crystalline structures of parallel chains. The other polymers are secreted as soluble polymers that must unfold and diffuse within the aqueous environment of the wall to their final destination. Because some of the polymers are insoluble when extracted from the wall, we speculate that they may be modified after secretion by the removal of structural components (e.g., branches) that facilitate solubility. Also, it has been proposed that some polymers are assembled into larger (less soluble) polysaccharides following secretion into the wall (*19*). One of the driving forces for assembly of the overall structure is thought to be the hydrogen bonding of hemicellulose to the surface of cellulose microfibrils (Fig. 2). Somewhat counterintuitively, biophysical studies have indicated that the presence of the hemicellulose cross-links weakens the mechanical strength of cell walls by preventing cellulose aggregation, thereby facilitating cell wall expansion (*20*).

The factors involved in pectin deposition are unknown. Pectins have been proposed to be important for control of wall porosity, for adhesion of adjoining cells (*21*), and in controlling the ionic environment of the cell wall (*1*). Additionally, analyses of mutations that alter the structure of RGII indicate that borate-diester cross-links between apiose residues in RGII molecules are also important for strengthening of the wall, intercellular adherence, and normal growth in vascular plants (*22*). Because the borate diester forms spontaneously, it provides a mechanism for forming cross-links after the polymers are assembled in place. Another example of in muro modification is the formation of calcium bridges between the carboxyl groups of HG chains to create interpolymeric adhesion. HG is thought to be made as a fully methylesterified polymer in the Golgi (*4*). Pectin methylesterases in the cell wall remove methyl groups, thereby making the carboxyls available to coordinate calcium ions that form interchain salt bridges. The existence of 67 genes for putative pectin methylesterases in *Arabidopsis* highlights the importance of this mechanism.

Measurements of the total sugar composition of cell walls from different tissues of *Arabidopsis* revealed that every tissue type has a different polysaccharide composition (*23*). Immunohistochemical studies with monoclonal antibodies that recognize polysaccharide epitopes provide examples of spatial and temporal differentiation of wall polysaccharides (*24*, *25*). These and other studies show that the composition of the wall is tightly controlled in different cell types and in relation to growth and development (*24*, *26*). Immunological studies have also shown that the various polymers are not uniformly distributed within the walls. RGII, for example, appears to be enriched near the plasma membrane (*27*), whereas polysaccharides such as HG are enriched in the middle lamella, where adjoining cell walls abut. The differences between various cell types in cell wall composition and structure could reflect different needs for elasticity, the mobility of various types of molecules in the cell wall, or poise with respect to pathogen signaling.

The observation that each cell type may have a distinct composition makes it problematic to interpret experimental results on the basis of analyses of organs composed of different cell types. The use of isolated Zinnia cells, which can be forced to undergo synchronized terminal differentiation to vascular cells in culture, represents a promising system for studying many aspects of cell wall biology (*28*, *29*). Additionally, the large size and layered organization of cambium in

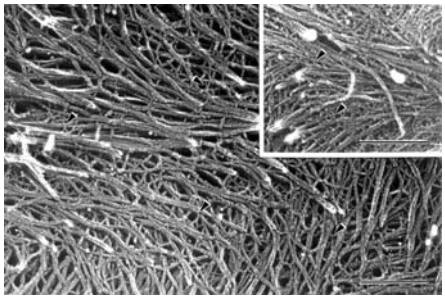

Fig. 1. Electron micrograph of outer cell walls of EDTA-extracted epidermal cells of pea *(Pisum sativum)* plants. Cellulose microfibrils and their cross-links are indicated by arrowheads. The inset shows the walls before extraction. Scale bars, 200 nm. [Image from (*16*)]

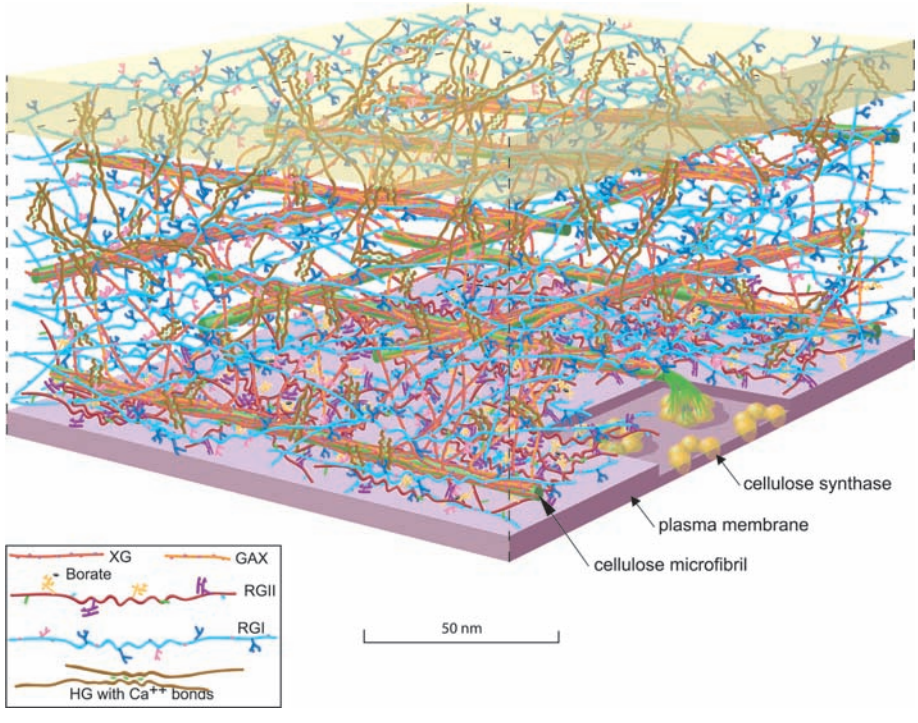

Fig. 2. Scale model of the polysaccharides in an *Arabidopsis* leaf cell. The amount of the various polymers is shown based approximately on their ratio to the amount of cellulose. The amount of cellulose shown was reduced, relative to a living cell (Fig. 1), for clarity. Because of the exaggerated distance between microfibrils, the hemicellulose cross-links [shown in dark orange (xyloglucan, XG) or light orange (glucoronoarabinoxylan, GAX)] are abnormally extended. Also, recent solid-state NMR studies have suggested that, in some plants, only about 8% of the surface of the cellulose microfibrils is occluded by XG (*89*). The figure is an elaboration of a model originally presented by McCann and Roberts (*90*). The figure was rendered by Abbey Ryan.

poplar trees facilitates sampling of steady-state mRNA levels in specific cell types at various stages of development by cutting thin sections with a cryomicrotome. Analysis of the mRNA on DNA chips and microarrays allowed a system-level analysis of secondary wall formation (*30*). The recent completion of the poplar genome sequence, and the fact that poplar and *Arabidopsis* have a similar complement of genes, will greatly facilitate the value of this experimental system.

Control, Synthesis, and Assembly

Remarkably little is known about the enzymes that catalyze synthesis of cell wall polysaccharides. Cellulose and callose (β-1,3-glucan) are the only polysaccharides for which proteins involved in the synthesis of the main chains are known. In higher plants, cellulose synthase forms a ''rosette'' complex in the plasma membrane (*31*). The complex is one of the largest protein complexes known, with a diameter about equal to that of a ribosome. It is thought that each of the six subunits that comprise a rosette contains five or six CESA proteins, each of which synthesizes one of the β-1,4-glycans that comprise a microfibril in typical higher plants (Fig. 2). In some organisms, such as the red alga *Erythrocladia subintegra*, rectangular complexes of up to 230 nm in length produce ribbons of cellulose rather than fibrils (*32*).

Arabidopsis has ten cellulose synthase (*CESA*) genes, three of which are required for primary wall synthesis and at least three of which are required for secondary wall synthesis. It now appears from mutant analysis that the various genes are not functionally redundant; three different CESA proteins must be simultaneously present to produce a functional cellulose synthase (*33*). It has been hypothesized that this could be due to the geometric constraints associated with assembling 30 to 36 subunits into a planar, membrane-localized complex of approximately 3 million daltons (*34*).

Genetic screens for mutants of *Arabidopsis* deficient in cellulose have implicated a number of factors other than the CESA proteins. The *KORRIGAN* gene encodes a membrane-localized cellulose (*35*–*37*). Bacterial cellulose synthesis also requires a cellulase for in vivo activity but not for in vitro activity, suggesting a role in cellular processes rather than catalysis. As in plants, bacterial cellulose synthase is a membrane complex containing 12 to 25 subunits (*38*). However, bacteria use cellulose not in their walls but rather to create biofilms and adherence. The *Arabidopsis COBRA* gene encodes a glycophosphatidyl inositol (GPI)–anchored protein of unknown function (*39*). Similarly, the *KOBITO* gene encodes a membrane protein of unknown function (*40*). The *ectopic deposition of lignin in pith* (*elp*) mutant is defective in a protein with sequence similarity to endochitinases (*41*). Because higher plants do not synthesize chitin, the ELP protein presumably hydolyzes another polysaccharide. Mutants deficient in glycosidase I and II, enzymes that catalyze the early steps of N-linked glycan maturation, are severely deficient in cellulose (*42*, *43*). Unfortunately, in the absence of a robust and facile in vitro assay for cellulose synthase activity in *Arabidopsis*, it has not yet been possible to assign specific roles to these gene products.

It is notoriously difficult to convincingly measure cellulose synthase activity in extracts from higher plants. One of the challenges is the presence in plant membrane preparations of a highly active β-1,3-glucan synthase that obscures β-1,4-glucan synthase activity, necessitating detailed structural analysis of the products of assays. However, several groups have observed activity and have made progress toward defining improved assay conditions (*44*, *45*). No exogenous primer was required to initiate synthesis of cellulose in vitro, raising doubts about the proposed involvement of sterol-β-glucoside as a primer (*46*). However, the discrepancy between in vivo and in vitro requirements for a cellulase in bacterial cellulose synthesis highlights the notion that in vitro conditions may not accurately reflect the in vivo conditions. Similarly, immunohistochemical evidence consistent with the idea that sucrose synthase may channel uridine 5′-diphosphate (UDP)–glucose to cellulose synthase (*47*) may be challenging to test in vitro.

Several *CESA* genes appear to be expressed throughout plants (*34*), even though cellulose synthesis is thought to be largely confined to expanding cells. This raises the possibility that cellulose synthesis is controlled posttranscriptionally. Bacteria, such as *Escherichia coli*, also exhibit constitutive expression of cellulase synthase (*38*). Enzyme activity is thought to be regulated by small effector molecules [i.e., cyclic di–guanosine 5′-monophosphate (GMP)] or through stabilization of the complex by additional proteins (*38*). Cyclic di-GMP has not been observed in plants, and *Arabidopsis* does not have an obvious homolog of the enzyme that makes cyclic di-GMP.

A second level of control is responsible for the oriented deposition of cellulose fibrils. Cellulose fibrils are generally deposited perpendicular to the axis of elongation restricting lateral swelling and allowing longitudinal expansion. A variety of correlative evidence suggests that the orientation of cellulose deposition is, in some way, regulated by the orientation of microtubules. More than 40 years ago, cells treated with colchicine were observed to display random orientation of cellulose fibrils (*48*). Consistent with this, the *fragile fiber* mutants encoding a kinesin-like protein (*fra1*) and a katanin-like protein (*fra2*) have been demonstrated to have abnormal orientation of cellulose deposition (*49*, *50*). However, studies of the conditional *mor1* mutant of *Arabidopsis*, which is deficient in microtubule polymerization at the nonpermissive temperature, have shown that ordered cellulose deposition is possible in the absence of assembled cortical microtubules and an existing cellulose template (*51*, *52*). It has also been observed that treatment of protoplasts with the cellulose synthase inhibitor isoxaben prevents characteristic orientation of the microtubules demonstrating cell wall–to-cytoskeleton feedback (*53*). We believe that these seemingly contradictory lines of evidence may reflect a variable relationship between the cytoskeleton and the cellulose synthase complexes, depending on the stage of cell wall synthesis and expansion. Recent progress in visualizing microtubules in live cells (*54*), combined with new tools for simultaneously visualizing cellulose synthase, may clarify this relationship.

Most noncellulosic polysaccharides are thought to be synthesized in the Golgi, secreted, and covalently linked in muro into larger polysaccharides (*19*). The majority of the synthetic enzymes are integral membrane proteins, most of which have been intractable to purification. Genes for pectin synthesis have been particularly challenging to identify. However, mutant screens for variation in cell wall sugar composition (*55*) or for mutants with phenotypes indicative of defective cell walls (*56*, *57*) have identified candidate genes for several of the enzymes involved. A tobacco mutant, defective in a putative glucuronyltransferase, has altered pectin content and defective intercellular attachment that appears to be due to a defect in RGII synthesis (*58*). The *quasimodo* mutant of *Arabidopsis* has reduced pectin because of a defect in a family 8 processive glycosyltransferase, which is a candidate for an HG synthase (*59*). Similar to most genes for enzymes implicated in cell wall synthesis in *Arabidopsis*, *quasimodo* is a member of a large family of related genes. A surprising finding was the discovery that a mutation in one of four isoforms of UDP-D-glucose 4-epimerase, an enzyme that acts in the formation of UDP-D-galactose, affected the synthesis of proteoglycans and polysaccharides but not galactolipids (*60*). This and several related observations have been interpreted as supporting the concept that substrate channeling may be a broadly important control point in polysaccharide biosynthesis (*61*).

There have also been important breakthroughs in the identification of enzymes involved in the synthesis of xyloglucan. An α-1,2-fucosyltransferase that adds the termi-

nal sugar to a branch in the xyglucan repeating unit was identified by purifying a protease-solubilized active fragment of the enzyme (*62*). The gene was subsequently found to complement the *mur2* mutant of *Arabidopsis*, which was identified by a direct screen for altered cell wall sugar composition (*63*). Similarly, the gene for a xyloglucan galactosyltransferase was identified by sequence similarity to a galactosyltransferase purified from fenugreek (*64*). This gene was found to correspond to the *mur3* mutant of *Arabidopsis* (*65*). Thus, substantial progress has been made by the application of both genetic and biochemical methods. Each of the cloned genes is represented in the *Arabidopsis* genome by a large number of related genes, and knowledge of the function of the founding member of a gene family will presumably greatly facilitate the subsequent assignment of function to the other members.

In principle, it should be possible to use reverse genetics methods to test the importance of candidate genes for cell wall functions. *Arabidopsis* has 29 cellulose synthase–like (*CSL*) genes with significant sequence similarity to cellulose synthase. Although mutations in several of the *CSL* genes have phenotypes, such as defective root hairs (*66*), resistance to bacterial attachment (*67*), or embryo lethality (*68*), it has not been possible to establish a primary biochemical defect in these or in mutants obtained by reverse genetics (*23*). A recent breakthrough in assigning function to these genes was the discovery that a *CSL* gene from guar catalyzed the accumulation of a β-linked mannan when expressed in transgenic soybean cells (*69*). In view of the problems associated with gene redundancy and potential lethality in pursuing a mutant approach to cell wall dissection, perhaps this approach of interspecies gene assays will prove to be broadly useful.

System Dynamics

A major challenge in plant biology is to understand how plant cell walls are modified to allow expansion and division. The network of polymers that resists turgor under normal circumstances must be relaxed during cell expansion so that the cell increases in volume, usually in a directional way, which gives rise to morphological effects at the tissue level. As the cell expands, new polysaccharides must be synthesized and integrated into the wall to retain the appropriate mechanical and functional properties.

Two classes of proteins have been specifically implicated in wall expansion. Xyloglucan endotransglycosylase (XET) catalyzes the ability to ''recombine'' two molecules of xyloglucan by endotransglycosylations (*2*, *20*). It is generally accepted that this activity allows controlled cell wall expansion by catalyzing transglycosylation of free xyloglucan with molecules bound to cellulose. In vivo activity has been elegantly demonstrated by infiltrating fluorescently labeled xyloglucan fragments into cell walls, where they become covalently integrated into larger xyloglucan molecules (*70*). Unfortunately, the large number of XET genes in *Arabidopsis* has prevented a compelling genetic test of the role of these enzymes (*71*).

Another intriguing class of proteins is the expansins, which were originally discovered on the basis of their ability to cause acid-induced extension of isolated walls (*72*). Expansins have weak sequence similarity to glucanases but have no detectable hydrolytic activity in enzyme assays. Evidence from in vitro assays (*73*) suggests that they disrupt noncovalent interactions between wall polymers. The large number of expansin genes in *Arabidopsis* has frustrated attempts to genetically test the role of these enzymes (*74*). Nonetheless, an important role for expansins was demonstrated by placing microspheres impregnated with an expansin near the apical meristems of tobacco or tomato plants (*75*, *76*). This caused the formation of a leaf at a location that disrupted the normal phyllotaxy of the plant, presumably by inducing cell expansion at an abnormal location.

Analysis of the transcriptional control of cell wall composition is just beginning (*30*). The relatively small number of enzymes that have been characterized at both the gene and enzymatic level poses a considerable restriction in the interpretation of results obtained with genomic methods. However, there have been numerous observations suggesting that plants can sense and respond to the functional properties of cell walls. For instance, it has been observed that under conditions in which cellulose synthesis is blocked by mutation (*42*) or by chemical inhibitors (*77*), large amounts of pectin accumulate. In some tissues, inhibition of cellulose synthesis also leads to ethylene- and jasmonate-dependent lignin accumulation (*78*). Whole-genome transcript profiling of *Arabidopsis* cells habituated to isoxaben, a specific inhibitor of cellulose synthase, revealed that more than 900 genes were up-regulated and another 900 were down-regulated (*79*). Thus, it appears that plants have mechanisms for sensing and responding to changes in cell wall integrity and mechanical performance (*12*, *80*). In this respect, the cell wall integrity system in yeast (*81*) may be a useful conceptual model for the mechanisms in plants.

The organization and composition of the yeast cell wall is so different from plant cell walls that it has not been used as a model for plants. However, because yeast cell walls perform functions similar to plant cell walls, they may use similar regulatory principles. It has been estimated that as many as 1200 genes affect cell wall structure and organization in *Saccharomyces cerevisiae* (*82*), suggesting a complex regulatory system. Several type I membrane proteins—Wsc1-4p, Mtl1p, and Mid2p—have been implicated as sensors of cell wall integrity (*81*, *83*). These proteins may sense changes in membrane stretching (*84*) and transduce signals by means of a guanine nucleotide exchange factor that activates the SLT2p/Mpk1p mitogen-activated protein kinase (MAPK) pathway by means of protein kinase C activation of a MAPK kinase kinase. No obvious homologs of the yeast sensor proteins have been found in plants (*80*), but there are large numbers of potential alternatives, such as wall-associated kinases and leucine-rich receptors, that are under investigation.

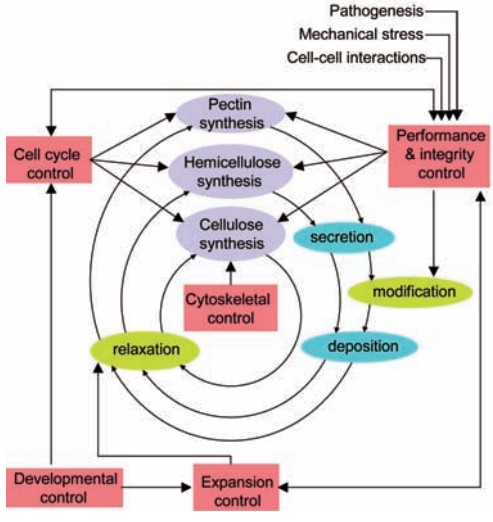

Fig. 3. A simplified system diagram for a primary cell wall. Synthesis and modification of polysaccharides are shown in purple and green, respectively. Cell biological processes are shown in blue and regulatory processes are shown in red. The diagram highlights the fact that wall synthesis is dynamic and cyclical. Genetic evidence suggests that cellulose provides a framework on which other polysaccharides (i.e., hemicellulose) assemble (*91*), presumably based simply on binding coefficients. Thus the cycle of cellulose synthesis lies at the heart of wall biogenesis. The factors that control pectin deposition are obscure but are assumed to be biophysical factors such as solubility, diffusion coefficients, and binding constants—all of which can be modified by minor changes to pectin structure such as the presence or absence of methyl-esterification or O-acetylation. Post-secretory modification of pectin (e.g., demethylation and borate-ester formation) provide mechanisms for modifying wall functionality without synthesis. The most notable feature of the diagram is the large number of inputs into a control process that we have termed "performance and integrity control." The existence of this unknown control process is inferred from responses to inhibitors, pathogens, and mutations.

Perspectives and Future Directions

A highly simplified system diagram incorporating the major concepts discussed here is presented in Fig. 3. The cyclical nature of the diagram emphasizes that the expansion of the cell wall and the integration of a new cell plate during cytokinesis are components of the cell cycle. Thus, we infer that many of the genes involved in primary cell wall synthesis and modification will be found to be controlled by factors that control other aspects of the cell cycle. However, cells that are programmed to continue dividing would be expected to have different controls than cells that are terminally differentiated. Each differentiated cell type probably has a different combination of controls to ensure that composition of the wall is compatible with the needs of that cell type. Although not emphasized here, cell walls can be modified in response to environmental stimuli. Thus, the two main inputs are developmental and environmental processes. Indeed, because cell size and cell shape are functions of cell wall expansion, any attempt to understand the mechanics of morphogenesis will ultimately lead to questions about the control of cell wall synthesis and expansion. We speculate that as methods for interrogation of cell wall structure and function improve, large numbers of morphologically abnormal mutants that cannot currently be understood in a developmental context will be found to lie at the interface of morphogenesis, the cell cycle, and cell wall biogenesis.

Viewing cell walls in a developmental context may help explain the large numbers of structurally similar genes for cell wall–related enzymes that are evident in the sequenced plant genomes. It is apparent that for some functions, such as cellulose synthesis, a small number of genes are used in most or all of the roughly 40 cell types in a plant. This is compatible with speculation that cellulose synthesis is not primarily controlled at the transcriptional level. By contrast, the large numbers of structurally related genes in other gene families may suggest that other cell wall–related processes are based on the participation of specialized genes in a tissue or temporal dependent manner. It is also likely that, because polysaccharides are composed of a small number of sugars but a relatively large number of different linkages, the members of large families of structurally similar genes encode enzymes that exhibit linkage- or context-dependent differences in catalysis.

The development of methods for determining where and when each gene is expressed in *Arabidopsis* and other plants (*85*) is a high priority in moving toward a more refined understanding of how walls are controlled. The power of transcript profiling with DNA chips or arrays to associate genes with processes cannot be fully realized as long as RNA samples are derived from mixtures of cell types. Hypotheses concerning gene function derived from transcript profiling can be rapidly tested by exploiting the extensive collection of indexed insertion mutations in *Arabidopsis* (*86*). At present, sequence-indexed insertions are available for approximately 22,600 of the genes in *Arabidopsis* (*87*).

Although powerful genomic resources are available in *Arabidopsis* (*86*, *88*), they are only a subset of the diverse resources that will be required to permit formulation of a detailed system model of cell walls. The development of tools, such as additional monoclonal antibodies or aptamers, differentiated cell cultures of *Arabidopsis*, diagnostic hydrolytic enzymes for structural analysis, and substrates for enzyme assays, are needed. These tools will facilitate analysis of mutants and will help to elucidate the function of enzymes, individual polysaccharides, and structural motifs that occur in the walls of *Arabidopsis* and other species. New biophysical methods that permit improved imaging and nanoscale interrogation or manipulation of cell walls may also facilitate a deeper understanding of how the components are organized and how that organization results in the observed physical properties. Looking over the horizon, hypothetical methods such as scanning probe nuclear magnetic resonance (NMR) or confocal EM would be very useful for visualizing the fine structure of cell walls.

Finally, the emphasis here on *Arabidopsis* should not obscure the substantial diversity in wall composition between plant species. For instance, in commelinoid monocots, most of the neutral hemicellulose and pectins are replaced by glucuronoarabinoxylan. As experimental methods and resources for studying complex polysaccharides and nanocomposites improve, this diversity will provide a rich source of information about structure-function relationships.

References and Notes

1. N. C. Carpita, D. M. Gibeaut, *Plant J.* **3**, 1 (1993).
2. S. C. Fry, *New Phytol.* **161**, 641 (2004).
3. M. C. McCann *et al.*, *Phytochemistry* **57**, 811 (2001).
4. B. L. Ridley, M. A. O'Neill, D. A. Mohnen, *Phytochemistry* **57**, 929 (2001).
5. B. Henrissat, P. M. Coutinho, G. J. Davies, *Plant Mol. Biol.* **47**, 55 (2001).
6. S. Rhee, E. Osborne, P. Poindexter, C. Somerville, *Plant Physiol.* **133**, 1170 (2003).
7. J. Vogel, T. Raab, C. Schiff, S. Somerville, *Plant Cell* **14**, 2095 (2002).
8. H. Kitano, *Science* **295**, 1662 (2002).
9. Z. Y. Wang, J. X. He, *Trends Plant Sci.* **9**, 91 (2004).
10. U. Mayer, G. Jürgens, *Curr. Opin. Plant Biol.* **7**, 599 (2004).
11. S. Cutler, D. Ehrhardt, *Proc. Natl. Acad. Sci. U.S.A.* **99**, 2812 (2002).
12. S. Vorwerk, S. C. Somerville, C. R. Somerville, *Trends Plant Sci.* **9**, 203 (2004).
13. J. C. Dumville, S. C. Fry, *Plant Physiol. Biochem.* **38**, 125 (2000).
14. H. Motose, M. Sugiyama, H. Fukuda, *Nature* **429**, 873 (2004).
15. Q. Hall, M. C. Cannon, *Plant Cell* **14**, 1161 (2002).
16. T. Fujino, Y. Sone, Y. Mitsuishi, T. Itoh, *Plant Cell Physiol.* **41**, 486 (2000).
17. M. C. McCann, B. Wells, K. Roberts, *J. Cell Sci.* **96**, 323 (1990).
18. J.-P. Vincken *et al.*, *Plant Physiol.* **132**, 1781 (2003).
19. E. M. Kerr, S. C. Fry, *Planta* **217**, 327 (2003).
20. E. Chanliaud, J. De Silva, B. Strongitharm, G. H. Jeronimdis, M. J. Gidley, *Plant J.* **38**, 27 (2004).
21. M. C. Jarvis, S. P. H. Briggs, J. P. Knox, *Plant Cell Environ.* **26**, 977 (2003).
22. M. A. O'Neill, T. Ishii, P. Albersheim, *Annu. Rev. Plant Biol.* **55**, 109 (2004).
23. T. Richmond, C. Somerville, *Plant Mol. Biol.* **47**, 131 (2001).
24. G. Freshour *et al.*, *Plant Physiol.* **131**, 1602 (2003).
25. W. Willats, L. McCartney, W. Mackie, J. Knox, *Plant Mol. Biol.* **47**, 9 (2001).
26. J. P. Knox, P. J. Linstead, J. King, C. Cooper, K. Roberts, *Planta* **181**, 512 (1990).
27. M. N. V. Williams, G. Freshour, A. G. Darvill, P. Albersheim, M. G. Hahn, *Plant Cell* **8**, 673 (1996).
28. D. Milioni, P. E. Sado, N. J. Stacey, K. Roberts, M. C. McCann, *Plant Cell* **14**, 2813 (2002).
29. T. Demura *et al.*, *Proc. Natl. Acad. Sci. U.S.A.* **99**, 15794 (2002).
30. J. Schrader *et al.*, *Plant Cell* **16**, 2278 (2004).
31. S. Kimura *et al.*, *Plant Cell* **11**, 2075 (1999).
32. I. Tsekos, K. Okuda, R. M. Brown Jr., *Protoplasma* **193**, 33 (1996).
33. N. Taylor, R. Howells, A. Huttly, K. Vickers, S. Turner, *Proc. Natl. Acad. Sci. U.S.A.* **100**, 1450 (2003).
34. W. R. Scheible, R. Eshed, T. Richmond, D. Delmer, C. Somerville, *Proc. Natl. Acad. Sci. U.S.A.* **98**, 10079 (2001).
35. F. Nicol *et al.*, *EMBO J.* **17**, 5563 (1998).
36. I. His, A. Driouich, F. Nicol, A. Jauneau, H. Höfte, *Planta* **212**, 348 (2001).
37. S. Sato *et al.*, *Plant Cell Physiol.* **42**, 251 (2001).
38. U. Römling, *Res. Microbiol.* **153**, 205 (2002).
39. G. Schindelman *et al.*, *Genes Dev.* **15**, 1115 (2001).
40. S. Pagant *et al.*, *Plant Cell* **14**, 2001 (2002).
41. R. Q. Zhong, S. J. Kays, B. P. Schroeder, Z. H. Ye, *Plant Cell* **14**, 165 (2002).
42. C. S. Gillmor *et al.*, *J. Cell Biol.* **156**, 1003 (2002).
43. J. E. Burn *et al.*, *Plant J.* **32**, 949 (2002).
44. J. Lai-Kee-Him *et al.*, *J. Biol. Chem.* **277**, 36931 (2002).
45. K. Okuda, L. Li, K. Kudlicka, S. Kuga, R. M. Brown Jr., *Plant Physiol.* **101**, 1131 (1993).
46. L. C. Peng, Y. Kawagoe, P. Hogan, D. Delmer, *Science* **295**, 147 (2002).
47. V. V. Salnikov, M. J. Grimson, D. P. Delmer, C. H. Haigler, *Phytochemistry* **57**, 823 (2001).
48. P. B. Green, *Science* **138**, 1404 (1962).
49. D. Burk, Z. Ye, *Plant Cell* **14**, 2145 (2002).
50. R. Q. Zhong, D. H. Burk, W. H. Morrison, Z. H. Ye, *Plant Cell* **14**, 3101 (2002).
51. R. Himmelspach, R. E. Williamson, G. O. Wasteneys, *Plant J.* **36**, 565 (2003).
52. K. Sugimoto, R. Himmelspach, R. E. Williamson, G. O. Wasteneys, *Plant Cell* **15**, 1414 (2003).
53. D. D. Fisher, R. J. Cyr, *Plant Physiol.* **116**, 1043 (1998).
54. S. L. Shaw, R. Kamyar, D. W. Ehrhardt, *Science* **300**, 1715 (2003).
55. W. Reiter, C. Chapple, C. Somerville, *Plant J.* **12**, 335 (1997).
56. M. Fagard, H. Höfte, S. Vernhettes, *Plant Physiol. Biochem.* **38**, 15 (2000).
57. R. E. Williamson, J. E. Burn, C. H. Hocart, *Cell. Mol. Life Sci.* **58**, 1475 (2001).
58. H. Iwai, N. Masaoka, T. Ishii, S. Satoh, *Proc. Natl. Acad. Sci. U.S.A.* **99**, 16319 (2002).
59. S. Bouton *et al.*, *Plant Cell* **14**, 2577 (2002).
60. G. J. Seifert, C. Barber, B. Wells, L. Dolan, K. Roberts, *Curr. Biol.* **12**, 1840 (2002).
61. G. J. Seifert, *Curr. Opin. Plant Biol.* **7**, 277 (2004).
62. R. Perrin *et al.*, *Science* **284**, 1976 (1999).
63. G. Vanzin *et al.*, *Proc. Natl. Acad. Sci. U.S.A.* **99**, 3340 (2002).
64. M. E. Edwards *et al.*, *Plant J.* **19**, 691 (1999).
65. M. Madson *et al.*, *Plant Cell* **15**, 1662 (2003).
66. B. Favery *et al.*, *Genes Dev.* **15**, 79 (2001).
67. Y. Zhu *et al.*, *Plant Physiol.* **132**, 494 (2003).
68. F. Goubet *et al.*, *Plant Physiol.* **131**, 547 (2003).
69. K. S. Dhugga *et al.*, *Science* **303**, 363 (2004).
70. K. Vissenberg, V. Van Sandt, S. C. Fry, J. P. Verbelen, *J. Exp. Bot.* **54**, 335 (2003).
71. K. Nishitani, *J. Plant Res.* **115**, 303 (2002).

72. S. McQueen-Mason, D. J. Cosgrove, *Proc. Natl. Acad. Sci. U.S.A.* **91**, 6574 (1994).
73. S. E. C. Whitney, M. J. Gidley, S. J. McQueen-Mason, *Plant J.* **22**, 327 (2000).
74. Y. Li, L. Jones, S. McQueen-Mason, *Curr. Opin. Plant Biol.* **6**, 603 (2003).
75. S. Pien, J. Wyrzykowska, S. McQueen-Mason, C. Smart, A. Fleming, *Proc. Natl. Acad. Sci. U.S.A.* **98**, 11812 (2001).
76. A. J. Fleming, S. McQueen-Mason, T. Mandel, C. Kuhlemeier, *Science* **276**, 1415 (1997).
77. E. Shedletzky, M. Shmuel, T. Trainin, S. Kalman, D. Delmer, *Plant Physiol.* **100**, 120 (1992).
78. A. Cano-Delgado, S. Penfield, C. Smith, M. Catley, M. Bevan, *Plant J.* **34**, 351 (2003).
79. I. Manfield *et al.*, *Plant J.* **40**, 260 (2004).
80. E. Pilling, H. Höfte, *Curr. Opin. Plant Biol.* **6**, 611 (2003).
81. R. Garcia *et al.*, *J. Biol. Chem.* **279**, 15183 (2004).
82. P. W. J. de Groot *et al.*, *Comp. Funct. Genomics* **2**, 124 (2001).
83. B. Philip, D. E. Levin, *Mol. Cell. Biol.* **21**, 271 (2001).
84. G. Smits, J. Kapteyn, H. van den Ende, F. Klis, *Curr. Opin. Microbiol.* **2**, 348 (1999).
85. K. Birnbaum *et al.*, *Science* **302**, 1956 (2003).
86. J. Alonso *et al.*, *Science* **301**, 653 (2003).
87. Information about the number of sequence-indexed insertions can be found at The *Arabidopsis* Information Resource (TAIR): http://arabidopsis.org/news/monthly/TAIR_News_Sept04.jsp.
88. J. C. Redman, B. J. Haas, G. Tanimoto, C. D. Town, *Plant J.* **38**, 545 (2004).
89. T. J. Bootten, P. J. Harris, L. D. Melton, R. H. Newman, *J. Exp. Bot.* **55**, 571 (2004).
90. M. McCann, K. Roberts, in *The Cytoskeletal Basis of Plant Growth and Form*, C. W. Lloyd, Ed. (Academic Press, London, 1991), pp. 109–130.
91. S. Turner, C. Somerville, *Plant Cell* **9**, 689 (1997).
92. We thank K. Roberts for thoughtful suggestions. This work was supported by grants from the U.S. Department of Energy (DE-FG02-03ER20133) and the NSF (MCB 0114562). T.H. and S.V. were recipients of fellowships from the Deutche Forschungsgemeinschaft. S.P. was the recipient of a fellowship from the Carl Tryggers Foundation (CTS 03258). H.Y. was supported by a fellowship from the NIH Stanford Training Program in Genomics.

Supporting Online Material
www.sciencemag.org/cgi/content/full/306/5705/2206/DC1
Figs. S1 to S6

10.1126/science.1102765

PRESIDENTIAL ADDRESS

What Is Good for Children Is Good for Mankind: The Role of Imagination in Discovery

Mary Ellen Avery

Thank you for this opportunity to share my vision of the future of scientific inquiry with a very special audience. Not surprisingly, my views on the nature of science have been shaped by my own background—my years as a chemistry major at Wheaton College in Massachusetts and, after that, at Johns Hopkins as a specialist in medicine and neonatology, with a focus on respiratory adaptations to extrauterine life. The creation of a human baby in 9 months is indeed a wonderful thing, all the more so for the dramatic physiological transition that is required for the infant to move from a liquid environment to breathing air, once the umbilical cord is clamped. We have much descriptive information, but little insight into the molecular adaptations that orchestrate the onset of sustained breathing and clearance of lung liquid. That sense of mystery—the sense of how much, yet also how little, we know about human physiology—is one of the things that attracts me to the field of neonatology.

In that I am hardly unique, of course. No less a figure than Albert Einstein held that the most beautiful thing we can experience is the mysterious, and called it "the source of all true art and science." That thought, in turn, leads naturally into what I take as my main theme here: the role of the imagination in scientific discovery. As scientists we are all steeped in the "scientific method" of problem solving, with its framing of hypotheses, testing, and reproducible observations. But the entire enterprise must start with imagination if it is new knowledge we are after. Shirley Malcom of AAAS, in accepting the 2003 Public Welfare Medal of the National Academy of Sciences, remarked that "making the impossible happen begins with imagining something different."

We can all think of examples from the history of science and technology. Almost exactly one hundred years ago, the Wright brothers had to believe it would be possible for a human to fly before they could make it a reality, though the thought of more than 300 people in a modern passenger plane may have taxed even their scientific imaginations. Marconi was able to imagine, and then invent, wireless communication, but I doubt that even he could have conceived of the worldwide real-time communication implicit in that initial discovery. I realized how much had taken place in my own lifetime after I visited the World War II Museum in London, and saw the small office with a single telephone that Churchill used to talk to Roosevelt. Now the U.S. president is able to fly nearly halfway around the world for a Thanksgiving dinner with distantly posted soldiers. And, of course, the imagination of an earlier president, John F. Kennedy, in framing the challenge of a safe lunar landing by humans led ultimately to the first steps by astronauts on the moon, and later to remotely controlled robots on Mars.

As scientists we are all steeped in the "scientific method" of problem solving, with its framing of hypotheses, testing, and reproducible observations. But the entire enterprise must start with imagination if it is new knowledge we are after.

The excitement of where the scientific imagination has led us in exploring outer space is matched, I think, by discoveries in the "inner space" of the very small—such as the incredible frontiers of nanotechnology, or the interior workings of the single cell. We have seen brilliant insights into the way biologic cells function, communicate, live, and die on cycles that are precisely timed over a period of years and, in some instances, over 100 years. The mapping of the human genome showed the power of imagination in defining a goal and enlisting scientists from around the world to collaborate in identifying the location of the genes on each of the 46 chromosomes. The function of most of these genes remains unknown, as does the function of noncoding regions sometimes referred to as "junk DNA." Yet powerful new tools, such as the breeding of strains of mice in which one gene is "knocked out," are enabling us to learn the functions of these genes. And the fact that each cell in the body has a complete copy of the genes, and that only identical twins share the same map, not only has transformed forensic medicine—providing the ability to identify each individual by DNA testing of specimens of hair or saliva, for example—but also has raised the promise of new medications and personalized approaches to medicine itself.

All of these discoveries and approaches to solving human problems began with "imagining something different." And the issues society faces now will require comparable scientific imagination. By the year 2050—within the lifetime of many in this audience—the human population is expected to grow from its current level of 6.3 billion to 8.9 billion. Will that increase be "good" or "bad"? I submit that it could be either. Poor outcomes could include pervasive poverty and its sequlae—hunger, deficiency diseases, armed conflicts, regional disparities in life span. Yet improved outcomes are also possible, depending on the extent to which we recognize and anticipate environmental change. "Good" will prevail if we acknowledge and anticipate the requirements implicit in such a population increase, and the expectation for a long and prosperous life. A long life-span depends on understanding how to maintain better health; that, in turn, requires a sustainable environment and access to health care.

The author is President of AAAS and Professor of Pediatrics, Harvard Medical School, Children's Hospital, Boston, MA. This essay is adapted from M. E. Avery's Presidential address at the AAAS meeting in February 2004.

CREDIT: IMAGE BANK

Published by AAAS

One example would be applying what is already known to benefit health: access to clean water, clean air, and appropriate nutrition, and ways to prevent epidemics and control the spread of infection, even in the absence of appropriate vaccines or antibiotics—such as what was so brilliantly executed in recent years in the experience with SARS.

Control of atmospheric pollution; proper disposal of nuclear waste; addressing inadequate food and water supplies: we all have our own list of needs for the future. High on my list right now is concern for the many thousands of children who are separated from parents by scourges such as ever-present war and the HIV pandemic. Every child needs to be wanted, to be assured of safety and love and education. We have known this truth for centuries, but ignored it all too often. I am appalled by the exploitation of children as soldiers; by brutalities such as amputations inflicted as punishment for child "offenders"; by the widespread use of land mines, which can grievously injure the curious child who asks, simply, "What is this?" In the United States, the largest industrial country, we see major regional differences in infant mortality (defined as deaths in the first year of life), with the differences skewed about 2.5 times toward nonwhite persons relative to white persons. The excess of nonwhite-infant deaths persists year after year. The Institute of Medicine recently distributed the findings of a study that highlighted the right to equal treatment and that set out a plan to end racial and ethnic disparities in clinical diagnosis and treatment in this country. Making that plan a reality will require that we mobilize the will and resources to do so.

Fortunately, the escalation in production of new knowledge promises a wonderful future in its application in solving human problems. We have recognized the horrors of war since the days of Homer. But over the same span, we have gone from a strictly oral means of sharing experiences, to inventions that potentially give every human on earth access to an incredible range of human experience, both from recorded history and from the daily news. Knowledge acquired by observation and experience is ours for the asking, through radio, video, e-mail, and satellite communications. And the availability of new knowledge has immense implications for our ability to teach and preach.

J. Robert Oppenheimer famously recalled that, as he watched the first controlled nuclear explosion at Alamogordo, New Mexico, he thought of words from the Hindu scripture, the Baghavad Gita: "I am become death, the destroyer of worlds." He understood that the bomb's creation raised the possibility of a global conflagration that could obliterate civilization itself. Yet that same recognition also spurred the meetings by concerned scientists to alert all of us to the dangers we face, the founding of the United Nations to promote a meeting place for resolution of conflict, and the support of efforts to help the children of the world through UNICEF, the United Nations Children's Fund.

I had the privilege of knowing and working with the late James Grant, the former head of UNICEF. His ability to make friends and suggest ways to lessen the burden of poverty in the nonindustrialized nations is legendary. He worked with dictators, presidents, and the press to highlight the desperate situation of many of the world's children. One example was his advocacy of oral-rehydration therapy to treat the dehydration caused by diarrhea, and the need for wells to provide clean water in the future. He communicated with the public by urging national leaders to be photographed with infants as they received oral hydration or immunization. Eradication of smallpox was a dream come true, and organizations such as UNICEF and Rotary International have been most helpful in financing these programs. Other organizations have enlisted the press to promote health practices, such as the highly successful "Back to Sleep" campaign in Australia to prevent sudden infant death syndrome (SIDS) by providing public information on the appropriate sleeping position for infants.

And so I return, inevitably, to where I began this address—to the subject of children. That is not merely because of my own background as a neonatologist, but also because, in a larger sense, what is good for children is good for mankind. And the idea of children naturally plays into my other theme: the imagination's role in the power of science to transform our thinking about the world around us. Think back to your own childhood. You were almost certainly curious and imaginative yourself, or you would not be here tonight. That kind of imagination has played a significant part not only in the pursuit of new knowledge, but also, throughout the centuries, in mythology, literature, and scripture, and in storytelling even before the creation of written languages.

Mythical figures persist today—from gargoyles to dragons and even to wizards. In 1998, J. K. Rowling of Edinburgh published her first novel about the schoolboy Harry Potter and his adventures in a school for wizards. The series of Harry Potter books has since captivated individuals from 8 to 80 years of age—even those who know it is "make believe." If you want to speak to your seatmate in an airplane, just pull out your Harry Potter paperback book; the odds are great that the person next to you has read it, or at least a family member has. (I have the good fortune to know a distinguished Edinburgh neonatologist, Ian Laing, who was present at the birth of Ms. Rowling's infant, and I thought perhaps we could lure them to be principal speakers at this meeting. However, though Ms. Rowling thanked us for the invitation, she replied that she thought she should give her attention to her 6-month-old daughter—a reason no pediatrician could protest!) Howard Bennett of George Washington University Medical Center, Washington, D.C., has even, in a 30 October 2003 letter to the *New England Journal of Medicine*, described the appearance of a new childhood ailment—"Hogwarts headaches," caused, perhaps, by the sustained suspense and tension of young readers as they spend long periods enchanted and excited by these

books. My 8-year-old grand-nephew, however, informs me that Harry Potter will surely be okay in the end, despite any danger, since "he is a true wizard."

And what has all of this to do with science? For an answer to that, I will rely once again on Albert Einstein—as quoted in an announcement for a recent exhibit on magic at the Museum of Science in Boston: "Underlying the seeming differences between science and magic are more similarities than you might imagine. Both disciplines rely on a process sparked by mystery and nurtured by curiosity." It is indeed a thrilling experience to create new knowledge.

CREDIT: JOE RAEDLE/NEWSMAKERS/GETTY IMAGES

References

1. E. Aries, M. MacDorman, D. M. Strobino, B. Guyer, *Pediatrics* **112**, 1215 (2003).
2. J. E. Cohen, *Science* **302**, 1172 (2003).
3. Physicians for Human Rights, www.phrusa.org/.
4. J. K. Rowling, *Harry Potter and the Prisoner of Azkaban* (Scholastic, New York, 1999).
5. H. J. Bennett, *N. Engl. J. Med.* **349**,1779 (2003).

Cumulative Sperm Whale Bone Damage and the Bends

Michael J. Moore* and Greg A. Early

Osteonecrosis, a chronic pathology of deep diving recognized in humans, is shown here to be a progressive condition in sperm whales, suggesting that the long-held dogma of complete immunity to decompression sickness ("the bends") in marine mammals should be revisited and that acute embolic disease may result from disruption of normal dive patterns.

Postmortem examination (*1*) of a 14.7-m adult male sperm whale, specimen NBWM 2003.95, showed that rib and chevron bone articulations, nasal bones, and deltoid crests (Fig. 1, fig. S1, and table S1) were pitted and eroded, much as described by Flower in 1868 (*2*). The lesions were multifocal and bilateral but asymmetric. Intervertebral disc and fused epiphyseal plate structure appeared normal, whereas a minority of zygapophyseal facets showed the same erosion and remodeling. Computer tomographs and x-rays showed good cortical bone density in the flipper, chevron bones, and vertebrae, with dense lamellar cortex and less dense medullary spongiform structure, but with joint surface erosions evident where the ribs and chevron bones articulated with the vertebrae and sternebrae. Histological examination revealed multifocal, chronic, and marked bone and cartilage erosion, ulceration, degeneration, and extensive proliferation and remodeling of cartilage and woven bone. Aetiology was unclear but premortem, with no histological indication of any infectious disease. Ziehl-Neelsen staining failed to show any definitive acid-fast bacteria. Bacterial cultures revealed no growth of organisms considered to be premortem pathogens. Culture for *Brucella* spp. was negative.

Consequent to these findings, we surveyed (*1*) 16 partial or complete sperm whale skeletons from the Pacific and Atlantic oceans, collected over a 111-year time span, of a broad size and age range. As body length increased, there was an increase in severity of bilateral erosion and remodeling of rib and chevron bone subarticular surfaces and deltoid crests (Fig. 1, fig. S1, and table S1). In calves, these showed regular small nutrient foramina. The nasal bones showed regular branching vessel indentations radiating from the lateral margin toward the midline. Early changes in juvenile rib (Fig. 1) and chevron bone (fig. S1A) subarticular surfaces included erosion around nutrient foramina and single, large, semispherical cavitations of 1.5 to 2.0 cm in diameter. In larger animals of both sexes, the regular pattern of nutrient artery foramina was further obscured by a mass of fenestrated, eroded, and remodeled bone in chevron and rib articular surfaces, deltoid crests (Fig. 1 and fig. S1), and nasal bones. The earliest stage of the nasal bone change was found in a 7.3-m male, in which the vascular tree was still evident, but substantial remodeling was already present.

Fig. 1. Progressive, erosive, and remodeling development of dysbaric osteonecrosis in sperm whale subarticular rib bone surfaces. The top to bottom panels show a progression from calf to mature adult. Scale bar 2 cm top panel, 1 cm rest. Dark areas indicate the vascular channels, which appear normal in the calf and increasingly eroded and enlarged in larger animals. Accession numbers top to bottom (table S1): MCZ1209, MCZ61406, NBWM 2003.95, and NBWM 2003.95.

Osteonecrosis best describes the bony changes we observed (supporting online text). Similar lesions have been attributed to dysbaric stress in fossil diving mosasaurs (*3*) and plesiosaurs (*4*).

In humans (*5*), osteonecrosis can follow dysbaric stress, hemoglobinopathy, hemopoietic disorders, hyperadrenocorticism, irradiation, or thermal injuries. Establishing the primary cause of osteonecrosis is usually based on history. All sperm whales routinely undergo dysbaric stress, whereas we have no cultural or histological evidence for any other single known cause of osteonecrosis that could have affected all the adult sperm whales we examined from the Atlantic and Pacific oceans over 111 years. Thus, the most parsimonious hypothesis is that nitrogen emboli induced the observed osteonecrosis.

It therefore appears that sperm whales may be neither anatomically nor physiologically immune to the effects of deep diving. This opens the question of decompression issues constraining surfacing behavior and implies that they and probably other cetacea may be open to acute embolic injury if forced to surface rapidly. The recent description of acute decompression-like sickness in beaked whales exposed to military sonar (*6*) may, therefore, reflect acute nitrogen embolism resulting when decompression sickness avoidance behavior, such as the dive traces previously described in sperm whales (*7*), is overridden by extended surfacing (supporting online text).

References and Notes

1. Materials and methods are available as supporting material on *Science* Online.
2. W. H. Flower, *Trans. Zool. Soc. London* **6**, 309 (1868).
3. B. M. Rothschild, L. D. Martin, *Science* **236**, 75 (1987).
4. B. M. Rothschild, G. Storrs, *J. Vertebr. Paleontol.* **23**, 324 (2003).
5. D. Resnick, *Diagnosis of Bone and Joint Disorders* (Saunders, Philadelphia, PA, 2002).
6. P. Jepson *et al.*, *Nature* **425**, 575 (2003).
7. W. Watkins *et al.*, *Mar. Mamm. Sci.* **18**, 55 (2002).

8. Funded in part through a grant from NOAA Fisheries' John H. Prescott Marine Mammal Rescue Assistance Program (award no. NA03NMF4390046). WHOI contribution no. 11227.

Supporting Online Material

www.sciencemag.org/cgi/content/full/306/5705/2215/DC1
Materials and Methods
SOM Text
Fig. S1
Table S1

21 September 2004; accepted 19 October 2004
10.1126/science.1105452

Department of Biology, Woods Hole Oceanographic Institution, Woods Hole, MA 02543, USA.

*To whom correspondence should be addressed. E-mail: mmoore@whoi.edu

Distributions of Microbial Activities in Deep Subseafloor Sediments

Steven D'Hondt,[1]* Bo Barker Jørgensen,[1] D. Jay Miller,[1] Anja Batzke,[2] Ruth Blake,[1] Barry A. Cragg,[1] Heribert Cypionka,[1] Gerald R. Dickens,[1] Timothy Ferdelman,[1] Kai-Uwe Hinrichs,[1] Nils G. Holm,[1] Richard Mitterer,[1] Arthur Spivack,[1] Guizhi Wang,[3] Barbara Bekins,[1] Bert Engelen,[2] Kathryn Ford,[1] Glen Gettemy,[1] Scott D. Rutherford,[4] Henrik Sass,[2] C. Gregory Skilbeck,[1] Ivano W. Aiello,[1] Gilles Guèrin,[1] Christopher H. House,[1] Fumio Inagaki,[1] Patrick Meister,[1] Thomas Naehr,[1] Sachiko Niitsuma,[1] R. John Parkes,[1] Axel Schippers,[1] David C. Smith,[1] Andreas Teske,[1] Juergen Wiegel,[1] Christian Naranjo Padilla,[1] Juana Luz Solis Acosta[1]

Diverse microbial communities and numerous energy-yielding activities occur in deeply buried sediments of the eastern Pacific Ocean. Distributions of metabolic activities often deviate from the standard model. Rates of activities, cell concentrations, and populations of cultured bacteria vary consistently from one subseafloor environment to another. Net rates of major activities principally rely on electron acceptors and electron donors from the photosynthetic surface world. At open-ocean sites, nitrate and oxygen are supplied to the deepest sedimentary communities through the underlying basaltic aquifer. In turn, these sedimentary communities may supply dissolved electron donors and nutrients to the underlying crustal biosphere.

Microbial life is widespread in the marine sediments that cover more than two-thirds of Earth's surface. Intact cells (*1*) and intact membrane lipids (*2*, *3*) provide evidence of prokaryotic populations in sediments as deep as 800 m below the seafloor (mbsf). Prokaryotic activity, in the form of sulfate (SO_4^{2-}) reduction and/or methanogenesis, occurs in sediments throughout the world ocean (*4*). The prokaryotes of subseafloor sediments have been estimated to constitute as much as one-third of Earth's total living biomass (*5*).

Despite the ubiquity of life in subseafloor sediments, little is known about it. The diversity of its metabolic activities, the composition of its communities, and the nature of its variation from one environment to another are largely unknown. Its relationship to the photosynthetic surface world is not fully understood. Its relationship to the deeper world of the underlying basaltic crust has not been tested.

To explore life in deeply buried marine sediments, we undertook Ocean Drilling Program (ODP) Leg 201. The expedition sites are located in the equatorial Pacific Ocean and on the continental margin of Peru (Fig. 1) (*6*). These sites are typical of subsurface environments that exist throughout most of Earth's ocean. Their water depths range from 150 m on the Peru Shelf to 5300 m in the Peru Trench. The sampled sediments ranged in subseafloor depth from 0 to 420 m, in temperature from 1° to 25°C, and in age from 0 to 35 million years ago (Ma) (*6*, *7*). Prokaryotic cells occur throughout the sampled sediment column at every site (Fig. 1) (*8*).

Diversity of metabolic activities. Dissolved electron acceptors such as SO_4^{2-} and nitrate (NO_3^-) exhibit subsurface depletion, whereas dissolved metabolic products such as dissolved inorganic carbon ($DIC = CO_2 + HCO_3^- + CO_3^{2-}$), ammonia ($\Sigma NH_3 = NH_3 + NH_4^+$), sulfide ($\Sigma H_2S = H_2S + HS^-$), methane ($CH_4$), manganese [inferred to be Mn(II)], and Fe [inferred to be Fe(II)] consistently exhibit concentration maxima deep in the drilled sediment columns (e.g., Fig. 1). These concentration profiles indicate that biologically catalyzed reactions consume and release metabolites deep in the sediment column at all of the sites. The microbial processes implicit in Fig. 1 include organic carbon oxidation, ammonification, methanogenesis, methanotrophy, sulfate reduction, and manganese reduction. Other processes that occur in these sediments include iron reduction and the production and consumption of formate, acetate, lactate, hydrogen, ethane, and propane (*6*).

These activities are unexpectedly diverse. The interstitial water chemistry of shallow marine sediments generally exhibits a predictable zonation, with peak concentrations of dissolved products from different redox processes [Mn(II), Fe(II), ΣH_2S, and CH_4] present at successively greater sediment depths (*9*–*12*). This succession of redox zones has been ascribed to competition between metabolic pathways; electron-accepting reactions that yield successively less negative standard free energies are hypothesized to predominate at successively greater depths because electron acceptors with higher free energy yields are depleted at shallower depths [e.g., (*9*, *11*)]. In shallow marine sediments that exhibit this zonation, terminal electron acceptors ultimately enter the sediment from the overlying ocean. As the reduced products from below enter successively shallower zones of SO_4^{2-}, Fe(III), Mn(IV), NO_3^-, and O_2 reduction, vertical cascades of electron-accepting processes are sustained (*11*). For example, O_2 may be used to oxidize Mn(II) to Mn(IV), which can oxidize Fe(II) to Fe(III), which might oxidize reduced sulfur, which ultimately could oxidize hydrogen or organic carbon.

In many respects, dissolved chemical profiles of Leg 201 sites exhibit this standard zonation. However, they also depart from it in four important ways. First, at site 1229, the introduction of dissolved SO_4^{2-} from below reverses the standard redox zonation by sustaining a zone with abundant SO_4^{2-} beneath a sulfate-depleted methane-rich zone (Fig. 2). At this site and at nearby site 1228, SO_4^{2-} is introduced at depth by upward diffusion from ancient brine (*6*). This deep brine is present along much of the Peru Shelf (*13*). At sites 1225 and 1226, SO_4^{2-} similarly diffuses upward into the deepest sediments from water circulating through the underlying basaltic aquifer. Sulfate is supplied to the deepest sediments in this manner throughout much of the eastern equatorial Pacific (*14*).

Second, at some sites, the expected zonation is locally reversed by the appearance of

[1]Ocean Drilling Program Leg 201 Shipboard Scientific Party. [2]Institut für Chemie und Biologie des Meeres, Universität Oldenburg, D-26111 Oldenburg, Germany. [3]University of Rhode Island Graduate School of Oceanography, Narragansett, RI 02882, USA. [4]Department of Environmental Science, Roger Williams University, Bristol, RI 02809, USA.

*To whom correspondence should be addressed at NASA Astrobiology Institute, University of Rhode Island Graduate School of Oceanography, South Ferry Road, Narragansett, RI 02882, USA. E-mail: dhondt@gso.uri.edu

large peaks in dissolved Mn and Fe concentrations far below the seafloor (e.g., Figs. 1 to 3). Such midcolumn peaks demonstrate that, in discrete intervals, concentrations of buried iron- and manganese-bearing minerals can be high enough and their rates of dissolution and reduction slow enough to continue long after metabolic activities with lower standard free energies have become predominant in shallower sediments.

Third, subsurface CH_4 maxima occur within the sediments of all Leg 201 sites, including the open-ocean sites where dissolved SO_4^{2-} concentrations are high (*6*) (Fig. 1). Similar maxima have recently been identified at many other open-ocean sites (*4*, *15*). They indicate that methanogenesis occurs deep beneath the seafloor in most, perhaps all, marine sediments, regardless of SO_4^{2-} availability. This result indicates that methanogenesis occurs long before electron acceptors that yield higher standard free energies have been depleted.

The fourth important departure occurs only at the open-ocean sites, where the succession of redox zones that extends from the seafloor to greater depths is mirrored by a similar succession that extends upward from the basement-sediment interface (Fig. 3). At sites 1225 and 1231, relatively high concen-

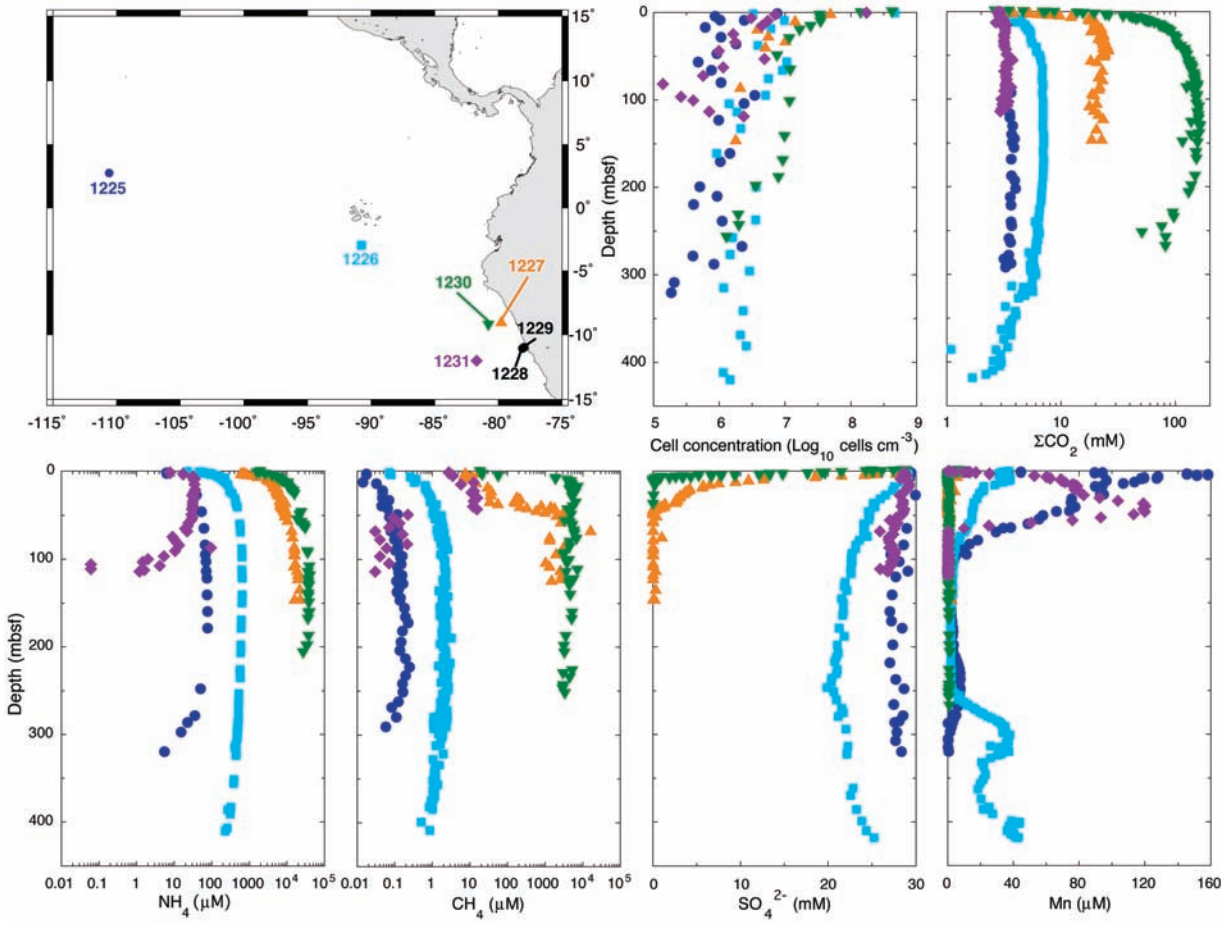

Fig. 1. Map of Leg 201 sites and concentration profiles of several dissolved chemical species at five of the sites (*17*). At sites 1225, 1226, and 1231, the deepest sample was taken just above the basaltic basement.

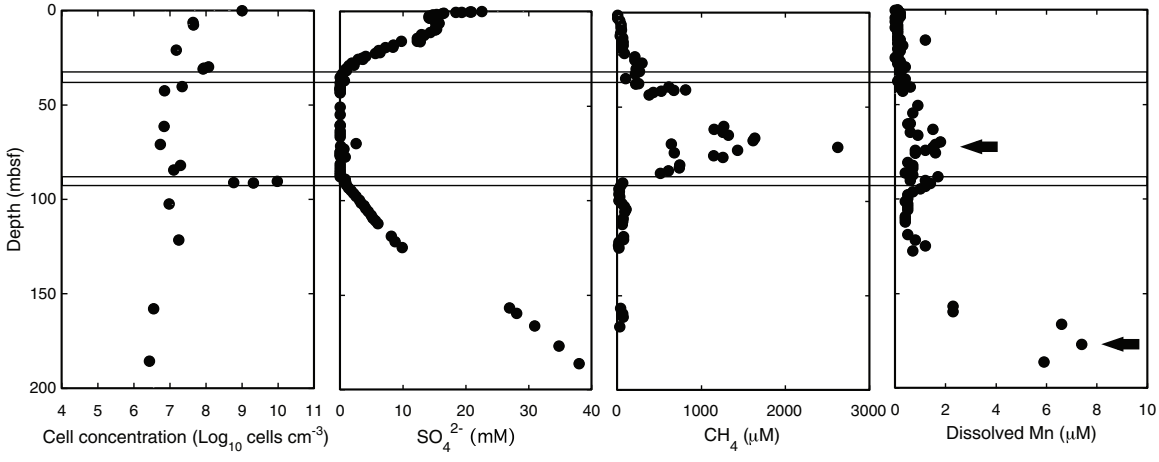

Fig. 2. Concentration profiles of cells and some dissolved chemicals at site 1229 (*17*). White bands mark sulfate-methane transition zones. Arrows mark midcolumn peaks in dissolved Mn concentrations.

trations of NO_3^- and traces of O_2 were discovered at the base of the sediment column (*16*, *17*). This NO_3^- and O_2 presumably enters the sediments from oxic water circulating through the underlying basaltic basement.

A local peak in dissolved Mn occurs just above this deep nitrate-reducing zone at both sites 1225 and 1231 (Fig. 3). A similar peak occurs in the basal sediments of site 1226. At all three sites, these Mn concentration maxima are stratigraphically overlain by maxima in dissolved Fe concentrations. These Mn and Fe maxima mark successive intervals of Mn and Fe reduction.

The deep occurrences of successive O_2, NO_3^-, Mn, and Fe redox zones at open-ocean sites have three immediate implications. First, the transport of O_2 and NO_3^- through the underlying basaltic aquifer sustains aerobic and nitrate-reducing prokaryotic communities in the deepest (11 to 35 Ma) sediments of these sites, although anaerobic communities are active in the overlying sediment. Second, this deep introduction of NO_3^- and O_2 may cause Mn and Fe oxidation fronts and thereby sustain continued Mn and Fe cycling at the base of the sediment column. Third, respiration along the flow path through the underlying basalts is insufficient to strip O_2 and NO_3^- from the circulating water. Respiration in these basaltic aquifers may be limited by electron donor availability (*18*).

These discoveries indicate that the energy-yielding activities of deep subseafloor sedimentary ecosystems are far more diverse than can be predicted from the standard redox zonation of shallow marine sediments. Although unexpected, the reversed redox successions of the deepest open-ocean sediments are consistent with the hypothesis that electron-accepting pathways with successively lower standard free energies predominate at successively greater distances from a source of oxic water. The reversed subseafloor succession of site 1229 (from methanogenesis to sulfate reduction) is similarly consistent with this hypothesis.

The occurrence of methanogenesis in sulfate-replete porewaters and the occurrences of Mn and Fe reduction in deep methanogenic zones and deep sulfate-reducing zones require different explanation(s) than the reversed redox zones. There are at least three possible explanations of these occurrences: (i) The organisms that undertake these different processes may rely on noncompetitive substrates (different electron donors) in deep marine sediments; (ii) organisms that rely on electron-accepting pathways with higher standard free energies may have higher energy requirements than organisms that rely on pathways with lower standard free energy yields; or (iii) the in situ free energies of these reactions may differ greatly from their standard free energies (for example, all of these reactions may yield similar free energies in deep subseafloor sediments where they co-occur). Whichever explanation ultimately applies, subseafloor occurrences of many electron-accepting activities cannot be predicted by simple extrapolation of the shallow marine redox zonation to sediments at greater depths.

Rates of electron-accepting activities. At steady state, fluxes of SO_4^{2-} and NO_3^- into a sediment column are respectively equal to net reduction rates of SO_4^{2-} and NO_3^- within that column. Also at steady state, the minimum rate of metal (Mn or Fe) reduction is equal to the flux of the dissolved metal from zones of net reduction (marked by local concentration peaks) to zones of net precipitation or oxidation (marked by concentration minima) (*19*).

Biogeochemical flux models based on concentration data and sediment physical properties were used to quantify rates of these electron-accepting activities at most Leg 201 sites (Table 1) (*17*, *19*). Net rates of SO_4^{2-} reduction in subseafloor sediments (>1.5 mbsf), net fluxes of ΣH_2S out of those sediments, and estimated Fe reduction rates within the sediments are much higher at the ocean-margin sites than at the open-ocean sites. In contrast, estimated Mn reduction rates and net NO_3^- reduction rates in the subsurface sediments (from >1.5 mbsf to the base of the drilled sediments) are higher at the open-ocean sites than at the ocean-margin sites. These net NO_3^- reduction rates entirely result from the introduction of NO_3^- from the underlying basaltic aquifers.

These rates of subseafloor activities vary predictably from open-ocean sites to ocean-margin sites (Table 1). At each site, the predominant energy-yielding pathways may be a function of total electron-accepting activity. For example, if the electron donor is C(0) for electron-accepting reactions, carbon oxidation by net SO_4^{2-} reduction appears to greatly outpace carbon oxidation by metal (Mn and Fe) reduction at the high-activity ocean-margin sites and the most active open-ocean site (Table 1) (*20*). In contrast, at the open-ocean site where net activities are lowest (site 1231), SO_4^{2-} reduction is not detectable and net respiration in sediments deeper than 1.5 mbsf may principally rely on reduction of Mn(IV) and Fe(III).

Biogeochemical linkages to the surface world and to life in underlying aquifers. The activities in Table 1 ultimately rely on electron acceptors from the photosynthetically oxidized surface world. O_2, NO_3^-, and SO_4^{2-} ultimately enter these sediments by diffusing down past the seafloor and, at the open-ocean sites, by transport upward from seawater flowing through the underlying basalts. The oxidized Mn and Fe were originally introduced to the sediments by deposition of Mn and Fe at the seafloor.

The activities in Table 1 probably also principally rely on electron donors from the photosynthetically oxidized surface world. The ultimate electron donors for subsurface eco-

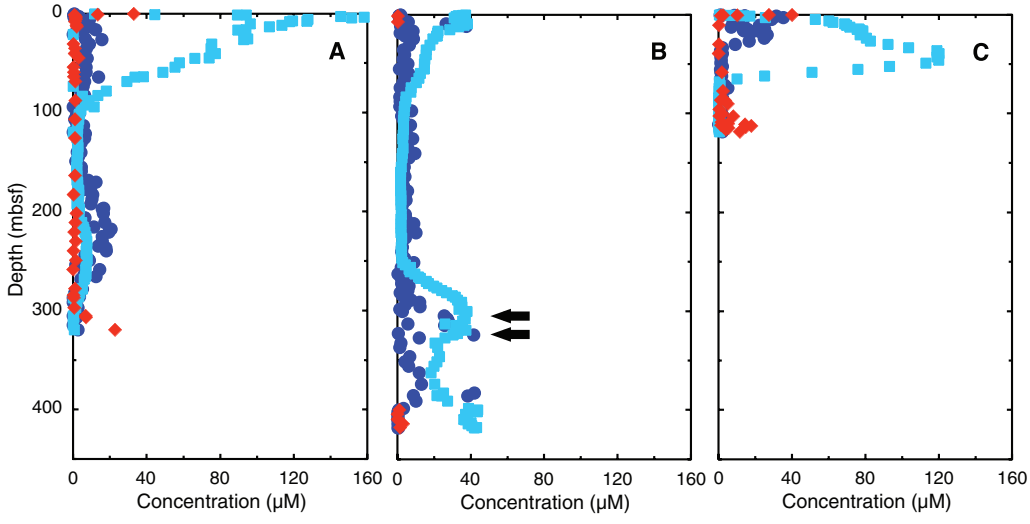

Fig. 3. Dissolved concentration profiles of NO_3^- (red diamonds), Mn (light blue squares), and Fe (dark blue circles) at open-ocean sites 1225 (**A**), 1226 (**B**), and 1231 (**C**). Arrows mark midcolumn peaks in dissolved concentrations of Mn and Fe at site 1226. At each site, the deepest sample was taken just above the basaltic basement.

systems have been hypothesized to include buried organic matter from the surface world (*9*, *10*), reduced minerals [such as Fe(II)-bearing silicates] (*21*, *22*), and thermogenic CH_4 from deep within Earth (*23*). Comparison of our subseafloor carbon oxidation estimates to published estimates of organic burial rates (*24*) suggests that buried organic carbon from the overlying photosynthetic world is abundant enough to fuel most or all of the estimated electron-accepting activities (Table 1).

The role of reduced minerals cannot be directly assessed with our data. However, thermodynamic considerations preclude oxidation of Fe(II) or Mn by Fe(III) or SO_4^{2-}. Consequently, reduced Fe and Mn are unlikely to be important subseafloor electron donors at any sites where SO_4^{2-} or Fe(III) is the principal electron acceptor. In the sediments of site 1231, where Mn(IV) appears to be the principal electron acceptor, Fe(II) may be an important electron donor.

Our data clearly indicate that activity in the sediments of our open-ocean sites is not fueled by thermogenic CH_4 from deep within Earth. Maximum concentrations in the middle of each open-ocean sediment column and minimum concentrations near the sediment-basement interface (Fig. 1) indicate that biogenic CH_4 and ΣNH_3 are produced deep in these sediments, and, at sites where chemical transport is dominantly diffusive, actually migrate downward toward the underlying basalts. In this manner, the deep sedimentary communities may provide electron donors and biologically accessible nitrogen to communities in the underlying basaltic aquifers.

Environmental variation in cell abundance and cultured isolates of subseafloor sedimentary communities. Cell concentrations vary with metabolic reaction rates and metabolic product concentrations from site to site (Fig. 1). For example, cell concentrations are highest at sites where concentrations of metabolic products (ΣNH_3, CH_4, DIC) and net rates of SO_4^{2-} reduction and Fe reduction are highest, and cell concentrations are lowest at sites where these rates and metabolic product concentrations are lowest (Fig. 1 and Table 1). The open-ocean sites contained some of the lowest average cell concentrations ever observed in deep-sea sediments, whereas sediments recovered from the Peru Shelf contained the highest concentrations ever observed beneath the seafloor (Fig. 2).

Cell concentration profiles are also closely related to dissolved reactant distributions within individual sites. For example, at site 1229, high cell concentrations occur in subseafloor sulfate-methane transition zones (Fig. 2). Diffusion of the two reactants (SO_4^{2-} and CH_4) to these zones provides an interface of high biochemical energy supply. At one such zone (92 mbsf), this interface supports cell densities that are an order of magnitude higher than at the seafloor (Fig. 2).

Bacteria were successfully cultured and isolated from multiple depths at every site (Table 2) (*17*). These cultures indicate that living bacteria are present throughout the entire range of subseafloor depths sampled by Leg 201 (1 to 420 mbsf) (Table 2). As assessed from the 16*S* ribosomal RNA (rRNA) genes of 168 isolates, these bacteria belong to at least six distinct lineages (Table 2) (*17*). Most of these isolates are closely related to known marine organisms. Others are more distant from known organisms. Most strikingly, the 16*S* gene of one isolate from open-ocean site 1225 differs from the 16*S* gene of its nearest known relative (a member of the Bacteroidetes) by 14% (Table 2). In combination with the recent discovery of deeply rooted but previously unknown archaeal 16*S* gene sequences in subseafloor sediments of site 1231 (*25*), this isolate demonstrates that previously undiscovered prokaryotes exist in deep subseafloor sediments of the open ocean.

Although the cultured bacteria constitute only a small fraction of the total cell count in each sample (up to 0.1%), these results hint of consistent patterns in the community composition of subsurface sediments. Some lineages appear to be cosmopolitan members of subseafloor sedimentary communities. The most commonly cultured taxa are Firmicutes that are most closely related to the spore-forming bacterium *Bacillus firmus* and α-Proteobacteria that are most closely related to *Rhizobium radiobacter*. These taxa were often recovered from open-ocean sediments with abundant dissolved SO_4^{2-} and little CH_4 (Table 2). They were also often recovered from ocean-margin sediments with abundant CH_4 and no dissolved SO_4^{2-}. Close relatives of *R. radiobacter* have also been recently isolated from Mediterranean subseafloor sediments (*26*). Recent surveys of archaeal 16*S* genes in subseafloor sediments suggest that some archaeal lineages [the Deep-Sea Archaeal Group and the Marine Benthic Group A] are similarly cosmopolitan members of subseafloor sedimentary communities (*27*).

Other lineages appear to be more selective in their subseafloor environmental affinities. For example, cultured γ-Proteobacteria were consistently found at ocean-margin sites (Table 2), where concentrations of organic matter, cell concentrations, and net metabolic rates are high. However, they were rarely found at open-ocean sites, where organic concentrations, cell counts, and net metabolic rates are low. In contrast, Actinobacteria were most consistently found in sulfate-reducing sediments of the open-ocean sites (sites 1225, 1226, and 1231) and ocean-margin site 1227.

In short, subseafloor sedimentary communities contain some taxa that inhabit a

Table 1. Estimated reduction rates and carbon oxidation equivalents at ODP Leg 201 sites. BDL, below detection limit; ND, not determined.

Leg 201 location	Water depth (m below sea level)	Net NO_3^- reduction (mol cm^{-2} year^{-1})	Estimated Mn reduction (mol cm^{-2} year^{-1})	Estimated Fe reduction (mol cm^{-2} year^{-1})	Net SO_4^{2-} reduction (mol cm^{-2} year^{-1})	ΣH_2S flux out of sediment column (mol cm^{-2} year^{-1})	Potential C oxidation by net NO^{3-} reduction (mol cm^{-2} year^{-1})	Potential C oxidation by estimated Mn(IV) reduction (mol cm^{-2} year^{-1})	Potential C oxidation by estimated Fe(III) reduction (mol cm^{-2} year^{-1})	Potential C oxidation by net SO_4^{2-} reduction (mol cm^{-2} year^{-1})	Organic carbon burial rate (*24*) (mol cm^{-2} year^{-1})
Peru margin sites											
Shelf site 1227	427	BDL	2.2×10^{-11}	1.0×10^{-7}*	0.9×10^{-6}	-0.7×10^{-6}	BDL	1.1×10^{-11}	2.5×10^{-8}	1.8×10^{-6}	3.1×10^{-6}
Slope site 1230	5086	ND	1.4×10^{-10}	2.5×10^{-7}*	2.5×10^{-6}	-2.0×10^{-6}	ND	0.7×10^{-10}	6.3×10^{-8}	5.0×10^{-6}	3.1×10^{-6}
Open Pacific sites											
Equatorial site 1225	3760	1.3×10^{-9}	2.9×10^{-8}	1×10^{-8}*	1.9×10^{-8}	BDL	1.6×10^{-9}	1.5×10^{-8}	2.5×10^{-9}	3.8×10^{-8}	4.5×10^{-7}
Equatorial site 1226	3297	ND	5.9×10^{-9}	7×10^{-8}*	1.4×10^{-7}	-1.3×10^{-9}	ND	3.0×10^{-9}	1.8×10^{-8}	2.8×10^{-7}	4.6×10^{-7}
Peru Basin site 1231	4813	8.0×10^{-9}	6.1×10^{-8}	3.9×10^{-8}	BDL	BDL	1.0×10^{-8}	3.0×10^{-8}	1.0×10^{-8}	BDL	9.4×10^{-7}

*Inferred from net S burial. Assumes all buried S goes to FeS_2.

Table 2. Cultured bacterial isolates from Leg 201 sediments. Species listed are type species from GenBank database.

Closest relative (16S rRNA sequence similarity)	Numbers of isolates (lowest and highest depth of discovery)						
	Open Pacific sites			Peru margin sites			
	1231	1225	1226	1227	1228	1229	1230
				α-Proteobacteria			
Rhizobium radiobacter (98%)		7 (1 to 198 mbsf)	2 (1 to 381 mbsf)	14 (12 to 102 mbsf)		5 (12 to 70 mbsf)	13 (1 to 124 mbsf)
Rhodobacter capsulatus (95%)*							1 (268 mbsf)
Rhodovulum sulfidophilum (96%)	1 (43 mbsf)						
				Firmicutes			
Bacillus firmus (97%)	14 (2 to 43 mbsf)		12 (1 to 420 mbsf)	8 (1 to 102 mbsf)		34 (1 to 187 mbsf)	
Bacillus simplex (96%)*			1 (1 mbsf)			1 (70 mbsf)	
Alkaliphilus transvaalensis (96%)*						4 (1 mbsf)	
Paenibacillus glucanolyticus (98%)		1 (198 mbsf)					
				γ-Proteobacteria			
Vibrio mediterranei (99%)	1 (101 mbsf)				6 (1 to 114 mbsf)	11 (1 to 187 mbsf)	
Vibrio diazotrophicus (99%)*					1 (114 mbsf)		4 (1 to 82 mbsf)
Photobacterium fischeri (94%)					1 (1 mbsf)		
Psychrobacter okhotskensis (98%)							3 (1 to 124 mbsf)
Marinobacter aquaeolei (95%)							1 (268 mbsf)
Marinobacter excellens (98%)*							2 (268 mbsf)
				Actinobacteria			
Micrococcus luteus (98%)		2 (1 to 307 mbsf)	1 (381 mbsf)				
Kocuria palustris (99%)				4 (21 to 40 mbsf)			
Oerskovia paurometabola (92%)	3 (2 to 101 mbsf)			5 (40 to 55 mbsf)			
				δ-Proteobacteria			
Desulfomicrobium norvegicum (99%)*		2 (103 mbsf)					
				Bacteroidetes			
Porphyromonas endodontalis (86%)		1 (198 mbsf)					

*Species names identify the type species in the GenBank database that are the closest relatives of the cultured isolates. The genetic distance between each cultured taxon and its closest relative is illustrated by the percent similarity of their 16S rRNA sequences.

broad array of redox environments and other taxa that appear to exhibit consistent preferences for specific subseafloor environments. At least some of the former taxa are cosmopolitan in their distribution. This broad distribution is not entirely surprising, given (i) the occurrence of so many of the same metabolic products and reactants at every site, (ii) the suitability of spore-forming bacteria for broad dispersal, and (iii) the possibility that individual taxa are responsible for different activities under different subseafloor conditions (*10*).

Much remains to be learned about life in subseafloor sediments. We do not yet know which organisms (cultured or uncultured) are responsible for which metabolic activities in these sediments. We have probably not yet reached the greatest sedimentary depths that subseafloor organisms attain. Their effects on global biogeochemical cycles and their effects on mineral, chemical, and biological resources are poorly constrained. The minimum energy fluxes required to sustain them remain unknown. Their total genetic diversity, rates of population turnover, detailed metabolic interactions, and community structures remain to be determined.

References and Notes

1. R. J. Parkes, B. A. Cragg, P. Wellsbury, *Hydrogeol. Rev.* **8**, 11 (2000).
2. K.-G. Zink, H. Wilkes, U. Disko, M. Elvert, B. Horsfield, *Org. Geochem.* **34**, 755 (2003).
3. H. F. Sturt, R. E. Summons, K. J. Smith, M. Elvert, K.-U. Hinrichs, *Rapid Commun. Mass Spectrom.* **18**, 617 (2004).
4. S. D'Hondt, S. Rutherford, A. J. Spivack, *Science* **295**, 2067 (2002).
5. W. B. Whitman, D. C. Coleman, W. J. Wiebe, *Proc. Natl. Acad. Sci. U.S.A.* **95**, 6578 (1998).
6. S. D'Hondt *et al.*, *Proc. ODP Init. Rep. 201* [CD-ROM] (2003).
7. The youngest sediments are from the seafloor. The oldest sediment is from the base of the sediment column at Peru Basin site 1231; its age is estimated to be late Eocene on the basis of planktic microfossil biostratigraphy (*6*).
8. Leg 201 microbiological studies relied on samples that had very low or undetectable contamination, as assessed by our contaminant tracing tests (*17*).
9. P. N. Froelich *et al.*, *Geochim. Cosmochim. Acta* **43**, 1075 (1979).
10. K. H. Nealson, *Annu. Rev. Earth Planet. Sci.* **25**, 403 (1997).
11. B. B. Jørgensen, in *Marine Geochemistry*, H. D. Schulz, M. Zabel, Eds. (Springer-Verlag, Berlin, 2000), pp. 173–207.
12. H. D. Schulz, in *Marine Geochemistry*, H. D. Schulz, M. Zabel, Eds. (Springer-Verlag, Berlin, 2000), pp. 85–128.
13. E. Suess *et al.*, *Proc. ODP Init. Rep. 112* (1988).
14. P. A. Baker, P. M. Stout, M. Kastner, H. Elderfield, *Earth Planet. Sci. Lett.* **105**, 522 (1991).
15. T. J. Bralower *et al.*, *Proc. ODP Init. Rep. 198* [CD-ROM] (2002).
16. Traces of dissolved O_2 were detected at the top and bottom of the site 1225 and site 1231 sediment columns (*6*). These data were too few and too imprecise to use for estimating O_2 fluxes (*17*).
17. See supporting data on *Science* Online.
18. From alteration textures and chemical traces, prokaryotic life has been inferred to occur in the glassy

rinds of oceanic basalts (*21*). Fe and S in subseafloor basalts are strongly oxidized in the first 10 million to 20 million years of the basalts' existence (*22*). Oxidation of these chemical species has the potential to support abundant biomass in basaltic aquifers (*22*, *23*). Our results indicate that by 11 Ma and 35 Ma at sites 1225 and 1231, respectively, such oxidation is insufficient to strip dissolved O_2 and NO_3^- from the circulating water, perhaps because the mineral surfaces in contact with water were largely oxidized when the basalt was younger.

19. At each site, the sediment column for which fluxes were calculated spans the interval from 1.5 mbsf to a point midway between the two deepest sample depths. At the open-ocean sites, this interval ends just above the sediment-basalt contact. Given an exponential decline in average cell concentrations with depth (*1*), more than 99% of the total biomass in sediments deeper than 1.5 mbsf lies within our calculational interval at each site.
20. Two moles of C(0) (organic carbon) are oxidized by reducing one mole of SO_4^{2-} to S^{2-}. Five moles of C(0) are oxidized by reducing four moles of NO_3^- to two moles of N_2. Four moles of Fe(III), or two moles of Mn(IV), are required to oxidize one mole of C(0).
21. M. R. Fisk, S. J. Giovannoni, I. H. Thorseth, *Science* **281**, 978 (1998).
22. W. Bach, K. J. Edwards, *Geochim. Cosmochim. Acta* **67**, 3871 (2003).
23. T. Gold, *Proc. Natl. Acad. Sci. U.S.A.* **89**, 6045 (1992).
24. R. A. Jahnke, *Global Biogeochem. Cycles* **10**, 71 (1996).
25. K. B. Sørensen, A. Lauer, A. Teske, *Geobiology*, in press.
26. J. Süß, B. Engelen, H. Cypionka, H. Sass, *FEMS Microbiol. Ecol.*, in press.
27. A. Lauer, A. Teske, *Int. J. Astrobiol.* **3** (S1), 63 (2004).
28. Samples, shipboard facilities, and expedition support were provided by the ODP. The NASA Astrobiology Institute (NAI) supported postcruise analysis of biogeochemical data and precruise development of shipboard biogeochemical techniques. Postcruise culturing studies were supported by grants from the Deutsche Forschungsgemeinschaft. We thank three anonymous reviewers for very helpful comments.

Supporting Online Material
www.sciencemag.org/cgi/content/full/306/5705/2216/DC1
Materials and Methods
References

7 June 2004; accepted 15 October 2004
10.1126/science.1101155

REPORTS

Electron Coherence in a Melting Lead Monolayer

F. Baumberger,* W. Auwärter,† T. Greber, J. Osterwalder‡

We used angle-resolved photoemission spectroscopy to measure the electronic dispersion and single-particle spectral function in a liquid metal. A lead monolayer supported on a copper (111) surface was investigated as the temperature was raised through the melting transition of the film. Electron spectra and momentum distribution maps of the liquid film revealed three key features of the electronic structure of liquids: the persistence of a Fermi surface, the filling of band gaps, and the localization of the wave functions upon melting. Distinct coherence lengths for different sheets of the Fermi surface were found, indicating a strong dependence of the localization lengths on the character of the constituent atomic wave functions.

The transition from the solid to the liquid state can have substantial effects on a material's electronic properties (*1*, *2*). In the case of semiconducting germanium, for example, the forbidden states in the band gap of the crystal are filled and the melt is metallic (*3*, *4*). Understanding the evolution of the electronic wave functions, which underlie such marked changes of the physical properties, represents a prime experimental and theoretical challenge. The main conceptual issue is the lack of any long-range order in liquid or amorphous materials. The periodicity of crystalline solids allows the classification of electronic wave functions as Bloch states (i.e., plane waves, modulated by lattice periodic functions, that extend through the entire crystal). In random systems, such as amorphous solids or liquids, the crystal momentum is no longer a good quantum number and the problem becomes analytically intractable (*1*, *5*, *6*).

Despite decades of intense research, many fundamental problems of the electronic structure of liquids remain unresolved (*7*). In particular, the character of the electronic wave functions (e.g., to what extent they are itinerant or localized) has eluded experimental investigation. The primary experimental problem is the loss of periodicity, which restricts the information provided by the most important experimental probes. A diffraction experiment, which can retrieve the full three-dimensional (3D) atomic structure of a crystalline material, yields only a 1D projection in the form of a pair-correlation length in a liquid or amorphous material (*8*). Analogously, angle-resolved photoemission spectroscopy (ARPES), which gives direct access to the single-particle spectral function $A(k,\omega)$ in crystals, only measures the projection of the momentum-resolved quantity on the energy coordinate (i.e., the spectral density) in a liquid.

Recently, it has been shown in an x-ray diffraction experiment that this limitation can be overcome by working on the interface of a liquid and a crystalline material, which led to the first experimental observation of the fivefold local symmetry (*9*), predicted for monatomic 3D liquids more than 50 years ago (*10*). We use a similar idea to directly measure the electron dispersion and spectral function in a 2D liquid: melted Pb. A crystalline Cu(111) substrate serves as a support with minimal influence on the atomic arrangement of the 2D Pb liquid, and at the same time ensures that the parallel momentum of the initial Pb states is conserved in the photoemission process. In a crystalline environment, the momentum needed for photoemission is supplied in discrete quantities by reciprocal lattice vectors, whereas in a liquid, the photoelectrons gather arbitrary momenta in the process. For a liquid monolayer, however, the momentum of the initial state can be retrieved, because the proximity of the crystalline substrate allows transfer of reciprocal lattice vectors to the liquid states.

Complete momentum distribution maps of the liquid film indicate two Fermi surface sheets, and the spectral function (measured independently for both sheets) reveals novel aspects of the electronic structure of liquids. Contrary to the usual assumptions that accompany the concept of a mobility edge, we find only a negligible energy dependence of the localization length (spatial extension of an exponentially decaying wave function) but a marked momentum dependence. This is interpreted as a manifestation of the different symmetries of the constituent atomic orbitals.

The experiments were performed in a modified VG-ESCALAB 220 spectrometer (*11*) using He Iα radiation (21.22 eV). The energy and angular resolutions were set to 60 meV and ±0.4°, respectively. Pb was evaporated resistively onto a clean Cu(111) surface held

Physikinstitut der Universität Zürich, Winterthurerstrasse 190, CH-8057 Zürich, Switzerland.

*Present address: Department of Applied Physics, Stanford University, Stanford, CA 94305, USA.
†Present address: Department of Physics and Astronomy, University of British Columbia, Vancouver, British Columbia V6T1Z4, Canada.
‡To whom correspondence should be addressed. E-mail: osterwal@physik.unizh.ch

at room temperature (RT) and the coverage was calibrated by x-ray photoelectron spectroscopy and low-energy electron diffraction (LEED) (Fig. 1A). For our ARPES experiments we selected a coverage of 0.8 monolayers (ML), for which we determined a melting temperature T_m of 568 K, in agreement with earlier structural studies (*12*). The melting is demonstrated in the temperature series of LEED patterns, shown in Fig. 1, B to D. Although the six principal Cu(111) diffraction spots remain sharp for all temperatures shown, the Pb-related spots smear out strongly and anisotropically, consistent with the theory of melting for a 2D crystal (*8*, *12*–*15*). Following the analysis of (*12*) for the structure factor along the radial direction close to a Pb(1,0) spot, we obtain the values $\xi(T)$ for the pair-correlation length displayed in Fig. 1F (*16*). For temperatures well above T_m these values drop to about 5 Å, which is of the order of the in-plane lattice constant, signaling the complete melting of the Pb layer.

Before introducing the ARPES results, we briefly describe the electronic states in liquids. In a disordered 2D system, we expect localized electronic states (*1*, *5*). For such states, we can still meaningfully define a momentum as the ensemble average of the momentum expectation value (*1*, *2*). At first glance, we might expect that localized states homogeneously fill momentum space. However, it has been shown that any structure in the atomic pair-correlation length causes maxima in the momentum distribution of the electronic states, and the localized eigenstates of an infinite system are expected to form continuously dispersing bands much like those in a crystalline solid (*1*, *17*). This situation is closely related to that of quasicrystals, where a few dominant points in the densely packed reciprocal lattice, which contribute large values in the Fourier expansion of the ionic potential, cause dispersive peaks in the spectral function. The observation of such dispersive excitations in nonperiodic systems, as recently achieved in quasicrystalline AlNiCo (*18*), is a fundamental task, even though it is clearly not a proof of extended states (*19*). The crucial difference between localized and itinerant states lies in the width of $A(k,\omega)$ at a fixed energy ω_0. This width also relates directly to the transport properties of the liquid (*2*). For a noninteracting solid, $A(k,\omega_0)$ is a sharp delta-function at the energy-momentum position of the electronic band. In the case of a liquid, the spectral function is broadened even without interactions, because a localized eigenstate cannot exhibit a sharp momentum (*2*).

Photoemission Fermi surface maps from the clean substrate and the solid Pb monolayer are shown in Fig. 2, A and B. The Pb-related features—a slightly hexagonal inner Fermi level crossing at $k_{//} \approx 0.6$ Å^{-1} and the small electron pockets at the $\overline{K}$-points (*20*)—are readily identified from a comparison with the density functional calculation for a free-standing planar Pb layer (Fig. 2C) [the intense Shockley surface state on Cu(111) (*21*) is quenched by the adlayer]. The inner part of the electron pockets at $\overline{K}$ is not very distinct in this representation of the data; it can be seen more clearly in the dispersion plot (see below).

The melting transition has a strong impact on the Fermi surface features of the Pb layer (Fig. 3). In these photoemission

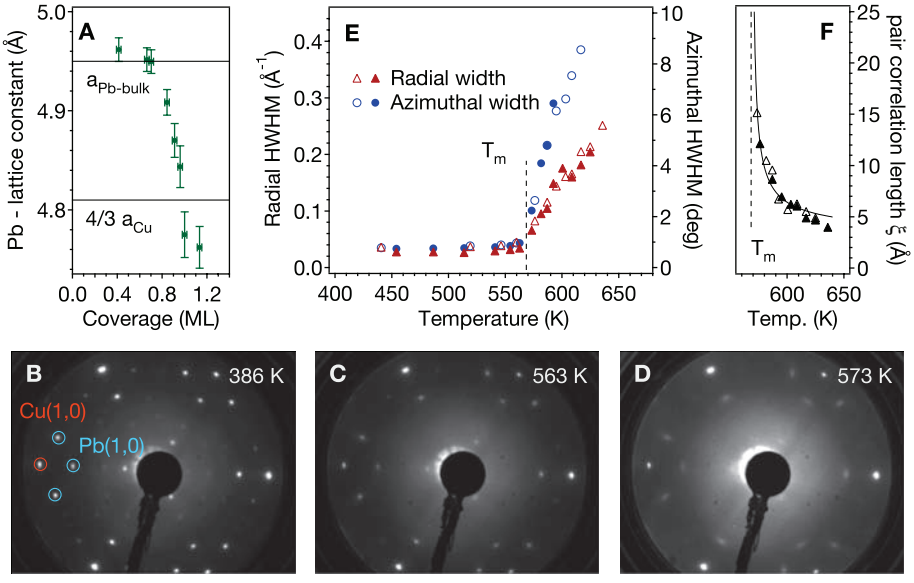

Fig. 1. Structural characterization of the melting transition. (**A**) Coverage dependence of the lattice constant of the first Pb layer on Cu(111). $a_{Pb\text{-}bulk}$ and a_{Cu} denote the respective bulk lattice constants of Pb and Cu. One monolayer (ML) of Pb is defined by the coverage of maximum compression; further Pb must grow in a second layer. (**B** to **D**) LEED patterns of a 0.8-ML film measured with an electron energy of 65 eV at temperatures above and below the melting transition. The Cu(111) principal spots show little temperature dependence, whereas the Pb-related spots smear out strongly. (**E**) Radial (triangles) and azimuthal (circles) half width at half maximum (HWHM) of a Pb(1,0) spot versus temperature. Empty and solid symbols denote measurements for increasing and decreasing temperatures, respectively. (**F**) Radial pair-correlation length ξ, calculated from the radial width of the diffraction spots, assuming a pair correlation function $\propto \exp[-|r|/\xi]$ ($r \to \infty$) (*16*). The solid line is a fit using the critical exponent of 0.37 for a 2D liquid (*14*).

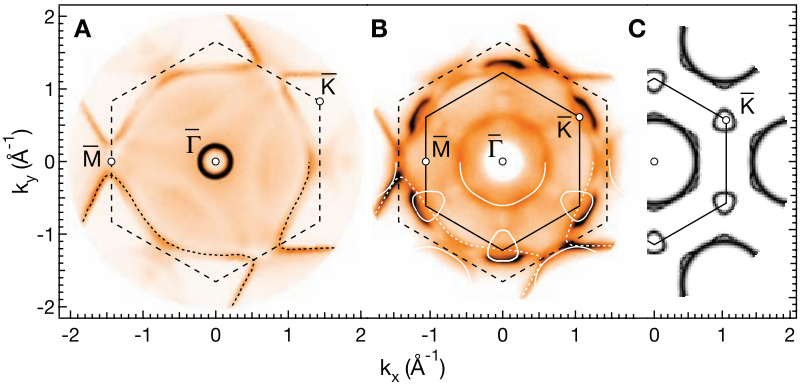

Fig. 2. Fermi surface of the solid Pb monolayer at room temperature. (**A**) Photoemission intensity at the Fermi energy from clean Cu(111), recorded for more than 10^4 emission angles and plotted as a function of the momentum component in the surface plane. The dark (i.e., high-intensity) contours represent sections through the volume Fermi surface of copper, displaying clearly the well-known *L*-point necks (*25*). The dark circle near the center of the plot is due to a free electron–like Shockley surface state (*21*). (**B**) Fermi surface map for the Cu(111) surface covered with 0.8 ML of Pb. The additional contours represent directly the 2D Fermi surface of the incommensurate, hexagonally packed Pb layer. Solid and dashed white lines trace the Pb- and Cu-related features, respectively, and serve as guides to the eye. The Brillouin zones of the incommensurate Cu (dashed) and Pb (solid) surface lattices are plotted in black. (**C**) Density functional theory calculation for a free-standing planar Pb layer, which may serve as a reference to identify the main features of the experimental Fermi surface map.

intensity maps, well-defined Cu contours are observed at all measurement temperatures and serve as a convenient reference for analyzing the Pb states in the liquid layer. Comparison of the Fermi surface in the solid phase at elevated temperature with the RT data in Fig. 2B shows that the dominant features remain unchanged, although the transition widths broaden considerably because of the increased electron-phonon interaction. However, at the melting transition (568 K) the Fermi surface topology changes radically. The electron pockets at the $\overline{K}$-points and the ring-like Fermi contour from the second Brillouin zone coalesce to form one slightly hexagonally modulated ring with $k_{//} \approx 1.4$ Å^{-1} while the inner Fermi surface in the first zone remains visible. Similar to the LEED spots, the Pb-related contours show a gradual smearing out with increasing temperature. The process is not finished at 568 K but proceeds well above T_m, reflecting the continuing decrease of the pair-correlation length. The broadening of the inner Fermi surface is much more severe, indicating a shorter coherence length for states with small momentum.

Before proceeding in the discussion of our results, we address the influence of the crystalline substrate on the spectra from the liquid Pb layer. Fig. 1A shows that the Pb layer grows incommensurate for all coverages—a rather unusual behavior that requires a very weak corrugation of the potential landscape felt by the adatoms. The absence of strong Umklapp features in the Fermi surface map in Fig. 2B indicates a similarly weak lateral coupling of the two electronic systems. Nonetheless, the Pb(1,0) spots in the LEED patterns of Fig. 1, B to D, do not coalesce fully in the azimuthal direction to form a uniform diffraction ring, in agreement with the results of (*12*). The persistence of some azimuthal modulation of the LEED intensities above T_m is likely not a manifestation of the hexatic phase of a 2D liquid (*8*) but reflects the weak (nonzero) corrugation of the substrate potential, which leads to a preferential orientational alignment of the sixfold symmetric elementary building blocks of the 2D liquid. The slight anisotropy of the Fermi surface in the liquid is a direct consequence of this remaining orientational long-range order. However, even in the solid film at elevated temperature, the electronic wave functions are only coherent over a few lattice constants. Therefore, their character can depend only on the short-range correlations, which we expect to be indistinguishable from those in an ideal 2D liquid.

The data in Fig. 4 allow a more detailed look at the electron phase coherence in the liquid film. Raw data showing the dispersion of the electronic states in the solid and liquid phase are shown in Fig. 4, A and B. In the following, we focus on the momentum profile indicated by the solid horizontal line 1.5 eV below the Fermi level, where the different states can be well separated. Three bands are observed: a broad transition from

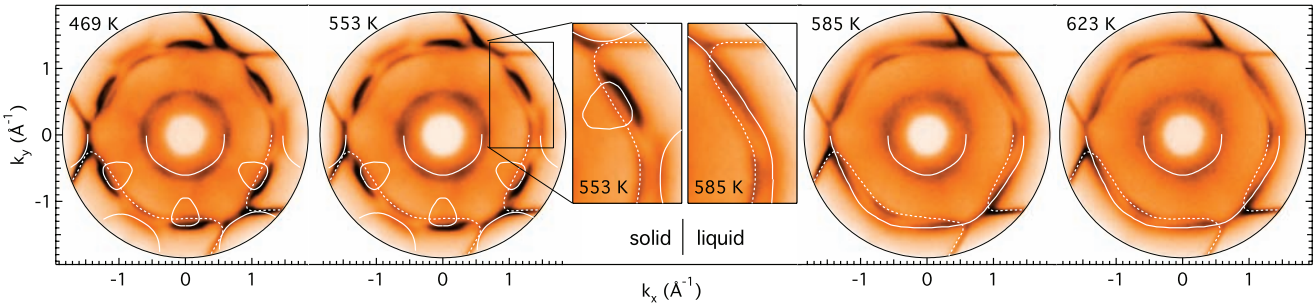

Fig. 3. Evolution of the Fermi surface through the melting transition. Shown are photoemission Fermi surface maps from a 0.8 ML Pb layer on Cu(111), measured at the temperatures indicated in the figure. Melting of the Pb layer occurs between 553 K and 585 K. Note that the copper Fermi surface contours remain sharp throughout the melting transition of the film. The dominant Pb and Cu contours are traced by the solid and dashed white lines, respectively. The inset enlarges the region where the electron pockets around the $\overline{K}$-points and the Fermi surface from the second Brillouin zone of the solid film coalesce to one large Fermi surface in the liquid.

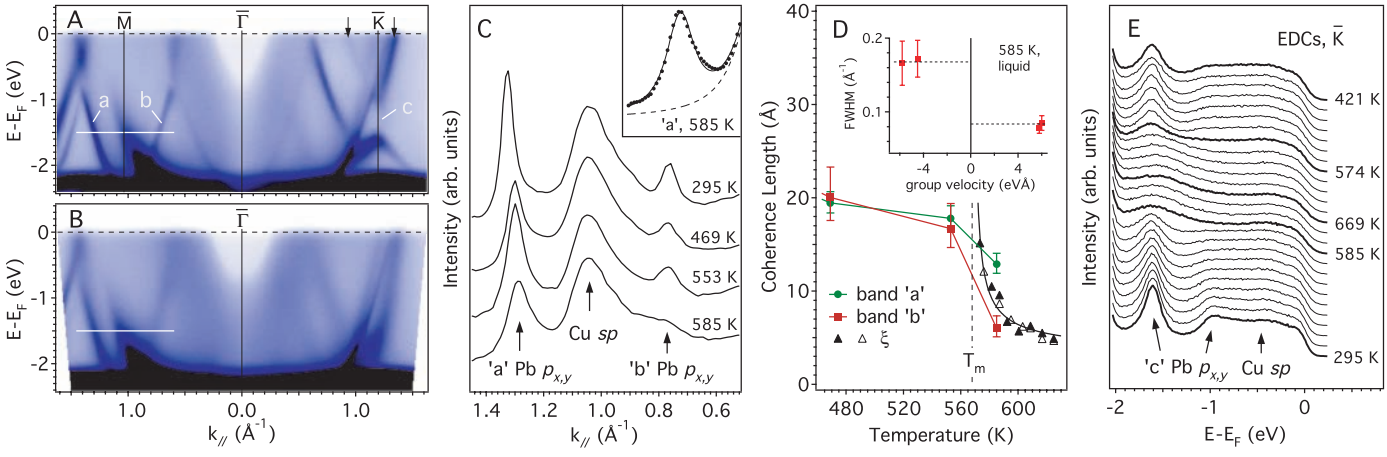

Fig. 4. Electron dispersion and spectral function in the liquid. (**A**) Band dispersion along $\overline{M}$ $\overline{\Gamma}$ $\overline{K}$ for the solid film at RT. The vertical arrows mark the Fermi level crossings of the $\overline{K}$-electron pockets. (**B**) Same as (A) for the liquid film at 585 K. (**C**) Momentum distribution curves at $E - E_F = -1.5$ eV, showing the evolution of the two Pb $p_{x,y}$ bands through the melting transition. The inset shows a Lorentzian spectral function on a smooth background fitted to the transition labeled a in the liquid film. (**D**) Coherence length of the Pb states on the inner and outer Fermi surface as a function of temperature. Error bars reflect the scatter of the results for different functional forms of the background. Also shown is the decay of the radial pair-correlation length in the liquid phase (black symbols, reproduced from Fig. 1F), fitted with the critical exponent for a 2D liquid of 0.37 (*14*). The inset demonstrates the correlation of the momentum broadening with the sign of the group velocity for various points in the band structure. (**E**) EDCs, taken at $\overline{K}$ for various temperatures, demonstrating the reversible filling and opening of a band gap at the melting temperature.

the Cu bulk *sp*-band in the center, framed by two Pb $p_{x,y}$ derived states, dispersing symmetrically around the Brillouin zone boundary of the solid film (*20*). Both Pb bands can clearly be identified in the liquid film, and the inset to Fig. 4C shows that the spectral function of the liquid layer remains to a good approximation Lorentzian (*22*, *23*). However, broadening and decay of intensity upon melting are markedly different for the two states, as is evident in the momentum distribution curves shown in Fig. 4C. The transition labeled b at $k_{//} \approx 0.8$ Å^{-1} washes out almost completely, whereas the peak a at 1.3 Å^{-1} is much less affected by the melting. Fig. 4D summarizes the behavior of $A(k,\omega_0)$ for different points in the band structure of liquid Pb. For all states, we find a clear momentum broadening at the melting transition (*24*). However, for states belonging to the outer Fermi surface, the broadening is only modest. These states therefore essentially conserve their character through the phase transition. Contrarily, states on the small Fermi surface change qualitatively from extended states in the solid film to highly localized states in the liquid. It is illustrative to convert wave numbers and peak widths for the transitions a and b to wavelengths $\lambda = 2\pi/k$ and radial coherence lengths Δk^{-1} of the photo hole wave functions. We find $\lambda = 4.8$ Å and $\Delta k^{-1} \geq 12$ Å for state a, versus $\lambda = 7.9$ Å and $\Delta k^{-1} \approx 4$ Å for state b. The latter state with longer wavelength thus exhibits supercritical damping and does not fulfill the basic condition for extended states: It may be considered fully localized (*1*). The same analysis has been carried out over the entire accessible energy range (–1.9 eV to E_F), and no marked change of the coherence length with energy was found.

A striking indication for loss of coherence can be observed at the nominal Brillouin zone boundary where the $\overline{K}$-gap around 1.5 eV binding energy disappears upon melting (feature c in Fig. 4, A and B). A set of energy distribution curves (EDCs) taken at $\overline{K}$ for various temperatures is shown in Fig. 4E. Clearly, the melting temperature represents a sharp break where the spectra change qualitatively: The two Pb-related peaks from below and above the band gap disappear, and a new very broad structure emerges close to the lower band edge. The momentum distribution of the liquid states that evolve in the band gap of the solid film is comparable to the states on the inner Fermi surface, indicating a high localization, consistent with basic models (*1*, *7*). Figure 4E also shows that the melting transition is fully reversible.

We propose that the key to the different behavior of states on the inner and outer Fermi surfaces lies in the character of the atomic wave functions that constitute the bands. Both wavelength and symmetry of the wave functions may be important. Intuitively, one might expect a higher susceptibility to disorder for states with a short wavelength (*17*), but this is opposite to the trend observed in the data. Thus, the key effect appears to be the symmetry of the constituent atomic wave functions. The band that forms the small Fermi surface exhibits a negative group velocity; that is, the band energy decreases with increasing wave vector. This is characteristic of *p*-type wave functions that change their phase at the nucleus site. In a tight-binding picture, the band minimum lies at the Brillouin zone boundary where neighboring atoms contribute to the overall wave function with opposite phases, thus maximizing the mutual overlap. In the liquid state the zone boundary no longer exists, and these states thus lose their phase reference. Bands with positive group velocity, such as those that form the outer Fermi surface in the liquid, are of even symmetry and refer their phases to the Γ point, which persists in the liquid state to serve as a phase anchor.

References and Notes

1. N. F. Mott, *Adv. Phys.* **16**, 49 (1967).
2. L. E. Ballentine, *Adv. Chem. Phys.* **31**, 263 (1975).
3. G. Kresse, J. Hafner, *Phys. Rev. B* **49**, 14251 (1994).
4. P. Oelhafen, M. G. Garnier, *J. Electron Spectrosc.* **124**, 211 (2002).
5. P. W. Anderson, *Phys. Rev.* **109**, 1492 (1958).
6. J. Hafner, M. Krajci, in *Physical Properties of Quasicrystals*, Z. M. Stadnik, Ed. (Springer, Berlin, 1999), pp. 209–256.
7. P. A. Lee, T. V. Ramakrishnan, *Rev. Mod. Phys.* **57**, 2287 (1985).
8. R. J. Birgeneau, P. M. Horn, *Science* **232**, 329 (1986).
9. H. Reichert *et al.*, *Nature* **408**, 839 (2000).
10. F. C. Frank, *Proc. R. Soc. London Ser. A* **215**, 43 (1952).
11. T. Greber *et al.*, *Rev. Sci. Instrum.* **68**, 4549 (1997).
12. B. H. Müller, Th. Schmidt, M. Henzler, *Surf. Sci.* **376**, 123 (1997).
13. J. M. Kosterlitz, D. J. Thouless, *J. Phys. C* **6**, 1181 (1973).
14. D. R. Nelson, B. J. Halperin, *Phys. Rev. B* **19**, 2457 (1979).
15. A. P. Young, *Phys. Rev. B* **19**, 1855 (1979).
16. In the vicinity of a diffraction spot, the structure factor takes the form $S(\mathbf{K}) \propto [1 + \xi^2 |\mathbf{K} - \mathbf{G}|^2]^{-3/2}$ for an asymptotic radial pair-correlation function $\propto \exp[-|r|/\xi]$ ($r \rightarrow \infty$), where **K** is the scattering vector, **G** is the reciprocal lattice vector associated with the particular LEED spot, and ξ is the temperature-dependent pair-correlation function.
17. S. F. Edwards, *Philos. Mag.* **6**, 617 (1961).
18. E. Rotenberg, W. Theis, K. Horn, P. Gilles, *Nature* **406**, 602 (2000).
19. F. Baumberger *et al.*, *Phys. Rev. Lett.* **92**, 196805 (2004).
20. F. Baumberger, A. Tamai, M. Muntwiler, T. Greber, J. Osterwalder, *Surf. Sci.* **532–535**, 82 (2003).
21. F. Reinert, G. Nicolay, S. Schmidt, D. Ehm, S. Hüfner, *Phys. Rev. B* **63**, 115415 (2001).
22. Numerical simulations for other liquid metals show rich structure in the spectral function (*23*). Currently, we cannot discern this structure in the low signal, but our data do not exclude non-Lorentzian line shapes.
23. S. K. Bose, O. Jepsen, O. K. Andersen, *Phys. Rev. B* **48**, 4265 (1993).
24. Momentum distribution curves have been fitted with a convolution of a Lorentzian and a Gaussian of 0.03 Å^{-1} full width at half maximum, which accounts approximately for the combined energy and momentum resolution.
25. P. Aebi, J. Osterwalder, R. Fasel, D. Naumovic, L. Schlapbach, *Surf. Sci.* **307–309**, 917 (1994).

26. We thank A. Seitsonen, J. Hutter, P. Zeppenfeld, K. M. Shen, N. J. C. Ingle, and Z.-X. Shen for fruitful discussions. Supported by the Swiss National Science Foundation.

12 August 2004; accepted 4 November 2004
Published online 25 November 2004;
10.1126/science.1103984
Include this information when citing this paper.

Detection of a Deep 3-μm Absorption Feature in the Spectrum of Amalthea (JV)

Naruhisa Takato,[1]* Schelte J. Bus,[2] Hiroshi Terada,[1] Tae-Soo Pyo,[1] Naoto Kobayashi[3]

Near-infrared spectra of Jupiter's small inner satellites Amalthea and Thebe are similar to those of D-type asteroids in the 0.8- to 2.5-micrometer wavelength range. A deep absorption feature is detected at 3 micrometers in the spectra of the trailing side of Amalthea, which is similar to that of the non-ice components of Callisto and can be attributed to hydrous minerals. These surface materials cannot be explained if the satellite formed at its present orbit by accreting from a circumjovian nebula. Amalthea and Thebe may be the remnants of Jupiter's inflowing building blocks that formed in the outer part or outside of the circumjovian nebula.

The jovian system has three classes of satellites: outer small satellites, large regulars (Galilean satellites), and inner small regulars. The outer small satellites were probably products of early capture from heliocentric orbits (*1*, *2*), and the Galilean satellites formed by circumjovian accretion (*1*, *3*), but the origin of the inner small satellites is still uncertain (*4*). There are four small satellites inside Io's orbit. Amalthea and Thebe are the outer two satellites among these, revolving at 2.54 and 3.11 Jupiter radii, respectively. The size of Amalthea is 270 by 165 by 150 km and that of Thebe is 116 by 98 by 84 km (*5*, *6*). Almathea and Thebe may have formed by accretion from the circumjovian nebula (*1*, *7*) because they have low-inclination ($i = 0.39°$ and 1.07°, respectively) and low-eccentricity ($e = 0.003$ and

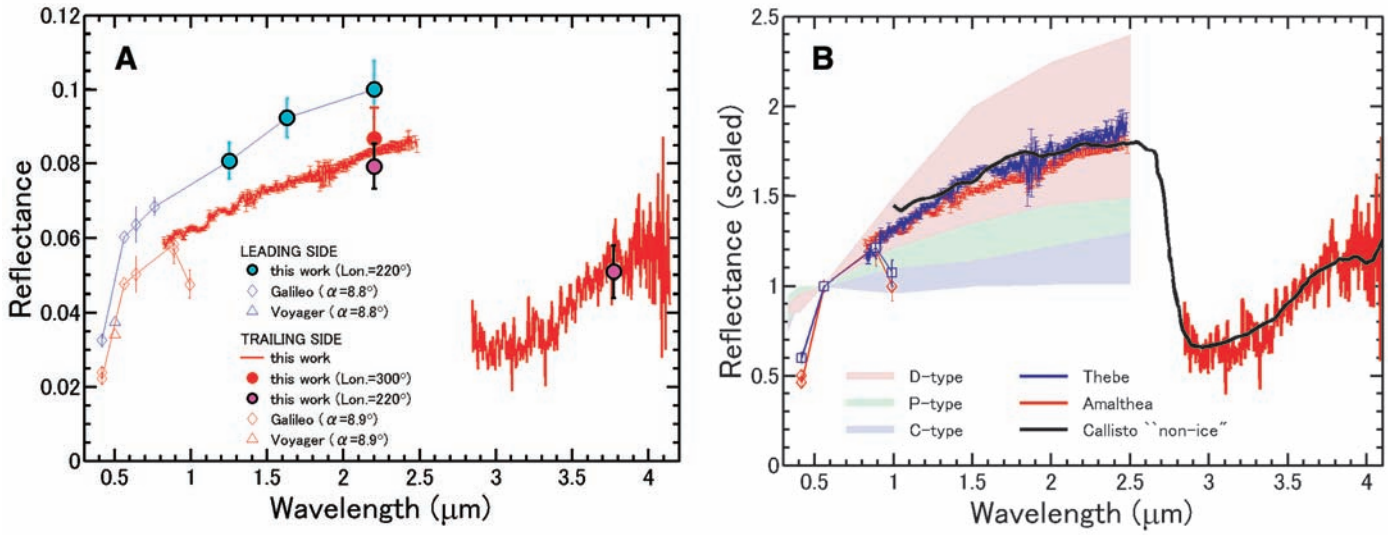

Fig. 1. (**A**) Reflectance spectra of Amalthea (JV), obtained with IRCS on Subaru Telescope and SpeX on IRTF, plotted with Voyager and Galileo reflectance data. The reflectances at *J*, *H*, *K*, and *L*′ bands are calculated from our photometric data by using the shape model for Amalthea (*13*). The spectrum of the trailing side in 0.8 to 2.5 μm is scaled to the mean *K*-band reflectance, and the spectrum in 2.8 to 4.2 μm is scaled to the *L*′-band reflectance. The error of the spectrum at 3.0 μm is about 30% (see fig. S1). The Galileo reflectance data are converted to the values at our observing phase angle (8.8° for the leading side and 8.9° for the trailing side) with the Hapke scattering model (*14*, *18*). The spectrum in 2.8 to 4.2 μm is smoothed with a Gaussian filter of 0.006 μm bandwidth. (**B**) Near-infrared spectra of the trailing side of Thebe (JXIV) and Amalthea (JV) compared with the spectra of Callisto and C-, P-, and D-type asteroids (SOM text). Open squares show Galileo's data of Thebe, and the other symbols are the same as in (A). The spectrum of Thebe obtained by our observations is scaled to match Galileo's data at 0.9 μm. The spectra of Amalthea and Thebe fit into D-type asteroids on the basis of their 0.8 to 2.5 μm spectral slopes.

0.018, respectively) orbits. Because the inner region of the circumjovian nebula was hot (>800 K), these satellites should be composed of refractory, high-density materials (*1*, *8*). However, recent gravity analysis of the Galileo spacecraft flyby of Amalthea indicates a low bulk density (<1 g cm^{-3}) (*9*), which is inconsistent with the circumjovian nebula origin and suggests that Amalthea is a captured asteroid, a scenario that is also consistent with its size, shape, and optical albedo (*5*).

Here, we report the near-infrared reflectance spectra of Amalthea and Thebe obtained by the near-infrared camera and spectrograph (IRCS) (*10*) at the Subaru Telescope and a medium-resolution spectrograph and imager (SpeX) (*11*) at the NASA Infrared Telescope Facility (IRTF) on Mauna Kea, Hawaii. Because the rotations of Amalthea and Thebe are synchronized with their revolution around Jupiter, half of each satellites' surface is always facing toward its direction of motion (leading side) and the other side is always trailing. We have obtained spectroscopic observations of the trailing side of Amalthea over the 0.8 to 4.2 μm wavelength range and of the trailing side of Thebe from 0.8 to 2.5 μm, as well as observations of solar analog stars for deducing the reflectance spectra of these satellites. We also obtained photometric measurements of Amalthea at *J* (1.25 μm), *H* (1.63 μm), and *K* (2.20 μm) bands for the leading side and at *K* and *L*′ (3.77 μm) bands for the trailing side when the Sun-Amalthea-Earth angle (phase angle) was between 8.8° and 10.0° (table S1). Scattered light from Jupiter was negligible in *K* band and longer wavelengths. In *J* and *H* bands, the scattered light cannot be ignored; thus, we removed the background by fitting a linear function to the data (*12*).

The photometric results were converted to a reflectance at each wavelength with the three-dimensional shape model of Amalthea provided by Voyager observations (*13*) to calculate the cross-sectional illuminated area visible from Earth. The reflectance spectrum of the trailing side of Amalthea from 0.8 to 2.5 μm is scaled to the mean *K*-band reflectance, and that from 2.8 to 4.2 μm is scaled to the reflectance at *L*′ band. The resulting reflectance spectra from the leading and trailing sides of Amalthea (Fig. 1A) include data from Voyager and Galileo photometry [converted to the phase angles of our observations by using the photometric model of Simonelli *et al.* (*14*)]. Our data are consistent with the Galileo measurements except for the 1.0 μm data point.

The reflectance spectra of Amalthea and Thebe both show red slopes with no distinct absorption features in the 0.8 to 2.5 μm range, closely resembling spectra of D-type asteroids over this wavelength interval (Fig. 1B). However, the spectra of D-type asteroids do not contain blue absorptions shortward of 0.6 μm like those seen in the spectra of Amalthea and Thebe. This blue absorption edge has been attributed to surface contamination by sulfur-bearing materials from Io (*4*) (SOM text).

A deep, broad absorption feature is seen at 3 μm in the spectrum for the trailing side of Amalthea. The depth of this absorption feature is 65 ± 13% of the continuum level at 2.5 μm. We confirmed this absorption feature by observing on two different nights (see fig. S1 for the discussion of the reliability of our 2.8 to 4.2 μm spectrum). This 3-μm absorption feature is an important diagnostic of the composition of Amalthea's surface. The absorption band near 3 μm indicates the hydroxyl (O–H) stretch fundamental or the first overtone of the water (H_2O) stretch modes.

Hydrous minerals exhibit absorption bands near 3 μm by structural hydroxyl or adsorbed and interlayer water. The 3-μm absorption feature and the red slope in the 0.8 to 2.5 μm range are very similar to the spectral features of non-ice components on Callisto (Fig. 1B) that are attributed to hydrous minerals (*15*). Hydrous minerals are also found in abundance in CI- and CM-class carbonaceous chondrite meteorites and the Tagish Lake meteorite, thought to be meteorite analogs of C- and D-type asteroids, respectively (*16*, *17*). The reflectance spectrum of the trailing side of Amalthea matches those of Tagish Lake and Murchison (CM2) in the 0.6 to 2.5 μm wavelength range (Fig. 2A). The 3-μm absorption band in Murchison and Ivuna (CI) matches that observed in Amalthea. These good matches

[1]Subaru Telescope, National Astronomical Observatory of Japan, 650 North Àohoku Place, Hilo, Hawaii 96720, USA. [2]Institute for Astronomy, University of Hawaii, 640 North Àohoku Place, Hilo, Hawaii 96720, USA. [3]Institute of Astronomy, Graduate School of Science, University of Tokyo, 2-21-1 Osawa, Mitaka, Tokyo 181-0015, Japan.

*To whom correspondence should be addressed. E-mail: takato@naoj.org

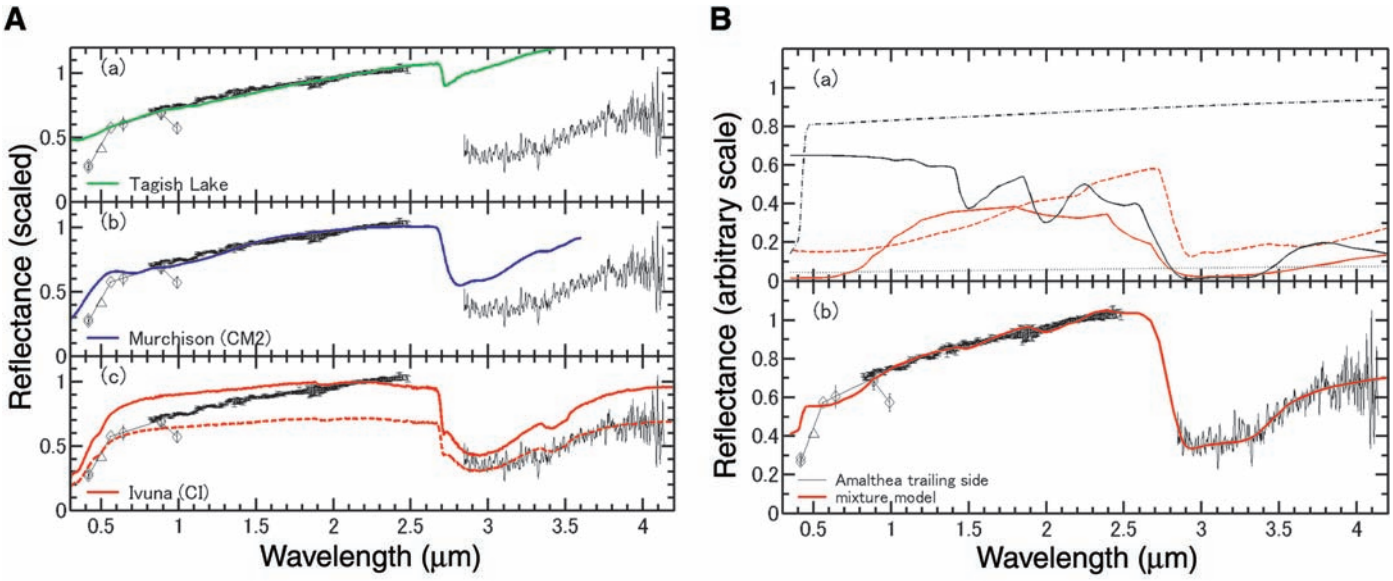

Fig. 2. (**A**) Spectral comparison of the trailing side of Amalthea (black line and symbols) with carbonaceous meteorites (a) Tagish Lake, (b) Murchison (CM2), and (c) Ivuna (CI) (shown in two different scalings) (*27*). The spectral slope in 0.6 to 2.5 μm well matches those of Tagish Lake and Murchison. Murchison has a 3-μm absorption feature that will roughly match the Amalthea spectra if the absorption is a little deeper, whereas Tagish Lake does not have the 3-μm absorption as deep as does Amalthea. Ivuna has a 3-μm absorption feature that matches the 3-μm feature of Amalthea well, although its 0.6 to 2.5 μm spectrum is flatter than Amalthea's. (**B**) An example of the model spectrum of Amalthea containing organics and water ice. (a) Reflectance spectra of Titan tholin (10 μm in diameter, solid red line) (*20*), poly-HCN (10 μm, broken red line) (*21*), water ice (10 μm, black line) (*28*), α-sulfur (10 μm, dash-dotted black line) (*29*), and graphite (20 μm, dotted black line) (*30*) calculated by using Hapke scattering theory (*18*) with the same scattering parameter as of Amalthea (*14*) at the phase angle of 8.9°. The reflectance of poly-HCN and α-sulfur are displayed 10 and 4 times enlarged, respectively, for clarity. (b) The spectrum of the trailing side of Amalthea (black lines and symbols) is compared with a model spectrum (red line) that is calculated for an intimate mixture of the five components indicated in (a).

in the 3-μm feature with Callisto non-ice components and carbonaceous chondrites strongly suggest that the surface of Amalthea contains hydrous minerals such as phyllosilicates, which are primarily responsible for the 3-μm absorption seen in CI and CM chondrite spectra (*16*). (See SOM text for a discussion on space weathering.)

Water ice is another possible candidate for producing the 3-μm absorption feature. However, water ice also has absorption bands at 1.5 μm and 2.0 μm that are not detected in our spectrum. It is difficult to reproduce the band ratios and the shape of our 3-μm feature by using mixture models of water ice and graphite and applying a Hapke scattering theory (*18*). Thus, water ice may not be the main contributor to the 3-μm feature observed in Amalthea. Because the degree of suppression of the absorption bands due to water ice depends on the albedos of other constituents and their degree of mixing (*19*), we cannot rule out the possibility of the existence of water ice as the agent for the 3-μm feature.

Organic materials have been suggested as the constituents that produce the red spectrum of the small bodies in the outer solar system, including D-type asteroids. Organic materials with red near-infrared spectra also exhibit a 3-μm absorption band due to their hydroxyl (Fig. 2B). The reflectance spectra of what is called a Titan tholin (the products of coronal discharges through a 9:1 mixture of N_2 and CH_4) (*20*) and an HCN polymer (poly-HCN) (*21*) suggest that such organic materials could be responsible for the 3-μm feature on Amalthea.

An example compound spectrum was calculated for a mixture of five components: 10 weight percent (wt %) Titan tholin (grain size diameter of 10 μm), 40 wt % poly-HCN (10 μm), 9 wt % water ice (10 μm), 12 wt % α-sulfur (10 μm), and 29 wt % graphite (20 μm). Water ice and α-sulfur are needed to match the spectral shape longward of 3.5 μm and shortward of 1.5 μm. This synthetic spectrum roughly reproduces the spectral shape of Amalthea over the interval from 0.8 to 4.0 μm. However, this model fit does not necessarily require the presence of organic materials, because the model is not unique and no characteristic absorptions of organic materials (e.g., C–H absorption band near 3.4 μm) are identified in our spectra.

Hydrous minerals or organic materials to which we ascribed the 3-μm feature are products of a low-temperature environment. Serpentine, a primary phase of hydrated silicates found in the matrix of CI and CM meteorites, cannot be formed at temperatures over ~400 K in a gas phase at 30 MPa (*8*). Similarly, most of the organic materials in the solar nebula evaporate at 600 K, with less than 1 wt % of the initial organic materials surviving at that temperature (*22*). Thus, Amalthea probably formed in a cold environment, with temperatures below ~600 K.

According to current formation models of the jovian satellites (*3*, *23*), temperatures of the circumjovian nebula at the present location of Amalthea exceeded 800 K. This model temperature is too high to form hydrous minerals or for the survival of organic materials. Therefore, our results suggest either that Amalthea formed in a cooler region of the circumjovian nebula at a greater distance than its present orbit or that it is a product of early capture from a heliocentric (asteroidal) orbit.

A possible scenario is that Amalthea, and possibly Thebe and two other inner satellites, Metis (JXVI) and Adrastea (JXV), were satellite embryos that formed near Callisto and then migrated into the inner region. Because the temperature of the circumjovian subnebula near Callisto was too cold for hydration, accretion or tidal heating may have occurred on Amalthea.

Another possibility is that Amalthea is a captured planetesimal. Most of the asteroids with heliocentric distances near Jupiter are D-types (*24*). Thus, it is likely that planetesimals with the same origins as D-type asteroids were captured into the early jovian system and spiraled inward under gas drag (*7*). Amalthea and the other three satellites can be the remnants of these planetesimals. Although most D-type asteroids do not show a 3-μm absorption feature (*25*), water ice is thought to have been a constituent of these asteroids, at least in their early history (*26*). Tidal heating might enhance the hydration of

Amalthea during the capturing process into the jovian system.

References and Notes

1. J. B. Pollack, F. Fanale, in *Satellites of Jupiter*, D. Morrison, Ed. (Univ. of Arizona Press, Tucson, 1982), pp. 872–910.
2. S. A. Astakhov, A. D. Burbanks, S. Wiggins, D. Farrelly, *Nature* **423**, 264 (2003).
3. R. M. Canup, W. R. Ward, *Astron. J.* **124**, 3404 (2002).
4. J. Gradie, P. Thomas, J. Veverka, *Icarus* **44**, 373 (1980).
5. J. Veverka *et al.*, *J. Geophys. Res.* **86**, 8675 (1981).
6. P. C. Thomas *et al.*, *Icarus* **135**, 360 (1998).
7. S. Peale, *Annu. Rev. Astron. Astrophys.* **37**, 533 (1999).
8. R. G. Prinn, M. Fegley Jr., in *Origin and Evolution of Planetary and Satellite Atmospheres*, S. K. Atreya, J. B. Pollack, M. S. Matthews, Eds. (Univ. of Arizona Press, Tucson, 1989), pp. 78–136.
9. J. D. Anderson *et al.*, American Geophysical Union Meeting, San Francisco, CA, 6 to 10 December 2002, P12C-13, pp. 3–4.
10. N. Kobayashi *et al.*, *Proc. SPIE* **4008**, 1056 (2000).
11. J. T. Rayner *et al.*, *Publ. Astron. Soc. Pac.* **115**, 362 (2003).
12. The intensity of the scattered light from Jupiter was about five times that of the background sky level and was 20% of the peak intensity of the object in *J* band. It was about half of the background and 10% of the peak intensity of the object in *H* band. A linear function was fitted to the scattered light, which was thus subtracted from the background. The errors of the photometry include the possible incompleteness of the removal of scattered light.
13. P. J. Stooke, *Earth Moon Planets* **56**, 123 (1992).
14. D. P. Simonelli *et al.*, *Icarus* **147**, 353 (2000).
15. T. B. McCord *et al.*, *J. Geophys. Res.* **103**, 8603 (1998).
16. L. A. Lebofsky, T. D. Jones, F. Herbert, in *Origin and Evolution of Planetary and Satellite Atmospheres*, S. K. Atreya, J. B. Pollack, M. S. Matthews, Eds. (Univ. of Arizona Press, Tucson, 1989), pp. 192–229.
17. T. Hiroi, M. E. Zolensky, C. M. Pieters, *Science* **293**, 2234 (2001).
18. B. Hapke, *Theory of Reflectance and Emittance Spectroscopy* (Cambridge Univ. Press, Cambridge, 1993).
19. R. N. Clark, P. G. Lucey, *J. Geophys. Res.* **89**, 6341 (1984).
20. B. N. Khare, C. Sagan, *Icarus* **60**, 127 (1984).
21. B. N. Khare *et al.*, *Can. J. Chem.* **72**, 678 (1994).
22. H. Nakano, A. Kouchi, S. Tachibana, A. Tsuchiyama, *Astrophys. J.* **592**, 1252 (2003).
23. R. N. Prinn, B. Fegley, *Astrophys. J.* **249**, 308 (1981).
24. J. Gradie, E. Tedesco, *Science* **216**, 1405 (1982).
25. J. P. Emery, R. H. Brown, *Icarus* **164**, 104 (2003).
26. A. S. Rivkin, E. S. Howell, F. Vilas, L. A. Lebofsky, in *Asteroids III*, W. F. Bottke Jr., A. Cellino, P. Paolicchi, R. P. Binzel, Eds. (Univ. of Arizona Press, Tucson, 2002), pp. 235–253.
27. Reflectance Experiment Laboratory (RELAB) database, www.planetary.brown.edu/relab/index.html.
28. S. G. Warren, *Appl. Opt.* **23**, 1206 (1984).
29. K. A. Fuller, H. D. Downing, M. R. Querry, in *Handbook of Optical Constants of Solids III*, E. D. Palik, Ed. (Academic Press, San Diego, 1998), pp. 899–922.
30. B. T. Draine, *Astrophys. J. Suppl. Ser.* **57**, 587 (1985).

31. We thank the Subaru adaptive optics team, the IRCS team, and M. Goto, who made the observations possible. This report is partly based on data collected at Subaru Telescope, which is operated by the National Astronomical Observatory of Japan.

Supporting Online Material

www.sciencemag.org/cgi/content/full/306/5705/2224/DC1
SOM Text
Figs. S1 and S2
Table S1
References

20 September 2004; accepted 22 November 2004
10.1126/science.1105427

First-Principles Theory for the $H + CH_4 \rightarrow H_2 + CH_3$ Reaction

Tao Wu,[1]* Hans-Joachim Werner,[2] Uwe Manthe[3,1]†

A full-dimensional quantum dynamics simulation of a hydrogen atom reacting with methane on an accurate ab initio potential energy surface is reported. Based on first-principles theory, thermal rate constants are predicted with an accuracy comparable to (or even exceeding) experimental precision. The theoretical prediction is within the range of the significantly varied experimental rate constants reported by different groups. This level of accuracy has previously been achieved only for smaller, three- or four-atom reactive systems. Comparison with classical transition state theory confirms the importance of quantum mechanical tunneling for the rate constant below 400 kelvin.

The quantitatively accurate theoretical description of chemical reactions has so far been restricted to gas-phase systems including up to four atoms (*1*, *2*). Most investigations view the reaction as a scattering process and calculate quantum state–resolved cross sections. However, recent work (*3*–*5*) suggests that thermal rate constants [$k(T)$'s] could be calculated accurately for larger systems if scattering calculations are avoided and a rigorous quantum dynamical description based on a transition state concept is employed instead.

Applied interest in accurate $k(T)$'s has become an important additional incentive for theory. Many relevant reactions in atmospheric and combustion chemistry involve only a moderate number of atoms, and $k(T)$'s are crucial to model these reaction chains. However, the measured rate constants reported by different groups or obtained by different techniques often vary significantly. At atmospherically relevant temperatures (below 300 K), only limited experimental data are available (*6*, *7*), and many rate constants must be extrapolated from high-temperature data. Moreover, for some reactions, the rate constants can be determined only from indirect experimental evidence or based on analogy. Thus, a theory that predicts $k(T)$'s accurately from first principles would be a valuable supplement.

Quantitative descriptions of chemical reactions require two steps: construction of accurate multidimensional potential energy surfaces (PESs) and accurate quantum dynamics simulations on these PESs. During the past decade, accurate quantum dynamics calculations for triatomic system have been almost routine. The first accurate calculations for a tetraatomic reaction, $H_2 + OH \rightarrow H + H_2O$ (*8*–*10*), appeared 10 years ago and many have followed. Progressing toward larger systems, the six-atom reaction

$$H + CH_4 \rightarrow H_2 + CH_3 \qquad (1)$$

has been a benchmark system for developments in the past several years (*5*, *11*–*20*). Recently, accurate quantum dynamics calculations (*3*, *5*) could be performed for this reaction. This leap from four-atom reactions to six-atom reactions (that is, from 6-dimensional to 12-dimensional quantum dynamics) was made possible by efficient schemes for multidimensional wave-packet propagations (*21*, *22*) and direct reaction rate calculations (*5*, *23*, *24*).

To achieve an accurate description of polyatomic chemical reactions, these developments in quantum dynamics techniques must be matched by a similarly accurate knowledge of the underlying PESs. However, accurate ab initio PESs are rarely available for systems including more than three or four atoms. The quantum dynamics calculations for the $H + CH_4 \rightarrow H_2 + CH_3$ reaction discussed above, for example, used a semi-empirical PES introduced by Jordan and Gilbert (JG PES) (*25*). Because the reaction barrier of the JG PES is significantly smaller than barriers obtained by recent high-level ab initio results, the JG PES could be expected to yield $k(T)$'s significantly larger than those produced by experiment (*12*). Consequently, the $k(T)$'s obtained from converged full-dimensional quantum dynamics calculations (*3*, *5*, *26*) did not agree well with experiment. However, several approximate quantum dynamics calculations using the JG PES could be validated by comparison with these benchmark results. Transition state theory calculations including tunneling corrections by Truhlar and co-workers (*17*, *18*), as well as different reduced dimensional

[1]Theoretische Chemie, Technische Universität München, Lichtenbergstrasse 4, 85747 Garching, Germany. [2]Institut für Theoretische Chemie, Universität Stuttgart, Pfaffenwaldring 55, 70569 Stuttgart, Germany. [3]Theoretische Chemie, Fakultät für Chemie, Universität Bielefeld, Postfach 100131, 33501 Bielefeld, Germany.

*Present address: Department of Chemistry, Zhejiang University, Hangzhou, 310027, China.
†To whom correspondence should be addressed. E-mail: uwe.manthe@uni-bielefeld.de

quantum dynamics studies from several groups (*11*, *12*, *14*), found good or reasonable agreement for $k(T)$. In contrast, reduced dimensional quantum dynamics calculations of Zhang, Zhang, and co-workers (*13*, *16*), which estimated $k(T)$ from an initial state-selected rate, yielded significantly lower rate constants. Their $k(T)$ values were even smaller than classical transition state theory rates, which is an unexpected result for a direct reaction with hydrogen transfer.

Because of the shortcomings of the JG PES, obtaining an accurate PES for the H + CH_4 reactions seemed desirable. However, the number of dimensions is a substantial problem for the construction of an accurate PES for any polyatomic reaction. Recently, Shepard interpolation (*27*, *28*) of high-level ab initio quantum chemistry data yielded progress in the construction of accurate multidimensional PESs (*1*). The results were combined with quantum dynamics simulations to accurately describe the benchmark tetraatomic reaction $H_2 + OH \rightarrow H + H_2O$ (*1*).

This report presents results for $k(T)$ of the $H + CH_4 \rightarrow H_2 + CH_3$ reaction, thus extending the range of accurate first-principles theory beyond tetraatomic reactions. A high-level ab initio PES was calculated, and quantum dynamics simulations on this new PES were performed. We briefly describe the methods used to obtain this description of the $H + CH_4 \rightarrow H_2 + CH_3$ reaction. The accuracy of the computed $k(T)$'s is estimated from theoretical arguments and compared with available experimental data. The results suggest that the $k(T)$'s predicted by first-principles theory are of comparable accuracy to available experimental data if not more accurate.

The present PES was constructed as an interpolation of high-level ab initio quantum chemistry data. Coupled cluster calculations [partially spin-restricted CCSD(T) (*29*–*31*)] with correlation-consistent basis sets [aug-cc-pVQZ (*32*) and cc-pVTZ (*33*)] were used. Correlation energies computed with the cc-pVTZ basis were scaled with a factor of 1.02 to match the aug-cc-pVQZ results. Calculations for different geometries showed that the scaling factor was approximately geometry-independent. The basis set dependence of energies on the reaction path was found to be small, and the resulting error caused by the basis set was estimated to be below 0.1 kcal/mol. At each geometry required for the interpolation, electronic energies, gradients, and all second derivatives were computed at this level of theory (using finite differences for the derivatives). The potential barrier of the $H + CH_4 \rightarrow H_2 + CH_3$ reaction obtained by the calculations is 14.93 kcal/mol.

To construct a PES based on these quantum chemical calculations, the Shepard interpolation approach (*27*, *28*) was used. The location of the reference points in the interpolation was chosen by a scheme specifically designed to construct PESs for reaction rate calculations (*34*). The scheme focuses on an accurate description of the PES in the vicinity of the reaction barrier. Interpolation points are added until converged results for the computed $k(T)$'s and cumulative reaction probabilities are obtained. A data set including electronic energies, gradients, and all second derivatives at 48 geometries was used in the present calculation (a Fortran subroutine providing this PES is available). The resulting error of the computed $k(T)$ due to interpolation inaccuracies is below 20%.

An accurate quantum dynamics calculation on the 12-dimensional PES for total angular momentum $J = 0$ was performed using the multiconfigurational time-dependent Hartree approach and flux correlation functions (*5*). Similar numerical parameters as in the previous calculations (*3*) on the semi-empirical JG PES have been required to achieve convergence. The J-shifting scheme (*35*) has been used to describe the effect of rotational motion on $k(T)$. Because the transition state of the reaction is rigid and its three principal moments of inertia are of significant size, errors in $k(T)$ resulting from J-shifting are expected to be only a few percent. Convergence studies have shown that the errors in $k(T)$ resulting from the quantum dynamics simulation are below about 10%.

The calculated $k(T)$'s for the $H + CH_4 \rightarrow H_2 + CH_3$ reaction (Fig. 1, solid line) are compared with experimental results from different groups (*36*, *37*) (Fig. 1A, symbols) in an Arrhenius plot. To give a pictorial impression of the estimated accuracy of the calculated rate constants, the size of the symbols displayed has been chosen to correspond to a relative error in $k(T)$ of 20%. The variation among the experimental data obtained by different groups significantly exceeds the estimated error margin of the theoretical results. At temperatures below 348 K, no experimental data are available. Only the present theoretical prediction provides $k(T)$'s at low temperatures. However, we hope that this theoretical work will challenge experimentalists to accurately measure $k(T)$'s at low temperatures and thus facilitate a detailed comparison between theory and experiment.

Sutherland *et al*. (*38*) recently recommended $k(T)$ values based on an analysis of measured rate constants in an extended temperature interval (Fig. 1, dashed line). In the temperature range from 348 to 500 K shown in Fig. 1A, these recommended

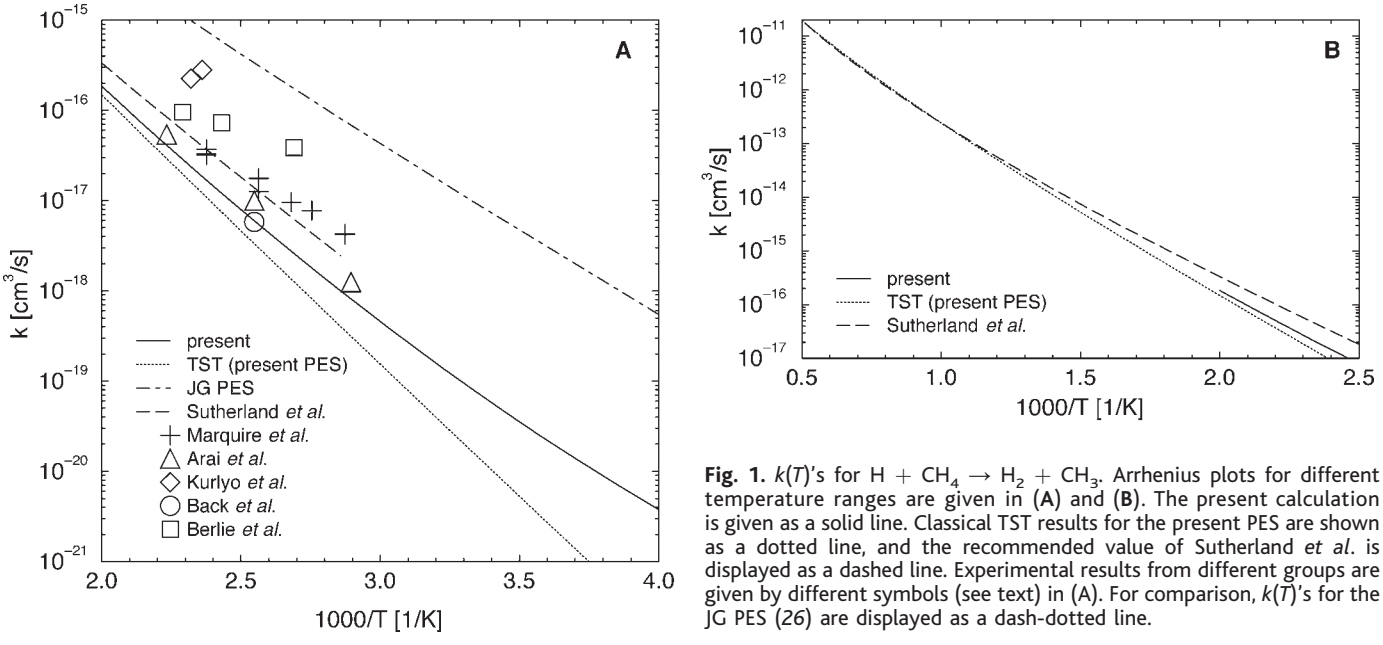

Fig. 1. $k(T)$'s for $H + CH_4 \rightarrow H_2 + CH_3$. Arrhenius plots for different temperature ranges are given in (**A**) and (**B**). The present calculation is given as a solid line. Classical TST results for the present PES are shown as a dotted line, and the recommended value of Sutherland *et al*. is displayed as a dashed line. Experimental results from different groups are given by different symbols (see text) in (A). For comparison, $k(T)$'s for the JG PES (*26*) are displayed as a dash-dotted line.

values exceed the theoretically predicted rate constants by a factor of about 2. Because Sutherland *et al*. based their recommendation in the low-temperature regime on the most recent experimental data obtained by Marquire *et al*. (*36*), this difference results from the difference between the present calculations and the experiments of Marquire *et al*.

The importance of the tunneling effect can be investigated by a comparison of the quantum mechanical calculations to classical transition-state theory (TST). At higher temperatures, 400 to 500 K, the difference between the TST results calculated from the present PES (Fig. 1, dotted line) and the quantum results is small, and thus tunneling is not particularly important. However, the TST results are significantly smaller than the quantum dynamics results at lower temperatures. The classical TST underestimates the thermal rate constant by a factor of 5 at room temperature and by a factor of 500 at 250 K. This discrepancy demonstrates the importance of tunneling at lower temperatures.

Because TST is reasonably accurate at higher temperatures, TST results obtained from the present PES can be used to predict $k(T)$'s at temperatures above 500 K, where presently no quantum dynamics results are available. Figure 1B shows rate constant results in an extended temperature interval ranging up to 2000 K. At high temperatures, the TST results for the present PES agree well with the experimentally recommended values of Sutherland *et al*. Given the uncertainties in the low-temperature experimental values (Fig. 1A), the comparison between the theoretical and experimental results in this extended temperature interval (Fig. 1B) might be considered more reliable. At high temperatures, quantum effects are negligible and $k(T)$ is determined mainly by the barrier height, so the agreement here between theory and experiment reflects the accuracy of the computed barrier height.

Finally, the rate constants obtained for the present PES are compared with quantum dynamics results calculated previously (*26*) for the JG PES (Fig. 1A, dash-dotted line). The shortcomings of the JG PES are obvious: $k(T)$ is overestimated by more than an order of magnitude. The difference is mainly due to the difference in the barrier heights: The JG PES shows a potential barrier of 10.9 kcal/mol, which is 4 kcal/mol smaller than the barrier height of the present PES.

References and Notes

1. D. H. Zhang, M. A. Collins, S.-Y. Lee, *Science* **290**, 961 (2000).
2. D. C. Clary, *Science* **279**, 1879 (1998).
3. F. Huarte-Larranaga, U. Manthe, *J. Chem. Phys.* **113**, 5115 (2000).
4. F. Huarte-Larranaga, U. Manthe, *J. Chem. Phys.* **117**, 4635 (2002).
5. U. Manthe, *J. Theor. Comp. Chem.* **1**, 153 (2002).
6. W. B. DeMore *et al.*, *Evaluation No. 12, JPL Publication 97-4* (Jet Propulsion Laboratory, Pasadena, CA, 1997), chapter on chemical kinetic and photochemical data for use in stratospheric modelling.
7. S. P. Snader *et al.*, *Chemical Kinetics and Photochemical Data for Use in Atmospheric Studies, Evaluation No. 14* (Jet Propulsion Laboratory, Pasadena, CA, 2003).
8. U. Manthe, T. Seideman, W. H. Miller, *J. Chem. Phys.* **99**, 10078 (1993).
9. D. Neuhauser, *J. Chem. Phys.* **100**, 9272 (1994).
10. D. H. Zhang, J. Z. H. Zhang, *J. Chem. Phys.* **101**, 1146 (1994).
11. T. Takayanagi, *J. Chem. Phys.* **104**, 2237 (1996).
12. H.-G. Yu, G. Nyman, *J. Chem. Phys.* **111**, 3508 (1999).
13. M. Wang, Y. Li, J. Zhang, D. Zhang, *J. Chem. Phys.* **113**, 1802 (2000).
14. D. Wang, J. Bowman, *J. Chem. Phys.* **115**, 2055 (2001).
15. J. Palma, J. Echave, D. C. Clary, *J. Phys. Chem. A* **106**, 8256 (2002).
16. M. Yang, D. H. Zhang, S.-Y. Lee, *J. Chem. Phys.* **117**, 9539 (2002).
17. J. Pu, J. Corchado, D. Truhlar, *J. Chem. Phys.* **115**, 6266 (2001).
18. J. Pu, D. Truhlar, *J. Chem. Phys.* **117**, 1479 (2002).
19. B. Kerkeni, D. C. Clary, *J. Chem. Phys.* **120**, 2308 (2004).
20. Y. Zhao, T. Yamamoto, W. H. Miller, *J. Chem. Phys.* **120**, 3100 (2004).
21. H.-D. Meyer, U. Manthe, L. S. Cederbaum, *Chem. Phys. Lett.* **165**, 73 (1990).
22. U. Manthe, H.-D. Meyer, L. S. Cederbaum, *J. Chem. Phys.* **97**, 3199 (1992).
23. W. H. Miller, *J. Chem. Phys.* **61**, 1823 (1974).
24. W. H. Miller, S. D. Schwartz, J. W. Tromp, *J. Chem. Phys.* **79**, 4889 (1983).
25. M. Jordan, R. Gilbert, *J. Chem. Phys.* **102**, 5669 (1995).
26. J. M. Bowman, D. Wang, X. Huang, F. Huarte-Larranaga, U. Manthe, *J. Chem. Phys.* **114**, 9683 (2001).
27. M. J. T. Jordan, K. C. Thompson, M. A. Collins, *J. Chem. Phys.* **102**, 5647 (1995).
28. K. C. Thompson, M. J. T. Jordan, M. A. Collins, *J. Chem. Phys.* **108**, 8302 (1998).
29. P. J. Knowles, C. Hampel, H.-J. Werner, *J. Chem. Phys.* **99**, 5219 (1993).
30. P. J. Knowles, C. Hampel, H.-J. Werner, *J. Chem. Phys.* **112**, 3106 (2000).
31. M. J. O. Deegan, P. J. Knowles, *Chem. Phys. Lett.* **227**, 321 (1994).
32. R. A. Kendall, T. H. Dunning Jr., R. H. Harrison, *J. Chem. Phys.* **96**, 6796 (1992).
33. T. H. Dunning Jr., *J. Chem. Phys.* **90**, 1007 (1989).
34. T. Wu, U. Manthe, *J. Chem. Phys.* **119**, 14 (2003).
35. J. M. Bowman, *J. Chem. Phys.* **95**, 4960 (1991).
36. P.-M. Marquire, A. G. Dastidar, K. C. Manthorne, P. D. Pacey, *Can. J. Chem.* **72**, 600 (1994).
37. D. Baulch *et al.*, *J. Chem. Phys. Ref. Data* **21**, 411 (1992).
38. J. W. Sutherland, M.-C. Su, J. V. Michael, *Int. J. Chem. Kinet.* **33**, 669 (2001).

39. Financial support was provided by the Deutsche Forschungsgemeinschaft (Projekt Quantenmechanische Beschreibung der Dynamik elementarer Reaktionsprozesse); the European Commission through the RTN program (HPRN-CT-1999-00007); and the Fond der Chemischen Industrie, which is gratefully acknowledged. We thank F. Huarte-Larrañaga for valuable discussions.

16 August 2004; accepted 19 November 2004
10.1126/science.1104085

Reduced Competition and Altered Feeding Behavior Among Marine Snails After a Mass Extinction

Gregory P. Dietl,[1]*† Gregory S. Herbert,[2]*‡ Geerat J. Vermeij[2]

Extinction may alter competitive interactions among surviving species, affecting their subsequent recovery and evolution, but these processes remain poorly understood. Analysis of predation traces produced by shell-drilling muricid snails on bivalve prey reveals that species interactions were substantially different before and after a Plio-Pleistocene mass extinction in the western Atlantic. Muricids edge- and wall-drilled their prey in the Pliocene, but Pleistocene and Recent snails attacked prey only through the shell wall. Experiments with living animals suggest that intense competition induces muricid snails to attack shell edges. Pliocene predators, therefore, probably competed for resources more intensely than their post-extinction counterparts.

Marine communities of the western Atlantic region experienced a regional mass extinction event at the end of the Pliocene that resulted in the loss of roughly 70% of species (*1*–*5*). Despite the magnitude of this event, there was little, if any, long-term diversity decline, suggesting that recovery was rapid (*2*–*4*). History reconstructed on the basis of taxonomic diversity alone, however, overlooks the fact that many ecologically important taxonomic groups were lost (*6*, *7*), restricted to refugia (*8*–*10*), or remain to this day locally depauperate (*5*, *11*). Because the types of species and their relative abundances affect the structure of the communities they build (*12*), understanding the nature of such ecological losses is critical for a full characterization of recovery from extinction.

Here we combine behavioral experiments with a modern predator-prey system with an analysis of its paleontological counterpart in the Plio-Pleistocene fossil record of Florida to investigate the effects of extinction on the intensity of competition among and within surviving predatory lineages. We use the term "competition" in its broadest sense to mean the effect of enemies on the ability of indi-

[1]Center for Marine Science, University of North Carolina, Wilmington, NC 28409, USA. [2]Department of Geology and Center for Population Biology, University of California, Davis, CA 95616, USA.

*These authors contributed equally to this work.
†Present address: Department of Geology and Geophysics, Yale University, New Haven, CT, 06520, USA.
‡Present address: Department of Geology, University of South Florida, Tampa, FL 33620, USA.

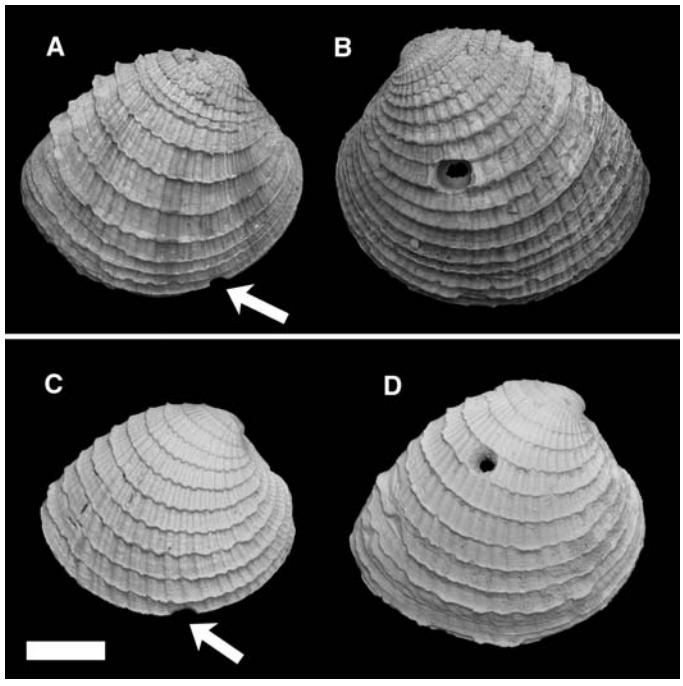

Fig. 1. Examples of drilling predation. (**A** and **B**) Edge- and wall-drilling traces of *C. dilectus* preying on *Chione elevata* under experimental lab conditions. (**C**) Edge-drilling trace; Pinecrest Beds, middle Pliocene. (**D**) Wall-drilling trace; Caloosahatchee Formation, late Pliocene. Scale bar, 1 cm.

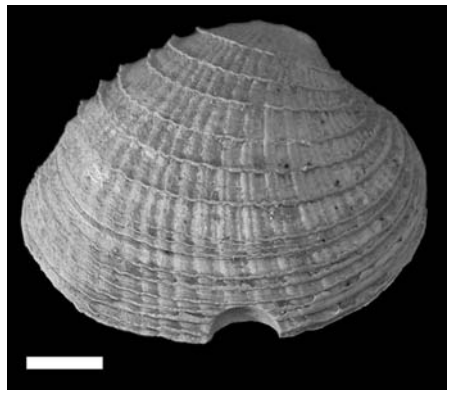

Fig. 3. Close-up view of a fossil edge-drilling trace; lower Pinecrest Beds, middle Pliocene, UF95903. Scale bar, 5 mm.

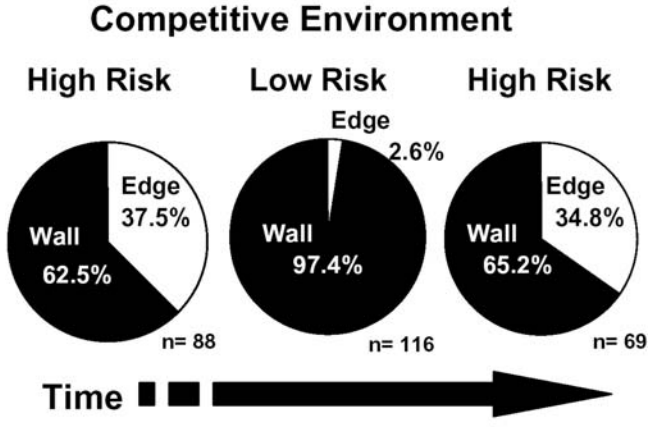

Fig. 2. Influence of high- and low-risk competitive environments on drilling behavior. Data from all experimental replicates were pooled because the purpose of this analysis was solely to examine the influence of the presence of competitors on drilling mode. There was no significant difference between the two high-risk treatments (Pearson chi-square test, $X^2 = 0.12$, $P = 0.7252$). When data from the high-risk treatments are pooled together and compared with the low-risk treatment, a Pearson chi-square test indicates that edge-drilling behavior is associated with the presence of competitors ($X^2 = 44.2$, $P < 0.0001$).

viduals to acquire and retain locally limiting resources. These enemies include animals that steal food from, prey on, interfere with, or take up resources faster than their victims.

In seagrass habitats of the northeastern Gulf of Mexico, the muricid gastropods *Chicoreus dilectus* and *Phyllonotus pomum* feed on their bivalve prey *Chione elevata* by slowly drilling a hole through the wall of the clam's shell (*13*) (Fig. 1, B and D). Wall-drilling often takes up to a week (*14*). During this time, snails are susceptible to losing their prey to kleptoparasites, especially other gastropods (*13*, *15*, *16*), as well as being eaten themselves (by fishes, crabs, and gastropods). By drilling the prey at the thin valve edge (Fig. 1, A and C) rather than through the thicker shell wall, snails reduce their predation time by a factor of 3 (*14*). The decreased risk of losing their food or their life will be most important when enemies are abundant and competition is intense (*17*, *18*). Edge drilling entails risks as well, because the feeding organ (proboscis) may be amputated when the prey closes its valves on the drilling snail (*19*, *20*). Edge drilling should therefore be avoided when competition and the risk of theft or predation are reduced.

To test how the presence of enemies influences shell-drilling behavior, we simulated high- and low-risk competitive environments for drilling snails (*21*). When we grouped *Chicoreus* together, individuals attacked their *Chione* prey at the shell edge 37.5% of the time ($n = 88$ attacks) (Fig. 2). When separated, however, snails abandoned the more rapid edge-attack behavior (2.6% of attacks, $n = 116$) (Fig. 2) (*22*). In a final experiment, when we reintroduced the same snails to highly competitive conditions, they again attacked at the shell edge (34.8% of attacks, $n = 69$) (Fig. 2) (*23*). These experiments confirm that edge drilling is used only when the risks of competition are high, whereas wall drilling is used when these risks are low. We suspect that the shift in behavior is a general response to enemies, including predators, although our experiments cannot address this possibility.

Post-extinction ecological changes in seagrass community structure, linked to long-term oceanographic changes and productivity decline after the final closure of the Central American Seaway (*24*, *25*), included a decline in the abundance of predatory gastropods (*11*). Pleistocene predators also may have been less powerful than their Pliocene counterparts (*17*). Such changes should have affected the intensity of competition in the broad sense among survivors of the extinction. Fewer and possibly weaker Pleistocene predators likely meant that *Chicoreus* and *Phyllonotus* interacted less often with enemies that threatened their lives or their capacity to retain food resources than they did during the Pliocene.

To test this hypothesis, we counted all *Chicoreus* and *Phyllonotus* edge- and wall-drilling traces in samples of *Chione* ranging from the early Pliocene to the Recent. Our analysis included 11,429 valves of *Chione* from Plio-Pleistocene shell beds of Florida and 5328 valves from 10 modern seagrass habitats along the west and northwest coasts of Florida. No other known predators could have produced the drill holes in Pliocene to Recent *Chione* valves (supporting online text).

In support of the hypothesis that competition intensity among predatory gastropods decreased after the Pliocene, we found that edge drilling accounted for 5.7% (50 out of 881) of the total number of complete drill holes we identified in mid- to late Pliocene *Chione* (Figs. 3 and 4). In one Pliocene-age sample, 4 of 17 complete holes were edge-drilled. In all, edge drilling was present in 15 of the 23 (65.2%) Pliocene samples. In striking contrast, none of the *Chione* from the early Pleistocene, middle Pleistocene, or Recent showed

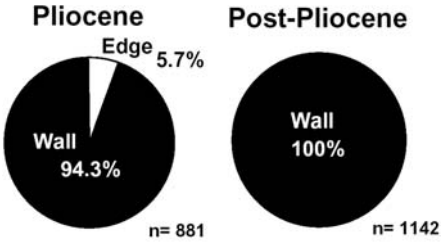

Fig. 4. Proportion of edge- and wall-drilling traces by time interval. A Fisher's exact test indicates that the presence of edge-drilling behavior is dependent on time ($P < 0.0001$).

any signs of edge drilling (0 of 1142 complete holes examined among 36 samples) (table S1). This absence is not due to a lack of drilling predation attempts. In one early Pleistocene sample, 37% of 217 valves examined were wall-drilled by *Chicoreus* and/or *Phyllonotus* predators. The lack of edge drilling today is also not an anthropogenic artifact. Evidence of edge drilling disappeared by the early Pleistocene, or nearly 2 million years before any human disturbance of seagrass ecosystems.

The loss of edge-drilled *Chione* after the Pliocene coincides with a regional extinction event in the western Atlantic (*1*–*5*, *11*, *26*), but it is not simply a function of the extinction of one or more Pliocene edge-drilling species. Edge drilling was induced quickly (within the first week of our competition experiment) in a species not known to edge-drill in the wild today, indicating that, once evolved, edge-drilling behavior is expressed only when likely to be advantageous—that is, when competition is high. Thus, we interpret our results to suggest that extinction linked to productivity decline indirectly caused surviving lineages of predatory snails to shift their attack behavior to reflect a less risky biotic environment.

The absence of edge-drilling behavior in the wild today and throughout the Pleistocene indicates that competition intensity has not returned to high pre-extinction levels despite nearly two million years for recovery. This delay may explain why the Pleistocene seems to be a time of evolutionary quiescence in terms of enemy-related adaptive innovation and specialization (*17*).

Our findings emphasize that extinction affects not just taxonomic diversity but also the nature of interactions among species, and therefore the form and intensity of selection to which members of recovery communities are subjected. A full characterization of recovery from extinction must, therefore, incorporate accounts of how species affect each other on ecological and evolutionary time scales, as well as the diversities and identities of species coexisting in recovery communities.

References and Notes

1. S. M. Stanley, *Palaios* **1**, 17 (1986).
2. J. B. C. Jackson, P. Jung, A. G. Coates, L. S. Collins, *Science* **260**, 1624 (1993).
3. W. D. Allmon, G. Rosenberg, R. W. Portell, K. S. Schindler, *Science* **260**, 1626 (1993).
4. W. D. Allmon, G. Rosenberg, R. W. Portell, K. S. Schindler, in *Evolution and Environment in Tropical America*, J. B. C. Jackson, A. F. Budd, A. G. Coates, Eds. (Univ. of Chicago Press, Chicago, 1996), pp. 271–302.
5. E. J. Petuch, *Science* **270**, 275 (1995).
6. G. J. Vermeij, *J. Paleontol.* **72**, 465 (1998).
7. D. P. Domning, *Palaeogeogr. Palaeoclimatol. Palaeoecol.* **166**, 27 (2001).
8. W. P. Woodring, *Am. Philos. Soc. Proc.* **110**, 425 (1966).
9. G. J. Vermeij, *Biogeography and Adaptation* (Harvard Univ. Press, Cambridge, MA, 1978).
10. E. J. Petuch, *Palaeogeogr. Palaeoclimatol. Palaeoecol.* **37**, 277 (1982).
11. J. A. Todd *et al.*, *Proc. R. Soc. London Ser. B.* **269**, 571 (2002).
12. M. E. Power *et al.*, *Bioscience* **46**, 609 (1996).
13. R. T. Paine, *Ecology* **44**, 63 (1963).
14. G. P. Dietl, G. S. Herbert, *Am. Malacol. Soc. Abs. Prog.* 44 (2002).
15. S. Ishida, *J. Exp. Mar. Biol. Ecol.* **305**, 233 (2004).
16. S. Morissette, J. H. Himmelman, *Anim. Behav.* **60**, 531 (2000).
17. G. J. Vermeij, *A Natural History of Shells* (Princeton Univ. Press, Princeton, NJ, 1993).
18. B. Van Valkenburgh, F. Hertel, *Science* **261**, 456 (1993).
19. G. J. Vermeij, *Biol. J. Linn. Soc.* **72**, 461 (2001).
20. R. A. Roller, D. W. Garton, W. B. Stickle, *Am. Malacol. Bull.* **2**, 63 (1984).
21. Materials and methods are available as supporting material on *Science* Online.
22. Because competition experiments were performed first (*21*), snails in our isolation experiment had past experience in a highly competitive environment. Even though each snail had past experience in edge-drilling *Chione*, however, 13 of the 16 individuals abandoned the behavior after transplant to a less competitive environment. The three individuals that edge-drilled once in isolation may have retained a "memory" of the temporary extreme competitive environment they experienced.
23. Our initial observations with *P. pomum* suggest a similar edge-drilling response to the threat of resource theft as we found in *C. dilectus*.
24. W. D. Allmon, S. D. Emslie, D. S. Jones, G. S. Morgan, *J. Geol.* **104**, 143 (1996).
25. H. W. Nesbitt, G. M. Young, *J. Geol.* **105**, 531 (1997).
26. W. D. Allmon, *Palaeogeogr. Palaeoclimatol. Palaeoecol.* **166**, 9 (2001).
27. We thank R. Alexander, D. Briggs, J. Emerson, P. Harries, and P. Kelley for comments; M. Oleson for assistance in collection and processing of fossil samples; C. Swanson for help with the experiments; and E. Petuch and R. Portell for access to fossil localities and/or museum collections and specimen loans. Supported in part by NSF grant EAR9706749 (G.J.V.); the Geological Society of America (G.S.H.); the Paleontological Society (G.S.H.); the Department of Geology, University of California at Davis (G.S.H.); and the Center for Marine Science, University of North Carolina at Wilmington (G.P.D.).

Supporting Online Material

www.sciencemag.org/cgi/content/full/306/5705/2229/DC1
Materials and Methods
SOM Text
Table S1
References

8 October 2004; accepted 18 November 2004
10.1126/science.1106182

The Duration of Forest Stages in Southern Europe and Interglacial Climate Variability

P. C. Tzedakis,[1]* K. H. Roucoux,[1] L. de Abreu,[2] N. J. Shackleton[2]

Foraminiferal oxygen isotope and pollen analyses from a deep-sea sequence off southwest Portugal show that the duration of temperate stages on land over the past 350,000 years varied considerably. The record shows forest contractions during intervals of low ice volume, coeval with declines in atmospheric methane, after which tree populations did not always recover. What emerges is that, although the broad timing of interglacials is consistent with orbital theory, their specific duration may be dictated by millennial variability. This complicates the prediction of the natural duration of interglacials, at least until the origin of this climate variability is understood.

Distinguishing long-term natural climate variability from anthropogenically forced change is an important challenge in the prediction of future climate. The study of past interglacials can provide important insights into patterns of natural climate variability during warm periods such as the present. Establishing the timing and duration of past interglacials is of interest because it might help clarify where we are in the current interglacial cycle and, by extension, when the onset of the next glacial period can be expected to occur.

A first step toward an improved understanding of interglacial duration was the realization that the Eemian (Last) Interglacial of northwestern Europe was not equivalent to the entire marine isotope stage (MIS) 5 of the deep-sea stratigraphy, but rather to a substage (MIS 5e) within it (*1*). This meant that, on average, interglacials over the past million years did not have a duration of half an eccentricity cycle [~50 thousand years (ky)], but rather half a precessional cycle (~10 ky). On this basis, our current interglacial (Holo-

[1]Earth and Biosphere Institute, School of Geography, University of Leeds, Leeds, LS2 9JT, UK. [2]Department of Earth Sciences, University of Cambridge, Godwin Laboratory, New Museums Site, Pembroke Street, Cambridge, CB2 3SA, UK.

*To whom correspondence should be addressed. E-mail: P.C.Tzedakis@leeds.ac.uk

cene), already 11.5 ky old, would appear to be at the limit of the average interglacial length. In contrast, Kukla *et al*. (*2*) have suggested that the Eemian lasted 23 ky and that terrestrial interglacial conditions extended well into the interval of global ice growth of MIS 5d. The implication is that the elapsed portion of the Holocene represents only about half of the typical length of an interglacial and that the onset of glacial conditions would still be several millennia away. However, the sustainability of such conclusions is undermined by the lack of sufficiently precise chronological control for pre-Holocene interglacials on land, which complicates correlations with variations in global ice volume as recorded in marine sequences. One way around this problem is to link land and sea records directly through joint pollen and marine proxy analyses. This allows an in situ assessment of phase relationships between climate changes and the vegetation response, bypassing correlation issues.

The Portuguese margin, where the combined effects of major river systems and a narrow continental shelf lead to the rapid delivery of terrestrial material, including pollen, to the deep-sea environment, has emerged as a critical area for linking marine and terrestrial records. In the south Portuguese margin, southwest of Lisbon, pollen is mainly transported by the outflow of the Tagus river, while aeolian transport is relatively limited (*3*). Recent results from core MD95-2042 (37°48′N, 10°10′W, water depth 3146 m) have led to a reevaluation of the timing and duration of Last Interglacial conditions in southern Europe (*4*, *5*). This new scheme proposed that the onset of interglacial conditions on land (represented by the full expansion of tree populations) occurred within MIS 5e, after deglaciation was complete, and was coincident with a rise to peak sea surface temperatures. Forest persisted for 16 ky, well into the interval of ice growth (MIS 5d). Contrary to earlier assumptions of land-sea synchroneity, these results provided support for the notion of a prolonged interglacial duration in southern Europe (*6*).

Here, we return to the Portuguese margin and attempt to establish whether the phasing between marine and terrestrial stages recorded in MIS 5e is a consistent characteristic of previous climatic cycles. Foraminiferal oxygen isotope and pollen analyses (*7*) were undertaken on the interval 190 to 350 thousand years before the present (ky B.P.), covering MIS 7 to 9, from a new core, MD01-2443 (37°52.85′N, 10°10.57′W, water depth 2925 m), which was retrieved in the same area as MD95-2042. Of the temperate periods considered here, MIS 9e has the highest temperatures of the past 400 ky in Antarctica (*8*, *9*) and estimated sea levels similar to or higher than the present (e.g., *10*). During both MIS 9c and MIS 9a, maximum Antarctic temperatures (*8*, *9*) and estimated sea levels (*10*) were lower than those during MIS 9e and the Holocene (*10*). Antarctic temperatures during MIS 7e exceeded peak Holocene values, whereas those in MIS 7c and 7a were as high as today (*8*, *9*). Direct determinations of MIS 7a sea level provide a range of –18 to –9 m relative to the present (*11*), while MIS 7c and 7e highstands approached present-day levels. In the continuous stratigraphical records from southern Europe, all of these intervals are characterized by forest development (*12*). In the Massif Central in France, the intervals equivalent to MIS 9e and 7e have been designated as interglacials containing a climatic optimum as warm as the Holocene (*13*). The interval equivalent to MIS 7c has also been assigned interglacial status because it contains the most floristically diverse

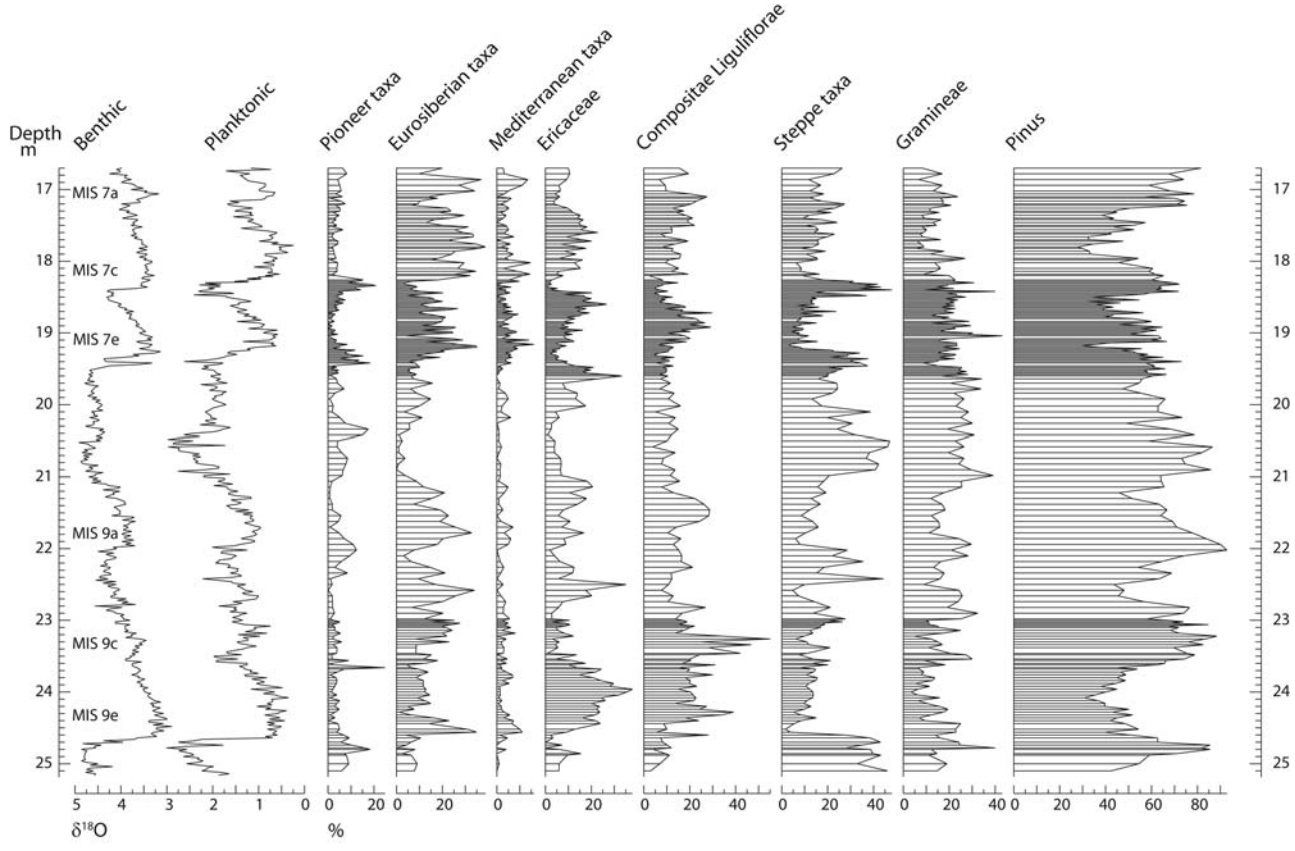

Fig. 1. MD01-2443 benthic and planktonic foraminifera isotope records and selected groups of pollen taxa: pioneer taxa (Cupressaceae and *Betula*), Eurosiberian taxa (total arboreal, excluding Mediterranean taxa, pioneer taxa, and *Pinus*), Mediterranean taxa (evergreen *Quercus*, *Olea*, *Pistacia*, *Phillyrea*, and *Cistus*), Ericaceae (dominated by *Erica* species and containing traces of *Calluna*), steppe taxa (*Artemisia*, Chenopodiaceae/Amaranthaceae, and *Ephedra*). Pollen abundances are expressed as percentages of the main sum, which includes all pollen except *Pinus*, Pteridophyte spores, and aquatics. *Pinus* is not included in the sum, because it is strongly overrepresented in marine sediments and would obscure the signal from other taxa (*7*).

forest development of MIS 7 in southern Europe (*14*). Although the distinction between interglacials and interstadials can be blurred depending on geographical position and proxy indicator, the above discussion suggests that MIS 9e, 7e, and 7c can be used as interglacial case studies to examine whether patterns of extended forest duration similar to the Eemian are observed during earlier climatic cycles (*15*).

Records of benthic and planktonic isotopes and selected groups of pollen taxa are shown in Fig. 1. The pollen record shows that isotopically light intervals are dominated by Eurosiberian (mainly deciduous *Quercus*) and Mediterranean (mainly evergreen *Quercus* and *Olea*) taxa. Glacial periods are characterized by pollen of steppe taxa and Gramineae, as well as *Pinus* (which, as in all marine sequences, is overrepresented). Transitional intervals are characterized by pioneer taxa. Ericaceae pollen, representing the development of heathland, occurs in both glacial and temperate phases. The age model (*7*) (fig. S1 and table S1) for the sequence was developed by aligning the benthic $\delta^{18}O$ record to the Antarctic Vostok deuterium (D/H) record (*8*), following the implications of (*16*). Figure 2 shows a good overall correspondence between temperate tree pollen percentages and planktonic isotope values, but also reveals the occurrence of major palynological changes during MIS 7e and 9e, which are not mirrored in the isotope values. Figure 2 also draws attention to similarities between the temperate tree pollen curve and the record of atmospheric methane (CH_4) from the Vostok ice core (*17*) in terms of the timing and patterns of events (but not always amplitude). This suggests that they both contain a Northern Hemisphere continental climate signal and that tropical/boreal wetland CH_4 production may be the primary control of atmospheric methane changes (*18*). On the other hand, decoupling between the two records, such as around 272 ky B.P. when temperate tree values reach an absolute minimum while CH_4 concentrations show an increase, may point to alternative sources of CH_4.

Table 1 shows the timing and duration of marine and terrestrial temperate stages between 190 and 350 ky B.P. in MD01-2443 and reveals that neither their lower nor their upper boundaries are generally coincident, but that is where analogies to MIS 5e phasing appear to end. At Terminations III and IV, forest expansion lags the benthic $\delta^{18}O$ curve by 1.4 and 2.8 ky, respectively, rather than the 6 ky of Termination II. This difference should not reflect increased distance from refugia and migrational lags during Termination II, because Portugal was a glacial refugium for temperate trees (*19*). More likely, it arises from the early Termination II deglaciation relative to the 65°N June insolation peak, compared with Terminations III and IV (*20*). The timing of interglacial forest expansion, on the other

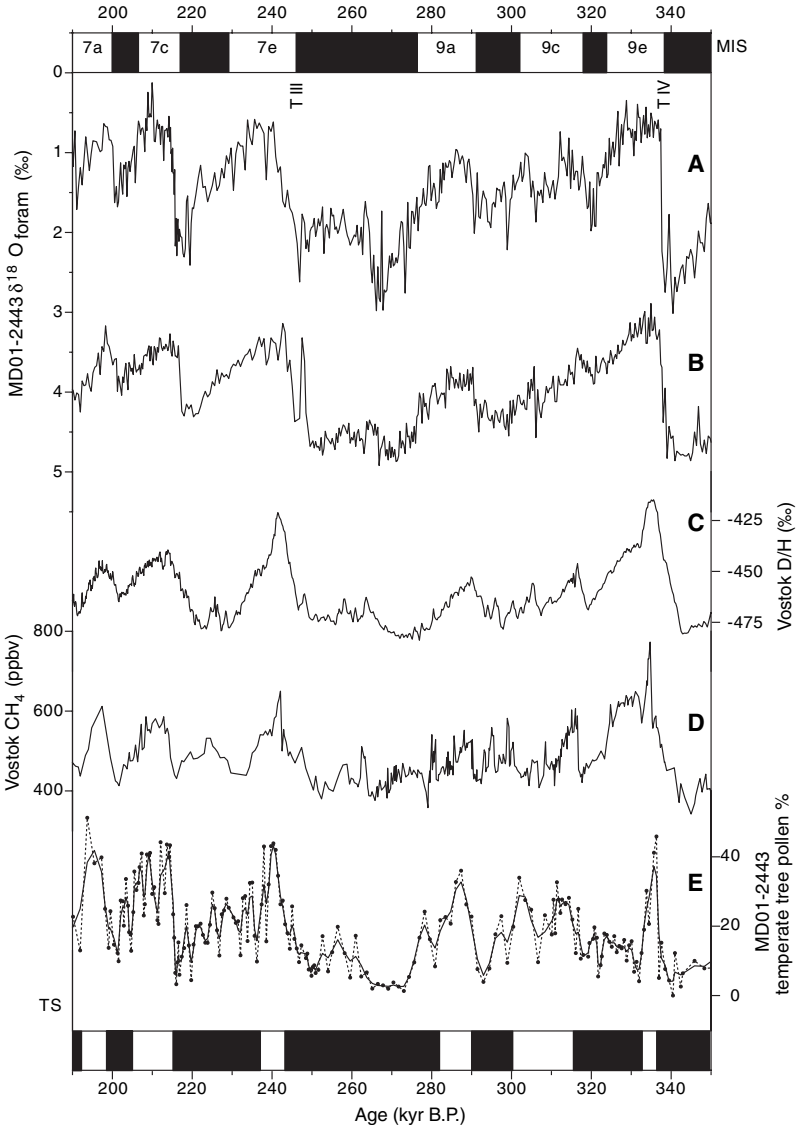

Fig. 2. Comparison of palaeoclimatic data sets over the interval 190 to 350 ky B.P. (**A**) Variations in $\delta^{18}O$ composition of planktonic foraminifera in marine core MD01-2443 in the Portuguese margin (this study). (**B**) Variations in $\delta^{18}O$ composition of benthic foraminifera in marine core MD01-2443 (this study). (**C**) Variations in deuterium (D/H) composition of ice in the Vostok ice core, Antarctica (*8*). (**D**) Variations in atmospheric CH_4 content from entrapped air in the Vostok ice core (*17*). (**E**) Variations in temperate tree pollen percentages in marine core MD01-2443 (this study). Temperate tree pollen is used here as the sum of Mediterranean and Eurosiberian taxa. It excludes *Pinus* (as overrepresented) and the pioneer taxa. The same arboreal pollen curve was used in (*3*–*5*) to define the Last Interglacial. Dashed line, actual values; continuous line, three-point moving average values. Ages are plotted on the Dome C time scale (*7*) (fig. S1 and table S1). Also shown are the marine isotope stage (MIS) and terrestrial stage (TS) as defined in MD01-2443 (white, temperate; black, glacial). Following (*12*), we consider the interval containing isotopic event 8.5 as belonging to MIS 9 and accordingly designate it as MIS 9a (rather than MIS 8e). Terminations III (T III) and IV (T IV) are also indicated.

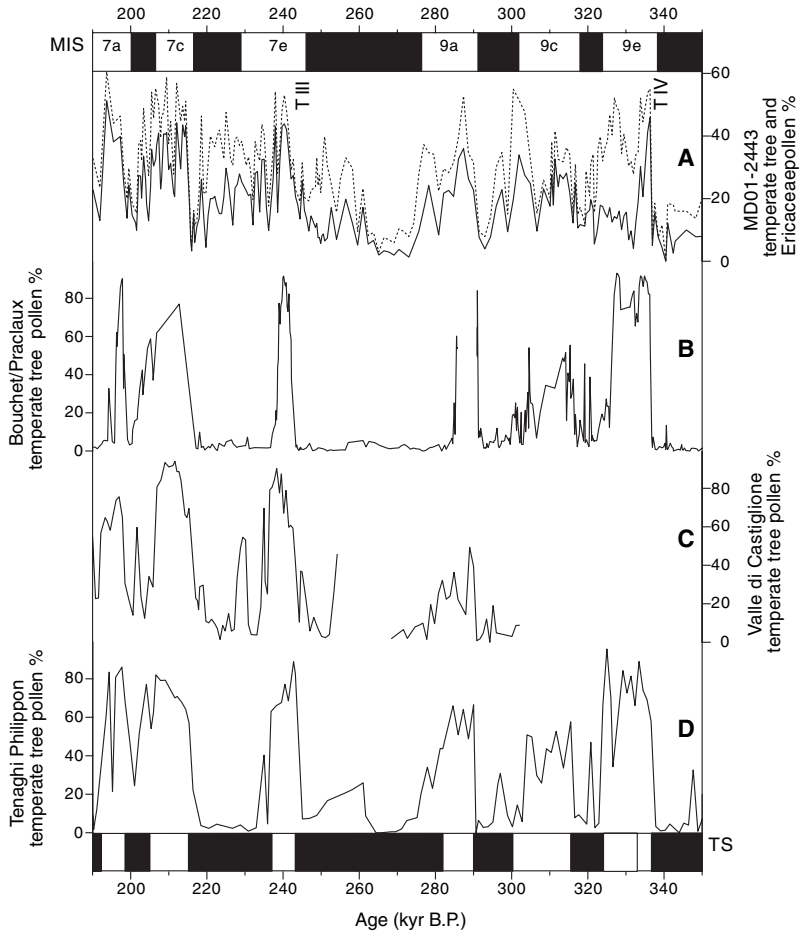

Fig. 3. Comparison of southern European pollen records over the interval 190 to 350 ky B.P. (table S2). (**A**) Area diagram of temperate tree (continuous line) and Ericaceae (dashed line) pollen percentages in MD01-2443 (this study). (**B**) Temperate tree pollen percentages in the Bouchet/Praclaux composite record from the Massif Central (*21*, *22*). The two records are spliced at MIS 9a (hence the record appears discontinuous there), using the common occurrence of a tephra layer. (**C**) Temperate tree pollen percentages in the Valle di Castiglione record, Lazio, Italy (*23*). The discontinuity at MIS 8 represents a core gap. (**D**) Temperate tree pollen percentages in the Tenaghi Philippon record, northeast Greece (*24*). The terrestrial records in [(B) to (D)] (correlations shown in table S2) are plotted in the same fashion as in (*12*). Age controls were applied only for the onset of forest periods. To ensure comparability, we used the same ages as the onset of forest stages in MD01-2443. No time constraints were used for the end of forest periods, thus allowing variations in stratigraphic length to be freely expressed. Also shown are marine isotope stage (MIS) and terrestrial stage (TS) as defined in MD01-2443 (white, temperate; black, glacial); the box corresponding to the MIS 9e forest stage shows the extended duration observed in the French and Greek records. Terminations III (T III) and IV (T IV) are also indicated.

hand, is more closely associated with the June insolation peak, which leads to variable phasing between the onset of terrestrial and marine stages from one Termination to another.

Table 1 also reveals considerable variability in the timing of forest declines relative to ice volume increases. In contrast to the evidence from MIS 5e, our results show that forests did not often persist into the interval of ice growth, ending either near the marine stage boundary or, in some cases, well before that. By extension, the duration of terrestrial temperate intervals in MIS 7 and 9 in SW Portugal, as defined by the presence of forest, does not follow any consistent pattern, varying from 10.3 to 4.4 ky (MIS 9c has a duration of 15 ky, but it represents a complex interval with two forest phases). The most notable departures in duration between the marine and terrestrial stages occur in MIS 7e and 9e. In MIS 7e, a forest decline coincident with an increase in Gramineae and Compositae Liguliflorae occurred at ~237 ky B.P., after which tree population abundance fluctuated but never reached earlier values. In MIS 9e, tree populations declined abruptly and steppe taxa and Compositae Liguliflorae increased at ~333 ky B.P., ~9 ky before the end of the marine stage.

An earlier comparison of the longest pollen records from southern Europe drew attention to what appeared to be notable departures in stratigraphic length (and hence the duration) of successive temperate stages of the past 450 ky (*12*), but in the absence of independent chronologies these conclusions remained tentative. We are now able to corroborate these preliminary conclusions using the MD01-2443 chronology, which reveals significant differences in the duration of successive forest stages. Figure 3 shows summary pollen records from the Massif Central, France (*21*, *22*), Lazio, Italy (*23*), and northeast Greece (*24*) and illustrates a close correspondence with MD01-2443 in terms of the duration of forest intervals. Thus, within MIS 7, the forest interval equivalent to MIS 7c had the longest duration, which would explain why it contains the most diverse and complete forest succession. During MIS 7e, a shift to drier and cooler conditions between ~237 and 239 ky B.P. led to forest decline across southern Europe and a premature ending of the terrestrial interglacial. A divergence between the records occurs in the length of the forest period corresponding to MIS 9e (~3.6 ky in MD01-2443 versus ~12 ky in the French and Greek records). However, all records show the occurrence of an arid/cold event at ~333 ky B.P. that led to forest decline. In Mediterranean Europe, arboreal populations recovered after that perturbation, but forests became dominated by conifers. In Portugal, an expansion of heathland after ~333 ky B.P. appears to have inhibited the reestablishment of arboreal populations, leading to a shorter local forest stage. It is worth noting, however, that even the longer-lived MIS 9e forest stages in France and Greece did not extend into the interval of ice growth (Fig. 3).

A notable feature of Antarctic temperature records is that the interglacials equivalent to MIS 5e, 9e, and 7e are characterized by an initial warm period, lasting ~4 ky and ending with an abrupt cooling, followed by a slower temperature decrease, which leads to the ensuing stadial (*8*, *9*, *25*). Figure 2 suggests that peak temperate tree frequencies in MIS 9e and 7e occurred within this early interval of maximum Antarctic temperatures. Within the uncertainties of our time scales, the tree population reductions observed at ~237 and ~333 ky B.P. appear to be coeval with declines in atmospheric CH_4. These changes occur within plateaux in $\delta^{18}O_{benthic}$ values, which do not show any appreciable variability over this interval. The important point here is that the records draw attention to

Table 1. Timing and duration of temperate stages in MD95-2042 (*4*, *5*) and MD01-2443 (this study), Portuguese margin. The marine isotopic stage (MIS) was defined using the midpoint of the transitions in the benthic isotope record. The onset of terrestrial temperate stages was defined as the point where temperate tree pollen values rise consistently above 20% and the end by the equivalent but opposite in sign changes (*29*). **T**, Termination; *, from MD95-2042.

MIS	Age of MIS boundaries (ky B.P.)	Duration of marine temperate stages (ky)	Age of terrestrial stage boundaries (ky B.P.)	Duration of terrestrial temperate stages (ky)
5d				
	116*		110*	
5e		16*		16*
T II	132*		126*	
6				
	190		192.5	
7a		10		6
	200		198.5	
7b				
	206.8		205	
7c		10		10.3
	216.8		215.3	
7d				
	229		237	
7e		17		6.2
T III	246		243.2	
8				
	276.6		282	
9a		14.4		8
	291		290	
9b				
	302		300.5	
9c		16		15
	318		315.5	
9d				
	324		333	
9e		14		3.6
T IV	338		336.6	
10				

abrupt events, occurring within interglacials on a global scale and not accompanied by changes in ice volume. These events may reflect expansions of the polar vortex, leading to outbreaks of polar air over southern Europe (*26*). The origin of this variability is not clear, but it does not appear to represent a linear response to orbital changes. What emerges is that, whereas the broad timing of interglacials is predicted by orbital (Milankovitch) theory, their specific duration appears to be dictated almost entirely by millennial variability rather than by the length of the half-precession cycle.

The absence of any clear patterns in terrestrial stage length raises doubts about the extent to which we are able to predict the natural duration of interglacials. The evidence presented here shows the occurrence of substantial (rather than subdued) changes within intervals of low ice volume, which in certain cases have contributed to a long-term decline of tree populations and a premature ending of the terrestrial interglacial, as in MIS 7e across southern Europe. Although the most prominent abrupt climate events hitherto have usually been associated with glacial climates, the above observations underscore the importance of understanding the origin of this intra-interglacial variability, especially in the context of future changes.

References and Notes

1. N. J. Shackleton, *Proc. R. Soc. London Ser. B.* **174**, 135 (1969).
2. G. Kukla, J. F. McManus, D.-D. Rousseau, I. Chuine, *Quat. Sci. Rev.* **16**, 605 (1997).
3. M. F. Sánchez Goñi, F. Eynaud, J. L. Turon, N. J. Shackleton, *Earth Planet. Sci. Lett.* **171**, 123 (1999).
4. N. J. Shackleton, M. Chapman, M. F. Sánchez-Goñi, D. Pailler, Y. Lancelot, *Quat. Res.* **58**, 14 (2002).
5. N. J. Shackleton, M. F. Sánchez-Goñi, D. Pailler, Y. Lancelot, *Global Planet. Change* **36**, 151 (2003).
6. P. C. Tzedakis, M. R. Frogley, T. H. E. Heaton, *Quat. Res.* **58**, 53 (2002).
7. Materials and methods are available as supporting material on *Science* Online.
8. J. R. Petit *et al.*, *Nature* **399**, 429 (1999).
9. O. Watanabe *et al.*, *Nature* **422**, 509 (2003).
10. C. Waelbroeck *et al.*, *Quat. Sci. Rev.* **21**, 295 (2002).
11. E. Bard, F. Antoniolli, S. Silenzi, *Earth Planet. Sci. Lett.* **196**, 135 (2002).
12. P. C. Tzedakis *et al.*, *Earth Planet. Sci. Lett.* **150**, 171 (1997).
13. J.-L. de Beaulieu *et al.*, *Quat. Sci. Rev.* **20**, 1593 (2001).
14. P. C. Tzedakis, J. F. McManus, H. Hooghiemstra, D. W. Oppo, T. A. Wijmstra, *Earth Planet. Sci. Lett.* **212**, 197 (2003).
15. In the fragmentary northern European stratigraphic record, the Reinsdorf and Schöningen/Wacken/Dömnitz interglacials have been considered equivalent to MIS 9e and 7e, respectively (*13*, *27*). Deposits from these periods are rarely represented in northern Europe, with the majority of interglacial records belonging to either the Eemian (MIS 5e) or the Holsteinian (MIS 11). One explanation for the paucity of MIS 7 and 9 temperate stages may be that in northern Europe these intervals were in fact interstadials that were neither warm enough nor long enough to leave a conspicuous mark on the stratigraphic record. However, a more likely explanation is that this apparent shortage is due to a lack of accommodation space for suitable depositional basins, in turn a function of the relatively smaller extent of the MIS 8 and 10 glaciations (*27*). In addition, similarities in palynological signature may have led to the erroneous chronostratigraphic assignment of many MIS 7 and 9 deposits to the Eemian and Holsteinian stages, respectively (*28*).
16. N. J. Shackleton, M. A. Hall, E. Vincent, *Paleoceanography* **15**, 565 (2000).
17. M. Delmotte *et al.*, *J. Geophys. Res.* **109**, D12104 (2004); doi:10.1029/2003JD004417.
18. E. J. Brook, S. Harder, J. Severinghaus, M. Bender, in *Mechanisms of Global Climate Change at Millennial Time Scales*, P. U. Clark, R. S. Webb, L. Keigwin, Eds. (American Geophysical Union, Washington DC, 1999), pp. 165–175.
19. K. H. Roucoux, N. J. Shackleton, L. de Abreu, J. Schönfeld, P. C. Tzedakis, *Quat. Res.* **56**, 128 (2001).
20. F. Parrenin, D. Paillard, *Earth Planet. Sci. Lett.* **214**, 243 (2003).
21. M. Reille, J.-L. de Beaulieu, *Quat. Res.* **44**, 205 (1995).
22. M. Reille, V. Andrieu, J.-L. de Beaulieu, P. Guenet, C. Goeury, *Quat. Sci. Rev.* **17**, 1107 (1998).
23. M. Follieri, D. Magri, L. Sadori, *Pollen Spores* **30**, 329 (1988).
24. T. A. Wijmstra, A. Smit, *Acta Bot. Neerl.* **24**, 297 (1976).
25. EPICA (European Project for Ice Coring in Antarctica) Community Members, *Nature* **429**, 623 (2004).
26. E. J. Rohling, P. A. Mayewski, P. Challenor, *Clim. Dyn.* **20**, 257 (2003).
27. C. Turner, *Quat. Int.* **47/48**, 41 (1998).
28. P. C. Tzedakis *et al.*, *Quat. Sci. Rev.* **20**, 1583 (2001).
29. The value of 50% arboreal pollen (AP) or 40% AP-*Pinus* has been traditionally used in land pollen sequences to define stage boundaries. However, the value of 20% temperate tree pollen is more appropriate here because of an increased herbaceous component characterizing marine sediments in the Portuguese margin. This is a function of the pollen signal integrating over a large area with a number of specific local environments, including coastal areas dominated by herbaceous communities. This is why during even peak interglacial conditions, maximum temperate tree values in MD01-2443 are ~50%, compared with 80 to 90% for terrestrial records. The 20% measure is equally applicable to the Last Interglacial section as defined in MD95-2042 (*4*, *5*).

30. We thank R. C. Preece and L. C. Skinner for comments on the manuscript; M. F. Sánchez Goñi, D. Magri, O. Phillips, and J. Lloyd for discussions; J.-L. de Beaulieu and M. Reille for the Bouchet/Praclaux data; and J. Corr, M. Hall, and J. Rolfe for technical support. We are grateful to F. Parrenin for the use of the new Vostok age model. Funding was provided by the European Union (EV K2-CT-2000-00089) for project Pole-Ocean-Pole (POP) and the Natural Environment Research Council (NER/B/S/2002/00358). We are grateful to I. N. McCave for locating the coring site and to the Terres Australes et Antarctiques Françaises, Institut National des Sciences de l'Univers, Centre National de la Recherche Scientifique, and Institut Français pour la Recherche et la Technologie Polaires for the coring operations aboard the Marion Dufresne II.

Supporting Online Material

www.sciencemag.org/cgi/content/full/1102398/DC1
Materials and Methods
Fig. S1
Tables S1 and S2
References

7 July 2004; accepted 9 November 2004
Published online 2 December 2004;
10.1126/science.1102398
Include this information when citing this paper.

Asynchronous Terrestrial and Marine Signals of Climate Change During Heinrich Events

Tim C. Jennerjahn,[1]* Venugopalan Ittekkot,[1] Helge W. Arz,[2] Hermann Behling,[3] Jürgen Pätzold,[3] Gerold Wefer[3]

Tropical regions have been reported to play a key role in climate dynamics. To date, however, there are uncertainties in the timing and the amplitude of the response of tropical ecosystems to millennial-scale climate change. We present evidence of an asynchrony between terrestrial and marine signals of climate change during Heinrich events preserved in marine sediment cores from the Brazilian continental margin. The inferred time lag of about 1000 to 2000 years is much larger than the ecological response to recent climate change and appears to be related to the nature of hydrological changes.

The recent increase in extreme climatic events, particularly in tropical regions, is thought by many to be a precursor of climate change. High-resolution investigations of past climate oscillations have found that changes between climate modes (warm versus cold and dry versus wet) can occur within decades (*1*), a period of time similar to that of recent climate change. Hence, understanding the controls of past high-frequency climate oscillations is a prerequisite for improving recent climate prediction. Occurrences of high-amplitude climate changes in the tropics during the past decade suggest that clues about the causes of climate instability during the Quaternary might be found in tropical regions (*2*). Despite a growing pool of high-resolution paleoclimate records from low latitudes, detailed knowledge on the distribution and amplitude of climate changes in space and time is still sparse, and the processes responsible are hardly understood (*3*). Uncertainties exist particularly in reconciling timing and amplitude of responses of tropical terrestrial and marine ecosystems to climate changes (*4*–*6*). Generally, it is assumed that the response of vegetation patterns lags climatic changes. Estimates of the lag range between decades on an ecosystem scale to 2000 to 3000 years on a continent scale but are mostly derived from records spanning the deglacial and Holocene periods [(*7*, *8*) and references therein]. However, estimates from the Pleistocene, with its millennial-scale climate oscillations, suffer from a lack of archives with variables independently denoting climate change and vegetation response. Understanding the processes determining the ecological response time to climate change is a prerequisite for meaningful use of terrestrial proxies in the interpretation of paleoclimate data. It also requires high-resolution climate archives from sites that are sensitive to changes in regional climate systems and capable of recording marine as well as terrestrial ecosystems' responses to climate change.

We found such a site on the continental margin off northeast Brazil (Fig. 1). Sediment cores covering late Quaternary sediments dating back to 85,000 years before the present (B.P.) were studied for information on oceanic and terrestrial responses to climate change by using a multiproxy approach. The area is situated between two moisture-carrying trade wind systems sensitive to climate changes caused by seasonal movements of the Intertropical Convergence Zone (ITCZ) (*9*) and exhibit high sedimentation rates. Thus, it is suitable for monitoring the consequences of high-frequency climate oscillations in the tropical Atlantic Ocean as well as on the South American continent.

Distribution patterns of newly obtained data on organic carbon (C_{org}) and carbonate ($CaCO_3$) contents and stable carbon and nitrogen isotopes ($\delta^{13}C_{org}$ and $\delta^{15}N$) in our cores are in agreement with previously measured geochemical parameters, pollen abundance and composition, and Fe/Ca and Ti/Ca ratios. They indicate millennial-scale sedimentation pulses coincident with the Younger Dryas (YD) and Heinrich events H1 to H8 known from the North Atlantic (*9*) (Figs. 2 and 3), although the time spans of the sedimentation pulses we observed do not always match exactly with those of the North Atlantic events. The most important finding of our study is a recurring internal sedimentation pattern during Heinrich events with opposing gradual changes in the parameters measured. The sedimentation rate increased from 10 to 15 cm kyear^{-1} to maxima to 30 cm kyear^{-1} during Heinrich events (*10*). Rapid decreases of $CaCO_3$ content from 30 to 40% in the beginning of a Heinrich event to <10% were accompanied by rapid increases of Fe/Ca and Ti/Ca ratios, indicating a shift from car-

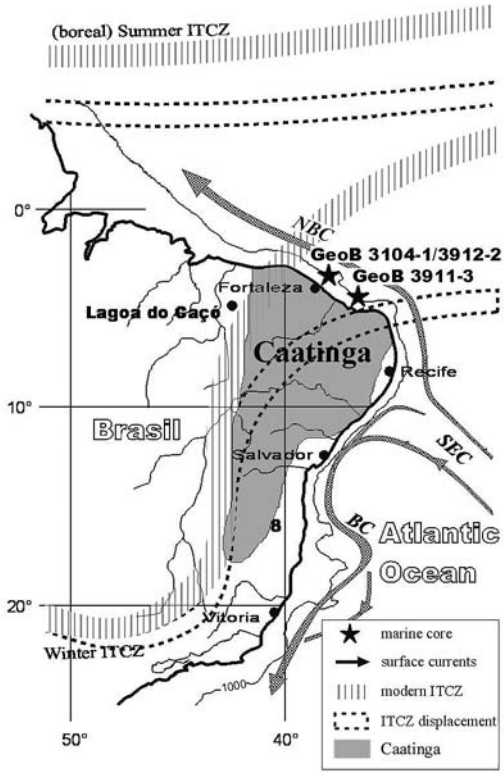

Fig. 1. Map of the investigated area with locations of cores GeoB 3104-1/GeoB 3912-1 (3°40.0′S, 37°43.0′W, and 767-m water depth) and GeoB 3911-3 (4°36.8′S, 36°38.2′W, and 828-m water depth), and Lagoa do Caçó (2°58′S and 43°25′W), as well as the actual positions of the ITCZ and its inferred southward displacement during the times of Heinrich events as suggested by our data. Also included are the major surface currents: the South Equatorial Current (SEC), the North Brazil Current (NBC), and the Brazil Current (BC). The major vegetation type of northeast Brazil is caatinga (primarily xerophytic thorn shrub), which is bordered by cerrado (savannah) to the west and Atlantic rainforest along the coastal stretch.

[1]Zentrum für Marine Tropenökologie, Fahrenheitstrasse 6, D-28359 Bremen, Germany. [2]GeoForschungs-Zentrum Potsdam, Telegrafenberg, 14473 Potsdam, Germany. [3]Deutsche Forschungsgemeinschaft (DFG) Forschungszentrum Ozeanränder (RCOM), Klagenfurter Strasse, 28359 Bremen, Germany.

*To whom correspondence should be addressed. E-mail: tim.jennerjahn@zmt-bremen.de

bonate to lithogenic deposition (*11*). After this initial increase, Fe/Ca and Ti/Ca ratios then gradually decreased toward the end of a Heinrich event. In contrast, the C_{org} content in our cores gradually increases from about 0.5% to 2.7% during Heinrich events, with a maximum near their ends $\delta^{13}C_{org}$ decreased from values between –20 per mil (‰) and –21‰, indicating its marine origin (*12*), to values between –23‰ and –24‰. The 3‰ decrease of $\delta^{13}C_{org}$ indicates a substantial contribution of terrestrial organic matter (OM) (Figs. 2 and 3). The latter may consist of plant, soil, and plankton, which has a $\delta^{13}C_{org}$ that is almost similar to but distinctly different from that of marine OM (*13*). $\delta^{15}N$ gradually decreased from about 10‰ to 5.5‰ in GeoB 3912-1 and from about 13‰ to 4.5‰ in GeoB 3911-3 toward the end of an event.

Variations in $\delta^{15}N$ should reflect changes in OM source and quality, with high values denoting high degrees of OM degradation during times of normal sedimentation and the onset of Heinrich events (*14*). Increased contribution of terrestrial plant materials, which meet part of their nitrogen demand by atmospheric nitrogen fixation ($\delta^{15}N$ = 0‰), and less degradation of the OM may have led to the lower $\delta^{15}N$ values observed during YD and Heinrich events. In conjunction with decreasing $\delta^{13}C_{org}$, the subsequent shift of $\delta^{15}N$ toward values observed in modern riverine and mangrove sediments indicates an increasing contribution of less degraded OM, mainly of terrestrial origin.

The fluxes and composition of pollen and fern spores generally display a similar distribution. Pollen influx gradually increased from <10 grains cm^{-2} $year^{-1}$ in the beginning of Heinrich events to a maximum of 60 grains cm^{-2} $year^{-1}$ in the second half of H1 (*10*). Fern spore fluxes indicate a successional vegetation pattern. Moss fern (*Selaginella*) fluxes increased rapidly during the first half and then decreased gradually toward the end of H1. In contrast, tree fern fluxes increase gradually from minimal flux in the beginning to a maximum in the end of H1. The lacustrine pollen record from Lagoa do Caçó displays a similar pattern. Taxa reflecting rapid reforestation in response to increased moisture were found at about 16 calendar kyear B.P. (*15*), not exactly at the same time we found maximum pollen and fern spore fluxes and terrigenous OM in our cores but also considerably lagging the onset of H1 (Figs. 2 and 3).

The internal sedimentation pattern during Heinrich events indicates an asynchrony between the response of marine and terrestrial ecosystems to rapid millennial-scale changes. On the basis of an observed increase of Fe/Ca and Ti/Ca ratios, the Heinrich events as a whole were previously thought to be periods of increased input of terrigenous materials resulting from increased precipitation and river discharge (*9*). Our newly obtained biogeochemical and stable isotope data, in combination with previous findings, allow us to better resolve the deposition history of these millenial-scale oscillations. In the beginning of such a Heinrich-type event, increased precipitation along the continental margin of northeast Brazil led to an initial outwash of exposed shelf sediments and increased river inputs of eroded topsoil, both poor in OM (*16*). This erosion period is indicated by high Fe/Ca and Ti/Ca ratios and low OM and pollen contents observed in our cores. Only pioneer vegetation like moss ferns, with a peak flux in the middle of H1, grew during this phase. Subsequently, the vegetation cover, including regionwide development of gallery and floodplain rainforests and montane forest, slowly expanded, stabilized the soil, and reduced erosion of OM-depleted mineral matter in the second half of H1. This expansion is indicated by the peak fluxes of tree fern spores and pollen in the second half of H1 (Fig. 2). In the second half of these wet periods, the enhanced production of fresh terrestrial OM and increased discharge of the rivers directly on the continental slope led to the observed high OM, pollen, and fern spore contents and low $\delta^{13}C_{org}$ and $\delta^{15}N$ in our cores.

We infer that the successional pattern from marine to terrigenous sedimentation within the pulses is a consequence of a time lag, on the order of 1000 to 2000 years, between the onset of rapid millennial-scale changes and the response of the continental bio- and geospheres. Our record preserved terrestrial as well as marine signals of climate change. It has an advantage over the traditional correlation of terrestrial with marine climate archives by avoiding chronology problems that become fundamental when correlating high-frequency records of climate change over great distances (*17*). The time lag we postulate cannot be just the transit time from the terrestrial source of the material to its marine sink for the following reasons. First, if the expansion of vegetation cover and increased fluvial input of eroded soil rich in the freshly produced plant OM were coeval with the rapid hydrological changes,

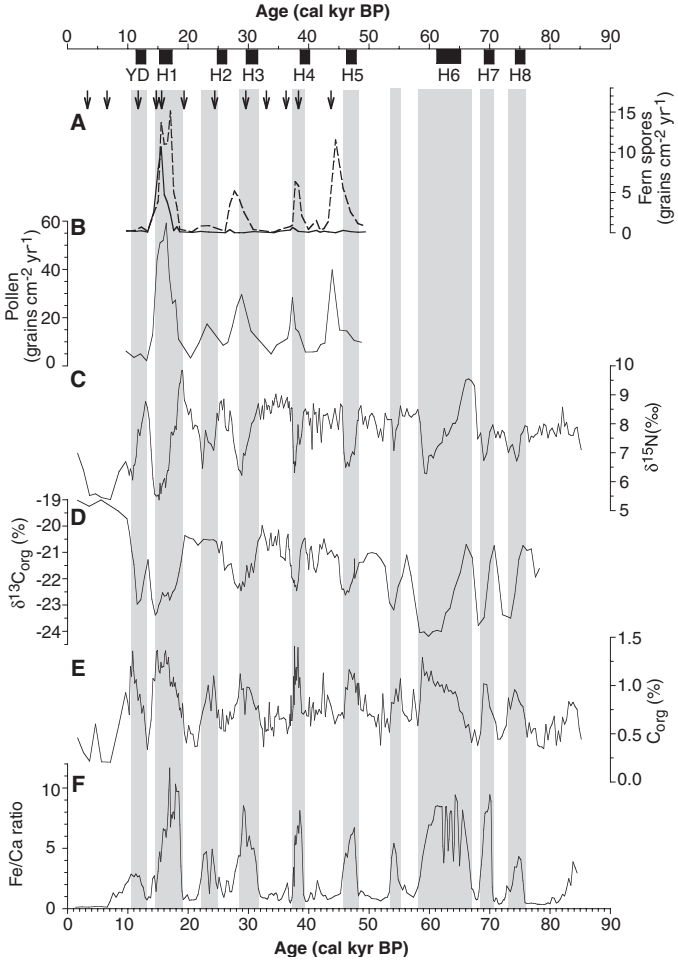

Fig. 2. Multiproxy sedimentation patterns of core GeoB 3104-1/GeoB 3912-1 from the past 85 kyear. Core GeoB 3912-1 extends the 48-kyear B.P. record of core GeoB 3104-1 to 86 kyear B.P. (*9*). Accelerator mass spectrometry (AMS) ^{14}C ages (black arrows) (*9*) and stratigraphic correlation with the Spectral Mapping Project (SPECMAP) $\delta^{18}O$ stack were used for age control. Time resolution of core GeoB 3104-1/3912-1 is about 200 years. (**A**) Moss fern (dashed line) and tree fern (solid line) spore fluxes in core GeoB 3104. (**B**) Pollen influx in core GeoB 3104-1 (*10*). (**C**) $\delta^{15}N$ of core GeoB 3912-1, given in ‰ versus atmospheric air. (**D**) $\delta^{13}C_{org}$ of core GeoB 3912-1, given in ‰ versus pee dee belemnite (PDB). (**E**) C_{org} content of core GeoB 3912-1. (**F**) Fe/Ca ratio of core GeoB 3912-1 (*9*). Timing of YD based on (*33*); H1 to H5, (*35*); and H6 to H8, (*36*). Shaded areas representing sedimentation pulses coincident with the YD and H1 to H8 are defined according to drastic changes in the Fe/Ca ratio.

we should have observed a peak of terrestrial OM in the beginning of the Heinrich events. Second, Fe/Ca and Ti/Ca ratios reflecting the input of lithogenics should have been high throughout the whole Heinrich event if there was no regulation by the increasing vegetation cover that gradually stabilized the soil and reduced erosion. Third, if the observed pattern were simply an artifact of material transport, the rise of pollen in the Lagoa do Caçó record should have preceded and not lagged that of our marine core.

The postulated time lag in our regional-scale example is much longer than the ecological response to recent climate change, which can be in the range of decades (*18*). It is also much longer than a time lag of a few decades postulated for the response of tropical vegetation to abrupt climate changes during the last deglaciation and derived from sedimentary records of climate and biomarker proxies in the Cariaco Basin (*7*). The reason for this apparent contradiction may lie in the difference of the prevailing climate and hydrology in the two regions. Like in the late Pleistocene, northeast Brazil currently is characterized by a semi-arid climate and caatinga vegetation (*10*). The dry period of about 8 months does not allow the development of rainforests that cannot survive a dry period longer than 4 months. It is conceivable that in the beginning of Heinrich events precipitation intensity rapidly increased during the rainy austral summer but not throughout the whole year. This first promoted erosion of the bare landscape. Subsequently, the seasonality of rainfall may have shifted toward a dry period shorter than 4 months, eventually allowing a regionwide expansion of wet forests. In the Cariaco Basin watershed, with its lowland and montane rainforest vegetation, annual precipitation is much higher and the contrast between dry and wet seasons less pronounced than in northeast Brazil. This would explain the almost immediate ecological response to climate change in the range of decades for the deglacial period in the Cariaco Basin watershed (*7*).

A detailed look at the differences in the amplitude of changes among Heinrich events provides further insight into the response of terrestrial and marine ecosystems to climate change. We found the maximum amplitude of changes during the longest lasting events, H1 and H6, in our cores. Pollen and fern spore fluxes are much lower during the shorter events, H2 to H5, and in the case of H5 they are out of phase with the other records. Low pioneer vegetation like moss ferns developed during all Heinrich events. Wet forests including tree ferns, however, could expand only during H1, as indicated by high fluxes during H1 and otherwise low fluxes of tree fern spores (Fig. 2). Our findings indicate that the magnitude of events H2 to H5, despite an overall increase in annual precipitation, may have been too small for a change of the seasonal distribution and thus the regionwide expansion of wet forests in northeast Brazil. Assuming that the abrupt vegetation change following deglacial climate change observed in Cariaco Basin sediments (*7*), which is in accordance with present-day observations (*18*), reflects the true ecological response to climate change, we infer that the delayed response of the continental bio- and geospheres to rapid millennial-scale climate changes observed in our cores results from the nature of hydrological changes affecting the seasonal rainfall pattern.

Both data and modeling studies have shown that phases of abrupt climate change coinciding with the Heinrich events known from the North Atlantic were phases of increased humidity and precipitation in tropical South America. A southward displacement of the ITCZ and enhanced northeast trade winds were suggested to be the source of moisture (*15*, *19*, *20*). Drier El Niño–like conditions in the Cariaco Basin watershed have been inferred for the late Holocene. These were ascribed to a southward migration of the ITCZ in consequence of warmer surface water in the equatorial Pacific and Atlantic like that currently observed during El Niño events (*21*). Warming of the western tropical Atlantic is also indicated for the YD and H1 (*22*, *23*). Therefore, it is most likely that the moisture brought to northeast Brazil during times of Heinrich events resulted from the southward displacement of the ITCZ and enhanced northeast trade winds (*24*).

These findings have important implications for the reconciliation of terrestrial and marine paleoclimate records and their use for the prediction of consequences of future climate change. In accordance with present-day observations of the ecological response to climate change (*18*), our findings underscore the importance of regional factors over approximated global averages in this respect for the recent past. Regional climate and hydrology have to be considered a major factor in determining the ecological response to rapid-scale climate change. This has to be taken into account when terrestrially derived proxies are used for the interpretation of paleoclimate records.

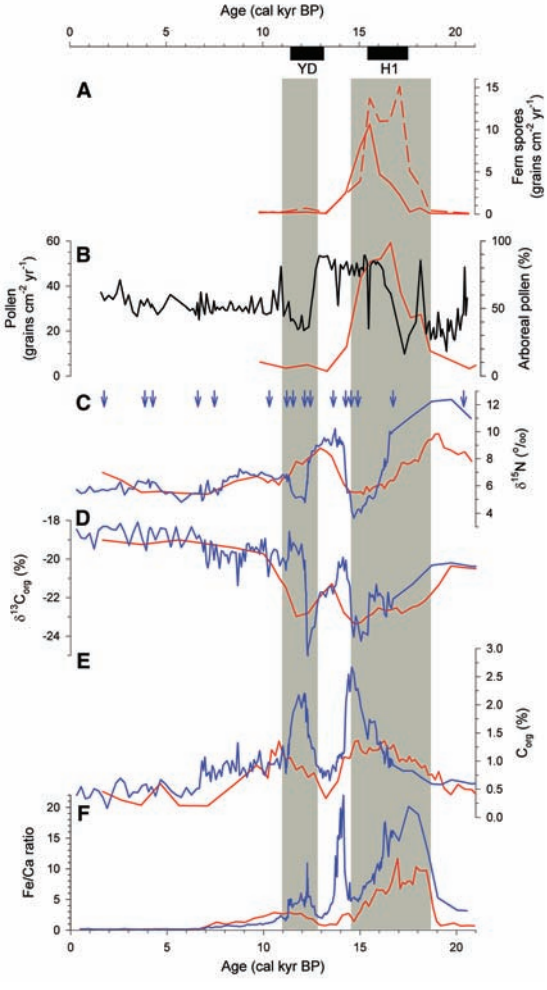

Fig. 3. Multiproxy sedimentation patterns of cores GeoB 3104-1/GeoB 3912-1 (red lines) and GeoB 3911-3 (blue lines) from the past 21 kyears compared with other paleoclimate indicators. AMS ^{14}C ages (blue arrows) (*9*) were used for age control in core GeoB 3911-3. Time resolution of core GeoB 3911-3 is about 60 years. (**A**) Moss fern (dashed line) and tree fern (solid line) spore fluxes in core GeoB 3104. (**B**) Pollen influx in core GeoB 3104-1 (left axis) and percentage of arboreal pollen (black line, right axis) in the lacustrine record of Lagoa do Caçó (*15*), northeast Brazil. (**C**) δ^{15}N of core GeoB 3912-1, given in ‰ versus atmospheric air. (**D**) $\delta^{13}C_{org}$ of core GeoB 3912-1, given in ‰ versus PDB. (**E**) C_{org} content of core GeoB 3912-1. (**F**) Fe/Ca ratio of core GeoB 3912-1 (*9*).

References and Notes

1. M. Sarnthein *et al.*, *Eos* **81**, 625 (2000).
2. R. A. Kerr, *Science* **292**, 660 (2001).
3. W. S. Broecker, S. Hemming, *Science* **294**, 2308 (2001).
4. E. Bard, F. Rostek, C. Sonzogni, *Nature* **385**, 707 (1997).
5. M. Stute *et al.*, *Science* **269**, 379 (1995).
6. I. Farrera *et al.*, *Clim. Dyn.* **15**, 823 (1999).
7. K. A. Hughen, T. I. Eglinton, L. Xu, M. Makou, *Science* **304**, 1955 (2004); published online 20 May 2004 (10.1126/science.1092995).
8. R. S. Bradley, *Paleoclimatology* (Academic Press, San Diego, CA, ed. 2, 1991).
9. H. W. Arz, J. Pätzold, G. Wefer, *Quat. Res.* **50**, 157 (1998).
10. H. Behling, H. W. Arz, J. Pätzold, G. Wefer, *Quat. Sci. Rev.* **19**, 981 (1999).
11. High x-ray fluorescence intensities of Ca are related to low Fe and Ti intensities and correlate well with the geochemical $CaCO_3$ content (*9*). Fe and Ti are related to siliciclastic components and have been shown to vary directly with the terrigenous mineral fraction of sediments (*25*). In a similar way, an increased supply of river-borne materials caused by millennial-scale hydrological changes has been inferred from increased Fe and Ti abundances in sediment cores from the Cariaco Basin (*26*).
12. G. Fischer, *Mar. Chem.* **35**, 581 (1991).
13. E. M. Galimov, *The Biological Fractionation of Isotopes* (Academic Press, San Diego, CA, 1985).
14. Sedimentary $\delta^{15}N$ can be altered by several processes, like degree of nutrient use in the water column, nitrification or denitrification, organic matter diagenesis, and material inputs from different sources (*27*, *28*). In our case, low primary productivity of the oligotrophic and well-aerated waters (*29*) suggests that $\delta^{15}N$ alteration due to denitrification or surface nutrient use is negligible. The notion that $\delta^{15}N$ reflects the degree of OM degradation in our cores is also supported by amino acid data. High proportions of the nonprotein amino acids β-alanine and γ-aminobutyric acid in the beginning of a Heinrich event, indicating a high degree of OM degradation (*30*), decrease gradually toward its end (*31*).
15. M.-P. Ledru, P. Mourguiart, G. Ceccantini, B. Turcq, A. Sifeddine, *Geology* **30**, 275 (2002).
16. Because the shelf break is located at about 50-m water depth in the investigated area, sea level was below it at least during the most pronounced events correlated with H1 and H6 but probably throughout the entire period of marine isotope stages 2 to 4 (*32*, *33*). Therefore, shelf erosion due to sea level change should have been unimportant throughout this period.
17. T. J. Crowley, *Paleoceanography* **14**, 271 (1999).
18. G.-R. Walther *et al.*, *Nature* **416**, 389 (2002).
19. P. A. Baker *et al.*, *Nature* **409**, 698 (2001).
20. A. J. Broccoli, *J. Clim.* **13**, 951 (2000).
21. G. H. Haug, K. A. Hughen, D. M. Sigman, L. C. Peterson, U. Röhl, *Science* **293**, 1304 (2001).
22. C. Rühlemann, S. Mulitza, P. J. Müller, G. Wefer, R. Zahn, *Nature* **402**, 511 (1999).
23. H. W. Arz, J. Pätzold, G. Wefer, *Earth Planet. Sci. Lett.* **167**, 105 (1999).
24. Alternatively, the moisture could originate from the south. If global wind systems became more zonal during cold phases as has been suggested (*34*), the boreal winter ITCZ should have shifted northward. In our case, this would imply a southern moisture source responsible for the increased precipitation during Heinrich events, which could have been provided from southeast trade winds and/or polar advections. Currently the high rainfall south of Recife is restricted to the coastal stretch. The orographic barrier of the Brazilian highlands prevents substantial transport of moisture to the north and to the west. Therefore and for reasons given in the text, a southern source of moisture is rather unlikely. The suggested southward migration of the ITCZ would also help to explain the time lag of about 1000 years between the pollen records of Lagoa do Caço and that of our marine core, despite the possible chronological uncertainties of site-to-site correlations. The southward displacement of the ITCZ has led to the observed patterns of sedimentation and vegetation development as described. The subsequent migration of the ITCZ to the northwest may then have led to a similar vegetation development about 1000 years later in the Lagoa do Caço region.
25. J. H. F. Jansen, S. J. Van der Gaast, B. Koster, A. Vaars, *Mar. Geol.* **151**, 143 (1998).
26. L. C. Peterson, G. H. Haug, K. A. Hughen, U. Röhl, *Science* **290**, 1947 (2000).
27. E. Wada, A. Hattori, *Nitrogen in the Sea: Forms, Abundances, and Rate Processes* (CRC Press, Boca Raton, FL, 1991).
28. M. A. Altabet, R. Francois, *Global Biogeochem. Cycles* **8**, 103 (1994).
29. H. T. Barretto, C. P. Summerhayes, *J. Sediment. Petrol.* **45**, 822 (1975).
30. T. C. Jennerjahn, V. Ittekkot, *Mar. Geol.* **161**, 129 (1999).
31. T. C. Jennerjahn *et al.*, unpublished data.
32. J. Chappell, N. J. Shackleton, *Nature* **324**, 137 (1986).
33. R. G. Fairbanks, *Nature* **342**, 637 (1989).
34. S. W. Hostetler, A. C. Mix, *Nature* **399**, 673 (1999).
35. L. Vidal *et al.*, *Earth Planet. Sci. Lett.* **146**, 13 (1997).
36. J. F. McManus *et al.*, *Nature* **371**, 326 (1994).

37. We thank M.-P. Ledru for providing pollen data from Lagoa do Caçó, A. Suthhof for helpful comments, and A. Cremer and D. Dasbach for laboratory work. The manuscript benefited from the constructive criticism of two anonymous reviewers. This work was supported by the German Federal Ministry for Education and Research and by the DFG to H.B. Data are available at www.pangaea.de.

7 July 2004; accepted 15 November 2004
Published online 2 December 2004;
10.1126/science.1102490
Include this information when citing this paper.

Seismological Constraints on Core Composition from Fe-O-S Liquid Immiscibility

George Helffrich[1]* and Satoshi Kaneshima[2]

Earth's core is composed primarily of iron (Fe) with about 10% by weight of lighter elements. The lighter elements are progressively enriched in the liquid outer core as the core cools and the inner core crystallizes. Thermodynamic modeling of Fe-O-S liquids shows that immiscible liquids can exist at outer-core pressures (136 to 330 gigapascals) at temperatures below 5200 kelvin and lead to layering in the outer core if the concentrations of the lighter elements are high enough. We found no evidence for layering in the outer core in the travel times and wave forms of *P4KP* seismic waves that reflect internally in the core. The absence of layers therefore constrains outer-core compositions in the Fe-O-S system to be no richer than 6 ± 1 weight % (wt %) O and 2 to 15 wt % S. A single core liquid composition of 10.5 ± 3.5 wt % S and 1.5 ± 1.5 wt % O is compatible with wave speeds and densities throughout the outer core.

The outer core is composed of liquid iron mixed with about 10 wt % lighter elements (*1*–*3*). Although these elements are a minor constituent by weight, they may affect the dynamic behavior of the core. The light elements may control the rate of cooling, the type of crystallization, and the final composition of the solid inner core (*4*, *5*). Partitioning of the light elements between the inner core and the liquid outer core affects the gravitational potential energy available to power the geodynamo as well (*6*, *7*).

Liquid immiscibility occurs widely in iron-rich liquid systems and is the physical basis for the smelting process. In iron-bearing systems such as Fe-O-S, Fe-C-S, and Fe-Si-S, one of the two coexisting liquids is rich in Fe, whereas the other is richer in S or O (*4*, *8*, *9*). The liquid densities differ appreciably, leading to buoyant separation and stratification in the system. As the core cools and the inner core crystallizes, enriching the outer core in the light element because it preferentially partitions into the liquid phase, immiscibility might also develop. The differences in the properties of the liquid could lead to layering in the core, and seismic analysis may be able to detect this layering. There is already suggestive seismic evidence of layering (*10*–*12*). To establish whether layering is possible, we need to determine whether immiscibility exists under core conditions, how thick the liquid layer might be, and what the densities and wave speeds in these liquids are.

To estimate layer thickness, we assume a mass-balance model of inner-core crystallization similar to that described in (*6*). The density jump $\Delta\rho_{ICB}$ at the inner core–outer core boundary is between 0.5 and 1.6 Mg m^{-3}, with values of <1.0 Mg m^{-3} most probable (*13*–*15*). This density increase reflects two processes: contraction from the liquid to the solid form and exclusion of the light element from the inner core's crystalline structure. Quantum-mechanical calculations of the properties of Fe at core conditions indicate that 0.21 Mg m^{-3} of $\Delta\rho_{ICB}$ is due to solid con-

[1]Earth Sciences, University of Bristol, Wills Memorial Building, Queen's Road, Bristol BS8 1RJ, UK. [2]Earth and Planetary Science, Tokyo Institute of Technology, 1-2-1 Ookayama, Meguro-ku, Tokyo 152-6551, Japan.

*To whom correspondence should be addressed. E-mail: george@geology.bristol.ac.uk

traction (*16*, *17*). Thus, ~0.3 to 0.8 Mg m^{-3} of density difference is due to transfer of the light element to the remainder of the outer core, which we assume to constitute an immiscible liquid layer. The product of density difference and the volume of the inner core gives the mass of material that, spread against the top of the outer core, could be seismically detectable. A range of densities and thicknesses is possible because of the density-thickness trade-off (Fig. 1) that would equal the mass of material transferred to the outer core through the crystallization of the inner core. Depending on $\Delta\rho_{ICB}$, the layer could be 2 to 12 km thick. For constraining core composition, the maximum layer thickness excludes the narrowest compositional range and so represents a conservative bound on composition (*18*).

To establish immiscibility in the core, the density of the liquid, and the seismic wave speeds in the liquid, we use a thermodynamic model of Fe-O-S liquids (*19*, *20*) with liquid thermophysical properties that we refined from high-pressure melting experiments in the Fe-FeS system (*21*, *22*) and Fe, FeO, and FeS (*23*–*25*). We calculate whether two liquids coexist, and the composition of the liquids, using a free-energy minimization method (*26*). We also calculate the density and *P*-wave speed for each liquid from their compositions and thermophysical properties (*25*). In the immiscible region, the iron-rich liquids match the density and *P*-wave speed of the core (*27*, *28*), indicating that immiscibility is possible there. The density of the S-rich liquid at 3500 and 4300 K [core-side temperature limits are derived from (*23*, *24*, *29*)] is, respectively, 9.29 and 8.97 Mg m^{-3}, and the *P*-wave speed is 8.23 and 8.36 km s^{-1}, or 6.2 and 9.4% less dense and 1.9 and 3.6% faster than values for the top of the outer core, depending on the temperature (*27*). The S-rich liquid density prescribes layer thicknesses between 2 and 8 km depending on the $\Delta\rho_{ICB}$ adopted (Fig. 1). As outer-core temperatures increase, the two-liquid field shrinks, and it disappears for temperatures >5200 K (Fig. 2). A hotter core also shrinks the feasible liquid range toward the Fe apex. Fe-O-S liquid temperatures of 7200 K are incompatible with observed core properties because even pure Fe densities and wave speeds would not match those of Earth.

To detect layering at the top of the outer core, we use *P4KP*, a seismic wave that enters the core, reflects three times internally, and then ascends to the surface through the core-mantle boundary (Fig. 3). *P4KP* is sensitive to core structure because each underside reflection will create a precursor from any layering present below the core-mantle boundary. *P4KP* also averages structure around the core because of the broadly separated multiple bounces. Observational data come from the J-Array network (fig. S1) (*30*), from four earthquakes in northern India and the Flores Sea. Individual seismograms are manually aligned to a reference phase, either *PcP* or *ScP*, and slant stacked (*31*, *32*) to isolate the weak *P4KP* arrival. The *P4KP* phase is identified by its differential travel time and differential slowness relative to the reference (*PcP* or *ScP*). The stacked wave forms, aligned on *P4KP*, show no consistent precursors before *P4KP* (Fig. 4A), suggesting that no layering is present with a constant thickness range up to 12 km, as expected for an immiscible liquid layer; a variable layer thickness is precluded by the density contrast involved (*33*, *34*). We also show stacked *P4KP* wave forms compared to synthetic seismograms calculated for $\Delta\rho_{ICB}$ = 0.82 Mg m^{-3} (*15*), requiring 3.3- and 3.4-km-thick layers at 3500 and 4300 K (Fig. 1). For this composition, which is representative of the liquid properties in the calculated immiscible field, the synthetic wave forms show a precursory shoulder and enhanced downswing that are not seen in the data (Fig. 4B) (*35*, *36*). Thus, within the mass-balance model assumptions, there is no evidence for layering due to immiscible liquid evolution in the outer core in either the travel times or the wave forms of *P4KP*.

This finding constrains outer-core compositions to be outside of the two-liquid field (Fig. 2). A liquid core composed of Fe-O-S must be no richer than 6 wt % oxygen and must contain ~2 to 15 wt % sulfur for temperatures between 3500 and 4300 K. Alternatively, core temperatures may be between 5200 and 7200 K, where only a single outer-core liquid exists, but this is unlikely given the ~ 4300 K upper bound on basal core-mantle boundary temperatures derived from lower mantle melting constraints and inner-core crystallization temperatures adiabatically extrapolated to the core-mantle boundary (*24*, *29*, *37*). If we assume the light-element concentration to be constant throughout the outer core, a composition that matches outer-core wave speeds and densities

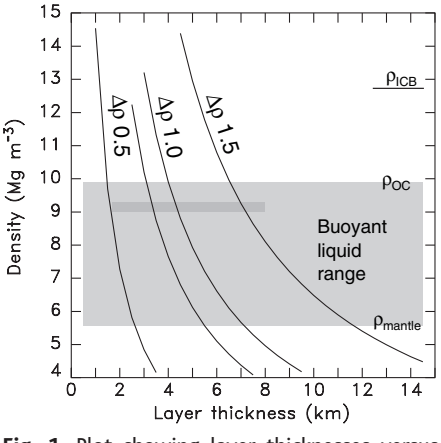

Fig. 1. Plot showing layer thicknesses versus layer density for a range of observed density jumps $\Delta\rho_{ICB}$ at the inner-core boundary. Shaded region delimits the feasible density range for buoyant outer-core liquids; darker region shows the density range of S-rich Fe-O-S liquids. If the liquids were denser than the top of the outer core, they would not rise; if they were less dense than the mantle's base, they would not be confined to the core. At constant mass, denser layers are thinner, and less dense layers are thicker. Calculation for each $\Delta\rho_{ICB}$ curve deducts the $\Delta\rho$ = 0.21 Mg m^{-3} due to liquid-solid contraction at constant composition (*16*, *17*). Layer thickness range is 2 to 11.6 ± 0.2 km for the seismically observed $0.5 \leq \Delta\rho_{ICB} \leq 1.6$ Mg m^{-3}, with values of $\Delta\rho_{ICB} < 1.0$ Mg m^{-3} most probable (*13*, *14*). The unlabeled curve is for $\Delta\rho_{ICB}$ = 0.82 Mg m^{-3} (*15*).

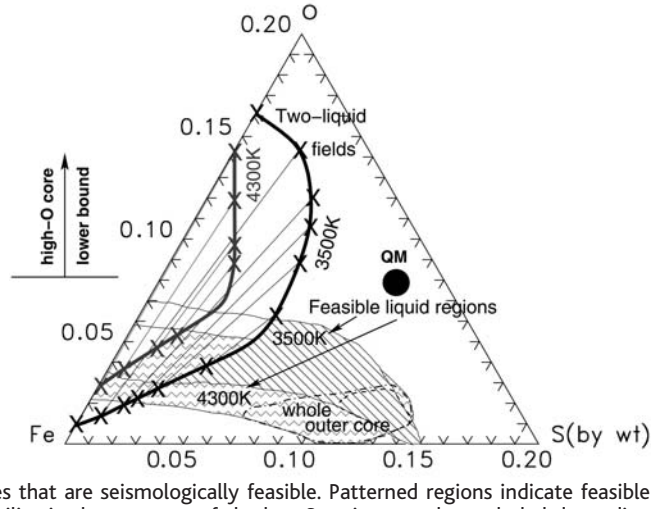

Fig. 2. Ternary diagram of liquid compositions in the Fe-O-S system showing region of two-phase liquid coexistence at the top of the outer core and at 3500 and 4300 K (concave regions within thick bounding lines) and compositions compatible with the core's seismic properties (*27*, *28*) (thin bounding lines). Tie-lines show compositions of coexisting liquids for different core compositions at 136 GPa calculated by free-energy minimization in the thermodynamic model. Immiscible liquids are present in core compositional ranges that are seismologically feasible. Patterned regions indicate feasible liquid range where immiscibility is absent; more of the low-S region may be excluded depending on the core's temperature. Dot indicates quantum-mechanical prediction (QM) from (*16*), and 8% O limit line indicates high-O core's lower bound (*42*). Dot-dashed lines enclose compositional subregion compatible with densities and wave speeds throughout the whole outer core (small along 3500 K adiabat, large along 4300 K adiabat).

is 10.5 ± 3.5 wt % S and 1.5 ± 1.5 wt % O (Fig. 2).

These constraints apply in the Fe-O-S system, but other elements might also influence immiscibility in the core. Nickel, in particular, might reduce immiscibility in Fe-Ni-O-S at higher pressures (*38*). However, the core may contain, in addition to Ni, lighter elements such as Si, C, and H, all of which give rise to liquid immiscibility (*3*, *4*, *39*) whose net effect on liquid behavior is unclear at core pressures. Volume-mixing nonideality in Fe-FeO might also shift seismically feasible core liquids to higher O contents, but would also expand the immiscibility region if O and S nonideality are similar. Thus, immiscibility constraints on core structure would still be applicable, although different in detail.

Although a thin liquid layer could be dispersed by convection within the core, a density difference as large as our calculated value suggests that such a layer is stable against convective stirring. Entrainment of buoyant droplets in a denser, convecting liquid is not energetically favorable; erosion of such a layer would require times longer than the age of Earth (*40*, *41*). We conclude that the outer core is not a layered liquid, which excludes a range of light-element combinations within certain immiscibility fields. In particular, our results rule out an O-rich core (8 wt %) envisaged in some high-temperature earth accretion scenarios (*42*) and quantum-mechanical calculations (*16*) because of its incompatibility with either outer-core wave speeds or with our observational immiscibility constraints. Extension of this analysis to other iron-bearing systems relevant to the core awaits melting experiments for the solid phases involved.

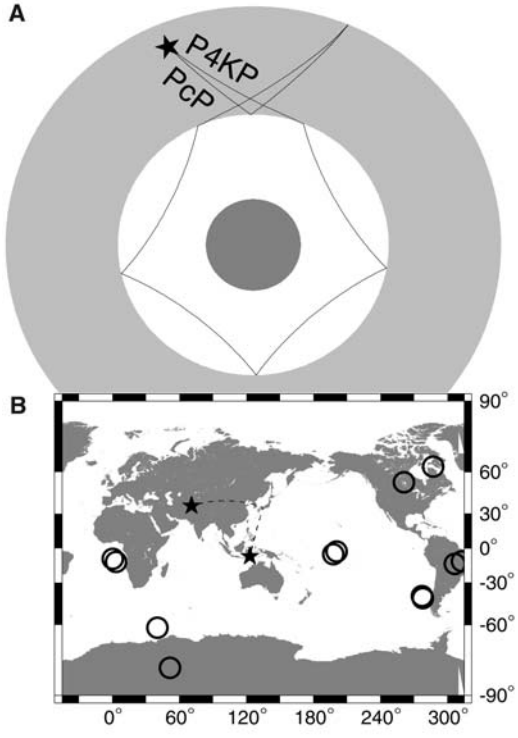

Fig. 3. (**A**) Section through Earth showing mantle (light gray), outer core and inner core (dark gray), and *PcP* and *P4KP* ray paths from a 600-km-deep source. *P4KP* enters the core, reflects three times off the underside of the core-mantle boundary, and leaves the core. *PcP* is the reference phase, relative to which we measure travel-time and slowness differences in order to minimize the influence of near-source and near-receiver heterogeneities. (**B**) Map of earthquake source regions (stars; two events from each region), *PcP* path to receiver region (dashed lines), and bounce points inside of core (circles). Events from northern India travel quasi-equatorially, bouncing once in the mid-Pacific, off the Chilean coast, and off the Angolan coast before reaching Japan. Sources in the Flores Sea are quasi-polar, bouncing under Canada, Brazil, and Antarctica. See table S1 for hypocentral information.

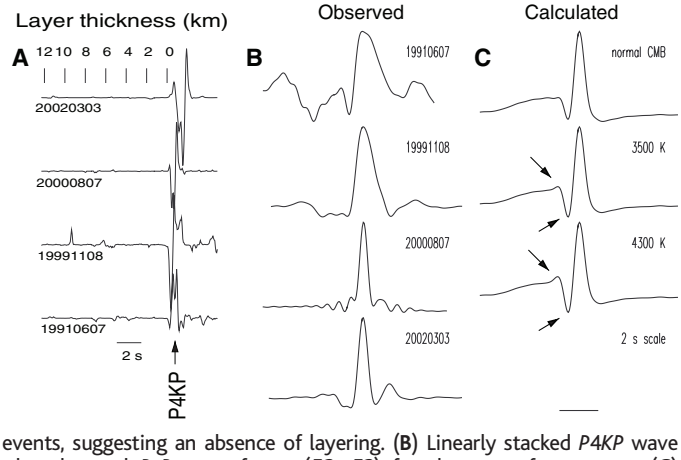

Fig. 4. (**A**) $N = 3$ phase-weighted stacked seismograms [N phase function exponent (*51*)] aligned on *P4KP*. The stacking method suppresses incoherent features in the seismogram but distorts the wave forms. Label on trace identifies the event by date. Scale at top shows expected arrival time for a reflection from a 2- to 12-km-thick layer below the core-mantle boundary. There is no consistent arrival visible in the four events, suggesting an absence of layering. (**B**) Linearly stacked *P4KP* wave forms deconvolved with the observed *PcP* wave forms (*52, 53*) for the same four events. (**C**) Synthetic *P4KP* and *PcP* wave forms calculated by reflectivity (*54*) using source-receiver geometry of the 2000/08/07 event, converted to velocity, and deconvolved like the data. Results for 3500 and 4300 K outer-core temperatures are shown, corresponding to a 3.3- and 3.4-km layer, respectively. Synthetics show precursory shoulder and pronounced downswing in advance of main *P4KP* arrival (arrows), which are absent in the observations.

References and Notes

1. F. Birch, *J. Geophys. Res.* **57**, 227 (1952).
2. D. J. Stevenson, *Science* **214**, 611 (1981).
3. J.-P. Poirier, *Phys. Earth Planet. Int.* **85**, 319 (1994).
4. B. J. Wood, *Earth Planet. Sci. Lett.* **117**, 593 (1993).
5. K. C. Creager, *Nature* **356**, 309 (1992).
6. D. E. Loper, *Geophys. J. R. Astron. Soc.* **54**, 398 (1978).
7. D. Gubbins, T. G. Masters, J. A. Jacobs, *Geophys. J. R. Astron. Soc.* **59**, 57 (1979).
8. D. C. Hilty, W. Crafts, J. Metals, *Trans. AIME* **4**, 1307 (1952).
9. V. Raghavan, *Phase Diagrams of Ternary Iron Alloys,* Part 2, *Ternary Systems Containing Iron and Sulphur* (Indian Institution of Metals, Calcutta, 1988).
10. T. Lay, C. J. Young, *Geophys. Res. Lett.* **17**, 2001 (1990).
11. B. L. N. Kennett, E. R. Engdahl, and R. Buland, *Geophys. J. Int.* **126**, 108 (1995).
12. The AK135 model is slower in the top 50 km of the outer core to account for the observed *SKKS-SKS* travel-time differences.
13. A. Souriau, M. Souriau, *Geophys. J. Int.* **98**, 39 (1989).
14. P. M. Shearer, G. Masters, *Geophys. J. Int.* **102**, 491 (1990).
15. G. Masters, D. Gubbins, *Phys. Earth Planet. Int.* **140**, 159 (2003).
16. D. Alfè, G. D. Price, M. J. Gillan, *Phys. Rev. B* **65**, 165118 (2002).
17. An alternative high-pressure equation of state yields solid contraction contribution to $\Delta\rho_{ICB} = 0.14$ Mg m^{-3} (*43*). Layer thickness uncertainty from this value is ±0.2 km.
18. If the mass expelled only partially constitutes an immiscible liquid layer, the analysis becomes a question of what outer-core compositions do not lead to immiscibility as the inner core crystallizes. In any Fe–light element binary T-X (temperature-composition) diagram with a two-phase liquid region, inner-core crystallization will drive the outer core to less Fe-rich compositions, possibly crossing into the two-liquid field. This will always be from compositions with lower light-element concentrations, thereby yielding the conservative, lower bound that we seek.
19. V. Kress, *Contrib. Mineral. Petrol.* **139**, 316 (2000).
20. The associated solution model uses the conservative assumption that the heat-capacity difference between different solution species is constant, which avoids unphysical behavior outside the model's calibration domain (*4*). The model supersedes an earlier asymmetric solution model (*44*) that describes the 1-atm Fe-O-S diagram of (*8*).
21. Y. Fei, J. Li, C. M. Bertka, C. T. Prewitt, *Am. Mineral.* **85**, 1830 (2000).
22. In contrast to earlier high-pressure experiments in the Fe-FeS system, recent experiments indicate lower Fe-FeS eutectic temperatures at high pressure (*45–47*).
23. R. Boehler, *Earth Planet. Sci. Lett.* **111**, 217 (1992).
24. R. Boehler, *Nature* **363**, 534 (1993).
25. The experimental melting brackets are used to derive zero-pressure liquid volume V_0, isothermal bulk modulus K, derivative K', and thermal expansivity α by equating the free energy of the solid and liquid components relative to zero free-energy change at the 1-atm melting temperature. Details of the equation of state are given in (*4*). Fe melting is experimentally constrained at outer-core pressure (136 GPa) and temperature, whereas FeO and FeS are constrained to 44 GPa. Values (V_0 cm^3 mol, K

GPa, K', α K^{-1}) for Fe are (7.00, 124.3, 6.90, 13.00 × 10^{-5}), for FeO are (12.95, 122.0, 4.30, 3.50 × 10^{-5}), and for FeS are (20.1449, 17.0, 8.00, 12.00 × 10^{-5}). The volume change due to phase transition in FeS and its phase boundary are from (*48*). Volumetric mixing nonideality in Fe-FeS liquids are parameterized as $(\bar{V}) = V_0(n - 1 + X)/n$, with $n = 7$ and 20 for Fe and FeS, respectively; other species volumes mix ideally. The thermodynamic model was validated against the low-pressure Fe-O-S liquidus (*8*), Fe-Fe_2O_3 phase diagram (*9*), and high-pressure Fe-FeS/Fe-Fe_3S eutectic experiments (*21*, *46*). Fitting Fe-FeS/Fe-Fe_3S eutectic experiments requires volume-mixing nonideality and leads to significant differences in Fe-rich liquid densities if neglected. Compositional uncertainty ~ ±1 wt %.

26. C. E. Harvie, J. P. Greenberg, J. H. Weare, *Geochim. Cosmochim. Acta* **51**, 1045 (1987).
27. A. Dziewonski, D. L. Anderson, *Phys. Earth Planet. Int.* **25**, 297 (1981).
28. The calculated core liquid densities and wave speeds within ±2% of PREM that we consider to be feasible match the outer-core properties.
29. A. Zerr, A. Diegler, R. Boehler, *Science* **281**, 243 (1998).
30. J-Array Group, *J. Geomagn. Geoelec.* **45**, 1265 (1993).
31. J. E. Vidale, H. M. Benz, *Nature* **356**, 678 (1992).
32. S. Kaneshima, G. Helffrich, *J. Geophys. Res.* **103**, 4825 (1998).
33. D. J. Stevenson, *Geophys. J. R. Astron. Soc.* **88**, 311 (1987).
34. Lateral thermal variations in the core larger than 10^{-4} K will drive convective motions. The thermal expansivity of the core is $\approx 10^{-4}$ K^{-1}, so lateral $\delta\rho/\rho > 10^{-8}$ will drive core flows. $\delta\rho/\rho$ for our calculated core liquids is $\approx 10^{-1}$, eliminating any topography on the boundary between the liquids.
35. A. Morelli, A. M. Dziewonski, *Geophys. J. Int.* **112**, 178 (1993).
36. SP6 was used to calculate synthetic seismograms because it predicts the observed *P4KP-PcP* travel times better than other whole-Earth models (PREM, *isap91*, or AK135). The reflectivity method was used to calculate seismograms with 3500 K properties V_p = 8.225 km s^{-1}, ρ = 9.293 Mg m^{-3}, and l = 3.3 km and 4300 K properties V_p = 8.361 km s^{-1}, ρ = 8.970 Mg m^{-3}, and l = 3.4 km, from ρ_{ICB} = 0.82 Mg m^{-3} (*15*).
37. K. Holland, T. J. Ahrens, *Science* **275**, 1623 (1997).
38. S. Urakawa, M. Kato, M. Kumazawa, in *High-Pressure Research in Mineral Physics*, M. Manghnani, Y. Syono, Eds. (American Geophysical Union, Washington, DC, 1987), pp. 95–111.
39. T. Okuchi, *Science* **278**, 1781 (1997).
40. V. S. Solomatov, D. J. Stevenson, *J. Geophys. Res.* **98**, 5375 (1993).
41. The rate of erosion of a density contrast across two layers is $d\Delta\rho/dt = -8\varepsilon\alpha F/(dC_p)$. For efficiency factor $\varepsilon = 6 \times 10^{-3}$, thermal expansivity $\alpha = 1.32 \times 10^{-5}$ K^{-1}, core heat flux F = 75 mW m^{-2}, convective layer thickness d 2260 km, and heat capacity C_p = 860 J kg^{-1} K^{-1}, an 850 kg m^{-3} layer contrast would be eroded in 1120 × 10^9 years. Parameter values are from (*49*). A rotating spherical geometry modifies the analysis, but appears to reduce the likelihood of entrainment (*50*).
42. D. C. Rubie, C. K. Gessmann, D. J. Frost, *Nature* **429**, 58 (2004).
43. F. D. Stacey, C. H. B. Stacey, *Phys. Earth Planet. Int.* **110**, 83 (1999).
44. V. Kress, *Contrib. Mineral. Petrol.* **127**, 127 (1997).
45. T. M. Usselman, *Am. J. Sci.* **275**, 278 (1975).
46. Y. Fei, C. M. Bertka, L. W. Finger, *Science* **275**, 1621 (1997).
47. J. Li, Y. Fei, H.-K. Mao, K. Hirose, S. R. Shieh, *Earth Planet. Sci. Lett.* **193**, 509 (2001).
48. Y. Fei, C. T. Prewitt, H.-K. Mao, C. M. Bertka, *Science* **268**, 1892 (1995).
49. S. Labrosse, J.-P. Poirier, J.-L. Le Mouël, *Phys. Earth Planet. Int.* **99**, 1 (1997).
50. J. R. Lister, B. A. Buffett, *Phys. Earth Planet. Int.* **105**, 5 (1998).
51. M. Schimmel, H. Paulssen, *Geophys. J. Int.* **130**, 497 (1997).
52. J. Park, V. Levin, *Bull. Seismol. Soc. Am.* **90**, 1507 (2000).
53. We used this cross-correlation method for the deconvolution with a 2-Hz cutoff. To window the arrivals in the linear stacks, we used the phase function for the phase-weighted stack (*51*), forcing it to be smooth in the neighborhood of the arrival by fitting it to a Lorenzian and tapering.
54. R. Kind, *J. Geophys.* **42**, 191 (1976).
55. We thank the Japan Society for the Promotion of Science for support; V. Kress for clarifications about the liquid thermodynamic model; G. Houseman, B. Wood, and the referees for suggestions that substantially improved the manuscript; and J. Jacobs for inspiration to learn more about the core. Seismograms were provided by Hinet (National Research Institute for Earth Science and Disaster Prevention, Tsukuba, Japan).

Supporting Online Material
www.sciencemag.org/cgi/content/full/306/5705/2239/DC1
Fig. S1
Table S1

4 June 2004; accepted 18 November 2004
10.1126/science.1101109

Global Identification of Human Transcribed Sequences with Genome Tiling Arrays

Paul Bertone,[1]* Viktor Stolc,[1,2]* Thomas E. Royce,[3] Joel S. Rozowsky,[3] Alexander E. Urban,[1] Xiaowei Zhu,[1] John L. Rinn,[3] Waraporn Tongprasit,[4] Manoj Samanta,[2] Sherman Weissman,[5] Mark Gerstein,[3]† Michael Snyder[1,3]†

Elucidating the transcribed regions of the genome constitutes a fundamental aspect of human biology, yet this remains an outstanding problem. To comprehensively identify coding sequences, we constructed a series of high-density oligonucleotide tiling arrays representing sense and antisense strands of the entire nonrepetitive sequence of the human genome. Transcribed sequences were located across the genome via hybridization to complementary DNA samples, reverse-transcribed from polyadenylated RNA obtained from human liver tissue. In addition to identifying many known and predicted genes, we found 10,595 transcribed sequences not detected by other methods. A large fraction of these are located in intergenic regions distal from previously annotated genes and exhibit significant homology to other mammalian proteins.

The prevailing gene structures encountered in many organisms consist primarily of coding sequences with few and short intervening regions, and thus their characterization is largely straightforward. In contrast, mammalian genes often contain many short exons interspersed with very large introns, making the identification of coding sequences difficult; a comprehensive and accurate map of human coding sequences therefore does not exist. Functional assays are expected to be essential for the identification of coding segments and verification of predicted genes.

In principle, genome tiling microarrays offer the opportunity to comprehensively investigate the RNA coding regions of any species using an unbiased approach. Recently, various microarray technologies have been applied to assess genome-wide transcription in bacterial and plant genomes (*1*–*3*), as well as transcription over human chromosomes 21 and 22 (*4*, *5*). Each of these methods identified many previously unannotated features, noting a high degree of novel transcription beyond that expected by existing gene annotation data. These studies clearly demonstrated the merit of the microarray approach to the problem of large-scale transcript mapping; however, until now the large size of mammalian genomes has precluded the construction of a genome-wide high-resolution tiling array.

Using maskless photolithographic DNA synthesis technology (*6*, *7*), we constructed 134 high-density oligonucleotide microarrays to represent ~1.5 Gb of nonrepetitive genomic DNA from each strand of the human genome (*8*, *9*). A total of 51,874,388 36-nucleotide (nt) probes, positioned every 46 nt on average, were selected to interrogate sense and antisense strands of the genome and synthesized at a feature density of ~390,000 probes per array [fig. S1 (*10*)]. To measure transcriptional activity, we hybridized the

[1]Department of Molecular, Cellular, and Developmental Biology, Yale University, New Haven, CT 06520–8103, USA. [2]Center for Nanotechnology, NASA Ames Research Center, Moffett Field, CA 94035, USA. [3]Department of Molecular Biophysics and Biochemistry, Yale University, New Haven, CT 06520–8114, USA. [4]Eloret Corporation, Sunnyvale, CA 94087, USA [5]Department of Genetics, Yale University School of Medicine, New Haven, CT 06520–8005, USA.

*These authors contributed equally to this work.
†To whom correspondence should be addressed. E-mail: michael.snyder@yale.edu (M.S.), mark.gerstein@yale.edu (M.G.)

arrays to fluorescence-labeled cDNA reverse-transcribed from triple-selected polyadenylated [poly(A)$^+$] liver tissue RNA pooled from several individuals (*10*).

We first performed a pilot study to test the reproducibility of the platform. Multiple arrays were probed with cDNA samples derived from identical and independent labeling reactions, producing technical replicates having r^2 correlations between 0.90 and 0.95 (*11*), indicating that the experiments are highly reproducible. To further reduce the effect of potential variation across individual cDNA samples, we used pooled reverse transcription products of 20 separate labeling reactions to probe the genome tiling arrays.

To correlate fluorescence intensity values with meaningful chromosomal features, we aligned the oligonucleotide probe coordinates with current gene annotation data, using the RefSeq (*12*) and Ensembl (*13*, *14*) databases. Alignment of the fluorescence intensities to the chromosomal coordinates of many known genes shows strong agreement between hybridization signals and annotated exons (Fig. 1A). To systematically determine the number of annotated genes detected with our approach, we devised a simple statistical method for scoring the observed transcriptional activity of annotated genes (*15*). This measurement essentially compares the fluorescence intensity of each probe within a gene against the median probe intensity across the entire microarray to determine whether they are significantly different. We scored 16,997 annotated genes from RefSeq, 35,823 genes from Ensembl, and 42,645 genes predicted by Genscan (*16*). Based on our criteria, transcription was detected from 64% (10,895), 57% (20,509), and 35% (14,884) of genes in each data set, respectively (Fig. 1B). These results agree with the expectation that fewer genes should be experimentally detected from annotation data sets that include putative genes predicted by homology or ab initio methods, as opposed to a curated collection of characterized genes. Nonetheless, our results provide the first genome-wide experimental confirmation that many of the predicted genes are transcribed, suggesting that they are functional. A subset of 9844 RefSeq genes with corresponding UniGene (*17*) annotations that indicate transcription in liver tissue was also examined; 70% (6907) of these were detected using our approach (Table 1).

In addition to detecting known and predicted genes, a primary goal of this study was to identify novel transcribed regions. Transcribed regions outside of previously annotated exons are expected to correspond primarily to (i) unannotated exons from alternatively spliced messages, (ii) under-represented 3′- and 5′-untranslated regions, (iii) non–protein-coding RNA transcripts, and (iv) novel transcripts coding for functional proteins. We considered aggregate transcription units consisting of at least five consecutive probes exhibiting fluorescence intensities in the top 90th intensity percentile, and the genomic coordinates of which lay within a 250-nt window (Fig. 2A). These were compiled from throughout the genome and their locations compared relative to those of annotated gene components (Fig. 2B). A total of 13,889 transcription units, ranging in size from 209 to 3438 nt, were identified in the genome by these criteria; ~400 are expected under the null hypothesis of zero transcription. One-third (4931) correspond to previously annotated exons; the remaining 8958 are new transcribed sequences that we refer to as transcriptionally active regions, or TARs (*5*). We located 1566 TARs within previously annotated introns on the same strand, raising the possibility that they correspond to overlooked exons. However, an equal number of TARs (1529) lie on the antisense strand of

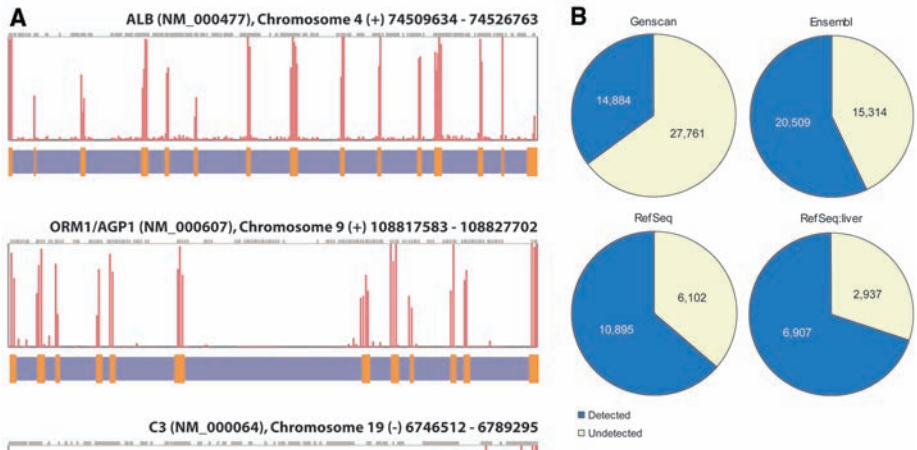

Fig. 1. (**A**) Annotated genes aligned with microarray fluorescence intensities. Comparison of the gene structures with intensity data shows strong agreement with expected exon-intron boundaries. The upper two examples illustrate uniform representation across the entire gene, whereas the lower two examples show a slight 3′ bias inherent in reverse-transcription labeling of mRNA. Gray segments at the top of each graph indicate the position of oligonucleotide probes tiled across nonrepetitive regions of the chromosome. (**B**) Proportion of genes detected from each of four annotation sources. The percentages of genes detected from each data set increase as the annotation shifts from solely ab initio predictions (Genscan) to fully characterized genes (RefSeq).

Table 1. Distribution of TARs relative to published gene annotation. Many TARs (40%) correspond to known exons; however, a significant fraction (38%) are located more than 10 kb from any previously annotated gene. BLAST results compare TARs to mammalian protein sequences and to the mouse genome. A total of 6934 (40%) of all TARs are homologs to the mouse genome (*e*-value $\leq 10^{-5}$), with 5656 (32%) homologous to protein sequences (25 to 30% of TARs belong to both categories), providing evidence for possible functional roles in humans.

	Total	Exons	Introns	<1 kb	1 to 10 kb	>10 kb
TARs	13,889	4,931	1,566	398	1,210	5,784
Poly(A)-associated TARs	3,628	1,991	229	153	303	952
Type I (AATAAA)	2,393	1,371	137	105	187	593
Type II (ATTAAA)	1,325	674	101	51	123	376
	BLAST: mouse genome			BLAST: mammalian proteins		
	$1e^{-5}$	$1e^{-10}$	$1e^{-20}$	$1e^{-5}$	$1e^{-10}$	$1e^{-20}$
TARs	5,419	4,747	3,761	4,349	4,008	3,311
Poly(A)-associated TARs	1,515	1,247	936	1,307	1,198	995
Type I (AATAAA)	1,044	862	637	905	830	685
Type II (ATTAAA)	517	423	328	436	401	340

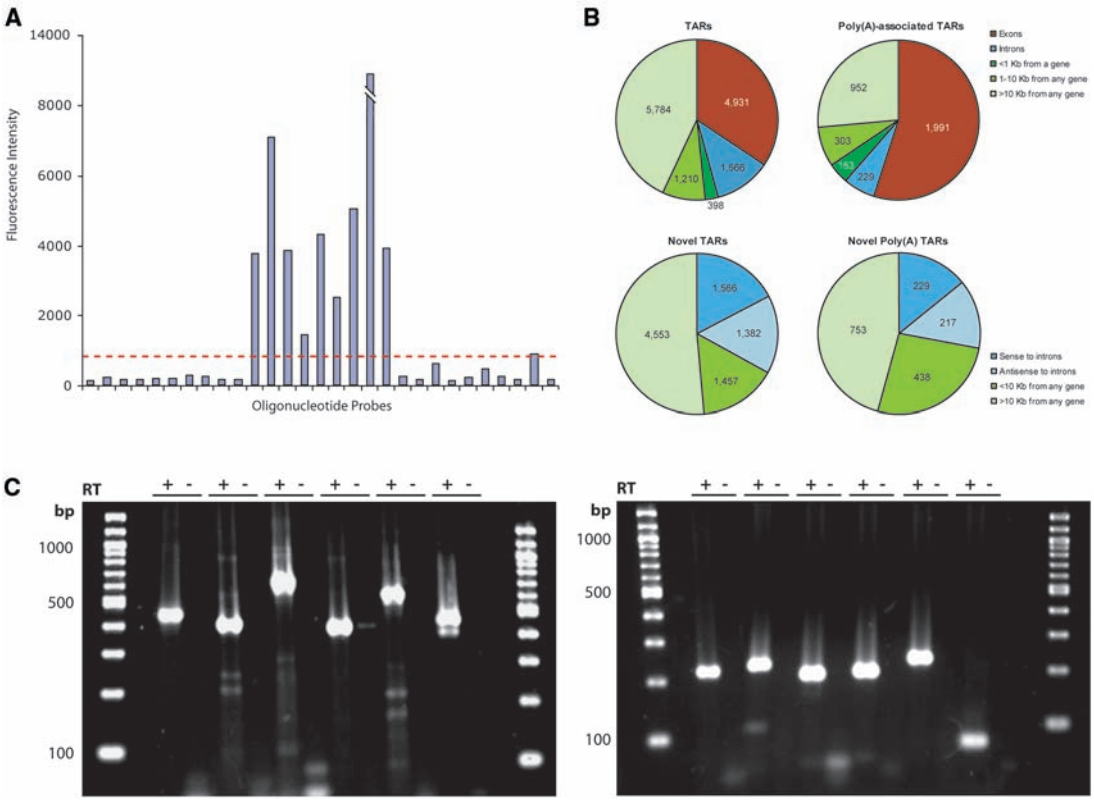

Fig. 2. (**A**) Example TAR: A series of consecutive probes in the genome with fluorescence intensities that rank above the 90th percentile over all probes on the array (indicated with a dashed line). (**B**) Distribution of TARs relative to annotated genes. Occupancy within gene components and proximity to known genes are depicted for all TARs (upper charts) and for novel TARs that lie outside annotated exons (lower charts). Most of the novel TARs are located more than 10 kb from any previously annotated gene, suggesting that these correspond to distinct transcribed sequences. (**C**) RT-PCR validation of TAR sequences. A group of variable-length TARs between 400 and 650 bp is shown (left) opposite a group of approximately equal-length poly(A)-associated TARs (right). PCR products are loaded adjacent to their corresponding negative control samples.

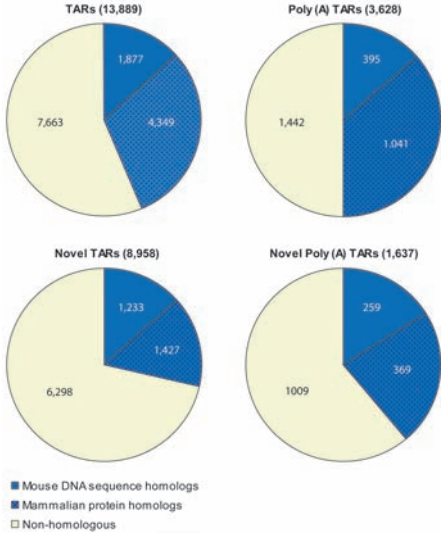

Fig. 3. Conservation between TARs and other mammalian sequences. Forty-one percent of TARs and 50% of poly(A)-associated TARs were found to be homologous, as were 29% and 39% of novel TARs from each category. A large number of TARs show significant similarity to known proteins (BLAST *e*-values $\leq 10^{-5}$), suggesting that many of these may be functional elements. A subset of these exhibited sequence similarity to regions of the mouse genome when restricted to similar *e*-values (solid blue sections).

introns, indicating that many of the intronic TARs likely represent novel transcription units. Over half of all TARs were found to be distal to annotated genes (greater than 10 kb from any gene), indicating the presence of an additional 5784 transcribed elements that are apparently unrelated to known genes.

We also used an independent set of criteria to identify TARs in which probe hybridization intensities were correlated with the presence of a polyadenylation signal 3′ of the active region. Here we considered transcription units of (exactly) five consecutive probes with fluorescence intensities in the top 80th intensity percentile appearing in windows of 250 nt, where the 3′ region contains or lies near a polyadenylation signal (*18*). Instances of "AATAAA" sequences were designated type I, and "ATTAAA" type II. An additional 3628 TARs were identified using this method; ~100 such instances are expected to occur at random in the genome. Most (1991) lie within annotated exons, whereas 952 are located more than 10 kb from any annotated gene. Of the 1371 type I and 674 type II poly(A) sequences identified within exons of known genes, 94% (1289) of type I and 90% (607) of type II instances occur in the 3′ exon of the gene in question, a strong indication of the effectiveness of this approach. The fraction of poly(A) TARs distinct from annotated exons (1637), combined with the 8948 novel TARs identified above, yields a total of 10,585 new transcribed sequences throughout the genome.

To validate the transcription of identified TARs with an independent method, we performed reverse transcriptase polymerase chain reaction (RT-PCR) assays using human liver poly(A)$^+$ RNA, targeting 48 poly(A)-associated and 48 non–poly(A)-associated TARs (*10*). Reactions were carried out in the presence and absence of reverse transcriptase; the latter served as a negative control. Of the 96 reactions, 90 (94%) amplified PCR products of the expected size in a single-pass assay with no detectable signal observed in the negative control (Fig. 2C). As a further validation, we compared the novel TARs against data derived from the second phase of the Kapranov *et. al* transcript mapping experiment on chromosomes 21 and 22 (*4*). We found that 41% of TARs match the transcribed fragments, or "transfrags," identified in their study. Because of the highly stringent selection of TARs in the present study, many low-abundance transcripts are not identified by these criteria, and we expect to have an appreciable false-negative rate.

We next compared the novel TARs with other mammalian DNA sequences to assess their potential for coding functional elements. BLAST (*19*) comparisons revealed that many TARs are homologous to sequences in the mouse genome. Of the 8958 novel TARs, 24% (2185) produced BLAST alignments with *e*-values less than 10^{-5}, with most of these (1486) having *e*-values less than 10^{-20}. This compares to 39%

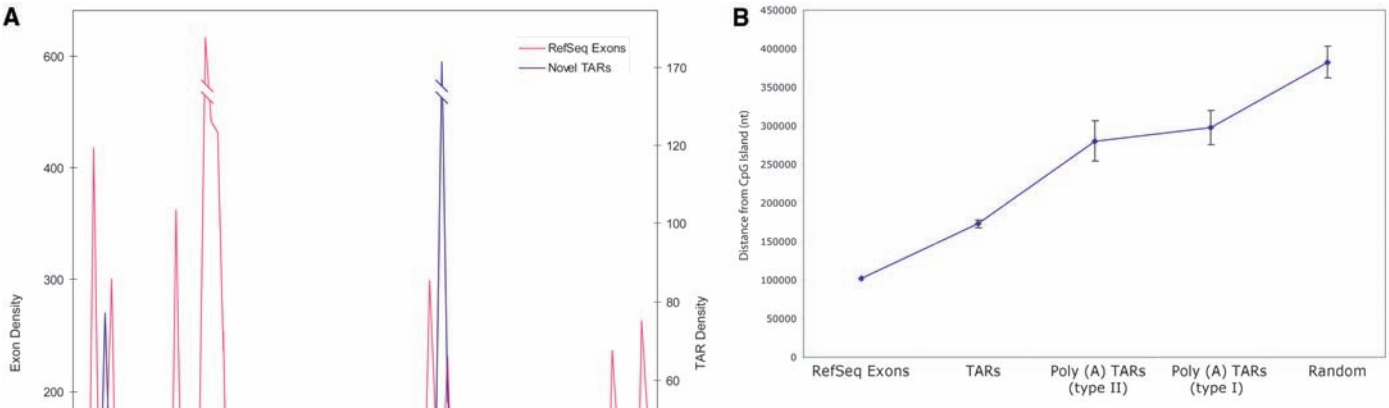

Fig. 4. (**A**) Density plot of RefSeq-annotated exons across human chromosome 3 compared with the density of novel transcriptionally active regions (TARs). The distribution of novel TARs is similar to that of annotated exons, indicating that they are colocated with genes on a global scale. Units on the abscissa are given in 1-Mb intervals. (**B**) Average distances to the nearest upstream CpG island for all RefSeq exons, novel TARs, novel poly(A)-associated TARs, and 1000 randomly selected locations in the genome. The distribution of novel TARs is similar to that of RefSeq exons, whereas the random locations are the most distant from CpG islands. As expected, the novel poly(A)-associated TARs are located at intermediate distances because they correspond primarily to 3′ exons.

(5419) of the initial set of 13,889 TARs (i.e., novel TARs and those corresponding to exons of known genes) that produced BLAST scores with *e*-values less than 10^{-5}; 3761 of these had *e*-values less than 10^{-20}. Similarly, 32% (532) of the 1637 novel poly(A)-associated TARs yielded BLAST alignments with *e*-values less than 10^{-5}, with 342 less than 10^{-20} (Fig. 3). Of the initial set of 5419 TARs and 1515 poly(A)-associated TARs found to be homologous to sequences in the mouse genome, 27% (1488) and 21% (321) from each category are located more than 10 kb from any previously annotated gene.

In addition to assessing the degree of genome conservation, we compared mouse proteins with TAR sequences that were translated in all possible reading frames (Table 1). A total of 16% (1427) and 12% (1091) of novel TARs produced BLAST matches less than 10^{-5} and 10^{-20}, respectively, compared with 31% (4329) and 24% (3311) of the total number of TARs with matches below these *e*-values. Higher percentages of poly(A)-associated TARs were found to be homologous to mouse proteins: 23% (369) of the novel subset and 36% (1307) of the total set of poly(A) TARs matched protein sequences with *e*-values less than 10^{-5}, with 19% (305) and 27% (995) in each category having *e*-values less than 10^{-20}. Thus, although many TARs are expected to encode proteins, novel TARs generally exhibit a lesser degree of sequence conservation than those intersecting known genes. This is particularly true for poly(A)-associated TARs owing to the higher degree of conservation of protein-coding sequences relative to 3′-untranslated regions.

To estimate the number of TARs potentially arising from the cross-hybridization of mRNA transcripts to sequences elsewhere in the genome, we compared 9408 novel TARs that additionally do not lie antisense to annotated exons to the library of human cDNA sequences in the Ensembl database. We found only 11% (1034) with at least 95% identity over a stretch of 150 nt. Of the remaining 8374 nonhomologous novel TARs, 347 were found to intersect the genomic coordinates of processed pseudogenes (*20*, *21*), providing evidence for possible pseudogenic transcription.

Finally, we examined the distribution of TARs relative to the locations of known genes and CpG islands. A density plot comparing TARs and RefSeq-annotated exons along chromosome 3 (Fig. 4A) revealed that TARs are located in the same regions as known genes. The density of TARs is correlated with the distribution of RefSeq-annotated genes along each chromosome (Pearson correlation coefficient $r^2 = 0.35$, $P < 0.002$). Comparison of distances to the nearest upstream CpG island indicates that the relative locations of novel TARs distal to annotated genes are similar to those of RefSeq exons, whereas the distal poly(A)-associated TARs are located farther away, which is expected because most of these should correspond to the 3′ ends of genes (Fig. 4B). The distances of all distal TARs to CpG islands were found to be significantly less than those of randomly selected locations ($P < 0.0001$).

Our findings demonstrate that it is possible to use high-resolution oligonucleotide microarrays for the comprehensive analysis of the human genome. Because many transcribed sequences are located in distinct intergenic regions distant from known genes, their precise mapping can only be accomplished using genomic tiling arrays in which nearly all of the nonrepetitive DNA is available for hybridization to RNA transcripts. Several bacterial artificial chromosome (BAC) clone-based genomic tiling arrays have been developed for comparative genomic hybridization (CGH) studies in humans (*22*, *23*); however, the identification of short transcription units requires interrogating the genome sequence at a resolution of tens of base pairs, a measurement that is not possible to obtain with BAC technology.

In summary, we identified thousands of new transcribed regions and confirmed the transcription of predicted genes on a global scale. Our results provide a draft expression map for the entire genome, revealing a much more extensive and diverse set of expressed sequences than was previously annotated. Conservation between many of the novel transcribed sequences and well-characterized mouse proteins provides strong evidence that a large number of them are likely to encode functional transcripts. Many conserved transcribed sequences are located in regions distal to known genes, and a notable fraction of these are of sufficient length to encode proteins of 300 or more amino acids. The remainder may encode small proteins, untranslated exons, or RNAs whose functions have yet to be elucidated

(*24*, *25*). These latter RNAs may serve alternate regulatory or structural roles and await detailed characterization.

References and Notes

1. D. W. Selinger *et al.*, *Nat. Biotechnol.* **18**, 1262 (2000).
2. B. Tjaden *et al.*, *Nucleic Acids Res.* **30**, 3732 (2002).
3. K. Yamada *et al.*, *Science* **302**, 842 (2003).
4. P. Kapranov *et al.*, *Science* **296**, 916 (2002).
5. J. L. Rinn *et al.*, *Genes Dev.* **17**, 529 (2003).
6. E. F. Nuwaysir *et al.*, *Genome Res.* **12**, 1749 (2002).
7. T. J. Albert *et al.*, *Nucleic Acids Res.* **31**, e35 (2003).
8. E. S. Lander *et al.*, *Nature* **409**, 860 (2001).
9. J. C. Venter *et al.*, *Science* **291**, 1304 (2001).
10. Materials and methods are available as supporting material on *Science* Online. Additional information can be found at http://transcriptome.gersteinlab.org. Experimental data and associated microarray designs are available in the NCBI Gene Expression Omnibus (GEO) under series GSE1904, sample records GSM34073 to GSM34213, and platform records GPL1539 to GPL1673.
11. P. Bertone *et al.*, data not shown.
12. K. D. Pruitt *et al.*, *Trends Genet.* **16**, 44 (2000).
13. T. Hubbard *et al.*, *Nucleic Acids Res.* **30**, 38 (2002).
14. E. Birney *et al.*, *Genome Res.* **14**, 925 (2004).
15. Each probe is assigned a value of 1 if its fluorescence intensity is greater than the median intensity of all probes on the array, and 0 otherwise. For a given gene, the expected count of 1's within annotated exons follows a binomial distribution; an unusually high count of 1's therefore yields low *P* values (sign test). Genes having *P* values < 0.05 were regarded as demonstrating positive hybridization.
16. C. Burge, S. Karlin, *J. Mol. Biol.* **268**, 78 (1997).
17. D. L. Wheeler *et al.*, *Nucleic Acids Res.* **31**, 28 (2003).
18. Polyadenylation signals are required to appear downstream of the 15th nucleotide of the 3′ oligonucleotide in the transcribed region. An additional 51 ($46 + 5$) downstream nucleotides are included in the calculation to ensure full coverage of the sequence.
19. S. F. Altshul *et al.*, *J. Mol. Biol.* **215**, 403 (1990).
20. P. M. Harrison *et al.*, *Genome Res.* **12**, 272 (2002).
21. Z. Zhang *et al.*, *Genome Res.* **13**, 2541 (2003).
22. P. G. Buckley *et al.*, *Hum. Mol. Genet.* **11**, 3221 (2002).
23. A. S. Ishkanian *et al.*, *Nat. Genet.* **36**, 299 (2004).
24. J. S. Mattick, *Bioessays* **25**, 930 (2003).
25. D. Kampa *et al.*, *Genome Res.* **14**, 331 (2004).

26. This work was supported by NIH grant P50 HG02357.

Supporting Online Material

www.sciencemag.org/cgi/content/full/1103388/DC1
Materials and Methods
Microarray hybridization protocols
DNA sequences of transcriptionally active regions
Fig. S1

29 July 2004; accepted 3 November 2004
Published online 11 November 2004;
10.1126/science.1103388
Include this information when citing this paper.

Use of Logic Relationships to Decipher Protein Network Organization

Peter M. Bowers,[1,2] Shawn J. Cokus,[3] David Eisenberg,[1,2] Todd O. Yeates[2,4]*

A major focus of genome research is to decipher the networks of molecular interactions that underlie cellular function. We describe a computational approach for identifying detailed relationships between proteins on the basis of genomic data. Logic analysis of phylogenetic profiles identifies triplets of proteins whose presence or absence obey certain logic relationships. For example, protein C may be present in a genome only if proteins A and B are both present. The method reveals many previously unidentified higher order relationships. These relationships illustrate the complexities that arise in cellular networks because of branching and alternate pathways, and they also facilitate assignment of cellular functions to uncharacterized proteins.

The sequencing of multiple genomes from diverse species has tremendous potential to impact our understanding of biology, both by providing a census of all proteins and by enabling subsequent analysis of their functions (*1*–*6*). Various patterns across multiple complete genomes have been used to infer biological interactions and functional linkages between proteins (*6*–*14*). These include observations of two distinct proteins from one organism being genetically fused into a single protein in another organism (*13*, *14*) and the tendency of two proteins to occur in chromosomal proximity across multiple organisms (*12*, *15*). When a sufficiently large number of genomes were fully sequenced, it became possible with the phylogenetic profile approach (*11*, *16*, *17*) to detect functional relationships between proteins exhibiting statistically similar patterns of presence or absence. Because sequenced genomes allow us to catalog all of the proteins encoded in each organism, we can determine the pattern describing a protein's presence or absence by searching for its homologs across *N* organisms, the result of which is an *N*-dimensional vector of ones (present) and zeros (not present) referred to as its phylogenetic profile.

Original implementations of the phylogenetic profile method sought to infer "links" between pairs of proteins with similar profiles (*11*). A subsequent variation on that idea linked proteins if their profiles represented the negation of each other (*18*, *19*). These ideas are consistent with the simplest notion of how two proteins might be related in a cell, with the presence of one protein implying the presence or absence of another. Such simple patterns might be expected when two proteins are required to form a structural complex or when two proteins carry out sequential steps in an unbranched metabolic pathway. However, such simple relationships cannot adequately describe the full complexity of cellular networks that involve branching, parallel, and alternate pathways. The observed complexity of cellular networks leads one to expect the existence of higher order logic relationships involving a pattern of presence or absence of multiple proteins. Furthermore, evolutionary divergence, convergence, and horizontal transfer events lead us to expect relationships between multiple gene families that are more complex than can be described by pairwise phylogenetic similarity. Analysis of cellular pathways and networks in terms of logic relations has attracted recent interest (*20*, *21*), and the growing number of sequenced genomes now makes it possible to search for logic relations.

Here, we perform a complete analysis of the logic relations possible between triplets of phylogenetic profiles and demonstrate the power of the resulting logic analysis of phylogenetic profiles (LAPP) in illuminating relationships among multiple proteins and inferring the coarse function of large numbers of uncharacterized protein families. There are eight possible logic relationships combining two phylogenetic profiles to match a third profile (Fig. 1A). For instance, protein C might be present if and only if proteins A and B are both present (denoted here as a type 1 logic relationship), from which we would infer that the function of protein C is necessary only when the functions of proteins A and B are both present. Alternatively, gene C may be present if and only if either A or B is present (a type 7 logic relationship), which is seen when different organisms use two different protein families in combination with a common third protein to accomplish some task (for example, a combination of A and C or B and C). Several of the eight possible logic relationships can be intuitively understood to describe commonly observed biological scenarios, whereas a few of the logic relationships are not easily related to real biological situations.

To identify protein triplets that exhibit the logic relationships described in Fig. 1, we first created a set of binary-valued vectors describing the presence or absence of

[1]Howard Hughes Medical Institute, [2]Institute for Genomics and Proteomics, [3]Department of Mathematics, [4]Department of Chemistry and Biochemistry, University of California, Los Angeles, Los Angeles, CA 90095, USA.

*To whom correspondence should be addressed. E-mail: yeates@mbi.ucla.edu

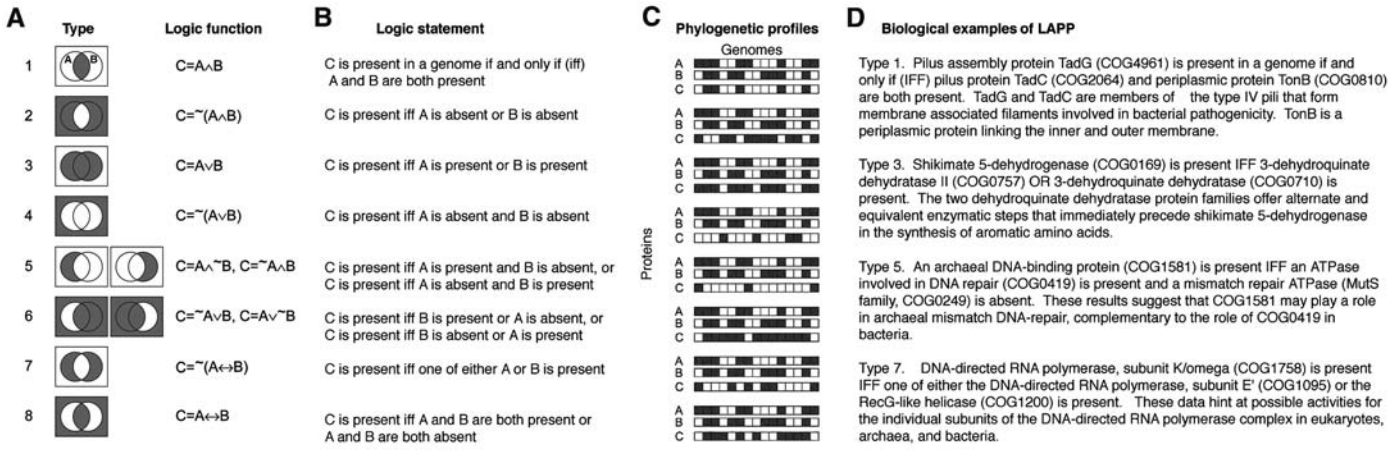

Fig. 1. Detection of pathway relationships among proteins based on a logic analysis of phylogenetic profiles (LAPP). (**A**) Venn diagrams and associated logic statements illustrate the eight distinct kinds of logic functions that describe the possible dependence of the presence of C on the presence of A and B, jointly. Logic functions are grouped together if they are related by a simple exchange of proteins A and B. The symbols ∧, ∨, ~, and ↔ indicate "logical AND," "logical OR," "logical negation," and "logical equality," respectively. (**B**) The meaning of each logic relationship is described in a single text sentence, (**C**) hypothetical phylogenetic profiles are used to illustrate the eight possible logic functions, and (**D**) for the four most commonly observed logic types, real biological examples are given that illustrate the ternary relationships identified from actual phylogenetic profiles.

each of the known protein families across 67 fully sequenced organisms. Specifically, the complete set of proteins was categorized into 4873 distinct families known as clusters of orthologous groups (COGs) (*22*, *23*). Next, we systematically examined all triplet combinations of the profiles and rank-ordered them according to how well the logical combination $f(a,b)$ of two profiles predicted a third profile, c. Further, we also required that neither profile a nor b alone was predictive of c. We calculated uncertainty coefficients for $U(c|a)$, $U(c|b)$, and the logically combined profile $U(c|f(a,b))$, where

$$U(x|y) = [H(x) + H(y) - H(x,y)]/H(x)$$

and H refers to the entropy of the individual or joint distributions (*24*). The value of U can range between 1.0, where x is a deterministic function of y, and 0.0, where x is completely independent of y. We selected triplets whose individual pairwise uncertainty scores described protein profile c poorly [$U(c|a) < 0.3$ and $U(c|b) < 0.3$] but whose logically combined profile [$U(c|f(a,b)) > 0.6$] described c well.

A hypothetical set of profiles can illustrate the approach (Fig. 1C). Under a type 3 logic relationship, protein C is present whenever protein A, protein B, or both are present. The pairwise comparisons of profiles (AC, BC, and AB) each yield limited information, whereas a phylogenetic profile logically combining proteins A and B matches the phylogenetic distribution of protein C exactly and has a triplet uncertainty score of $U = 0.48$. In contrast, a triplet containing hypothetical randomized profiles with the same number of protein homologs as in the previous example has a triplet uncertainty coefficient of $U = 0.03$ and does not correspond closely to any of the eight logic types.

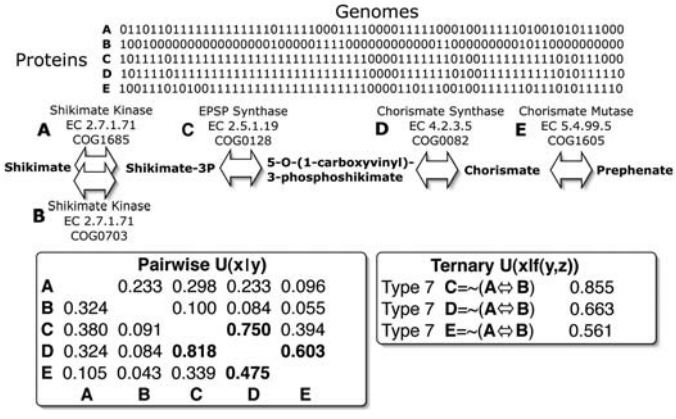

Fig. 2. Three logic examples from the aromatic amino acid synthesis pathway, obtained as high-scoring ternary relationships in an analysis of all possible 62 billion protein triplets. In this example, a calculation based on traditional pairwise phylogenetic profile analysis links only the terminal enzymes in the pathway (proteins C and D and D and E). The triplet and pairwise uncertainty coefficients, U, highlight the additional associations observed with ternary relationships, A and B with C, D, and E.

Logic analysis of phylogenetic profiles yields thousands of computed relationships among protein families that cannot be detected by traditional pairwise phylogenetic analysis, enabling a more intricate description of predicted relationships (Fig. 2 and fig. S1). The synthesis of aromatic amino acids proceeds through the shikimate pathway. A logic analysis of five participating proteins shows that shikimate can be converted to the end product prephenate by one of two possible routes, leading to a type 7 logic relationship. When either one shikimate kinase protein family (protein A, COG1685) or an alternate shikimate kinase protein family (protein B, COG0703) is present in an organism, then excitatory postsynaptic potential (EPSP) synthase must also be present (protein C, COG0128) ($U = 0.85$) to carry out the subsequent enzymatic step. The same type 7 logic relationship is also observed between alternate shikimate kinase enzymes and the successive chorismate synthase (protein D, COG0082) and chorismate mutase (protein E, COG1605) enzymatic steps of the pathway. The ordering of the metabolic steps that follow shikimate kinase is predicted by the value of successive U coefficients, where EPSP synthase (second step, $U = 0.85$) is most strongly linked to shikimate kinase, followed directly by the chorismate synthase (third step, $U = 0.66$) and lastly by chorismate mutase (fourth step, $U = 0.56$). We can conclude that organisms synthesize chorismate and prephenate from shikimate with the use of only one of two possible alternate routes: pathways consisting of either ordered enzymes A-C-D-E or enzymes B-C-D-E.

Our LAPP recovers 750,000 previously unknown relationships among protein families ($U(c|(f(a,b))) > 0.60$; $U(c|b) < 0.30$; $U(c|a) < 0.30$), whose validity can be assessed by comparing known annotations of the linked proteins (tables S2 to S5). The ability to recover links between proteins annotated as belonging to a major functional category has been used widely to corroborate computational inferences of protein interactions (*4*, *5*). We

assessed the accuracy of the logic relationships obtained for the triplet profiles by using the metrics and threshold values detailed above, where each protein family is annotated as belonging to one or more of the 20 COG major functional categories. Figure 3A shows a section taken from a three-dimensional histogram that describes the frequency of observed logic relationships in which protein A of the triplet is annotated as belonging to the COG functional category N, cell motility. One of the most frequently observed triplet relationships in this section relates three proteins belonging to the cell motility category, confirmation that the triplet associations link proteins closely related in function. Other triplets involve two proteins from the motility category and a third protein of another COG category, producing recognizable horizontal and vertical bands in the histogram. For instance, the category combinations NNU (COG category U, intracellular trafficking and secretion) and NNS (COG category S, unknown function) are also plentiful. Connections between these categories make intuitive sense and facilitate placement of unannotated proteins within the context of specific cellular networks of interacting proteins.

The LAPP method leads to a set of statistically significant ternary relationships (Fig. 3B and fig. S2) that are distinct from and more numerous than the relationships that can be inferred by using traditional pairwise analysis. A matrix of randomized phylogenetic profiles, containing the same individual and pairwise distributions as the native profiles, was used to assess the probability of observing a given uncertainty coefficient score by chance. Triplets with $U > 0.60$ are observed from the unshuffled vectors $\sim 10^2$ times more frequently than from shuffled profiles and $\sim 10^4$ more frequently when $U > 0.80$. A P value for each triplet relationship can be calculated by enumerating all possible values of U that could be obtained from shuffled profiles while maintaining the individual and pairwise distributions, where P is equal to the number of trials that exceed the observed value of U divided by the total number of trials. More than 98% of the identified triplets ($U > 0.6$) have $P < 0.05$, and more than 75% of the identified triplets have $P < 0.005$. Lastly, the eight distinct logic types occur with widely varying frequencies within the set of significant ternary relationships (Fig. 3C), a trend consistent with our understanding of evolution and biological relationships. Logic types 1, 3, 5, and 7 are observed frequently in the biological data, whereas logic types 2, 4, and 8 are more difficult to relate to simple cellular logic and are observed only rarely.

The 50 most significant computed ternary relationships from Fig. 3A are shown in network form (Fig. 3D). The proteins linked include secreted virulence factors, adhesin proteins necessary for bacterial pathogenesis,

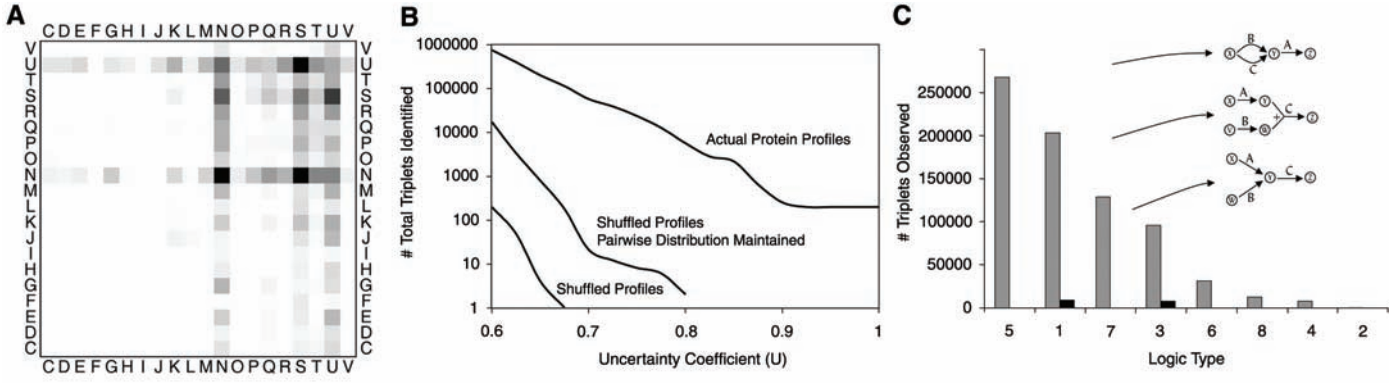

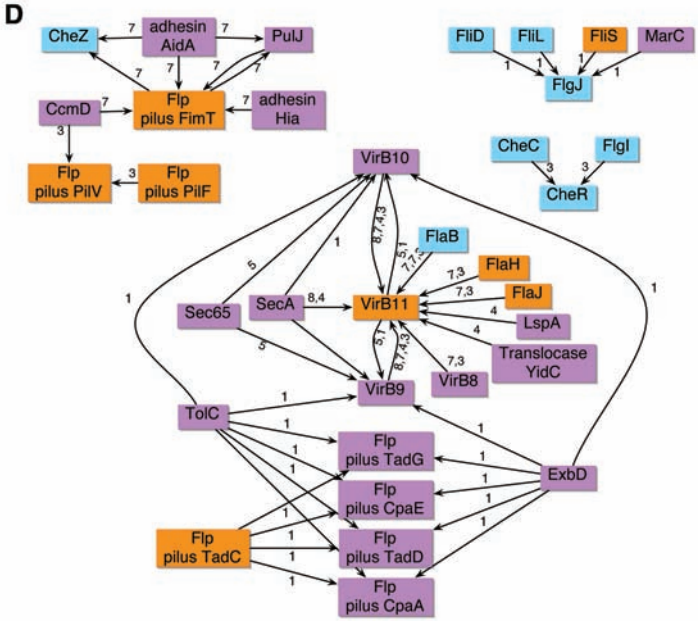

Fig. 3. A benchmark analysis of the ability of LAPP to identify functionally related proteins. (**A**) A section from a three-dimensional histogram describing the prevalence of ternary relationships among high-scoring triplets. The histogram is for logic function type 3 and covers triplets of proteins A, B, and C whose COG major functional categories (table S3) are described by N, *x* axis, and *y* axis, where N is cell motility. Because protein families are not uniformly distributed across COG categories, *Z* scores are plotted to facilitate comparison of histogram bin counts. The mean μ and variance σ^2 for each bin was calculated for a distribution of 750,000 triplets with randomly selected protein families, and an observed bin count, n, was transformed by $Z = (n - \mu)/\sigma$; the gray scale is linear, with white corresponding to $Z = 0.0$ and black to $Z = 75$. (**B**) A plot of the cumulative number of protein triplets recovered at an uncertainty coefficient score greater than a given threshold. LAPP analysis of a randomized matrix, containing shuffled profiles that preserved the overall individual and pairwise distributions (fig. S2), reveals only ~20,000 triplets with high coefficient scores. In contrast, we detect 750,000 triplets from an analysis of the original, unshuffled biological protein profiles. (**C**) A histogram showing the number of identified triplets ($U > 0.6$) for each of the eight logic function types for randomized (black) and real (gray) phylogenetic profiles. Diagrams illustrate one possible pathway arrangement consistent with that type of logic. Some diagrams describe potential pathways combined across multiple organisms, but the three proteins of interest may not always occur together in any single given genome. (**D**) An illustration of the 50 highest scoring relationships ($U > 0.75$) involving proteins from the cell motility and intracellular trafficking and secretion functional categories. Cell motility proteins are colored light blue, intracellular trafficking and secretion are colored magenta, and proteins annotated as both are colored in orange. Edges are shown between proteins A-C and B-C of each logic triplet, with each edge labeled according to the logic function type used to associate the proteins' families.

chemotaxis proteins, and translocase proteins. The network contains previously unknown interactions that suggest mechanisms connecting bacterial pathogenesis and chemotaxis. For instance, CheZ, a chemotaxis dephosphorylase that regulates cell motility, is linked to the surface receptor and virulence factors adhesin AidA and Flp pilus-associated FimT.

The new higher order protein associations detected by LAPP provide a framework for understanding the complex logical dependencies that relate proteins to one another in the cell. They may also be useful in modeling and engineering biological systems, generating biological hypotheses for experimentation, and investigating additional protein properties. It is likely that the logic relationships between proteins in the cell extend beyond ternary relationships to include much larger sets of proteins. We anticipate that the ideas underlying the logical analysis of phylogenetic profiles can be extended to the investigation of other kinds of genomic data, such as gene expression, nucleotide polymorphism, and phenotype data.

References and Notes

1. S. Li *et al.*, *Science* **303**, 540 (2004); published online 2 January 2004 (10.1126/science.1091403).
2. M. Strong, P. Mallick, M. Pellegrini, M. J. Thompson, D. Eisenberg, *Genome Biol.* **4**, R59 (2003).
3. L. Giot *et al.*, *Science* **302**, 1727 (2003); published online 6 November 2003 (10.1126/science.1090289).
4. P. M. Bowers *et al.*, *Genome Biol.* **5**, R35 (2004).
5. C. von Mering *et al.*, *Nucleic Acids Res.* **31**, 258 (2003).
6. A. H. Y. Tong *et al.*, *Science* **303**, 808 (2004).
7. Y. Ho *et al.*, *Nature* **415**, 180 (2002).
8. A. C. Gavin *et al.*, *Nature* **415**, 141 (2002).
9. T. Ito *et al.*, *Proc. Natl. Acad. Sci. U.S.A.* **98**, 4569 (2001).
10. P. Uetz *et al.*, *Nature* **403**, 623 (2000).
11. M. Pellegrini, E. M. Marcotte, M. J. Thompson, D. Eisenberg, T. O. Yeates, *Proc. Natl. Acad. Sci. U.S.A.* **96**, 4285 (1999).
12. R. Overbeek, M. Fonstein, M. D'Souza, G. D. Pusch, N. Maltsev, *Proc. Natl. Acad. Sci. U.S.A.* **96**, 2896 (1999).
13. E. M. Marcotte *et al.*, *Science* **285**, 751 (1999).
14. A. J. Enright, I. Iliopoulos, N. C. Kyrpides, C. A. Ouzounis, *Nature* **402**, 86 (1999).
15. M. D. Ermolaeva, O. White, S. L. Salzberg, *Nucleic Acids Res.* **29**, 1216 (2001).
16. M. Pellegrini, M. Thompson, J. Fierro, P. Bowers, *J. Cell. Biochem. Suppl.* **37**, 106 (2001).
17. J. Wu, S. Kasif, C. DeLisi, *Bioinformatics* **19**, 1524 (2003).
18. E. Morett *et al.*, *Nat. Biotechnol.* **21**, 790 (2003).
19. S. V. Date, E. M. Marcotte, *Nat. Biotechnol.* **21**, 1055 (2003).
20. R. Milo *et al.*, *Science* **298**, 824 (2002).
21. R. Milo *et al.*, *Science* **303**, 1538 (2004).
22. R. L. Tatusov, E. V. Koonin, D. J. Lipman, *Science* **278**, 631 (1997).
23. R. L. Tatusov *et al.*, *BMC Bioinformatics* **4**, 41 (2003).
24. H. Theil, *Statistical Decomposition Analysis with Applications in the Social and Administrative Sciences*, vol. 14 of *Studies in Mathematical and Managerial Economics* (North-Holland, Amsterdam, 1972), pp. xvi, 337.

25. This work was supported by the U.S. Department of Energy and the Howard Hughes Medical Institute.

Supporting Online Material

www.sciencemag.org/cgi/content/full/306/5705/2246/DC1
Materials and Methods
Figs. S1 and S2
Tables S1 and S2

28 July 2004; accepted 22 November 2004
10.1126/science.1103330

Reproductive Effort, Molting Latitude, and Feather Color in a Migratory Songbird

D. Ryan Norris,[1,4]* Peter P. Marra,[3] Robert Montgomerie,[1] T. Kurt Kyser,[2] Laurene M. Ratcliffe[1]

Toward the end of the breeding season, migratory songbirds face crucial tradeoffs between the timing of reproduction, molt, and migration. Using stable hydrogen isotopes, we show that male American redstarts investing in high levels of reproduction late in the season adopt a unique strategy of combining molt and migration. Tail feathers molted during migration also reflect less orange-red light, indicating reduced carotenoid concentration. Thus, we show how reproduction in a migratory animal can influence both life history strategies (location of molt) and social signals (feather color) during subsequent periods of the annual cycle.

Each year, toward the end of the temperate breeding season, billions of songbirds face crucial energetic tradeoffs between the costs of reproduction, the replacement of feathers (molt), and the hazards of long-distance migration to the tropics (*1*). To date, our inability to track individual birds moving between their breeding and wintering grounds has made studying the interaction between these events virtually impossible. Using stable hydrogen isotopes and reflectance spectrometry, we investigate how reproduction affects both molting latitude and the color of molted feathers in an 8-g neotropical-nearctic migratory songbird, the American redstart (*Setophaga ruticilla*).

Redstarts (Fig. 1A) are socially monogamous, single-brooded passerine birds that provide biparental care to young for 2 to 3 weeks after the young leave the nest (*2*). Individuals breed in the deciduous forests of temperate North America and winter in the Caribbean and Middle America. From 2001 to 2004, we sampled tail feathers from individually marked males at a breeding site in Ontario, Canada (44°34′ N, 76°19′ W). These males were known to have bred at the same location the previous year (*3*). In eastern North America, stable hydrogen isotope (δD) values in precipitation follow a strong latitudinal gradient where low (more negative) values correspond to higher latitudes (Fig. 1B) (*4*). δD signatures in precipitation are transferred through food webs to higher-order consumers, including birds (*5*). Because feathers are metabolically inert after growth, δD values sampled from feathers in a given breeding season indicate the molting latitude from the previous autumn.

[1]Department of Biology, [2]Department of Geological Sciences and Engineering, Queen's University, Kingston, Ontario K7L 3N6, Canada. [3]Smithsonian Environmental Research Center, Post Office Box 28, 647 Contees Wharf Road, Edgewater, MD 21037, USA. [4]Centre for Applied Conservation Research, Forest Sciences Center, University of British Columbia, Vancouver, British Columbia V6T 1Z4, Canada.

*To whom correspondence should be addressed. E-mail: ryann@biology.queensu.ca

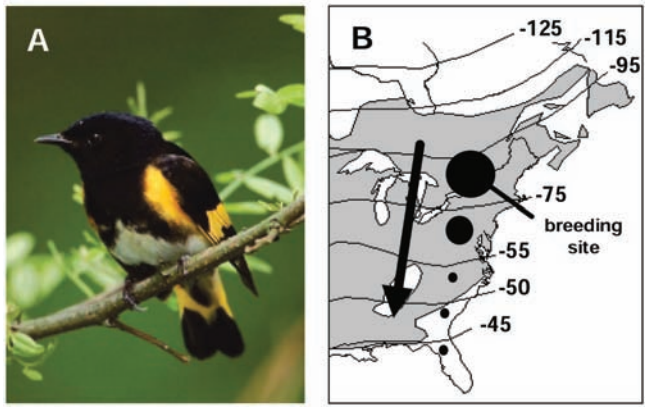

Fig. 1. (**A**) Adult male American redstart after complete autumn molt. [Photograph by Robert Royse] (**B**) Distribution of post-breeding molt locations determined from δD values of tail feathers (n = 30). Contour lines indicate expected δD values throughout eastern North America (*4*). The eastern portion of the breeding range is shaded light gray (*2*). The size of the circles represents the frequency distribution of molt locations: large (near breeding grounds), n = 18 individuals; medium, n = 9; small, n = 1. The arrow shows the most likely fall migration route based on band-recapture data (*16*).

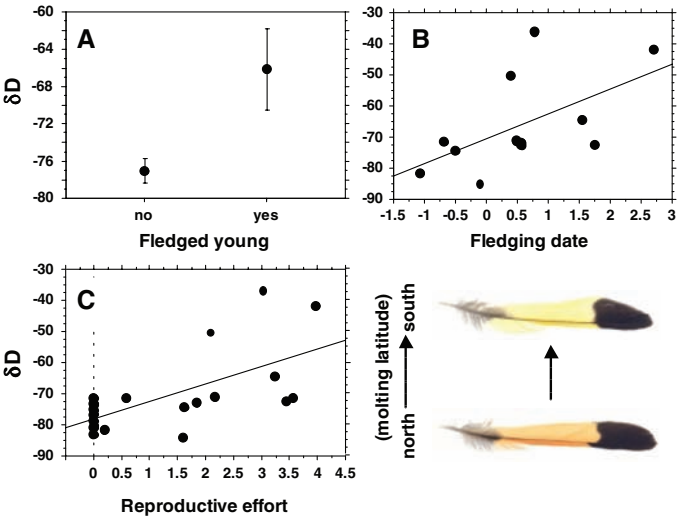

Fig. 2. Relation between molting latitude (δD) and reproduction of male American redstarts during the preceding breeding season. (**A**) Males that fledged young (n = 12) had lower mean (±SE) δD values than males that did not fledge young (n = 9, t = –2.09, P = 0.05). (**B**) Males that fledged young later in the season (fledging date standardized by year) tended to molt farther south, on average, than males that fledged young early in the season (r^2 = 0.32, P = 0.05, n = 12). (**C**) Males with high reproductive effort scores were more likely to molt south of the breeding grounds than males with low scores (r^2 = 0.41, P = 0.002, n = 21). Reproductive effort scores are a combination of the number of young fledged and fledging date (zeros = males that did not fledge young). (Lower right) Example of the color of a tail feather from a male that molted on the breeding grounds (bottom) versus a male that molted south of the breeding grounds (top).

Our analysis shows that 40% (12 out of 30) of males molted on staging areas up to 2000 km south of their breeding grounds [δD values for these birds were more positive than expected from the breeding ground signatures (Fig. 1B) (*6*)]. We then tested whether molting latitude was related to the amount and timing of parental care that adult males provided during the preceding breeding season. Males that successfully fledged young tended to molt tail feathers farther south than males that failed to fledge young (Fig. 2A). Among males that fledged young successfully, individuals that raised young late in the season tended to molt farther south than males that raised young early in the season (Fig. 2B). To look at these factors simultaneously, we developed an index of reproductive effort that took into account both the timing and the amount of parental care (*7*). Males with the highest reproductive effort scores were most likely to molt during migration, whereas males with scores of zero molted on the breeding grounds (Fig. 2C).

Using reflectance spectrometry (*3*), we also examined the influence of molt-migration on the signal quality of a male's feathers. Red chroma, a measure of the relative amount of light reflected in the red (575 to 700 nm) segment of the bird-visible spectrum (320 to 700 nm), was negatively correlated with δD (r^2 = 0.31, P = 0.004, n = 24). Thus, feathers molted farther south were less saturated with orange-red coloration than feathers molted on the breeding grounds (Fig. 2C), indicating that they also had lower carotenoid concentration (*8*).

Our findings show the importance of understanding how interactions among events that occur during different periods of the annual cycle can shape the ecology, behavior, and life history of migratory animals. Within a relatively short time period, migratory birds face tradeoffs between three of the most energetically demanding activities of the year. A short-lived migratory songbird providing parental care late in the breeding season is more likely to replace its feathers on staging areas during migration than on the breeding grounds after reproduction. Molting during migration may subsequently reduce survival during the following winter by delaying arrival in the tropics and limiting access to high-quality habitat. Winter habitat quality is known to influence physical condition and departure for spring migration, as well as the timing of arrival and reproduction on the temperate breeding grounds (*9*, *10*).

Molt-migration can also influence feather color, a trait important for sexual selection during the following breeding season. Carotenoids in feathers are naturally occurring pigments that reflect immunocompetence (*11*), signal male quality, and affect female mate choice in many bird species (*12*). Physiological stress during molt can reduce carotenoid deposition in feathers (*13*), suggesting a mechanism by which redstarts that overlap molt and migration produce these poorer quality sexual signals.

Finally, studies using stable isotopes to measure both the geographic connectivity of populations between tropical and temperate regions (*14*) and breeding dispersal (*15*) assume that feathers provide an accurate chemical signature of the past year's breeding location. Our results suggest that this technique may miscalculate the numbers and locations of birds breeding at north-temperate latitudes and that future studies should consider molt ecology when using stable isotopes to track birds year-round.

References and Notes

1. R. B. Payne, in *Avian Biology, Vol. 2*, D. S. Farner, J. R. King, Eds. (Academic Press, New York, 1972), pp. 103–155.
2. T. W. Sherry, R. T. Holmes, in *The Birds of North America, No. 277*, A. Poole, F. Gill, Eds. (Academy of Natural Sciences, Philadelphia, PA, 1997), pp. 1–31.
3. Materials and methods are available as supporting material on *Science* Online.
4. K. A. Hobson, L. I. Wassenaar, *Oecologia* **109**, 142 (1997).
5. L. I. Wassenaar, K. A. Hobson, *Environ. Sci. Technol.* **35**, 1845 (2001).
6. δD values from the tip and base of feathers were highly correlated (r^2 = 0.66, P < 0.0001, n = 18) with the slope (1.2 ± 0.2 SE) and intercept (14.6 ± 11.7 SE) of the geometric mean regression not significantly different from 1 and 0, respectively (t-test slope: t = 1.03, P > 0.10; intercept: t = 1.24, P > 0.10; df = 32), suggesting that retrices of each individual were generally molted at a single location. We present results from δD values of the feather base only. δD values were similar between years (analysis of variance: $F_{2,27}$ = 0.95, P = 0.40), so data collected from 2002–2004 were pooled.
7. To calculate reproductive effort, we added the z scores (standardized by year) of fledging date (timing of breeding) and the number of young raised, then added 1.0 to each score to remove negative values, allowing individuals that did not fledge young to be assigned a score of zero. Thus, the highest scores for reproductive effort represented individuals that fledged many young late in the breeding season.
8. L. Saks *et al.*, *Funct. Ecol.* **17**, 555 (2003).
9. P. P. Marra, K. A. Hobson, R. T. Holmes, *Science* **282**, 1884 (1998).
10. D. R. Norris *et al.*, *Proc. R. Soc. London Ser. B* **271**, 59 (2004).
11. K. J. McGraw, D. R. Ardia, *Am. Nat.* **162**, 704 (2003).
12. G. E. Hill, *A Red Bird in a Brown Bag: The Function and Evolution of Colorful Plumage in the House Finch* (Oxford Univ. Press, New York, 2002).
13. G. E. Hill, *J. Avian Biol.* **31**, 559 (2000).
14. D. R. Rubenstein *et al.*, *Science* **295**, 1062 (2002).
15. G. R. Graves, C. S. Romanek, A. R. Navarro, *Proc. Natl. Acad. Sci. U.S.A.* **99**, 8096 (2002).
16. R. T. Holmes, T. W. Sherry, in *Ecology and Conservation of Neotropical Migrant Landbirds*, J. M. Hagan III, D. W. Johnston, Eds. (Smithsonian Institution Press, Washington, DC, 1992), pp. 563–575.

17. We thank K. Klassen, A. Vuletich, and K. Scott for help analyzing feather samples and K. Langin, D. White, and many others for excellent field assistance. Supported by NSF grant 0089565 (P.P.M.), the Natural Sciences and Engineering Research Council of Canada (L.M.R., T.K.K., R.M., and D.R.N.), the Canadian Foundation for Innovation and Ontario Innovation Trust (T.K.K. and L.M.R.), the Smithsonian Institution (P.P.M. and D.R.N.), and the American Museum of Natural History (D.R.N.).

Supporting Online Material

www.sciencemag.org/cgi/content/full/306/5705/2249/DC1
Materials and Methods
SOM Text
References

2 August 2004; accepted 5 October 2004
10.1126/science.1103542

Dephosphorylation of the Calcium Pump Coupled to Counterion Occlusion

Claus Olesen,[1]* Thomas Lykke-Møller Sørensen,[1]*
Rikke Christina Nielsen,[1]* Jesper Vuust Møller,[2]† Poul Nissen[1]†

P-type ATPases extract energy by hydrolysis of adenosine triphosphate (ATP) in two steps, formation and breakdown of a covalent phosphoenzyme intermediate. This process drives active transport and countertransport of the cation pumps. We have determined the crystal structure of rabbit sarcoplasmic reticulum Ca^{2+} adenosine triphosphatase in complex with aluminum fluoride, which mimics the transition state of hydrolysis of the counterion-bound (protonated) phosphoenzyme. On the basis of structural analysis and biochemical data, we find this form to represent an occluded state of the proton counterions. Hydrolysis is catalyzed by the conserved Thr-Gly-Glu-Ser motif, and it exploits an associative nucleophilic reaction mechanism of the same type as phosphoryl transfer from ATP. On this basis, we propose a general mechanism of occluded transition states of Ca^{2+} transport and H^+ countertransport coupled to phosphorylation and dephosphorylation, respectively.

The Ca^{2+}-ATPase, or calcium pump, belongs to the family of P-type ATPases that also includes Na^+,K^+-ATPase and H^+-ATPase as prominent members. These pumps use the energy released by the hydrolysis of ATP to translocate specific cations across membranes against their electrochemical gradient (*1*) via formation of an aspartylphosphorylated intermediate. The Na^+,K^+-ATPases and H^+-ATPases are responsible for the formation of a membrane potential in animal and plant phyla, and they maintain the electrochemical gradients that drive most cotransport processes. The Ca^{2+}-ATPases transport Ca^{2+} out of the cytoplasm as required in conjunction with the use of this cation in intracellular signaling (*2*). The functional cycle of P-type ATPases is typically described in terms of E1 and E2 states, as illustrated (Fig. 1A) for sarco(endo)plasmic reticulum Ca^{2+} ATPase (SERCA): (i) in a first reaction, the reversible [adenosine diphosphate (ADP)–sensitive] γ-phosphoryl transfer from ATP to the side chain of a conserved aspartic acid residue yields a high-energy intermediate state (E1~P) with occluded cations (Ca^{2+}); (ii) active cation transport across the membrane associated with a conformational change then leads to the downhill transition of the ATPase from the E1~P to the E2-P (ADP-insensitive) state; (iii) hydrolysis of the E2-P state is accompanied by the translocation in opposite direction of an appropriate counterion (protons for the Ca^{2+} ATPase) through the cation conducting pathway; and (iv) completion of the functional cycle takes place by dissociation of the counterions and renewed binding of cytoplasmic cations (Ca^{2+}) and ATP. In this report, we address the structural changes that take place when Ca^{2+} ATPase is converted from the E1~P Ca^{2+} occluded state to the E2-P dephosphorylation transition state associated with proton counterions.

Structural studies of the calcium-bound form of SERCA have shown it to be composed of three cytoplasmic domains—the A (actuator), P (phosphorylation), and N (nucleotide binding) domains—and 10 transmembrane segments, M1 through M10, which contain the two embedded Ca^{2+} binding sites (*3*). The ATP binding site in the E1 conformation has been described (*4*, *5*) along with the coupled phosphoryl transfer and calcium occlusion mechanism (*4*). Also the structural properties of a calcium-free intermediate (E2) state stabilized by thapsigargin (*6*) and (deca)vanadate (*7*) or MgF_4^{2-} (*8*) as analogs of inorganic phosphate have been described. Lastly, a K^+ binding site has been identified in the P domain and shown to be important for dephosphorylation of the E2-P state (*9*). Comparison of the known SERCA structures as well as a wealth of biochemical data point to movements of the A domain and its linker regions (*10*) as being critical for the functional transitions of SERCA and Na^+,K^+-ATPase (and probably for other P-type ATPases as well). The generally conserved Thr-Gly-Glu-Ser (TGES) motif in the A domain was recently shown to be essential for the dephosphorylation of the E2-P phosphoenzyme in a reaction where the glutamic acid residue was proposed to activate the attacking water molecule (*11*).

To understand the dephosphorylation mechanism that concludes the two-step process of ATP hydrolysis in the P-type ATPases, we crystallized SERCA, solubilized by $C_{12}E_8$ in a calcium-free form in the presence of native lipids, thapsigargin, and aluminum fluoride, by using the vapor diffusion method (*12*). This E2-AlF_4^- form mimics the transition state of hydrolysis of the E2-P enzyme (*13*). Crystallographic data extending to 3.0 Å resolution were collected with synchrotron radiation, and the structure was solved by molecular replacement using search models of individual domains. Functionally important ligands (Mg^{2+}, K^+, AlF_4^-, and thapsigargin) were readily identified in the electron density maps, and a complete model of the protein was obtained (Fig. 1B and fig. S1). An unbiased F_o-F_c difference map showed density for three water molecules at coordinating positions for Mg^{2+} and AlF_4^- (Fig. 1B). The final model yields a free R factor of 26.5% and shows proper geometry (*12*).

We find that the E2-AlF_4^- structure of SERCA (Fig. 1C) differs from the E2-MgF_4^{2-} complex, which mimics the product complex of E2-P hydrolysis (*13*), even though they have the same overall conformation (*8*). The structural details at the phosphorylation site are not the same, reflecting the differences between a product and a transition state complex. Superpositioning of our structure on the M7-M10 segment or on the P domain of structures representing the E1~P state (*4*) and the E2 state (*6*) reveals large conformational changes (Fig. 2, A and B, and fig. S2). These changes must include the downhill transitions of the high-energy intermediate, resulting in the release of calcium into the lumen. Indeed, we find the A domain to function as the actuator (*14*), linking the changes at the phosphorylation site of the cytoplasmic region to the ion conducting pathway of the transmembrane region as described below.

In the E1~P structure (represented by a Ca_2E1~ADP:AlF_4^- complex), we noted that the ADP moiety glues the N and P domain together (*4*). Release of the ADP leaving group upon phosphoryl transfer therefore facilitates an ~50° rotation of the N domain relative to the P domain, as is observed in the E2-AlF_4^- structure (Fig. 2A). This enables the A domain to initiate the 108° rotation and 8 Å shift around the P domain as required for bringing the TGES motif of the A domain in apposition to the phosphorylation site (Fig. 2A). Because three polypeptide segments link the A domain to the membrane, these movements directly affect the orientation of M1 through M3 and (by intramembranous helix-helix interactions) also the orientation of M4 through M6, relative to the constant M7-M10 segment

[1]Centre for Structural Biology, Department of Molecular Biology, University of Aarhus, Gustav Wieds Vej 10C, DK-8000 Aarhus C, Denmark. [2]Department of Biophysics, Institute of Physiology and Biophysics, University of Aarhus, Ole Worms Allé 185, DK-8000 Aarhus C, Denmark.

*These authors contributed equally to this work.
†To whom correspondence should be addressed. E-mail: jvm@biophys.au.dk (J.V.M.); pn@mb.au.dk (P.N.)

(Fig. 2A). Along with kinks in M4 and M5, the P domain is also rotated relative to the M7-M10 segment by ~30°. These conformational changes destabilize the Ca^{2+} binding sites in the membrane. However, the relative orientation of M1 and M2 and the kink of M1 are maintained as in the occluded E1~P state and prevent calcium from escaping to the cytoplasm.

How, then, is calcium released to the lumen? Before formation of the transition state of hydrolysis of the E2-P state, as represented here by the E2-AlF_4^- structure, SERCA occupies an E2-P ground state displaying low-affinity calcium binding sites exposed to the lumen, and Ca^{2+} is released in partial exchange for protons (*15*). However, in the E2-P transition state the access to the lumen is closed, and the four carboxylate residues, which were previously involved in calcium binding in the E1 states,

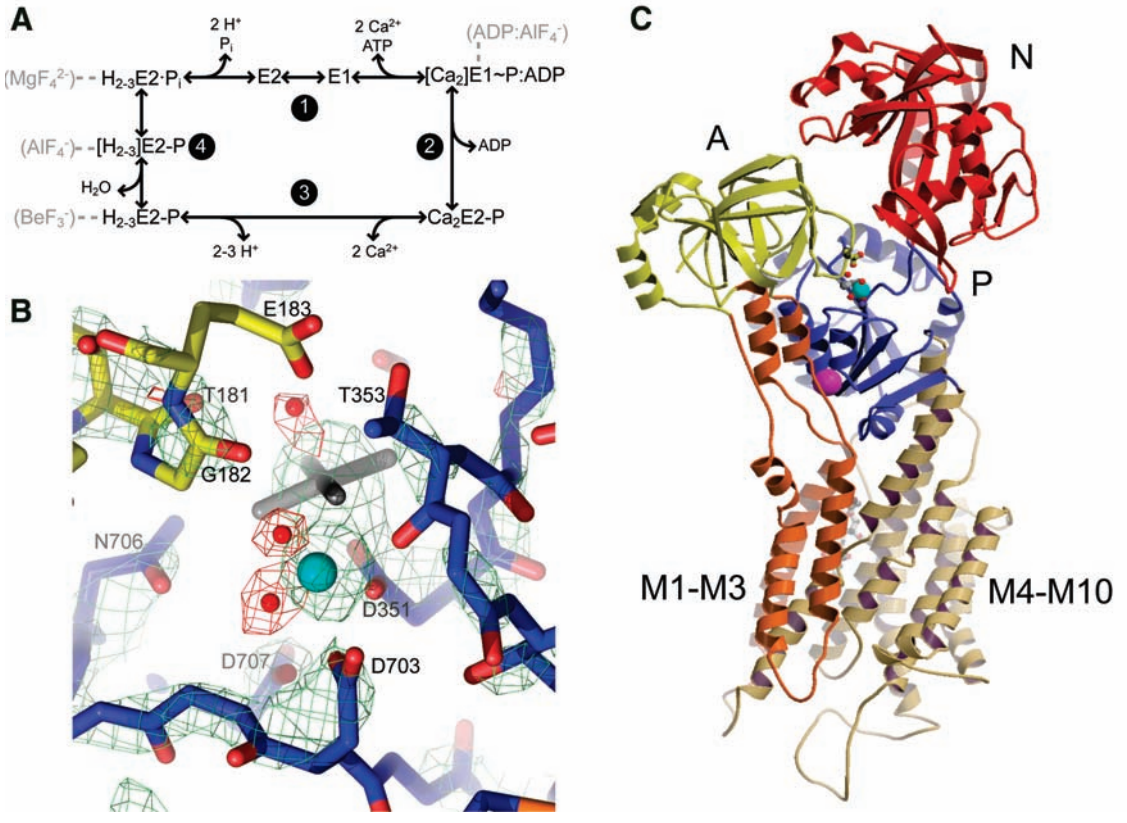

Fig. 1. Structure of the E2-AlF_4^- complex. (**A**) Schematic overview of the functional cycle of SERCA depicted by E1 and E2 states. Intermediates and transition states mimicked by fluorides are indicated in gray. (**B**) Electron density showing the structure of the dephosphorylation site. A σ_A-weighted $2F_o$-F_c electron density map shown at a high contour level (green mesh, 3.5 σ) indicates the position of Mg^{2+} and AlF_4^- (cyan sphere and gray sticks, respectively). Three water molecules are revealed as prominent peaks in an unbiased F_o-F_c difference map (red mesh, 3.6σ contour level). Two water molecules complete the octahedral coordination of Mg^{2+}, and one water molecule is located for inline attack on the aluminum fluoride, activated by the side chain of Glu^{183}. This and the following figures (except Fig. 3, D and E) were prepared by using PyMOL (*27*). (**C**) Structural cartoon of the overall structure with the A domain in yellow, the P domain in blue, the N domain in red, and transmembrane segments M1 through M3 in orange and M4 through M10 in wheat. The residues Glu^{183} (yellow stick) and Asp^{351} (blue stick), the AlF_4^- group (gray), and the Mg^{2+} ion (cyan sphere) are shown at the interface between the A and P domains in an orientation similar to that of (B). The K^+ ion stabilizes a five-helix cluster and is shown as a magenta sphere located on the P domain. The thapsigargin inhibitor (white stick) binds to the back of the transmembrane region in this orientation.

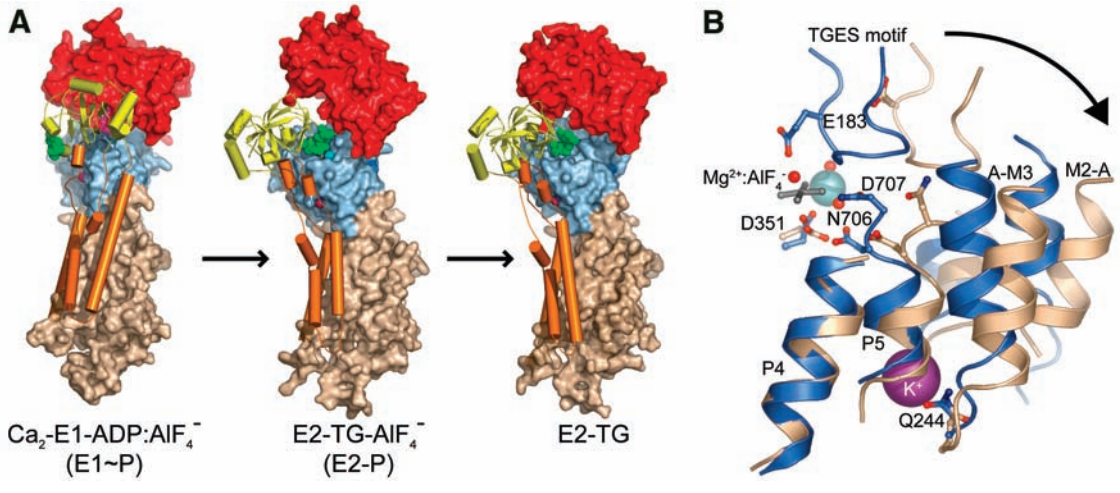

Fig. 2. Conformational changes ranging from the E1~P through the E2-P transition state to the E2 state. (**A**) Crystal structures aligned by superpositioning of the M7-M10 segment. The N domain, P domain, and M4-M10 helices are shown as red-, blue-, and wheat-colored surfaces, respectively, and the A domain and M1-M3 are shown in yellow and orange cartoon representation, respectively. The K^+ ion is shown in magenta, Mg^{2+} in cyan, and the TGES motif of the A domain as green spheres. (**B**) Conformational changes at the five-helix cluster upon phosphate release are revealed by comparison of the E2-AlF_4^- and E2 structures (blue and wheat, respectively, both with thapsigargin). Helices P5 and P6 of the P domain switch upon phosphate release and displace the helices of the M2-A and A-M3 linkers. The K^+ ion (magenta) stabilizes this region of the protein.

are again buried in the membrane, but now without Ca^{2+} or positively charged amino acid residues in their vicinity (Fig. 3). The carboxylate groups are therefore likely to be in a protonated state, because they would be in a highly unfavorable environment if present as negatively charged residues. In other words, the protons for countertransport must be in place to allow formation of the E2-P hydrolysis state. Similarly, potassium for countertransport is required for the hydrolysis of the Na^+,K^+ ATPase E2-P phosphoenzyme to occur (*16*). In support of a proton-dependent transition to the E2-P transition state of SERCA, alkaline pH is indeed observed to reduce the rate of dephosphorylation (*17*), in contrast to observations on the Na^+,K^+ ATPase (*18*). It is difficult to assess the exact distribution of proton counterions among the four carboxylates, because the net Ca^{2+}/H^+ exchange performed by SERCA is electrogenic (*19*, *20*), involving an estimated net movement of two to three proton charges by countertransport from the lumen at typical physiological conditions (*21*, *22*).

Our biochemical data (obtained in the absence of thapsigargin) support the conclusion that the E2-AlF_4^- structure mimicking the transition state of hydrolysis represents a proton-occluded state, because this state has a low affinity for Ca^{2+}, in contrast to E2. This is revealed by a strong resistance to Ca^{2+}-mediated reactivation (Fig. 3D). These data also confirm that the occluded state observed in the crystal structure is not an artifact caused by the use of thapsigargin, in accordance with tryptophan fluorescence data (*13*). The Ca^{2+}-mediated reactivation occurs by a strongly cooperative mechanism, as expected for binding of two Ca^{2+}, but with an affinity four orders of magnitude lower than that for the uncomplexed E2 form, thus requiring Ca^{2+} concentrations in the millimolar range (Fig. 3D). Reactivation of the E2-AlF_4^- complex can occur both from the outside and inside of sarcoplasmic reticulum vesicles (Fig. 3E). It is therefore probable that in these experiments the E2-P ground state and the E2-P transition state are in a reversible equilibrium that shifts toward the E2-P ground state at high Ca^{2+}. By contrast, the crystal structure, with bound thapsigargin and in the absence of Ca^{2+}, clearly depicts the transition state with occluded protons and no access to the lumen, in accordance with isotope exchange data (*23*).

Besides the closure of the transmembrane region as mediated by protonation of the ion conducting pathway, the E2-AlF_4^- structure exhibits a layer of positively charged amino acid residues near the lumen-exposed surface (Fig. 3A). This is likely to be another important structural element of the closed state because it inhibits the approach of luminal Ca^{2+} by electrostatic repulsion.

To understand how occlusion of the bound counterions (protons) is coupled to dephosphorylation, we have to turn our attention to the cytoplasmic domains. At the phosphorylation site, the planar AlF_4^- group is located right between the conserved Asp^{351} side chain of the P domain and a water molecule brought in position by the main-chain carbonyl of Thr^{181} and the side chain of Glu^{183} of the TGES motif in the A domain (Figs. 1B and 4A). This is in agreement with mutational studies (*11*, *24*). The Glu^{183} side chain appears to provide general base catalysis by abstracting a proton from the water molecule as it attacks the phosphate group (here represented by AlF_4^-).

The TGES motif with the water molecule overlaps the position of ADP in the Ca_2E1-ADP:AlF_4^- form (*4*) when superimposed on the P domain, and the phosphorylation site displays the same chemical environment in both forms (Fig. 4A). Indeed, both reactions seem to exploit a strongly associative mechanism of inline, nucleophilic attack as revealed by ~2 Å bonding distances between the aluminum atom and coordinating oxygens, thus indicative of covalent bonds. The estimates of bonding distances are fairly well defined for a linear arrangement even though the resolution is moderate, and the distances are distinguished from a dissociative arrangement. The associative reaction mechanism is the key element to explain the coupling mechanisms of SERCA. It provides a strict demand for a defined conformational state to fulfil the inline arrangement enabling the reaction. Neither phosphorylation nor dephosphorylation can be initiated before the exact spatial conformation has been attained, and this again requires that Ca^{2+} or protons are bound and occluded at the ion conducting pathway, respectively. In support of this view, the E2-BeF_3^- complex

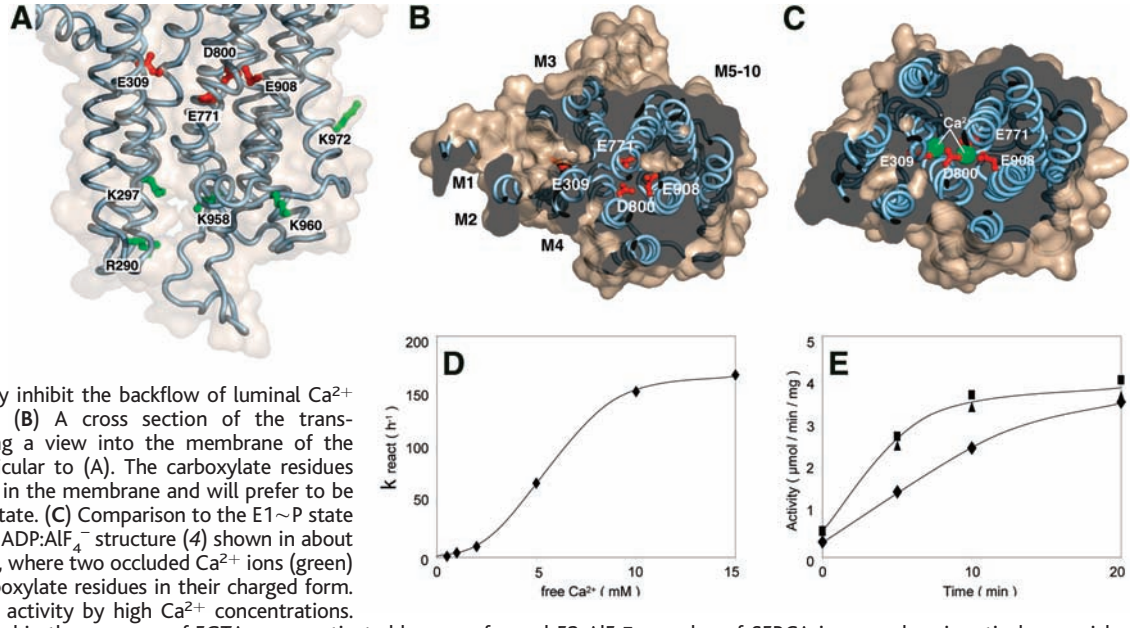

Fig. 3. Proton counterion occlusion in the E2-P transition state. (**A**) Distribution of the carboxylate residues of the cation conducting pathway (red sticks) and of the positively charged arginine and lysine residues (green sticks) in the transmembrane region (blue coil) of the E2-AlF_4^- structure. The positively charged residues are positioned toward the lumen, and in addition to the hydrophobic barrier they probably inhibit the backflow of luminal Ca^{2+} by electrostatic repulsion. (**B**) A cross section of the transmembrane region, providing a view into the membrane of the E2-AlF_4^- structure perpendicular to (A). The carboxylate residues (red) are completely buried in the membrane and will prefer to be in a preferably protonated state. (**C**) Comparison to the E1~P state [represented by the Ca_2E1~ADP:AlF_4^- structure (*4*) shown in about the same orientation as (B)], where two occluded Ca^{2+} ions (green) are coordinated by the carboxylate residues in their charged form. (**D**) Reactivation of ATPase activity by high Ca^{2+} concentrations. The E2-AlF_4^- complex formed in the presence of EGTA was reactivated by raising the free Ca^{2+} concentration to 0.5 to 15 mM. Reactivation rate constants were calculated by logarithmic analysis from the evolution of activity as a function of time on small aliquots drawn from the sample. About 80% of the original activity was recovered from all samples. (**E**) Effect of luminal exposure for reactivation of Ca^{2+}-ATPase. At time zero, preformed E2-AlF_4^- complex of SERCA in sarcoplasmic reticulum vesicles was exposed to 2 mM free Ca^{2+}, with (squares) or without (diamonds) ionophore A23187 (at an ionophore/protein weight ratio of 1%). Activity was measured at timed intervals on small aliquots of the sample. Triangles show the response of purified (permeable) Ca^{2+}-ATPase vesicles. For further details, see (*12*).

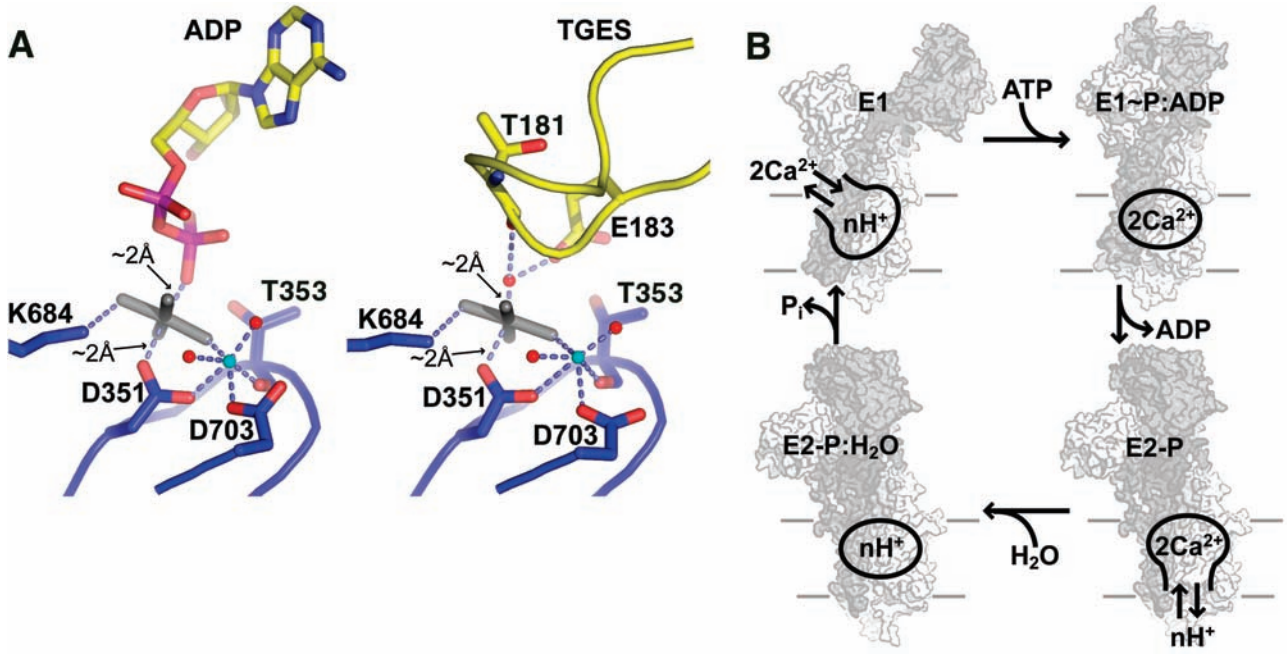

Fig. 4. A general, associative mechanism of nucleophilic attack at the phosphorylation site. (**A**) Comparison of the phosphorylation site in the AlF_4^- analog between the transition state of γ-phosphoryl transfer (E1~P:ADP, left) and that of aspartyl-phosphate hydrolysis (E2-P:H_2O, right). Mg^{2+} is shown as a cyan sphere with liganding oxygens and water molecules in red. The aluminum fluoride is shown in gray, and bond distances to aluminum are indicated. A water molecule is located for inline attack on the aluminum fluoride via interaction with the side chain of Glu^{183} and the main chain carbonyl group of Thr^{181}. The ADP moiety and the TGES motif of the A domain occupy overlapping positions. (**B**) A schematic representation of the opening and closure of cytoplasmic and luminal entrances to the ion conducting pathway in the calcium pump. Ca^{2+} transport and H^+ countertransport are coupled to phosphorylation and dephosphorylation, respectively. For clarity, the scheme is reduced to four functional transitions reflecting the essence of steps 1 to 4 in Fig. 1A. The unknown structure of the E2-P ground state is represented by the E2-P transition state.

and the native E2-P ground state of SERCA have been found to display a hydrophobic environment at the phosphorylation site, in contrast to the E2-AlF_4^- complex, and to be far more sensitive to Ca^{2+}-mediated reactivation (*13*). This result indicates that the phosphorylation site is not properly assembled for hydrolysis as long as the ion conducting pathway is exposed to the lumen.

Dephosphorylation and release of the inorganic phosphate leaving group results in the formation of the E2 state and revokes the affinity to cytoplasmic calcium (*7*). In the E2-AlF_4^- structure, a cluster of five small helices, three of which are contributed by the P domain and two by the M2-A linker and the A-M3 linker, has formed (Fig. 2B). The cluster features an integral K^+ site that has been shown to be responsible (*9*) for the stimulatory effect of monovalent cations on the dephosphorylation of SERCA (*25*). The K^+ site is formed by residues of two of the small C-terminal helices of the P domain, P5 and P6, and in the E2-AlF_4^- structure it is also coordinated by the side chain oxygen of Gln^{244} of the A-M3 linker. The helix cluster and the TGES motif anchor the A domain and M1-M3 to the P domain. During phosphorylation, the orientations of the P-domain P5 and P6 helices of the cluster are observed to switch because of interactions of Asn^{706} and Asp^{707} with the phosphorylation site that do not occur in the dephosphorylated forms; thereby these helices can be visualized to act as a sensor of phosphate release (Fig. 2B) exerting a push on the helices of the M2-A and A-M3 linkers. Also, the TGES motif of the A domain moves away from the phosphorylation site as observed in the E2-thapsigargin structure (Fig. 2B). As a result of these dislocations the N domain can return toward the P domain by an ~25° rotation (fig. S2). We infer that the conformational changes unlock the A domain and M1 through M3 on the cytoplasmic side, which may be sufficient to explain why the binding of cytoplasmic Ca^{2+} is now strongly enhanced, whereas access from the luminal side remains closed.

On the basis of the crystal structures and the functional data, we can extract a simple rationale for the operation of the SERCA pump in terms of two entrances (a cytoplasmic and a luminal one) controlling the active cation transport processes (Fig. 4B and movie S1): Phosphoryl transfer from ATP locks the cytoplasmic door on Ca^{2+}, whereas the subsequent release of the ADP leaving group opens the luminal door for Ca^{2+}/H^+ exchange. Hydrolysis of the phosphoenzyme locks the luminal door on H^+, and subsequent release of the inorganic phosphate leaving group opens the cytoplasmic door for H^+/Ca^{2+} exchange. The present known Ca^{2+} ATPase structures result in a model to explain the coupling rules earlier proposed by Jencks (*26*). In this model, the strict conformational requirements of the associative reaction mechanisms of phosphoryl transfer and hydrolysis at the phosphorylation site provide the basis for coupling, a principle that should be generally applicable to P-type ATPases.

Note added in proof: During the final stages of preparation of this paper for publication, Toyoshima and colleagues published online the structure of an E2-MgF_4^{2-} form, representative of the E2-P_i product complex of Ca^{2+}-ATPase (*8*). Overall their structure compares well with ours, but it must be emphasized that our study deals with a transition state analog of E2-P. As an important point, Toyoshima *et al.*, as well as Lancaster in an accompanying perspective article (*28*), consider the E2-MgF_4^{2-} form to reveal the luminal gating mechanism of the E2-P ground state. Furthermore, it is suggested that the closure of the luminal gate is triggered by phosphate release, rather than an earlier step. These interpretations are different from ours.

References and Notes

1. J. V. Møller, B. Juul, M. le Maire, *Biochim. Biophys. Acta* **1286**, 1 (1996).
2. E. Carafoli, *Proc. Natl. Acad. Sci. U.S.A.* **99**, 1115 (2002).
3. C. Toyoshima, M. Nakasako, H. Nomura, H. Ogawa, *Nature* **405**, 647 (2000).
4. T. L.-M. Sørensen, J. V. Møller, P. Nissen, *Science* **304**, 1672 (2004).
5. C. Toyoshima, T. Mizutani, *Nature* **430**, 529 (2004).
6. C. Toyoshima, H. Nomura, *Nature* **418**, 605 (2002).
7. P. Zhang, C. Toyoshima, K. Yonekura, N. M. Green, D. L. Stokes, *Nature* **392**, 835 (1998).

8. C. Toyoshima, H. Nomura, T. Tsuda, *Nature* **432**, 361 (2004).
9. T. L.-M. Sørensen *et al.*, *J. Biol. Chem.* **279**, 46355 (2004).
10. J. V. Møller, G. Lenoir, M. Le Maire, B. S. Juul, P. Champeil, *Ann. N. Y. Acad. Sci.* **986**, 82 (2003).
11. J. D. Clausen, B. Vilsen, D. B. McIntosh, A. P. Einholm, J. P. Andersen, *Proc. Natl. Acad. Sci. U.S.A.* **101**, 2776 (2004).
12. Materials and methods are available as supporting material on *Science* Online.
13. S. Danko, K. Yamasaki, T. Daiho, H. Suzuki, *J. Biol. Chem.* **279**, 14991 (2004).
14. C. Toyoshima, G. Inesi, *Annu. Rev. Biochem.* **73**, 269 (2004).
15. A. Barth, W. Kreutz, W. Mantele, *J. Biol. Chem.* **272**, 25507 (1997).
16. I. M. Glynn, *J. Physiol.* **462**, 1 (1993).
17. T. Sørensen, B. Vilsen, J. P. Andersen, *J. Biol. Chem.* **272**, 30244 (1997).
18. B. Forbush III, I. Klodos, in *The Sodium Pump: Structure, Mechanism, and Regulation*, J. H. Kaplan, P. de Weer, Eds. (Rockefeller Univ. Press, New York, 1991), pp. 211.
19. F. Cornelius, J. V. Møller, *FEBS Lett.* **284**, 46 (1991).
20. X. Yu, S. Carroll, J. L. Rigaud, G. Inesi, *Biophys. J.* **64**, 1232 (1993).
21. D. Levy, M. Seigneuret, A. Bluzat, J. L. Rigaud, *J. Biol. Chem.* **265**, 19524 (1990).
22. X. Yu, L. Hao, G. Inesi, *J. Biol. Chem.* **269**, 16656 (1994).
23. T. Seekoe, S. Peall, D. B. McIntosh, *J. Biol. Chem.* **276**, 46737 (2001).
24. M. Toustrup-Jensen, B. Vilsen, *J. Biol. Chem.* **278**, 11402 (2003).
25. M. Shigekawa, L. J. Pearl, *J. Biol. Chem.* **251**, 6947 (1976).
26. W. P. Jencks, *J. Biol. Chem.* **264**, 18855 (1989).
27. W. L. DeLano, PyMOL Molecular Graphics System (2002); available online at http://www.pymol.sourceforge.net.
28. C. R. Lancaster, *Nature* **432**, 286 (2004).
29. We thank B. Holm, B. Nielsen, and C. Lauridsen for expert technical assistance; the staff at the Protein Structure Factory beamline BL14.1 of Free University Berlin at Berliner Elektronenspeicherring-Gesellschaft für Synchrotronstrahlung m. b. H., the staff at European Synchrotron Radiation Facility (ESRF) beamline ID29; J. L. Karlsen and R. Jørgensen for extensive computer support; and J. Nyborg for fruitful scientific discussions. This work was supported by an Ole Rømer Research grant; the Center for Structural Biology; the Dansync program under the Danish Natural Science Research Council; a grant from the Lundbeck Foundation (P.N.), and grants from the Danish Medical Research Council, Aarhus University Research Foundation, and Novo Nordic Foundation (J.V.M.). Coordinates and structure-factor amplitudes have been deposited to the Protein Data Bank under code 1XP5.

Supporting Online Material
www.sciencemag.org/cgi/content/full/306/5705/2251/DC1
Materials and Methods
Figs. S1 to S4
Table S1
Movie S1

12 October 2004; accepted 23 November 2004
10.1126/science.1106289

Mouse Brain Organization Revealed Through Direct Genome-Scale TF Expression Analysis

Paul A. Gray,[1,3]*† Hui Fu,[2,3]* Ping Luo,[1,3]* Qing Zhao,[4] Jing Yu,[5] Annette Ferrari,[3] Toyoaki Tenzen,[5] Dong-in Yuk,[4] Eric F. Tsung,[6]‡ Zhaohui Cai,[6] John A. Alberta,[3] Le-ping Cheng,[1,3] Yang Liu,[1,3] Jan M. Stenman,[5] M. Todd Valerius,[5] Nathan Billings,[4] Haesun A. Kim,[2,3]§ Michael E. Greenberg,[1,8] Andrew P. McMahon,[5] David H. Rowitch,[4,7] Charles D. Stiles,[2,3]‖ Qiufu Ma[1,3]‖

In the developing brain, transcription factors (TFs) direct the formation of a diverse array of neurons and glia. We identifed 1445 putative TFs in the mouse genome. We used in situ hybridization to map the expression of over 1000 of these TFs and TF-coregulator genes in the brains of developing mice. We found that 349 of these genes showed restricted expression patterns that were adequate to describe the anatomical organization of the brain. We provide a comprehensive inventory of murine TFs and their expression patterns in a searchable brain atlas database.

The mammalian nervous system contains thousands of distinct neuronal and glial cell types that are distinguished on the basis of morphology, projection, and marker gene expression (*1*). Transcription factors (TFs) play a pivotal role in brain development by directing the formation of neurons and glia from uncommitted progenitor cells (*2*). To determine the extent to which TFs describe the diversity of the mammalian central nervous system (CNS), we visualized the spatial and temporal expressions of TF-encoding genes on a genome-wide scale in the developing mouse CNS.

To identify unique genomic loci that encode putative TFs in the mouse genome, we analyzed and annotated existing public and private databases (*3*–*6*). Candidates were classified as TFs only if their predicted protein sequence included a Protein Families Database (Pfam)–defined TF-DNA binding domain (*3*). We identified 1445 unique transcriptional units in the mouse genome with putative TF-DNA binding domains. The nonoverlapping genes for each DNA binding family (*7*, *8*) are summarized in Table 1 and tables S1 and S2. Recent protein prediction databases have estimated that there are over 2300 different TF proteins in the mouse genome (*6*, *9*). This higher number is primarily due to the separate counting of each possible protein variant as a unique transcriptional unit, as well as the duplicate counting of genes with multiple DNA binding domains. The largest single class of TF proteins (~678 members, not including nuclear hormone receptors) was the zinc-finger family. Homeobox TFs had 227 members, and there were 50 nuclear hormone receptors and 116 basic helix-loop-helix (bHLH) TFs (Table 1 and table S1). The human genome encodes 20,000 to 25,000 genes (*10*). If a similar number of genes are encoded in the mouse genome, then TF genes make up more than 7% of the total.

We designed gene-specific polymerase chain reaction (PCR) primer pairs to produce in situ hybridization probes for 1174 TF-encoding genes. This probe set covers 91% of genes that belong to 32 out of the 33 major TF families (table S1). For the remaining (also the largest) gene family, which encodes zinc-finger proteins (divided into 12 subgroups), 71% of the genes were covered by the probe set (table S1). These primers were used to perform PCR on cDNA templates prepared from embryonic day 13.5 (E13.5) and newborn [postnatal day zero (P0)] mouse brains. A small number of additional probes were acquired from embryonic mouse kidney or testis cDNA. Among the 1174 TF-encoding genes screened, 972 (83%) showed positive PCR products. We monitored the recovery of nuclear hormone receptors as a metric for sensitivity. We cloned 46 of the 50 nuclear hormone receptors that are encoded in the mouse genome. Only one nuclear hormone receptor known to be expressed in the brain, the androgen receptor (*11*), was missed by our procedure. In total, 983 TF-encoding genes were subsequently cloned or acquired (Table 1 and table S1). We also cloned 104 transcription cofactor genes (Table 1 and table S1), yielding a total number of 1087 genes, which are collectively referred to as TF-encoding genes. These cloned in situ plasmids

[1]Department of Neurobiology, [2]Department of Microbiology and Molecular Genetics, Harvard Medical School, Boston, MA 02115, USA. [3]Department of Cancer Biology, [4]Department of Pediatric Oncology, Dana-Farber Cancer Institute, 1 Jimmy Fund Way, Boston, MA 02115, USA. [5]Department of Molecular and Cellular Biology, Harvard University, 16 Divinity Avenue, Cambridge, MA 02138, USA. [6]Informatics Program, [7]Division of Newborn Medicine, [8]Division of Neuroscience, Children's Hospital, Boston, MA 02115, USA.

*These authors contributed equally to this work.
†Present address: Molecular Neurobiology Laboratory, The Salk Institute, 10010 North Torrey Pines Road, La Jolla, CA 92037, USA.
‡Present address: Department of Biology, Boston College, 140 Commonwealth Avenue, Chestnut Hill, MA 02467, USA.
§Present address: Department of Biological Sciences, Rutgers University, 101 Warren Street, Newark, NJ 07102 USA.
‖To whom correspondence should be addressed. E-mail: Qiufu_Ma@dfci.harvard.edu (Q.M.); Charles_Stiles@dfci.harvard.edu (C.D.S.)

have been deposited at the American Type Culture Collection (ATCC) for open distribution.

We synthesized digoxigenin-labeled probes for the TF-encoding genes. To visualize TF expression at an early developmental stage, we analyzed the expression of 1013 TF-encoding genes using whole-mount in situ hybridization on E10.5 mouse embryos. Of these 1013, at least 142 were clearly expressed in a spatially restricted manner (table S6 and fig. S7). We also performed in situ hybridization for 1034 TF genes on transverse sections through the E13.5 and P0 head and trunk, as well as on sections through the postnatal cerebellum at P7, P15, and P21. Of 1034 genes examined in the E13.5 and/or P0 nervous system, 349 showed spatially restricted expression patterns (table S3). For TFs that belong to non–zinc-finger families, ~38% of them showed restricted expression patterns in the CNS. However, only ~10% of zinc-finger genes showed restricted patterns. Collectively, ~27% of all the TFs exhibited spatially restricted patterns (table S3).

We divided the CNS into seven general areas for annotation: the cortex, striatum (and other basal ganglia), thalamus, hypothalamus, midbrain, hindbrain, and spinal cord. Very few of the 349 TFs with spatially restricted expression patterns were expressed in only one region of the brain (table S4). Nearly all TF-encoding genes expressed in the neonatal brain were also detected in postmitotic neurons at E13.5. Digital images of the entire in situ hybridization set have been deposited in the Mahoney Transcription Factor Atlas (*12*), as well as in the Jackson Laboratory's Gene Expression Database (*13*).

The in situ hybridization data show that postmitotic anatomical diversity within the CNS can be described by TF expression. For example, the neocortex is a highly laminated and regionally organized anatomical structure (*14*). We found that several dozen TF-encoding genes occupy different dorsoventral positions or different laminae of the neocortex (Fig. 1). In the striatum, a major basal ganglia component crucial for movement control is organized in a somatotopic fashion (*15*). This somatotopic organization is echoed by the gradient expression of many TF-encoding genes in this area (fig. S1). The thalamus and hypothalamus are organized into discrete anatomical and functional nuclei that are marked by the overlapping expression pattern of specific TFs within these regions (figs. S2 and S3). In the retina, a large number of TF genes are expressed with distinct density within the retinal ganglion and amacrine cell layers (figs. S4 and S5), which may correlate with the morphological diversity of these cell types (*1*). In the postnatal cerebellum, laminar-specific TF expression marks the immature and mature granule cells and Purkinje cells (fig. S6).

The genome-scale whole-mount and section in situ hybridizations also identified over

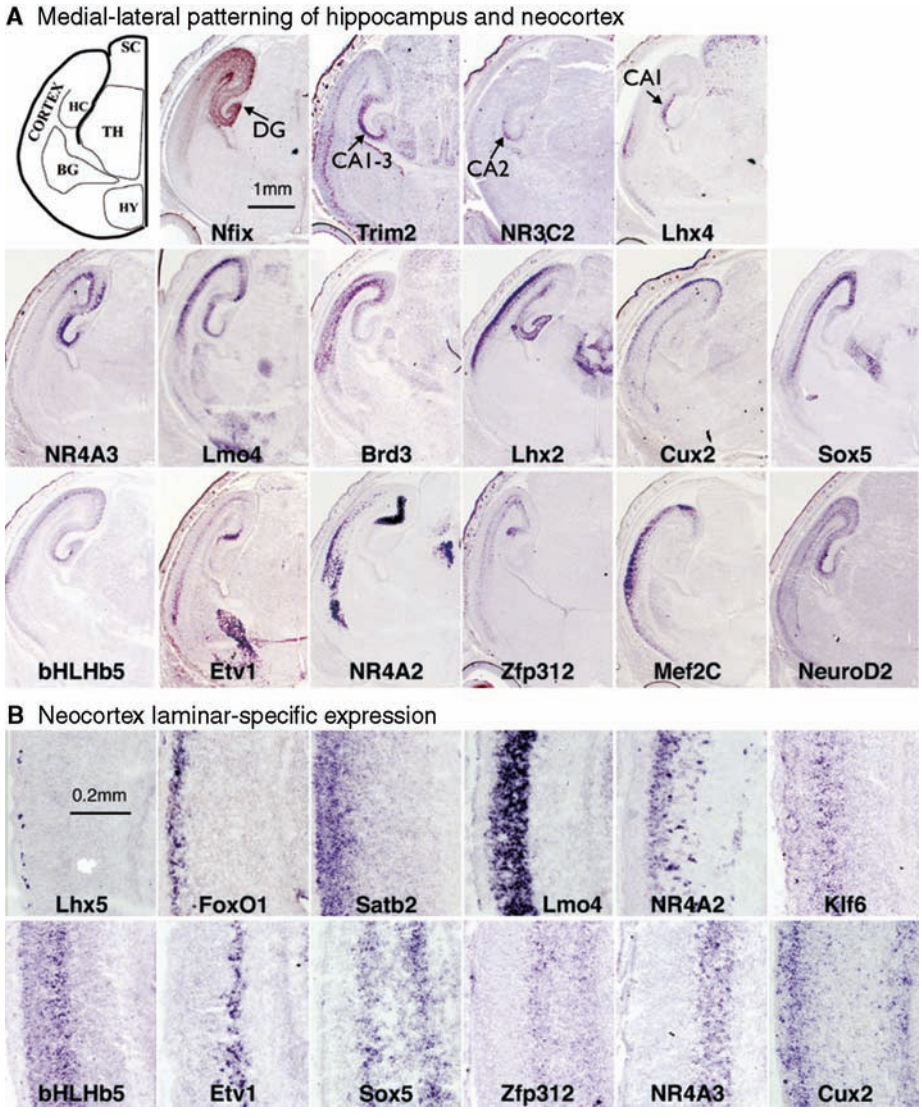

Fig. 1. Diversity of transcription factor expression in the P0 mouse cerebral cortex. Nonradioactive in situ hybridization patterns for 20 representative TFs or TF cofactors on sections through the forebrain of P0 mice are shown. Labels at the bottoms of individual panels indicate Locuslink gene names. (**A**) Over a dozen TF-encoding genes occupy different dorsoventral positions of the hippocampus (top row) and neocortex (middle and bottom rows). (**B**) A dozen genes show laminar specific expression in the neocortex. HC, hippocampus; BG, basal ganglia; SC, superior colliculus; TH, thalamus; HY, hypothalamus; DG, hippocampal dentate gyrus; CA1 to 3, hippocampal CA1, CA2, and CA3 regions. Scale bar in (A), 1 mm; all images in this section show the same magnification. Scale bar in (B), 0.2 mm; all images in this section show the same magnification.

100 TF genes expressed in spatially restricted patterns within non-neuronal tissues such as the nose, oral cavity, teeth, salivary gland, inner ear bone, mandibular bone, eye muscle, facial muscle, skin, and others (fig. S8 and table S4). Although not the explicit focus of this study, the open-source TF data set generated in this work provides detailed information, enabling comprehensive study of developing cranial facial tissues. The in situ plasmid set provided here can be used to define TF expression patterns in other tissues and at other developmental times in neural tissues.

Our atlas of TF expression provides a visual filter for functional analysis of the TF gene set in brain development. Over 7% of the murine genome may encode TFs. However, our studies suggest that at a given developmental stage, fewer than 27% of these TF-encoding genes are expressed in spatially restricted patterns consistent with a direct role in the formation of specific neural types. The regulatory elements for these spatially restricted TFs might be useful reagents for driving the expression of reporter genes that will mark specific neural cell types, as described recently by Gong *et al.* (*16*). The TF expression profile in postmitotic neurons will be useful to study the expression of neural-specific genes encoding ion channels, neurotransmitter receptors, and synaptic proteins, whose molecular control remains largely unknown. On a clinical front, TF mutations

Table 1. Nonredundant numbers of putative TFs in the mouse genome. Columns describe the total number of unique genomic loci encoding predicted DNA binding TFs by domain and the numbers and relative percentages analyzed. The second to last column describes the number of family members available as Genetrap cell lines in the Baygenomics and/or German Gene Trap Consortium libraries. The last column describes the percentage of family members with available enhancer trap cell lines. Genes that encode multiple DNA binding domains are listed and counted in one family for clarity. Nuclear hormone receptors are not included in zinc-finger genes. Transcription cofactors and these non-TF genes we analyzed are also included. Asterisks indicate the cofactor and non-TF gene numbers we analyzed rather than the total number in the genome. HMG, high-mobility group; bZIP, basic helix-loop-helix and leucine zipper proteins; non-TFs, genes that do not encode TFs; nuclear rec, nuclear hormone receptors; ZF, zinc finger; ETS, erythroblast transformation–specific; PHD, plant homeodomain; btb/poz, broad-complex, tramtrack, and bric-a-brac/poxvirus and zinc-finger proteins.

Domain	No. of genes	No. cloned	% cloned	Genetrap available	% trapped
Homeobox	227	170	74.9	12	5.3
bHLH	116	100	86.2	22	19.0
HMG	58	41	70.7	14	24.1
bZIP	57	41	71.9	16	28.1
Nuclear Rec	50	46	92.0	10	20.0
Forkhead	40	29	72.5	12	30.0
ETS	28	26	92.9	8	28.6
ZF C_2H_2	490	287	58.6	171	34.9
ZF PHD	60	44	73.3	42	70.0
ZF C_2CH	39	18	46.2	11	28.2
ZF btb/poz	28	18	64.3	8	28.6
Other	252	163	64.7	124	49.2
TF Total	1445	983	68.0	450	31.1
Cofactors*	133	104	78.2	48	36.1
Non-TFs*	336	261	77.7	95	28.6
Total genes	1914	1348	70.4	493	25.8

have already been shown to underlie certain disorders in speech (*17*), appetite control (*18*), breathing patterns (*19*), and autism (*20*) in humans. The TF atlas presented here may have practical overtones for understanding additional neurological or behavioral disorders in children and adults.

References and Notes

1. R. H. Masland, *Curr. Biol.* **14**, R497 (2004).
2. R. Shirasaki, S. L. Pfaff, *Annu. Rev. Neurosci.* **25**, 251 (2002).
3. E. L. Sonnhammer, S. R. Eddy, E. Birney, A. Bateman, *Nucleic Acids Res.* **26**, 320 (1998).
4. V. Matys *et al.*, *Nucleic Acids Res.* **31**, 374 (2003).
5. D. L. Wheeler *et al.*, *Nucleic Acids Res.* **32**, D35 (2004).
6. P. D. Thomas *et al.*, *Genome Res.* **13**, 2129 (2003).
7. D. Stryke *et al.*, *Nucleic Acids Res.* **31**, 278 (2003).
8. J. Hansen *et al.*, *Proc. Natl. Acad. Sci. U.S.A.* **100**, 9918 (2003).
9. R. H. Waterston *et al.*, *Nature* **420**, 520 (2002).
10. International Human Genome Sequencing Consortium, *Nature* **431**, 931 (2004).
11. N. M. Shah *et al.*, *Neuron* **43**, 313 (2004).
12. The Mahoney Transcription Factor Atlas is available at http://mahoney.chip.org/mahoney/.
13. See the Jackson Laboratory's Gene Expression Database, accession no. J:91257, available at www.informatics.jax.org/.
14. D. D. O'Leary, Y. Nakagawa, *Curr. Opin. Neurobiol.* **12**, 14 (2002).
15. E. R. Kandel, J. H. Schwartz, T. M. Jessell, *Principles of Neural Science* (McGraw-Hill, New York, 2000).
16. S. Gong *et al.*, *Nature* **425**, 917 (2003).
17. C. S. Lai, S. E. Fisher, J. A. Hurst, F. Vargha-Khadem, A. P. Monaco, *Nature* **413**, 519 (2001).
18. J. L. J. Holder, N. F. Butte, A. R. Zinn, *Hum. Mol. Genet.* **9**, 101 (2000).
19. J. Amiel *et al.*, *Nature Genet.* **33**, 459 (2003).
20. N. Gharani, R. Benayed, V. Mancuso, L. M. Brzustowicz, J. H. Millonig, *Mol. Psychiatry* **9**, 474 (2004).

21. We thank J. Olsen, J. Chan, and P. Santos for their technical assistance and R. DePinho for providing the National Institute on Aging 15K cDNA set. We also thank R. Segal and S. Pfaff for critical reading of this manuscript. The work was supported by the Charles Dana Foundation, the National Institute of Neurological Disorders and Stroke (Q.M., C.D.S., D.H.R., and A.P.M.), the National Institute of Dental and Craniofactial Research (Q.M.), the National Institute of Diabetes and Digestive and Kidney Dieseases (A.P.M.), a Ford Foundation Postdoctoral Fellowship for Minorities (P.A.G.), a Parker B. Francis Fellowship in Pulmonary Medicine (P.A.G.), and the Pew Trust (Q.M.).

Supporting Online Material

www.sciencemag.org/cgi/content/full/306/5705/2255/DC1
Materials and Methods
Figs. S1 to S8
Tables S1 to S7
References

7 September 2004; accepted 15 November 2004
10.1126/science.1104935

Activity-Dependent Internalization of Smoothened Mediated by β-Arrestin 2 and GRK2

Wei Chen,[1]* Xiu-Rong Ren,[2] Christopher D. Nelson,[2] Larry S. Barak,[3] James K. Chen,[4]† Philip A. Beachy,[4] Frederic de Sauvage,[5] Robert J. Lefkowitz[2]*

Binding of Sonic Hedgehog (Shh) to Patched (Ptc) relieves the latter's tonic inhibition of Smoothened (Smo), a receptor that spans the cell membrane seven times. This initiates signaling which, by unknown mechanisms, regulates vertebrate developmental processes. We find that two molecules interact with mammalian Smo in an activation-dependent manner: G protein–coupled receptor kinase 2 (GRK2) leads to phosphorylation of Smo, and β-arrestin 2 fused to green fluorescent protein interacts with Smo. These two processes promote endocytosis of Smo in clathrin-coated pits. Ptc inhibits association of β-arrestin 2 with Smo, and this inhibition is relieved in cells treated with Shh. A Smo agonist stimulated and a Smo antagonist (cyclopamine) inhibited both phosphorylation of Smo by GRK2 and interaction of β-arrestin 2 with Smo. β-Arrestin 2 and GRK2 are thus potential mediators of signaling by activated Smo.

Hedgehog (Hh) signaling is mediated by regulation of a protein called Smoothened (Smo) that spans the cell membrane seven times (7MS), activation of which sets in motion transcriptional events that control growth and patterning in vertebrate development (*1*, *2*). Dysregulated Smo activity also leads to several forms of cancer (*3*–*7*). Hh binds to a receptor that spans the cell membrane 12 times, Patched (Ptc), and relieves inhibitory control of Smo by Ptc. However, almost nothing is known of the mechanisms operating just downstream of Smo to mediate and modulate its actions. β-Arrestins are cytosolic proteins that bind to most activated 7MS receptors after the receptors have been phosphorylated by GRKs, which promotes internalization of the receptors and some forms of signaling (*8*, *9*). Elements that regulate receptor functions often show

[1]Department of Medicine, [2]Howard Hughes Medical Institute, Departments of Medicine and Biochemistry, [3]Department of Cell Biology, Duke University Medical Center, Durham, NC 27710, USA. [4]Howard Hughes Medical Institute, Department of Molecular Biology and Genetics, Johns Hopkins University School of Medicine, Baltimore, MD 21205, USA. [5]Department of Molecular Oncology, Genentech, South San Francisco, CA 94080, USA.

*To whom correspondence should be addressed. E-mail: lefko001@receptor-biol.duke.edu (R.J.L.) and w.chen@duke.edu (W.C.).

†Present address: Department of Molecular Pharmacology, Stanford University School of Medicine, Stanford, CA 94305, USA

activity-dependent interaction with the receptor. Thus, we tested the hypothesis that β-arrestins and GRKs might interact with and regulate Smo.

β-Arrestin 2 tagged with green fluorescent protein (βarr2-GFP), when expressed alone, was diffusely distributed throughout the cytoplasm of human embryonic kidney 293 (HEK293) cells (Fig. 1A). Expression of βarr2-GFP together with a fusion protein of Smo with a portion of Myc (Myc-Smo), which is constitutively active when overexpressed in mammalian cells (*10*, *11*), led to redistribution of βarr2-GFP from the cytosol to the plasma membrane, where it was found in a punctate pattern (Fig. 1B). Under these conditions, 32 ± 6% of cells expressing βarr2-GFP demonstrated such translocation (Fig. 1C). This pattern is similar to that observed after recruitment of βarr2-GFP to other activated 7MS receptors (*12*, *13*). Furthermore, in such cells, more Smo was detected in the cytosol (fig. S1, B to D) than was seen when Smo was expressed alone (fig. S1A). β-Arrestin1-GFP, when expressed alone, was also evenly distributed in the cytosol (fig. S2A); however, no recruitment to Smo was observed (fig. S2B).

We tested whether Ptc, an inhibitor of Smo (*14*), might itself bind β-arrestin–GFP. Ptc covalently tagged with a FLAG epitope, when expressed alone, was distributed primarily at the plasma membrane (fig. S1E). Localization of β-arrestin1–GFP (*15*) or βarr2-GFP (Fig. 2A) was not altered in cells also expressing Ptc, and expression of βarr2-GFP did not alter the distribution of Ptc (fig. S1, F to H). However, expression of Ptc together with Myc-tagged Smo and βarr2-GFP markedly inhibited localization of βarr2-GFP at the plasma membrane (Fig. 1B vs. Fig. 2B). Under these conditions, only 4 ± 2% of cells expressing βarr2-GFP demonstrated translocation (Fig. 1C). These data suggest that βarr2-GFP binds to the active form of Smo. Secreted Sonic hedgehog ligand (Shh) binds to Ptc and blocks its inhibitory effect on Smo activity (*10*, *16*). Thus, Shh treatment might be expected to restore association of βarr2-GFP with Smo in cells expressing Ptc, Smo, and βarr2-GFP. Therefore, we mixed cells expressing the secreted active form of Shh (ShhN) with cells expressing Ptc, Smo, and βarr2-GFP and cultured them for 12 hours. Of the βarr2-GFP–expressing cells, 22 ± 2% showed translocation of βarr2 under these conditions, compared with only 4 ± 2% when the added cells had been transfected with empty vector rather than ShhN (Fig. 1C).

To further explore whether βarr2-GFP binds to the active form of Smo, we used cyclopamine, a compound that acts as a direct antagonist of Smo (*10*). Recruitment of βarr2-GFP to the plasma membrane was abolished when cells were treated with 8 μM cyclo-

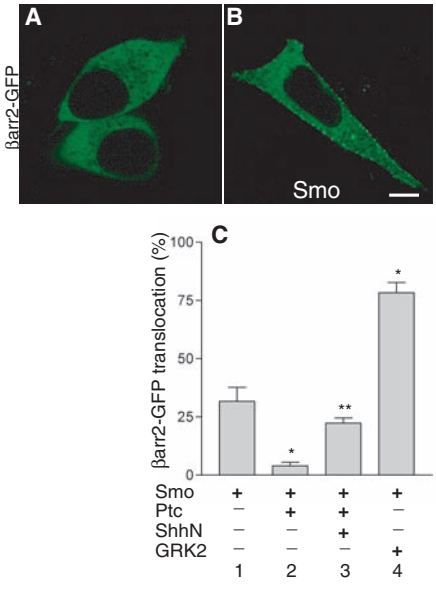

Fig. 1. Localization of βarr2-GFP to the plasma membrane in cells overexpressing Smo. Confocal images of βarr2-GFP expressed alone (**A**) or with Myc-Smo (**B**) in HEK293 cells. (**C**) Effects of Ptc, ShhN, and GRK2 on recruitment of βarr2-GFP to the plasma membrane. βarr2-GFP was expressed with Myc-Smo (bar 1), Myc-Smo and FLAG-Ptc (bar 2), Myc-Smo and FLAG-Ptc (cocultured with HEK293 expressing ShhN, an active form of Shh) (bar 3), or Myc-Smo and GRK2 (bar 4) in HEK293 cells. Data are presented as the percentage of βarr2-GFP–expressing cells with recruitment of βarr2-GFP and are the means ± SEM of three independent experiments. $*P < 0.05$ (compared with bar 1) and $**P < 0.005$ (compared with bar 2) (unpaired *t* test). Scale bar, 10 μm.

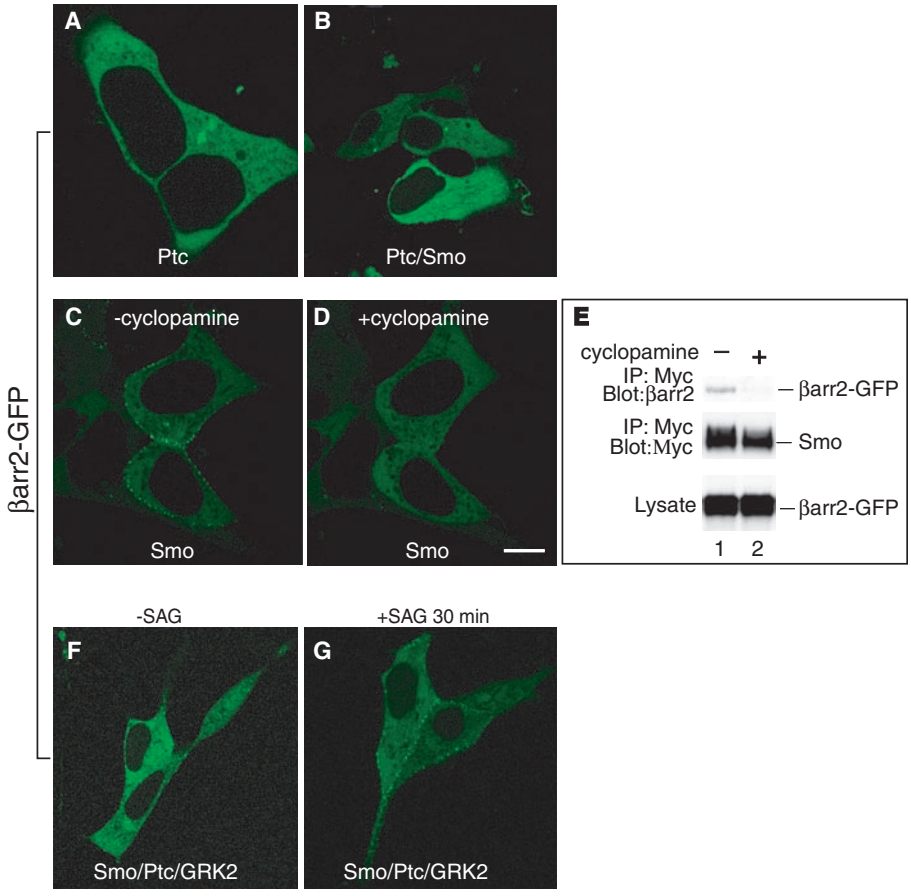

Fig. 2. Ptc and cyclopamine inhibit membrane recruitment of βarr2-GFP, and SAG relieves Ptc inhibition of recruitment of βarr2-GFP to the plasma membrane. Confocal images of βarr2-GFP expressed with FLAG-Ptc (**A**), FLAG-Ptc and Myc-Smo (**B**), and Myc-Smo (**C** and **D**) in HEK293 cells. Cells were left untreated (A to C) or treated with 8 μM cyclopamine (D) at 37°C for 5 min. Recruitment of βarr2-GFP to Smo was ablated by treatment with cyclopamine (C versus D), but not with dimethylsulfoxide (DMSO), a vehicle for cyclopamine. (**E**) Effect of cyclopamine on interaction of βarr2-GFP with Smo. HEK293 cells stably expressing Myc-Smo and βarr2-GFP were left untreated (lane 1) or treated with cyclopamine (6 μM, lane 2) at 37°C for 1 hour. Cell extracts were immunoprecipitated with anti-Myc affinity gel. Immunoprecipitates were immunoblotted with antibodies against βarr2 (A2CT) (top) or antibodies against Myc (middle). Whole-cell lysates were immunoblotted with A2CT antibodies (bottom). (**F** and **G**) Confocal images of cells stimulated with 0.3 μM SAG at 37°C for 0 min (F) and 30 min (G). HEK293 cells were transfected with βarr2-GFP, FLAG-Ptc, Myc-Smo, and GRK2. Scale bar, 10 μm. Representative images or a blot of three independent experiments are shown.

pamine for 5 min at 37°C (Fig. 2, C and D). Further evidence for interaction of βarr2 and Smo within a protein complex and for the inhibitory effect of cyclopamine on such an interaction was obtained from cellular coimmunoprecipitation studies in which cyclopamine virtually eliminated the constitutive association of these two proteins (Fig. 2E).

In *Drosophila*, stimulation by Shh leads to activation and phosphorylation of Smo (*17*). However, the kinase responsible for Smo phosphorylation has not been identified. Because the interaction of β-arrestin with 7MS receptors is generally initiated by GRK-mediated phosphorylation of the receptor (*8*, *9*), we tested whether Smo phosphorylation might be mediated by GRK2, a ubiquitously expressed member of this kinase family. Expression of Myc-Smo in [^{32}P]orthophosphate-labeled HEK293 cells revealed phosphorylation of Smo by endogenous kinases (Fig. 3). Transfection of the cells with small interfering RNA (siRNA) directed against GRK2, which decreased GRK2 expression by ~95% (Fig. 3), led to a decrease in Smo phosphorylation relative to that in cells treated with control siRNA (Fig. 3; fig. S3). These data suggest that GRK2 contributes to phosphorylation of Smo in vivo.

Because GRK2 influences phosphorylation of Smo, we tested its effect on the recruitment of βarr2-GFP to Smo. In the absence of coexpressed GRK2, 32 ± 6% of cells expressing βarr2-GFP demonstrated βarr2-GFP translocation to the plasma membrane (Fig. 1C). Expression of GRK2 with Smo increased the percentage of cells with recruitment of βarr2-GFP to the plasma membrane to 78 ± 4% (Fig. 1C). Amounts of Smo expressed were similar in the presence or the absence of overexpressed GRK2 (*15*). GRK2 alone had no effect on βarr2-GFP translocation in the absence of overexpressed Smo (*15*).

An agonist for Smo, benzo[*b*]thiophene-2-carboxamide, 3-chloro-*N*-[4- (methylamino)cyclohexyl]-*N*-{[3-(4-pyridinyl)phenyl]methyl}-(9CI) (SAG), has been identified that relieves the inhibitory effect of Ptc on Smo (*18*). Incubation of cells with SAG (0.03 nM to 3 μM) at 37°C for 1 hour did not further enhance recruitment of βarr2-GFP to the plasma membrane in HEK293 cells expressing Smo and βarr2-GFP, probably because overexpressed Smo is already constitutively active (*11*, *15*). However, exposure of cells to SAG (0.3 μM) at 37°C for 30 min or 1 hour did relieve Ptc inhibition of translocation of βarr2-GFP to the plasma membrane by Ptc in HEK293 cells expressing Ptc, Smo, GRK2, and βarr2-GFP (Fig. 2, F and G; fig. S4). The increased recruitment of βarr2-GFP to the plasma membrane was dependent on the concentration of SAG used, with 50% maximal effect at ~30 nM (fig. S5).

These experiments indicate that recruitment of βarr2-GFP to Smo faithfully monitors the activation state of Smo. Because endogenous GRK2 appears to phosphorylate Smo (Fig. 3; fig. S3), we next tested whether Smo phosphorylation in the presence of endogenous or transfected GRK2 also reflects the activation state of Smo. Expression of GRK2 with Smo led to more phosphorylation of Smo (Fig. 4). In the absence of GRK2 coexpression, stimulation of cells with SAG for 15 min resulted in no change of Smo phosphorylation; however, in the presence of GRK2 expression, SAG stimulation led to a 1.3-fold increase of Smo phosphorylation (Fig. 4). Exposure of cells to the antagonist cyclopamine for 15 min led to a 30% decrease of Smo phosphorylation in the absence of coexpressed GRK2 and a 55% decrease in the presence of coexpressed GRK2 (Fig. 4). Expression of Ptc with Smo in the presence or absence of coexpressed GRK2 resulted in a 35 or 30% decrease in Smo phosphorylation, respectively (Fig. 4). These data indicate that phosphorylation of Smo also reflects its activation state.

SAG 1.1 (*19*) and cyclopamine regulated Smo trafficking as well (fig. S6). When a fusion of Smo with yellow fluorescent protein (Smo-YFP) was expressed in HEK293 cells, it was expressed at the plasma membrane and in the cytosol, possibly because of the presence of partially processed or constitutively internalized Smo (fig. S6A). Treatment of cells with SAG 1.1 for 1 hour led to internalization of Smo-YFP (fig. S6B). The internalized Smo-YFP was recycled back to the plasma membrane after treatment of the cells with cyclopamine for 4 hours (fig. S6C). SAG 1.1 did not affect the rate of internalization of the transferrin receptor (*15*).

β-Arrestins target 7MS receptors such as β_2-adrenergic receptor (β_2AR) to clathrin-coated pits to mediate their internalization (*8*). To test whether Smo undergoes similar regulation, we expressed both Smo-YFP and β_2AR-RFP (red fluorescent protein) in the same HEK293 cells and stimulated them for 1 hour with SAG 1.1 and isoproterenol. Both receptors were internalized and colocalized (fig. S7). Expression of a dominant-negative mutant of dynamin (in which Lys^{44} was replaced by Ala) also blocked internalization of

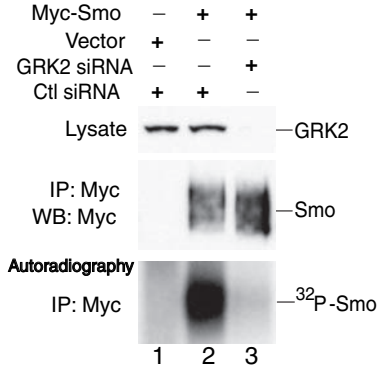

Fig. 3. Phosphorylation of Smo mediated by GRK2. Decreased phosphorylation of Smo in cells lacking GRK2. HEK293 cells were transfected with control siRNA and DNA empty vector (lane 1), or Myc-Smo (lanes 2 and 3) along with control siRNA (lane 2) or siRNA directed against GRK2 (lane 3). Cells were incubated with [^{32}P]orthophosphate at 37°C for 1 hour. Proteins from cell extracts were either immunoblotted with antibodies against GRK2 (top) or immunoprecipitated with anti-Myc affinity gel. Immunoprecipitates were either immunoblotted with antibodies to Myc (middle) or processed for autoradiography (bottom). A representative blot of three independent experiments is shown.

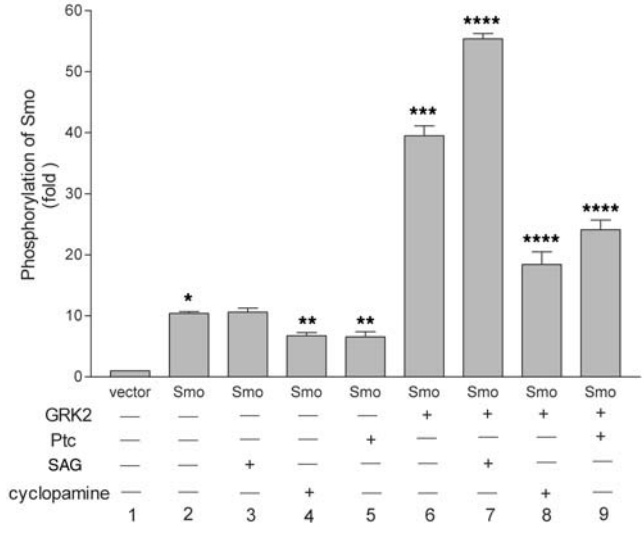

Fig. 4. Effects of GRK2, Ptc, SAG, and cyclopamine on Smo phosphorylation. HEK293 cells were transfected with vector (bar 1), or Myc-Smo (bars 2 to 9), and FLAG-Ptc or GRK2 (bars 5 to 9) as indicated. Cells were labeled with [^{32}P]orthophosphate at 37°C for 1 hour and then left untreated or treated with 0.3 μM SAG (bars 3 and 7) or 2 μM cylopamine as indicated at 37°C for 15 min. Proteins from cell extracts were immunoprecipitated with anti-Myc affinity gel. Immunoprecipitated Smo was processed for autoradiography. Data are presented as fold changes of Smo phosphorylation over that in cells transfected with control vector. *$P < 0.005$ (compared with bar 1); **$P < 0.02$ and ***$P < 0.0001$ (compared with bar 2); ****$P < 0.005$ (compared with bar 6) (unpaired *t* test). The results shown are the means ± SEM of three independent experiments.

Smo-YFP stimulated by SAG 1.1 (fig. S8). Moreover, in cells coexpressing Myc-Smo and βarr2-GFP, endogenous clathrin and βarr2-GFP colocalized in a punctate pattern at the plasma membrane (Fig. 5, A to C). These data indicate that expression of βarr2 causes association of Smo with clathrin-coated pits for internalization.

We used siRNA directed against βarr2 or GRK2 to reduce the amounts of endogenous βarr2 or GRK2 expressed in HEK293 cells [to ~10% of that in control cells (fig. S9, A and B)]. Smo-YFP expressed in cells treated with control siRNA was distributed at the plasma membrane and in the cytosol (Fig. 5D). Stimulation of cells with SAG 1.1 for 30 min resulted in internalization of Smo-YFP (Fig. 5, D and E). However, SAG 1.1-induced internalization of Smo-YFP was abolished in cells transfected with siRNA directed against βarr2 or GRK2 (Fig. 5, F to I). The percentage of cells showing SAG 1.1-induced internalization of Smo was increased in cells overexpressing βarr2 or GRK2 (fig. S10).

Here, we have demonstrated that βarr2 and GRK2 mediate clathrin-dependent internalization of Smo. However, it is possible that they may also modulate or mediate aspects of Smo signaling as is the case for other 7MS receptors (*8*, *20*, *21*). Indeed, β-arrestin 2 knockdown in zebrafish embryos by morpholino antisense leads to a lethal developmental phenotype (*22*) that is remarkably similar to that seen after genetic knockouts of either Smo or Gli2 (*23–25*).

Although Smo is reported to activate $G\alpha_i$ directly or indirectly in frog melanophores (*26*), no genetic evidence to support coupling of Smo to G proteins has been reported. Several cytosolic components downstream of Smo such as Costal2 (Cos2), Fused (Fu), Suppressor of Fused, and Cubitus interruptus (Ci) have been identified in *Drosophila*, and the protein complex containing Cos2, Fu, and Ci has been recently reported to associate with Smo via Cos2 (*27–30*). However, βarr2 and GRK2 interact with mammalian Smo in an activation-dependent manner and, thus, may provide a platform for development of screening assays to discover ligands that directly regulate the activity of this important oncogenic receptor that might be useful as therapeutic agents.

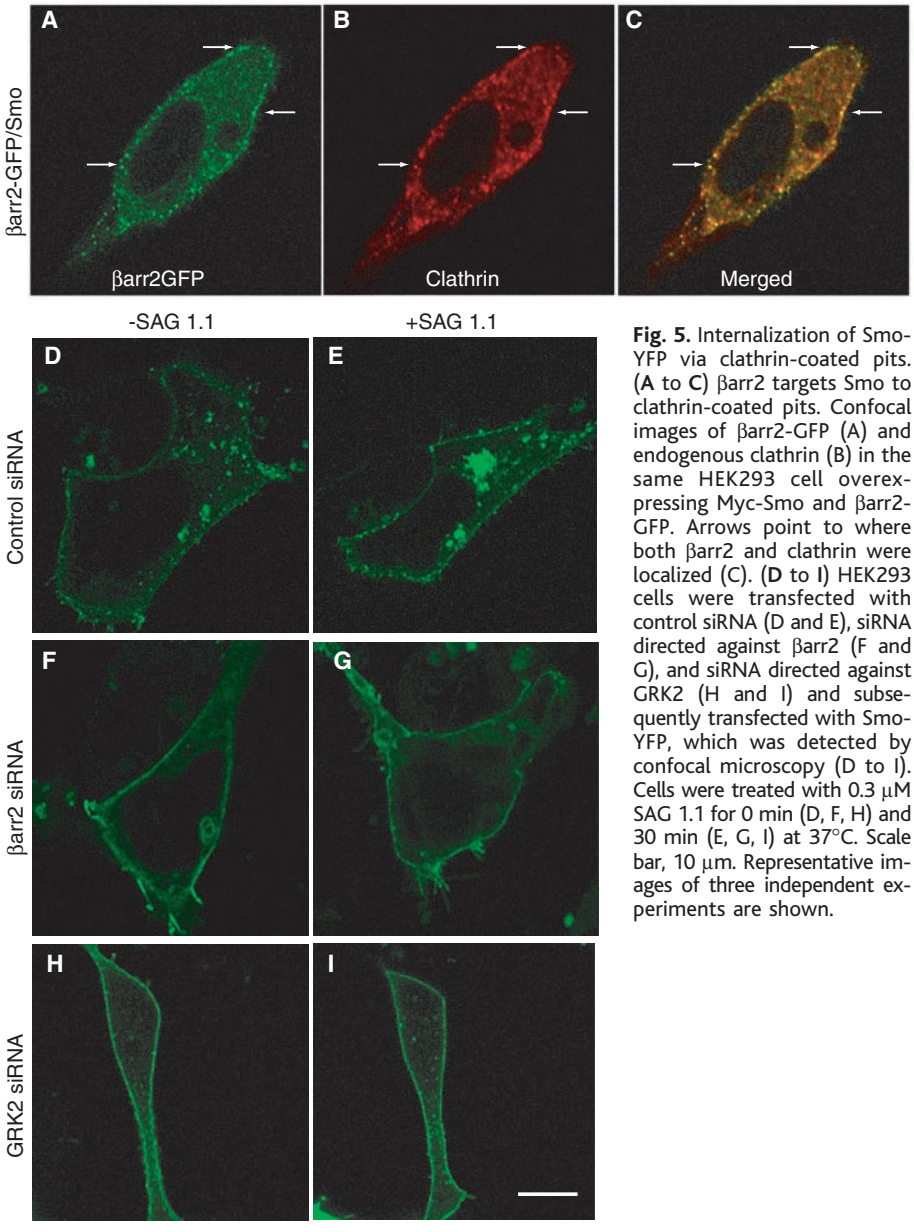

Fig. 5. Internalization of Smo-YFP via clathrin-coated pits. (**A** to **C**) βarr2 targets Smo to clathrin-coated pits. Confocal images of βarr2-GFP (A) and endogenous clathrin (B) in the same HEK293 cell overexpressing Myc-Smo and βarr2-GFP. Arrows point to where both βarr2 and clathrin were localized (C). (**D** to **I**) HEK293 cells were transfected with control siRNA (D and E), siRNA directed against βarr2 (F and G), and siRNA directed against GRK2 (H and I) and subsequently transfected with Smo-YFP, which was detected by confocal microscopy (D to I). Cells were treated with 0.3 μM SAG 1.1 for 0 min (D, F, H) and 30 min (E, G, I) at 37°C. Scale bar, 10 μm. Representative images of three independent experiments are shown.

References and Notes

1. M. M. Cohen Jr., *Am. J. Med. Genet.* **123A**, 5 (2003).
2. P. W. Ingham, A. P. McMahon, *Genes Dev.* **15**, 3059 (2001).
3. J. Xie *et al.*, *Nature* **391**, 90 (1998).
4. R. Wechsler-Reya, M. P. Scott, *Annu. Rev. Neurosci.* **24**, 385 (2001).
5. D. M. Berman *et al.*, *Nature* **425**, 846 (2003).
6. D. N. Watkins *et al.*, *Nature* **422**, 313 (2003).
7. S. P. Thayer *et al.*, *Nature* **425**, 851 (2003).
8. L. M. Luttrell, R. J. Lefkowitz, *J. Cell Sci.* **115**, 455 (2002).
9. J. A. Pitcher, N. J. Freedman, R. J. Lefkowitz, *Annu. Rev. Biochem.* **67**, 653 (1998).
10. J. Taipale *et al.*, *Nature* **406**, 1005 (2000).
11. M. Hynes *et al.*, *Nature Neurosci.* **3**, 41 (2000).
12. L. S. Barak, S. S. Ferguson, J. Zhang, M. G. Caron, *J. Biol. Chem.* **272**, 27497 (1997).
13. R. H. Oakley, S. A. Laporte, J. A. Holt, L. S. Barak, M. G. Caron, *J. Biol. Chem.* **276**, 19452 (2001).
14. J. Taipale, M. K. Cooper, T. Maiti, P. A. Beachy, *Nature* **418**, 892 (2002).
15. W. Chen *et al.*, data not shown.
16. R. B. Pepinsky *et al.*, *J. Biol. Chem.* **273**, 14037 (1998).
17. N. Denef, D. Neubuser, L. Perez, S. M. Cohen, *Cell* **102**, 521 (2000).
18. J. K. Chen, J. Taipale, K. E. Young, T. Maiti, P. A. Beachy, *Proc. Natl. Acad. Sci. U.S.A.* **99**, 14071 (2002).
19. Materials and methods are available as supporting material on *Science* Online.
20. P. H. McDonald *et al.*, *Science* **290**, 1574 (2000).
21. L. M. Luttrell, *J. Mol. Endocrinol.* **30**, 117 (2003).
22. A. M. Wilbanks *et al.*, *Science* **306**, 2264 (2004).
23. F. J. van Eeden *et al.*, *Development* **123**, 153 (1996).
24. M. J. Barresi, H. L. Stickney, S. H. Devoto, *Development* **127**, 2189 (2000).
25. W. Chen, S. Burgess, N. Hopkins, *Development* **128**, 2385 (2001).
26. D. L. DeCamp, T. M. Thompson, F. J. de Sauvage, M. R. Lerner, *J. Biol. Chem.* **275**, 26322 (2000).
27. L. Ruel, R. Rodriguez, A. Gallet, L. Lavenant-Staccini, P. P. Therond, *Nature Cell Biol.* **5**, 907 (2003).
28. S. K. Ogden *et al.*, *Curr. Biol.* **13**, 1998 (2003).
29. J. Jia, C. Tong, J. Jiang, *Genes Dev.* **17**, 2709 (2003).
30. L. Lum *et al.*, *Mol. Cell* **12**, 1261 (2003).

31. We thank M. Caron, R. Wechsler-Reya, and A. Meloni for critical discussion and reading of the manuscript; H. Kendall and L. Langevin for technical assistance; and E. Hall and D. Addison for secretarial assistance. Supported in part by NIH grant HL 16037 (R.J.L.), HL 61365 (L.S.B.). R.J.L. and P.A.B. are Investigators of the Howard Hughes Medical Institute.

Supporting Online Material

www.sciencemag.org/cgi/content/full/306/5705/2257/DC1
Materials and Methods
Figs. S1 to S10
References and Notes

17 August 2004; accepted 29 October 2004
10.1126/science.1104135

Epithelial-to-Mesenchymal Transition Generates Proliferative Human Islet Precursor Cells

Marvin C. Gershengorn,* Anandwardhan A. Hardikar, Chiju Wei, Elizabeth Geras-Raaka, Bernice Marcus-Samuels, Bruce M. Raaka

Insulin-expressing beta cells, found in pancreatic islets, are capable of generating more beta cells even in the adult. We show that fibroblast-like cells derived from adult human islets donated postmortem proliferate readily in vitro. These mesenchymal-type cells, which exhibit no hormone expression, can then be induced to differentiate into hormone-expressing islet-like cell aggregates, which reestablishes the epithelial character typical of islet cells. Immunohistochemistry, in situ hybridization, and messenger RNA measurements in single cells and cell populations establish the transition of epithelial cells within islets to mesenchymal cells in culture and then to insulin-expressing epithelial cells.

A goal of diabetes research is to generate large numbers of cells from islets of Langerhans (beta cells) for replacement therapy (*1*–*3*). Although beta cells proliferate in vivo (*4*) and in vitro (*5*), well-differentiated cells do not proliferate rapidly (*6*). It is likely that expansion of mature islet cells would not yield adequate cell numbers. Stem cells with potential for extensive proliferation and differentiation have been postulated but have not been identified definitively within the adult pancreas (*7*–*13*). Epithelial cells within the adult pancreas, however, could be isolated in vitro as undifferentiated cells and could be induced to expand and redifferentiate, thereby serving as islet precursors. Indeed, epithelial-to-mesenchymal transition (EMT) has been documented in vitro and in vivo during development and carcinogenesis (*6*, *14*–*16*). We show that cells from adult human islets undergo reversible EMT to produce proliferating precursors of islet-like cell aggregates (ICAs). The unexpected plasticity of human islet-derived precursor cells (hIPCs) may be exploited to generate cells for replacement therapy.

We demonstrated previously (*17*) that clonal human pancreatic cancer (PANC-1) cells and hIPCs can transition into hormone-expressing ICAs. PANC-1 cells transitioned from epithelial cells that proliferate in adherent monolayers into spherical ICAs after a change from serum-containing medium (SCM) to serum-free medium (SFM). In SCM, PANC-1 cells exhibit a "ductal" phenotype, expressing cytokeratins-7 and -19 (Ck-7/19) but no insulin or glucagon, whereas ICAs exhibit an endocrine phenotype with cells expressing insulin or glucagon. PANC-1 ICAs could be maintained in SFM for several weeks, and the phenotype could be reversed by reexposure to SCM (fig. S1A) (*18*). ICAs deaggregated rapidly with cells flattening and migrating out within 18 hours (movie S1) to recreate a population indistinguishable from parental cells by 48 hours (fig. S1A). After 12 hours in SCM, most cells that had migrated expressed Ck-7/19 and about 10% of these cells co-expressed insulin, which suggests that endocrine cells were transitioning to the ductal phenotype (movie S2). PDX1, a factor involved in insulin gene transcription (*19*), was observed primarily within ICAs.

During ICA formation in SFM, Ck-19 mRNA decreased by a factor of ~10, whereas proinsulin mRNA increased by a factor of at least 1000 from an initially undetectable level (Fig. 1A). Low levels of proglucagon transcript were detected in ductal cells and increased about 100-fold during transition. When 30-day ICAs were exposed to SFM supplemented with fetal bovine serum or epidermal growth factor (EGF) (Fig. 1A), deaggregation was associated with decreases in proinsulin and increases in Ck-19 transcript levels. When these cells were reexposed to SFM without EGF, proinsulin mRNA was up-regulated and Ck-19 mRNA was down-regulated. Furthermore, when PANC-1 ICAs were returned to SCM, some cells that migrated were positive for proinsulin mRNA and Ck-7/19 peptides (Fig. 1B), which indicated that the transition from ductal to endocrine phenotype was reversible. Transcript levels for the intermediate filament protein Ck-19 remained relatively high even when it was not detectable by immunostaining. This may be because Ck-19 stains better when in filamentous form in migratory cells rather than in nonfilamentous form in ICAs.

Transition from one epithelial phenotype to another may involve a mesenchymal intermediate (*16*). Vimentin, another intermediate filament protein, is used as a marker of mesenchymal cells (*16*). After 3 hours in SFM, PANC-1 cells migrating into ICAs (*17*) expressed vimentin in filaments, whereas parental PANC-1 cells in SCM did not (fig. S1B). Thus, PANC-1 cells appear to undergo epithelial-to-mesenchymal-to-epithelial transitions.

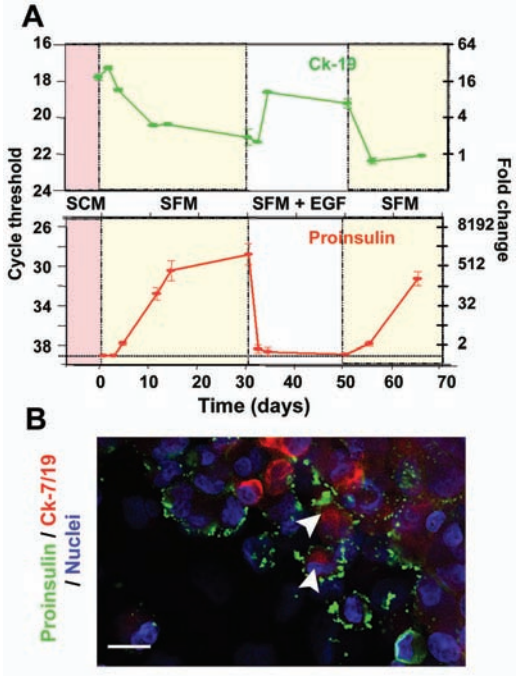

Fig. 1. PANC-1 cells undergo reversible epithelial-to-mesenchymal-to-epithelial transition. (**A**) Transition from "ductal" to endocrine phenotype. Cells were incubated in SCM and changed to SFM as described (*17*) on day 0, to SFM + EGF on day 30, and to SFM on day 50. Proinsulin and Ck-19 mRNAs were measured by quantitative RT-PCR. (**B**) Cells expressing proinsulin mRNA or Ck-7/19 peptide or both (arrowheads) were present 18 hours after ICAs were exposed to SCM. Scale bars, 10 μm.

Clinical Endocrinology Branch, National Institute of Diabetes and Digestive and Kidney Diseases, National Institutes of Health, Bethesda, MD 20892–8029, USA.

*To whom correspondence should be addressed. E-mail: marving@intra.niddk.nih.gov

Like PANC-1 cells, hIPCs are proliferative cells that can be induced by serum deprivation to differentiate into hormone-expressing ICAs (see below). Having observed reversible EMT in PANC-1 cells, we hypothesized that hIPCs derived from islet epithelial cells by EMT, specifically from a heterogeneous population of adherent cells that emerge from islets (fig. S2A). After 2 days in culture, more than 40% of cells were positive for C-peptide (peptide derived from the connecting region), and 3% were positive for vimentin (Fig. 2A); cells expressing both proteins were not observed. By day 7, 28% were positive for vimentin, C-peptide–positive cells decreased to 36% and, most important, 3% were positive for both proteins. The trend of increasing vimentin and decreasing C-peptide expression continued through day 14. It is noteworthy that cells positive for both proteins were not observed at the later time, which suggests that double-positive cells may reflect a transient state as C-peptide–positive cells transition to vimentin-positive hIPCs. In general, insulin-positive cells were smaller than vimentin-positive cells. Size is a characteristic of different phenotypes within a single hIPC population, because cultures of "small" cells contained cells of both sizes within 3 days (fig. S3, A and B).

In situ hybridization (*18*) showed that some adherent cells emerging from islets were positive for proinsulin mRNA and for vimentin protein (Fig. 2B), even though most cells were vimentin-negative (Fig. 2A). Vimentin staining was filamentous as in mesenchymal cells (*6*) and migratory PANC-1 cells (fig. S1B). Similarly, cells emerging from islets after 4 days express filamentous arrays of nestin, smooth muscle actin, and vimentin (fig. S2B). These data suggest that hIPCs are derived from insulin-expressing cells by EMT. To test this hypothesis, we measured proinsulin transcript in randomly selected, adherent single cells during the first 17 days of culture (Fig. 2C). During days 2 through 8, when the number of viable cells remained constant, most cells were positive

Table 1. Expression of representative epithelial and mesenchymal mRNAs in human islets and hIPCs. Total RNA was prepared from human islets within 3 days of organ donation from a single donor (Single) or pooled from 3 donors (Pooled) and from hIPCs derived from 3 individual donors (A, B, or C) at passages 8 (p8), 10 (p10), or 16 (p16). INS, proinsulin; GCG, proglucagon; GCK, glucokinase; PDX1, insulin promoter factor 1; GLP1R, glucagon-like peptide 1 receptor; CDH1, E-cadherin; CLDN3, claudin 3; CLDN4, claudin 4; OCLN, occludin; PECAM1, platelet/endothelial cell adhesion molecule (CD31); VIM, vimentin; NES, nestin; ACTA2, smooth muscle actin alpha 2; ACTG2, smooth muscle actin γ 2; ENG, endoglin (CD105); MMP2, matrix metalloproteinase 2; SNAI1, snail homolog 1; SNAI2, snail homolog 2; THY1, Thy-1 cell surface antigen; P4HA1, prolyl 4-hydroxylase alpha subunit. ND, not determined.

	qRT-PCR cycle threshold				
	Human islets		hIPCs		
	Single	Pooled	A, p8	B, p16	C, p10
Epithelial					
INS	14	14	27	>38	>38
GCG	19	20	33	35	>38
GCK	23	24	>38	>38	ND
PDX1	23	24	34	>38	ND
GLP1R	24	25	>38	>38	ND
CDH1	20	21	30	30	30
CLDN3	23	24	31	31	34
CLDN4	18	18	27	28	30
OCLN	20	21	26	26	27
PECAM1	24	24	34	31	35
Mesenchymal					
VIM	18	19	14	15	16
NES	26	27	24	24	23
ACTA2	24	25	17	18	16
ACTG2	33	31	23	21	23
ENG	25	25	21	22	22
MMP2	23	22	17	17	17
SNAI1	26	26	24	26	24
SNAI2	25	25	21	22	22
THY1	25	26	18	18	19
P4HA1	22	24	20	20	21

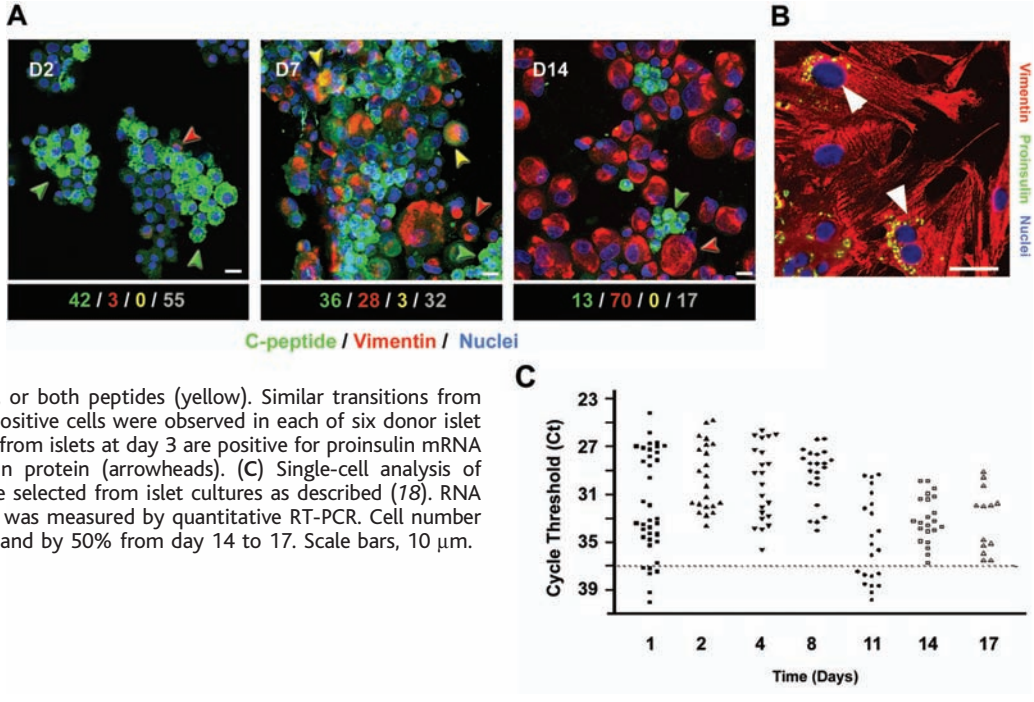

Fig. 2. hIPCs are derived from insulin-expressing cells by epithelial-to-mesenchymal transition in vitro. (**A**) Cells migrating out from adult human islets lose expression of C-peptide and express vimentin protein in filaments. Islet cultures were harvested with trypsin at days 2 (D2), 7 (D7), and 14 (D14); cytospun; and immunostained for C-peptide and vimentin. From >400 cells, the percentage positive for C-peptide (green), vimentin (red), both peptides (yellow), or neither (gray) is shown below each panel. Arrowheads identify cells expressing C-peptide (green), vimentin (red), or both peptides (yellow). Similar transitions from mostly negative to mostly vimentin-positive cells were observed in each of six donor islet cultures. (**B**) Some cells migrating out from islets at day 3 are positive for proinsulin mRNA by in situ hybridization and vimentin protein (arrowheads). (**C**) Single-cell analysis of proinsulin mRNA. Individual cells were selected from islet cultures as described (*18*). RNA was isolated and proinsulin transcript was measured by quantitative RT-PCR. Cell number increased twofold from day 11 to 14 and by 50% from day 14 to 17. Scale bars, 10 μm.

for proinsulin, although transcript levels were distributed over three orders of magnitude. This suggests that our culture conditions select for proinsulin mRNA-positive cells. From day 11 to 17, the level of proinsulin transcript declined in individual cells. Most important, as the cell number doubled from day 11 to 14 and increased again by one-half from day 14 to 17, the percentages of proinsulin-positive cells were 95% (day 14) and 100% (day 17). If proliferative hIPCs had arisen from proinsulin transcript-negative cells, e.g., "stem cells," a doubling of cell number would have decreased proinsulin transcript–expressing cells to 50%, and a further increase in cell number by one-half would have decreased proinsulin-expressing cells to 33%. This did not occur. In two other islet preparations, proinsulin mRNA remained detectable in 79% and 74% of cells after 14 days in culture. To demonstrate directly that insulin-expressing cells were proliferating, we labeled cells after 7 days in culture with BrdU for 40 hours and co-stained them with antibodies to BrdU and to C-peptide (fig. S4, A and B). Of the 38% of the cells in this experiment that were C-peptide–positive, more than one-fifth were also positive for BrdU, which indicated that these cells were proliferating. Taken together, our findings are most consistent with the conclusion that proliferating hIPCs originate by EMT from cells initially expressing insulin.

After 2 weeks in culture, islets had flattened to generate a monolayer of cells; residual "islets" were comprised of granular, dead cells. Harvested and reseeded cells displayed a nearly homogeneous, fibroblast-like morphology (fig. S5A). hIPCs at this stage, about 14 days after islets were placed into culture, were defined as passage 0. In 3 to 4 days, the culture reached confluence (fig. S5A). During the transition from cells within islets to hIPCs, markers for epithelial cells including E-cadherin, claudins 3 and 4, occludin, and PECAM1, as well as those specific for endocrine cells including proinsulin, proglucagon, glucokinase, PDX1, and GLP1R, decreased, whereas markers of mesenchymal cells including vimentin, nestin, smooth muscle actins α 2 and γ 2, endoglin, matrix metalloproteinase 2, snail homologs 1 and 2, Thy-1 cell surface antigen, and prolyl 4-hydroxylase increased (Table 1). Cells isolated by Beattie *et al*. (*20*) and Bouckenooghe *et al*. (*21*) appear similar to hIPCs, and they may have arisen by EMT also. Unlike many other primary cell populations derived from human or rodent islets (*10*, *20*), hIPCs exhibit substantial proliferative potential for about 90 days (doubling time of 60 hours) (fig. S5B). Cells isolated from islets by Habener and colleagues (*7*, *22*) proliferated well and may be similar to hIPCs. Cryopreserved cells resumed growth after a brief lag period at rates similar to those of cells never frozen. During the initial 3 months in culture, hIPCs expanded by almost 10^{12}. As a primary culture, hIPC proliferation slowed at later passages. hIPCs from three different islet preparations at passages 4 to 14 exhibited normal karyotypes. At early passages, hIPC populations are positive for proinsulin mRNA, but the level decreased continuously and became undetectable by passage 10 (fig. S5B). The gradual loss of proinsulin transcript may reflect the long half-life of proinsulin mRNA, estimated to be about 30 hours in rodents (*23*). Other endocrine-specific transcripts, including proglucagon, glucagon-like peptide 1 receptor, and glucokinase, also decreased and were undetectable by passage 10 (Table 1).

Up to passage 30, hIPCs could differentiate into ICAs when deprived of serum. Before differentiation, hIPCs showed immunostaining for vimentin (94% of cells), nestin (75%), and smooth muscle actin (98%) in prominent filaments (fig. S2B) like mesenchymal cells (*6*, *16*) and were negative for C-peptide. In contrast, cells within ICAs expressed C-peptide and glucagon (Fig. 3A). C-peptide staining was used to exclude detection of insulin in SFM (*24*). Immunostaining for C-peptide and glucagon of 7-day ICAs from passages 10, 12, or 14 showed that 27 ± 4% of cells stained positively for C-peptide and 17 ± 2%, for glucagon (Fig. 3A). The transition of hIPCs into ICAs increased proinsulin mRNA at least 1000-fold over initially undetectable levels and proglucagon mRNA over 100-fold (Fig. 3B). Transcripts for glucagon-like peptide 1 receptor and glucokinase also increased more than 10-fold. Thus, endocrine-specific transcripts increased when mesenchymal hIPCs transitioned into epithelial ICAs. Expression of claudin 3 and 4 mRNAs (*25*) increased whereas expression of smooth muscle actin alpha2 and gamma2 mRNAs (*16*) decreased in ICAs, further supporting the epithelial transition.

Proinsulin transcript induction was compared at different passages. At passages 3, 4, or 6, proinsulin transcript increased about 10-fold over initially detectable levels (Fig. 3C) whereas at passages 10 through 18, it increased at least 100- to 1000-fold over initially undetectable levels. At passages later than 27, smaller increases in proinsulin transcript were observed. Induction of proinsulin transcript by 100-fold or more occurred consistently in ICAs generated from mid-passage hIPCs from six separate donor islets (fig. S6). Although hIPC ICAs reproducibly exhibited marked induction of proinsulin mRNA expression, the level attained was less than 0.02% of that in human islets. Thus, hIPC ICAs are not comparable to islets in the levels of insulin (or glucagon) expression. However, cells within hIPC ICAs exhibit the following features of islets: Insulin C-peptide is detected by immunostaining (Fig. 3A); in preliminary experiments, ICAs secreted C-peptide under basal and stimulated conditions in vitro (*26*) and human C-peptide was measured in blood from three of six SCID mice implanted with ICAs under their kidney capsules, and after 14 days, implants

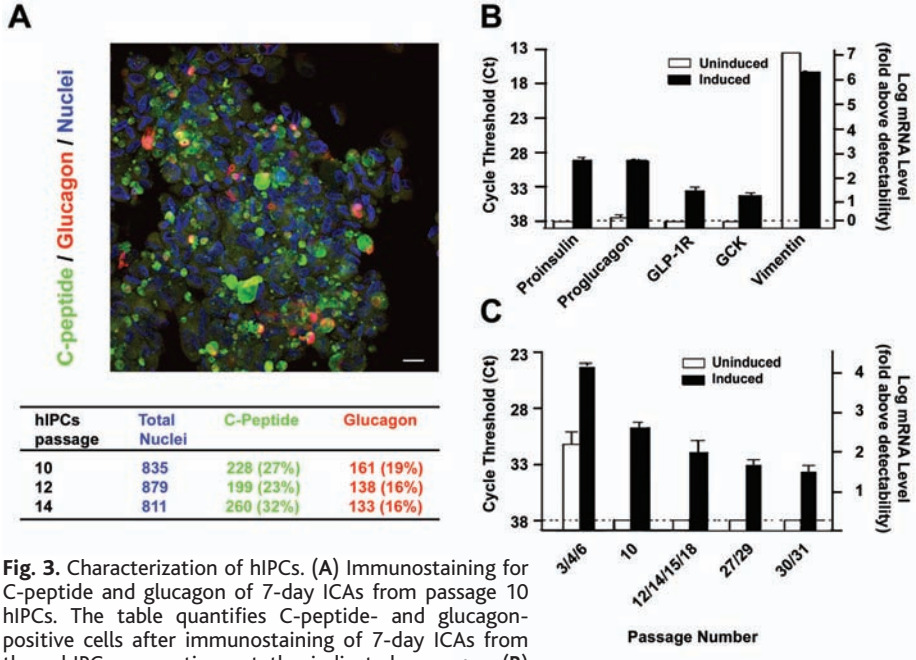

hIPCs passage	Total Nuclei	C-Peptide	Glucagon
10	835	228 (27%)	161 (19%)
12	879	199 (23%)	138 (16%)
14	811	260 (32%)	133 (16%)

Fig. 3. Characterization of hIPCs. (**A**) Immunostaining for C-peptide and glucagon of 7-day ICAs from passage 10 hIPCs. The table quantifies C-peptide- and glucagon-positive cells after immunostaining of 7-day ICAs from three hIPC preparations at the indicated passages. (**B**) Proinsulin, proglucagon, glucagon-like peptide-1 receptor (GLP-1R), and glucokinase (GCK) mRNAs increased, and vimentin mRNA decreased, during induction of ICA formation. (**C**) Induction of proinsulin mRNA at different hIPC passages. Scale bar, 20 μm.

from these three mice immunostained for human C-peptide. The blood levels of human C-peptide in the three mice were 0.22, 0.51, and 0.91 ng/ml and similar levels were found to reverse hyperglycemia in mice transplanted with insulin-expressing cells differentiated from human fetal liver progenitor cells (*27*).

In most previous attempts to generate beta cells in culture from adult islets, maintenance of insulin expression during culture was attempted (*5*, *20*, *21*). The cells obtained in these experiments did not expand well nor did they exhibit marked induction of insulin expression. Another approach was to select for cells that expressed genes, e.g., nestin, that were thought to identify precursor cells (*7*, *22*). Although the origin of these cells was not considered, they were derived from adherent islet cells and are likely similar to hIPCs, because about 75% of hIPCs are immunopositive for nestin. We show that hIPCs are "true" endocrine pancreas precursor cells that exhibit a mesenchymal phenotype before transition into epithelial clusters containing cells expressing insulin or glucagon. Indeed, hIPCs are highly proliferative and can be expanded by a factor of $>10^{12}$ and, therefore, could serve as cells for replacement therapy for diabetes if their insulin output, in particular that in response to glucose, could be optimized and they could be shown to be safe and effective upon implantation.

The origin of hIPCs is important because it provides information about the potential plasticity of insulin-expressing cells, and perhaps of other epithelial cell types, at least after culture in vitro. In contrast to the prevailing view that the source of pancreas-derived precursor cells is adult stem cells, we provide strong evidence that hIPCs are derived from insulin-expressing cells by EMT. This conclusion would be strengthened by permanently marking insulin-expressing cells in situ for cell lineage analysis as performed in mouse models (*4*, *28*), but these experiments are not possible in humans. Our studies, however, do not negate the possibility that adult stem cells are present within islets and contribute to beta cell generation in vivo.

Last, although our observations regarding EMT were made with insulin-expressing cells in vitro, a similar phenomenon may occur in vivo. Using genetically engineered mice, Dor *et al*. recently provided evidence that new insulin-expressing beta cells are derived from "preexisting" beta cells in vivo (*4*). These authors concluded, "Adult pancreatic β-cells are formed by self-duplication." Another interpretation of their data, consistent with our observations, is that new beta cells are generated from preexisting beta cells by reversible EMT.

References and Notes

1. A. M. Shapiro *et al.*, *N. Engl. J. Med.* **343**, 230 (2000).
2. B. Soria, *Differentiation* **68**, 205 (2001).
3. T. Zwillich, *Science* **289**, 531 (2000).
4. Y. Dor, J. Brown, O. I. Martinez, D. A. Melton, *Nature* **429**, 41 (2004).
5. A. Lechner, J. F. Habener, *Am. J. Physiol. Endocrinol. Metab.* **284**, E259 (2003).
6. E. D. Hay, *Acta Anat.*(Basel) **154**, 8 (1995).
7. H. Zulewski *et al.*, *Diabetes* **50**, 521 (2001).
8. V. K. Ramiya *et al.*, *Nat. Med.* **6**, 278 (2000).
9. J. G. Cornelius, V. Tchernev, K. J. Kao, A. B. Peck, *Horm. Metab. Res.* **29**, 271 (1997).
10. S. Bonner-Weir *et al.*, *Proc. Natl. Acad. Sci. U.S.A.* **97**, 7999 (2000).
11. S. Bonner-Weir, A. Sharma, *J. Pathol.* **197**, 519 (2002).
12. R. M. Seaberg *et al.*, *Nat. Biotechnol.* **22**, 1115 (2004).
13. A. Suzuki, H. Nakauchi, H. Taniguchi, *Diabetes* **53**, 2143 (2004).
14. J. P. Thiery, *Curr. Opin. Cell Biol.* **15**, 740 (2003).
15. J. P. Thiery, *Nat. Rev. Cancer* **2**, 442 (2002).
16. R. Kalluri, E. G. Neilson, *J. Clin. Invest.* **112**, 1776 (2003).
17. A. A. Hardikar, B. Marcus-Samuels, E. Geras-Raaka, B. M. Raaka, M. C. Gershengorn, *Proc. Natl. Acad. Sci. U.S.A.* **100**, 7117 (2003).
18. Materials and methods are available as supporting material on *Science* Online.
19. H. Ohlsson, K. Karlsson, T. Edlund, *EMBO J.* **12**, 4251 (1993).
20. G. M. Beattie *et al.*, *Diabetes* **48**, 1013 (1999).
21. T. Bouckenooghe *et al.*, *Cell Transplant.* **12**, 799 (2003).
22. E. J. Abraham, C. A. Leech, J. C. Lin, H. Zulewski, J. F. Habener, *Endocrinology* **143**, 3152 (2002).
23. M. Welsh, D. A. Nielsen, A. J. MacKrell, D. F. Steiner, *J. Biol. Chem.* **260**, 13590 (1985).
24. J. Rajagopal, W. J. Anderson, S. Kume, O. I. Martinez, D. A. Melton, *Science* **299**, 363 (2003).
25. S. Tsukita, M. Furuse, *Ann. N.Y. Acad. Sci.* **915**, 129 (2000).
26. M. C. Gershengorn *et al.*, unpublished observations.
27. M. Zalzman *et al.*, *Proc. Natl. Acad. Sci. U.S.A.* **100**, 7253 (2003).
28. P. L. Herrera, *Int. J. Dev. Biol.* **46**, 97 (2002).

29. We thank D. M. Harlan, National Institute of Diabetes and Digestive and Kidney Diseases, National Institutes of Health, Bethesda, MD, for providing adult human cadaveric pancreatic islets.

Supporting Online Material

www.sciencemag.org/cgi/content/full/1101968/DC1
Materials and Methods
Figs. S1 to S6
References and Notes
Movies S1 and S2

25 June 2004; accepted 11 October 2004
Published online 25 November 2004;
10.1126/science.1101968
Include this information when citing this paper.

β-Arrestin 2 Regulates Zebrafish Development Through the Hedgehog Signaling Pathway

Alyson M. Wilbanks,[1,4] Gregory B. Fralish,[1,4] Margaret L. Kirby,[3] Larry S. Barak,[1,4] Yin-Xiong Li,[1,2,3]* Marc G. Caron[1,2,4]*

β-arrestins are multifunctional proteins that act as scaffolds and transducers of intracellular signals from heptahelical transmembrane-spanning receptors (7TMR). Hedgehog (Hh) signaling, which uses the putative 7TMR, Smoothened, is established as a fundamental pathway in development, and unregulated Hh signaling is associated with certain malignancies. Here, we show that the functional knockdown of β-arrestin 2 in zebrafish embryos recapitulates the many phenotypes of Hh pathway mutants. Expression of wild-type β-arrestin 2, or constitutive activation of the Hh pathway downstream of Smoothened, rescues the phenotypes caused by β-arrestin 2 deficiency. These results suggest that a functional interaction between β-arrestin 2 and Smoothened may be critical to regulate Hh signaling in zebrafish development.

Hedgehog (Hh) molecules are highly conserved morphogens that play a central role in cell proliferation and embryonic patterning (*1*, *2*). In humans, inhibitory mutations of the Sonic Hedgehog (Shh) pathway result in developmental defects such as holoprosencephaly (*3*), whereas mutations that constitutively activate the pathway lead to basal cell carcinomas (*4*) and medullablastomas (*5*). Despite extensive studies of the Hh pathway, the sequence of events leading to a biological function has yet to be fully defined. In vertebrates, extracellular Shh glycoprotein binds to the 12-transmembrane-spanning protein, Patched (Ptc), and relieves the inhibitory effect of Ptc on Smoothened (*6*). Smoothened is a signaling molecule that causes downstream uncoupling of the negative regulator Su(fu) protein from the Gli transcription factors (*7*). The subsequent nuclear translocation and DNA binding of Gli1 and Gli2, and possibly of Gli3, is followed by the increased transcription of a number of genes, including *ptc* itself (*8*) and *nkx2.2* (*9*). In contrast, the proteolytic cleavage of Gli3, promoted by cAMP-dependent protein kinase (PKA) phosphorylation in the absence of a

[1]Department of Cell Biology, [2]Department of Medicine, [3]Department of Pediatrics, [4]Howard Hughes Medical Institute Laboratories, Center for Models of Human Disease, Institute for Genome Science and Policy, Duke University Medical Center, Durham, NC 27710, USA.

*To whom correspondence should be addressed. E-mail: caron002@mc.duke.edu (M.G.C.); lyx@duke.edu (Y.-X.L.)

Hh signal converts Gli3 into a repressor of target genes (*10*). Inactivation of particular genes in the Hh signaling pathway, including *shh*, *smoothened*, and *gli2*, is lethal to zebrafish development (*11*–*13*). The resulting mutant embryo lines—*sonic-you* (*syu*), *slow-muscle-omitted* (*smu*), and *you-too* (*yot*), respectively—are collectively known as the "you-type mutants" in reference to their distinguishing phenotype of U-shaped somites. Several other phenotypes are observed in these mutants and detailed in (*14*) (fig. S1, D and H; fig. S2D).

Studies have found a wide breadth of functions for β-arrestins (*15*–*18*), although none to date have revealed a role for these proteins in development. Analysis of the current zebrafish genome reveals two arrestin genes, visual and cone, as well as two β-arrestin genes, 1 and 2. Although several expressed-sequence-tag clones of β-arrestin 2 have been identified in cDNA libraries from embryonic zebrafish tissues, no clones of β-arrestin 1 have been identified to date. Microinjection of embryos with morpholino (MO) designed to target the 5′ UTR of β-arrestin 2 mRNA (βarr2-MO) resulted in almost complete inhibition of the expression of β-arrestin 2 protein (Fig. 1), as determined by protein immunoblotting (*14*). We used a control MO against visual cone arrestin (VA-MO) to demonstrate functional specificity between the arrestin family members.

Embryos injected with the βarr2-MO exhibited, over the subsequent 120 hours after fertilization, phenotypic similarities to *smu* embryos in which the *smoothened* gene is mutated; VA-MO–injected embryos were similar to wild-type embryos at every stage inspected. We compared the effects of two distinct alleles of *smu* mutants, both generated by viral insertion. One mutant allele, hi1640, produces a severe phenotype resulting from viral insertion into an exon of the *smoothened* gene (*13*), whereas the less severe phenotype of the hi2329b allele is due to viral insertion in a *smoothened* intron (*19*). At 24 hours after fertilization, non-injected embryos and those injected with VA-MO (collectively referred to as control embryos) had straight bodies (Fig. 2, A and B) and chevron-shaped somites (Fig. 2, F and G). By contrast, βarr2-MO, hi2329b, and hi1640 embryos displayed ventrally curved bodies, underdeveloped heads (Fig. 2, C through E), and U-shaped somites (Fig. 2, H through J). Other phenotypes, including partial cyclopia (fig. S1, A to D), lack of optic nerve at the midline (fig. S1, E to H), absence of craniofacial muscle and pectoral fin development (fig. S2, A to F), and reduction of floor plate development (fig. S3, A to F), were also observed.

Three muscle fiber types, including slow muscle, fast muscle, and muscle pioneer slow muscle cell fibers, develop in the segmentation period (10 to 24 hours after fertilization) of the zebrafish embryo (*20*). Muscle pioneer (MP) cells and the development of slow muscle fibers, but not that of fast muscle fibers, require Shh signaling originating from the notochord (*21*). The S58 antibody is specific to slow isotypes of myosin heavy chain and labels both MP and non-MP slow muscle fibers (*22*). Control embryos at 24 hours after fertilization labeled with S58 show the organized development of slow muscle fibers at a density of ~20 fibers per somite (Fig. 2, K and L). By contrast, the number of fibers per somite decreases in βarr2-MO and hi2329b embryos to ~10 fibers per somite (Fig. 2, M and N), whereas the hi1640 embryos display <1 slow muscle fiber per somite (Fig. 2O).

Zebrafish adaxial cells differentiate into MPs in response to Shh signals derived from the notochord by 12 hours after fertilization (*20*). These MPs are the earliest cells to elongate and flatten into muscle fibers that span the somite by 24 hours after fertilization and express the Engrailed protein detectable by the 4D9 antibody (*22*–*25*). Using whole-mount immunohistochemistry with 4D9, we visualized, as described previously (*25*), robust Engrailed staining in MP cells located at the horizontal myoseptum as well as in the surrounding muscle fibers from control embryos (Fig. 2, P and Q). By contrast, 4D9 staining of βarr2-MO, hi2329b, and hi1640 embryos was reduced in both the horizontal myoseptum and surrounding muscle fibers (Fig. 2, R to T). Combined, these data suggest that the phenotype resulting from the βarr2-MO is due to disruption of the Shh pathway.

To confirm that the phenotypes revealed by β-arrestin 2 knockdown are indeed a result of inhibiting the Hh signaling pathway, we performed in situ hybridization with probes designed to bind Shh target genes, specifically *nkx2.2* and *ptc*. In wild-type embryos, increased expression of both genes occurs in response to Shh signaling by 27 hours after fertilization (*9*, *26*). The injection of *Shh* mRNA into embryos at the one-cell stage

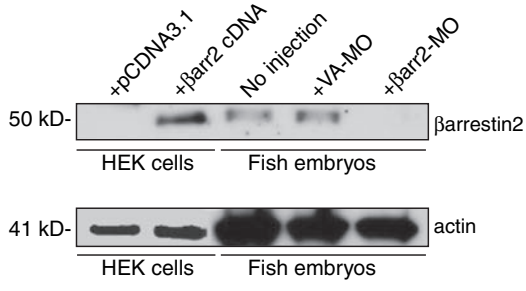

Fig. 1. Western blot analysis of zebrafish β-arrestin 2 expression. Lysate (500 ng protein) from human embryonic kidney (HEK) 293T cells transiently transfected with either pCDNA3.1(+) vector alone (lane 1) or with zebrafish β-arrestin 2 cDNA (lane 2). Lysate extracts from zebrafish embryos (48 hours after fertilization, two per lane) that were not injected (lane 3) or were injected with VA-MO (lane 4) or βarr2-MO (lane 5) were probed with antibody to trout β-arrestin 2, followed by a secondary horseradish peroxidase–conjugated antibody to rabbit, and then visualized by enhanced chemiluminesence. Equal loading of protein was verified by stripping and reprobing the blot with antibodies to actin. Densitometer quantification of three independent experiments reveals an average of 96 ± 3% reduction in β-arrestin 2 expression with βarr-MO.

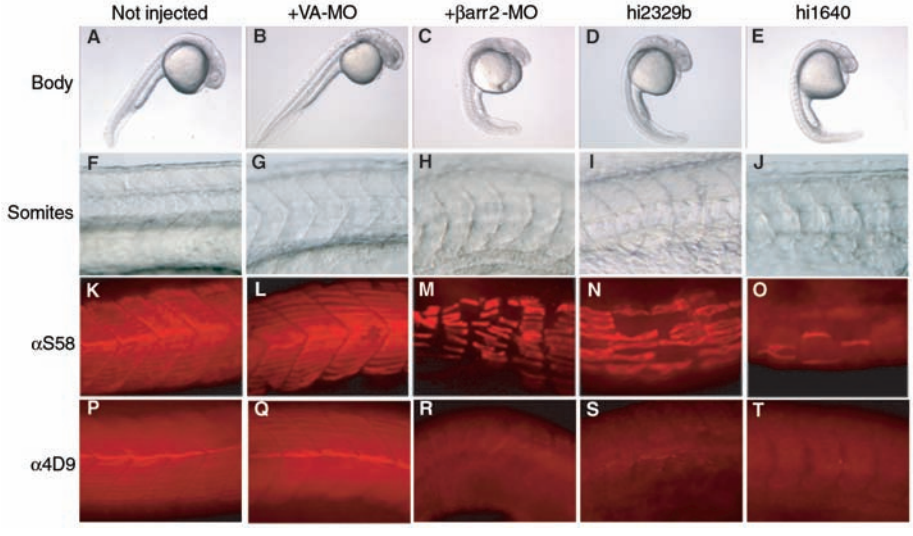

Fig. 2. Phenotypes of βarr2-MO embryos and Smoothened mutants hi2329b and hi1640 at 24 hours after fertilization. (**A** to **E**) Lateral views of whole zebrafish bodies. (**F** to **J**) Lateral views of somites, dorsal toward the top, anterior to the right. (**K** to **O**) S58 antibody staining of embryos. (**P** to **T**) 4D9 antibody staining of embryos.

also induces the ectopic expression of *nkx2.2* in dorsal and lateral regions of the brain by 27 hours after fertilization (*9*). In situ hybridization of zebrafish embryos at 27 hours after fertilization with *nkx2.2* antisense probes revealed a normal brain pattern of *nkx2.2* expression in control embryos (Fig. 3, A and B), whereas this signal was absent in the embryos injected with βarr2-MO (Fig. 3C). Furthermore, injection of *Shh* mRNA (100 ng) alone or combined with the VA-MO resulted in a broader ectopic induction of *nkx2.2* (Fig. 3, D and E). By contrast, injection of *Shh* mRNA combined with βarr2-MO caused a complete loss of *nkx2.2* transcription throughout the entire embryo (Fig. 3F). These results suggest that the loss of β-arrestin 2 blocks the Hh signaling pathway downstream of the Shh signal but upstream of the pathway's target genes. This hypothesis was strengthened by a double in situ hybridization approach using antisense probes to *ptc* and *shh* simultaneously. Control embryos at 27 hours after fertilization had a normal expression pattern of *ptc* in medial somites and ventral spinal cord and normal *shh* expression in midline cells at the position of the floor plate (Fig. 3, G, H, J, and K). By contrast, βarr2-MO embryos exhibited a small decrease of *shh* expression in midline cells [as do the hi1640 embryos (*13*)] along with a complete loss of *ptc* expression (Fig. 3, I and L). These results demonstrate that the βarr2-MO does not inhibit the endogenous expression of *shh* but does lead to a loss of expression of *ptc*, consistent with the loss of function of an intermediate of the Hh signaling pathway.

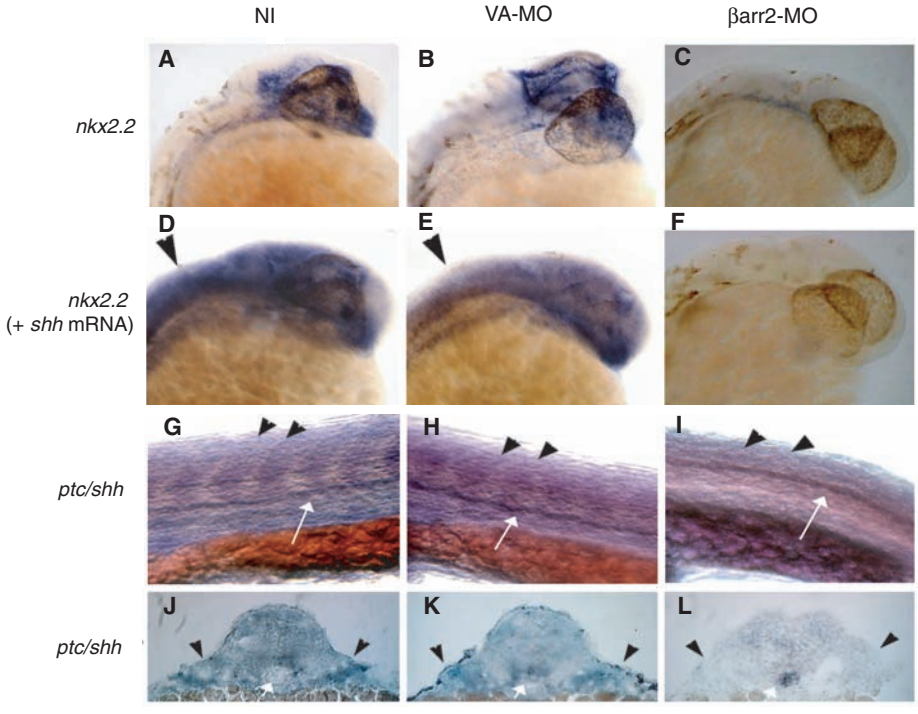

Fig. 3. In situ hybridizations of zebrafish embryos at 27 hours after fertilization for downstream genes of the Hh signaling pathway. Embryos were not injected (NI) or were injected, as indicated, with MO to visual cone arrestin or with β-arrestin 2 mRNA. (**A** to **F**) In situ hybridization with *nkx2.2* probe. *Shh* mRNA (100 ng) was injected either alone (D), with VA-MO (E), or with βarr2-MO (F). Shown are lateral views (dorsal toward the top, anterior to the left). (**G** to **L**) Double in situ hybridization with *shh* (blue stain, white arrows indicating expression at the midline) and *ptc* (red stain, dark arrows) probes on whole mounts [(G) to (I)] or sectioned embryos [(J) to (L)].

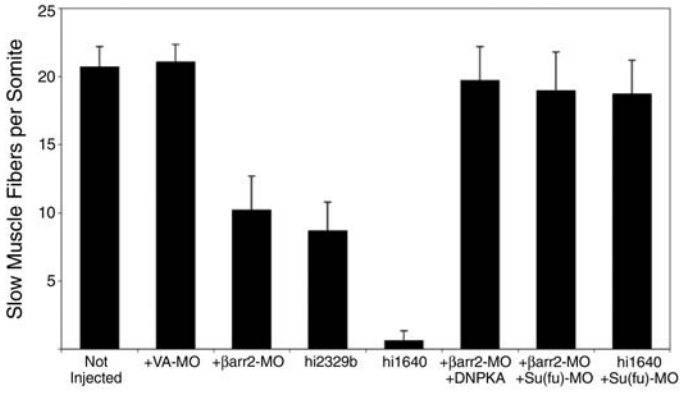

Fig. 4. Loss of slow muscle fiber development in βarr2-MO is restored with DNPKA mRNA or Su(fu)-MO. Quantitative analysis of slow muscle fiber number per somite in embryos 24 hours after fertilization, injected as indicated. Embryos were stained with S58 antibody. Slow muscle fibers in three to five somites on ~20 embryos per experiment were counted.

To reinforce this contention, we further evaluated the effects of two distinct approaches able to support signaling in the absence of Shh signaling. Su(fu) is an inhibitory component of the Hh signaling pathway that maintains the cytoplasmic localization of the transcription factors Gli1 and Gli2 in the absence of a Hh signal (*5*). We therefore reasoned that the loss of Su(fu) expression would result in the nuclear translocation of Gli1 and Gli2, and increased expression of Hh target genes in the absence of a Hh signal. We designed a MO against Su(fu) [Su(fu)-MO] for injection into one-cell zebrafish embryos. PKA is another negative regulator of the Hh pathway and phosphorylates substrates, resulting in proteolytic cleavage of Gli3, which then acts to repress Hh target gene expression (*27*). Dominant negative PKA (DNPKA) mRNA, when injected into embryos, results in a broader expression of Hh target genes and a rescue of the phenotypes of *smu* mutants (*21*). To assess whether either DNPKA or a Su(fu)-MO is able to rescue the βarr2-MO treated phenotypes, we injected the βarr2-MO in combination with either DNPKA mRNA or the Su(fu)-MO and scored for the number of slow muscle fibers per somite at 24 hours after fertilization with the S58 antibody (Fig. 4). Lower numbers of fibers per somite were observed in βarr2-MO or hi2329b embryos (~10 per somite) than in control embryos (~20 per somite). The hi1640 embryos have even fewer fibers (<1 per somite), which suggests that in βarr2-MO or hi2329b embryos the Hh signaling is decreased but not completely inhibited. Either DNPKA mRNA or the Su(fu)-MO completely rescued the inhibition of slow muscle fiber development in those embryos resulting from the βarr2-MO, as did the Su(fu)-MO on the hi1640 embryos (to ~20 per somite), although some of the gross phenotypes still remained evident in the hi1640 mutants (fig. S4, A to D) (*28*).

Our findings indicate that β-arrestin 2 acts as a regulator of the zebrafish Hh signaling pathway during embryogenesis. This could potentially be mediated by an interaction between β-arrestin 2 and the Smoothened protein, as is documented in Chen *et al.*'s paper on mammalian homologs (*29*). Indeed, in cell-based assays zebrafish β-arrestin 2 translocates to the plasma membrane upon expression of Smoothened in the absence of Patched (*28*). The involvement of β-arrestin 2, a pleotropic molecular adaptor of seven transmembrane proteins, in the Hh signaling

pathway provides a previously unappreciated paradigm to elucidate how this pathway initiates transcription to promote growth, differentiation, and malignancies.

References and Notes

1. K. Nyakken, N. Perrimon, *Curr. Opin. Genet. Dev.* **12**, 503 (2002).
2. M. Hammerschimidt, A. Brook, A. P. McMahon, *Trends Genet.* **13**, 14 (1997).
3. E. Belloni *et al.*, *Nature Genet.* **14**, 353 (1996).
4. H. Hahn *et al.*, *Cell* **85**, 841 (1996).
5. M. Taylor *et al.*, *Nature Genet.* **31**, 306 (2002).
6. D. Stone *et al.*, *Nature* **384**, 129 (1996).
7. Q. Ding *et al.*, *Curr. Biol.* **9**, 1119 (1999).
8. J. Concordet *et al.*, *Development* **122**, 2835 (1996).
9. K. Barth, S. Wilson, *Development* **121**, 1755 (1995).
10. G. Wang *et al.*, *Cell* **100**, 423 (2000).
11. F. van Eeden *et al.*, *Development* **123**, 153 (1996).
12. M. Barresi *et al.*, *Development* **127**, 2189 (2000).
13. W. Chen, S. Burgess, N. Hopkins, *Development* **128**, 2385 (2001).
14. Materials and methods are available as supporting material on *Science* Online.
15. P. McDonald *et al.*, *Science* **290**, 1574 (2000).
16. S. Fergusson *et al.*, *Science* **271**, 363 (1996).
17. A. Claing *et al.*, *Prog. Neurobiol.* **66**, 61 (2002).
18. L. M. Luttrell, R. J. Lefkowitz, *J. Cell Sci.* **115**, 455 (2002).
19. N. Hopkins, unpublished data.
20. H. Stickney *et al.*, *Dev. Dyn.* **219**, 287 (2000).
21. M. Barresi *et al.*, *Development* **127**, 2189 (2000).
22. M. Crow, F. Stockdale, *Dev. Biol.* **113**, 238 (1986).
23. N. Patel *et al.*, *Cell* **58**, 955 (1989).
24. M. Ekker *et al.*, *Development* **116**, 1001 (1992).
25. K. Hatta *et al.*, *Development* **112**, 821 (1991).
26. H. Schauerte *et al.*, *Development* **125**, 2983 (1998).
27. M. Hammerschmidt *et al.*, *Genes Dev.* **10**, 647 (1996).
28. A. Wilbanks, unpublished observations.
29. W. Chen *et al.*, *Science* **306**, 2257 (2004).

30. We thank R. Lefkowitz for valuable guidance and critical discussions; M. Zdanowicz and P. Zhang for excellent technical assistance; A. Amsterdam, B. Hogan, and P. Beachy for critical review of the manuscript; and N. Hopkins, R. Jahns, L. Hein, A. Schier, F. Stockdale, and R. Moon for providing key reagents. Supported by NIH grants GM069086-01 (to G.B.F.), HL36059 (to M.L.K.), HL61365 (to L.S.B.), and NS19576 (to M.G.C.).

Supporting Online Material

www.sciencemag.org/cgi/content/full/306/5705/2264/DC1
SOM Text
Materials and Methods
Figs. S1 to S4
References

17 August 2004; accepted 29 October 2004
10.1126/science.1104193

Role of the Kinase MST2 in Suppression of Apoptosis by the Proto-Oncogene Product Raf-1

Eric O'Neill,[1] Linda Rushworth,[1] Manuela Baccarini,[3] Walter Kolch[1,2]*

The ablation of the protein kinase Raf-1 renders cells hypersensitive to apoptosis despite normal regulation of extracellular signal–regulated kinases, which suggests that apoptosis protection is mediated by a distinct pathway. We used proteomic analysis of Raf-1 signaling complexes to show that Raf-1 counteracts apoptosis by suppressing the activation of mammalian sterile 20–like kinase (MST2). Raf-1 prevents dimerization and phosphorylation of the activation loop of MST2 independently of its protein kinase activity. Depletion of MST2 from Raf-1$^{-/-}$ mouse or human cells abrogated sensitivity to apoptosis, whereas overexpression of MST2 induced apoptosis. Conversely, depletion of Raf-1 from Raf-1$^{+/+}$ mouse or human cells led to MST2 activation and apoptosis. The concomitant depletion of both Raf-1 and MST2 prevented apoptosis.

Mitogen-activated protein kinase (MAPK) pathways are primordial signaling systems that enable cells to respond to external cues. In metazoans, the proteins Ras, Raf, and MEK act sequentially to activate the MAPK extracellular signal–regulated kinase (ERK). This pathway has a crucial role in the control of cell proliferation, differentiation, and survival (*1*–*3*), which is demonstrated by its frequent hyperactivation in human tumors, most notably those caused by active mutations in Ras (*4*) or B-Raf (*5*). The Raf family of serine-threonine kinases comprises three members: Raf-1, B-Raf, and A-Raf. All Raf isoforms are activated by binding to the guanosine triphosphate (GTP)–bound form of Ras, and they share MEK as the only commonly recognized substrate (*1*–*3*). However, studies in knock-out mice revealed distinct physiological functions of the Raf isozymes (*6*), which suggest the existence of other effectors.

Ablation of the Raf-1 gene causes widespread apoptosis and embryonic lethality despite normal regulation of ERK through B-Raf (*7*, *8*). Raf-1$^{-/-}$ fibroblasts are hypersensitive to apoptosis that is induced by selected stimuli, including serum withdrawal and stimulation of the death receptor Fas (*7*, *8*). This hypersensitivity suggests that Raf-1 can protect fibroblasts from apoptosis independently of B-Raf and ERK. When knocked back in, a Raf-1 mutant, Raf-1YY340-341FF, which cannot be activated, fully rescued the Raf-1$^{-/-}$ phenotype, which resulted in viable mice (*7*). This result indicates that full activity of Raf-1 may not be required for suppression of apoptosis.

To search for new partners in Raf-1 signaling, we immunopurified proteins associated with Flag-tagged Raf-1 that were expressed in COS-1 cells, and identified them by mass spectrometry (Fig. 1A). Proteins known to interact with Raf-1, including 14-3-3, heat shock protein 50 (Hsp50), and Hsp90 (*3*), associated with Raf-1 under conditions of both serum starvation and stimulation. A 55-kD band, which preferentially coprecipitated with Raf-1 from serum-starved cells, contained the mammalian sterile 20–like kinase (MST2). In untransfected serum-deprived cells, endogenous MST2 coimmunoprecipitated with endogenous Raf-1, and Raf-1 was detected in MST2 immunoprecipitates (Fig. 1B). In addition, Raf-1YY340/341FF and Raf-1 K375M, a catalytically inactive mutant, could interact with MST2 in transfected cells (Fig. 1C). Pulldown assays with bacterially expressed Raf-1 deletion proteins (fig. S1) showed that MST2 bound to amino acids 151 and 303 of Raf-1. This region diverges between Raf isoforms and is thought to mediate isozyme-specific interactions with other proteins (*9*). MST2 did not bind B-Raf (fig. S2), which suggests that MST2 is part of a Raf-1–specific signaling pathway.

MST2 was identified as a kinase that is activated by the pro-apoptotic agents staurosporine and Fas ligand (*10*, *11*). Treatment of COS-1 cells with staurosporine or antibody to Fas reduced the amount of MST2 associated with Raf-1 (Fig. 2A). Mitogenic and pro-apoptotic signaling are often linked in order to prevent unwanted proliferation (*12*). Therefore, we compared the functional consequences of disrupting the endogenous MST2–Raf-1 complex in response to mitogens or stress signals (Fig. 2B). Staurosporine caused activation of MST2, but not of the Akt kinase, and induced cleavage of poly(ADP-ribose) polymerase (PARP), which indicates activation of caspase and promotion of apoptosis. In contrast, serum growth factors and oncogenic RasV12 induced Akt activation, which is characteristic of survival pathways that promote cell survival. However, they did not stimulate MST2 activity or PARP cleavage. Serum

[1]The Beatson Institute for Cancer Research, Garscube Estate, Switchback Road, Glasgow G61 1BD, UK. [2]Sir Henry Wellcome Functional Genomics Facility, Institute of Biomedical and Life Sciences, University of Glasgow, Glasgow G12 8QQ, UK. [3]Max F. Perutz Laboratories, University Departments at the Vienna Biocenter, Department of Microbiology and Genetics, University of Vienna, Dr. Bohr Gasse 9, A-1030 Vienna, Austria.

*To whom correspondence should be addressed. E-mail: wkolch@beatson.gla.ac.uk

deprivation did not activate MST2, Akt, or caspases, suggesting that serum withdrawal may allow apoptosis by decreasing survival signaling rather than by actively promoting death signaling.

We found no evidence that MST2 regulates Raf-1 (*13*). However, Raf-1 interfered with MST2 activation on several levels. MST2 is activated through homodimerization followed by transphosphorylation of a critical threonine in the activation loop (*14*). MST2 formed homodimers in Raf-1$^{-/-}$ cells. However, reconstituting Raf-1$^{-/-}$ cells with increasing amounts of exogenous Raf-1 caused disassembly of the MST2 dimers in a dose-dependent manner (Fig. 2C). MST2 was constitutively phosphorylated at the activating threonine residue in Raf-1$^{-/-}$ cells but not in Raf-1$^{+/+}$ cells. Reconstitution of the Raf-1$^{-/-}$ cells with Raf-1 or catalytically inactive Raf-1 completely abrogated both MST2 phosphorylation and kinase activity of MST2 (Fig. 2D), which indicated that the effects of Raf-1 did not depend on its kinase activity. Because Raf-1 associates with phosphatases, including PP2A (*15*, *16*), and because the PP2A inhibitor okadaic acid can cause activation of MST2 (*14*), we examined whether Raf-1 might recruit a phosphatase that dephosphorylates MST2. Recombinant MST2 was activated by autophosphorylation (*14*) and incubated with Raf-1 or catalytically inactive Raf-1 immunoprecipitated from COS-1 cells. Both Raf-1 immunoprecipitates readily caused dephosphorylation of MST2, which was prevented by okadaic acid (Fig.

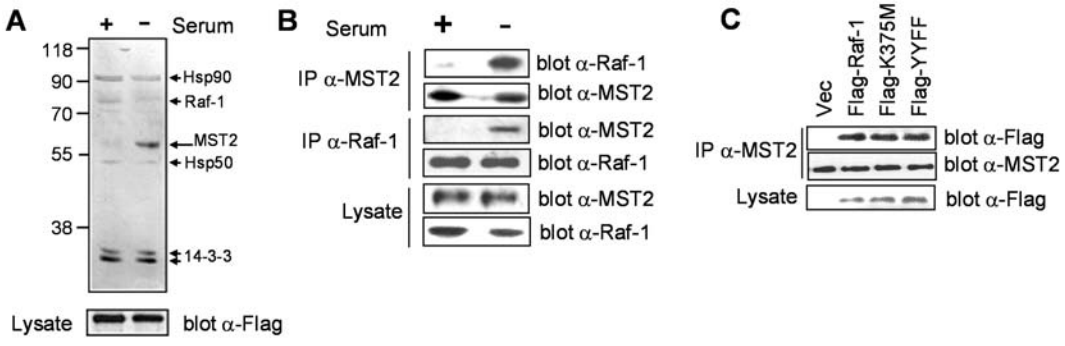

Fig. 1. MST2 is a component of Raf-1 signaling complexes. (**A**) Flag–Raf-1 was immunoprecipitated from COS-1 cells kept in 10% (+) or 0.1% (-) serum. Flag–Raf-1 immunoprecipitates were separated by SDS-polyacrylamide gel electrophoresis and silver stained. Associated proteins were identified by mass spectrometry. (**B**) Immunoprecipitation (IP) of endogenous MST2 and endogenous Raf-1 from COS-1 cells kept in 10 or 0.1% serum. Raf-1 and MST2 were detected by Western blotting. (**C**) Immunoprecipitation of endogenous MST2 from COS-1 cells expressing Flag–Raf-1, K375M (catalytically inactive mutant), or YY340-341FF (non-activatable Raf-1 mutant). Cells were maintained in 0.1% serum and proteins were detected by Western blotting. α, antibody; vec, vector.

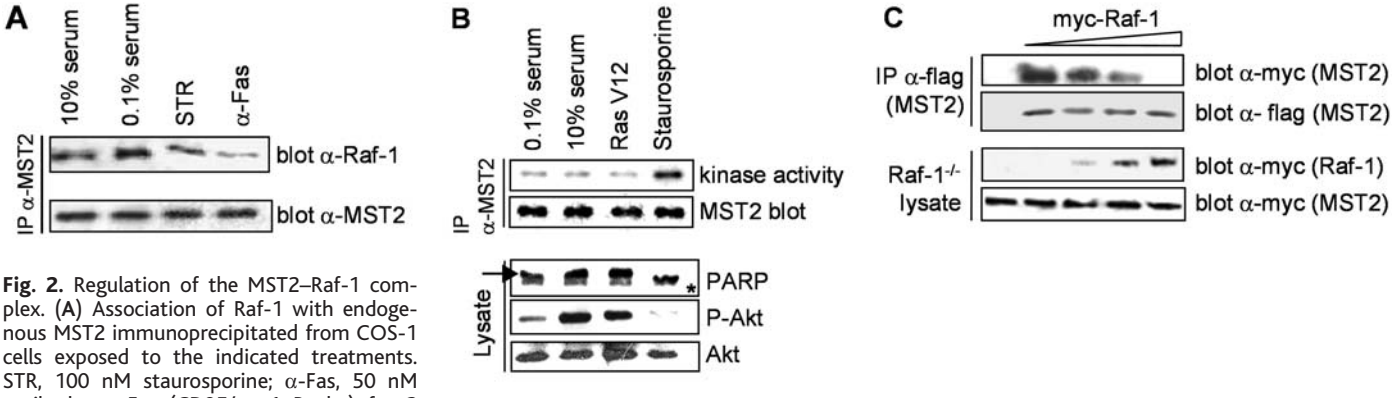

Fig. 2. Regulation of the MST2–Raf-1 complex. (**A**) Association of Raf-1 with endogenous MST2 immunoprecipitated from COS-1 cells exposed to the indicated treatments. STR, 100 nM staurosporine; α-Fas, 50 nM antibody to Fas (CD95/apo1 Roche) for 2 hours. Endogenous Raf-1 was detected by Western blotting. (**B**) Immunoprecipitation of MST2 from cells transfected with RasV12 or treated as indicated. MST2 kinase activity was determined by an in-gel kinase assay. Amounts of MST2 in the immunoprecipitates were determined by Western blotting. PARP cleavage and activation of Akt were assayed in the same lysates by Western blotting as indicated. Full-length PARP is marked by an arrow; cleaved PARP is marked by an asterisk. (**C**) Immunoprecipitation of Flag-MST2 from Raf-1$^{-/-}$ cells expressing myc-MST2 and Flag-MST2 in the presence of 0.1% serum. MST2 dimerization was detected by Western blotting. Flag-MST2 immunoprecipitates were associated with Myc-MST2 protein. Myc-Raf-1 was transfected at concentrations of 0, 0.1, 0.5, and 1.0 μg of plasmid DNA. (**D**) Immunoprecipitation of MST2 from serum-starved parental Raf-1$^{+/+}$ (+/+) and Raf-1$^{-/-}$ (−/−) fibroblasts transfected with Flag-Raf-1, Flag-Raf-1-K375M, or vector control. Endogenous MST2 was immunoprecipitated, and phosphorylated MST2 was detected by Western blotting with an antibody to phosphothreonine (*25*, *26*). Subsequently, blots were washed and MST2 was visualized with antibody to MST2. (**E**) Purified recombinant MST2 protein (Upstate) was in vitro phosphorylated and activated, then incubated with Flag immunoprecipitates from COS-1 cells expressing Flag-Raf-1, Flag-K375M, or vector control. Phosphatase inhibitor (1mM okadaic acid) was added as indicated. Western blots were developed with the phosphospecific antibody to MST2, stripped, and incubated with a pan-MST2 antibody.

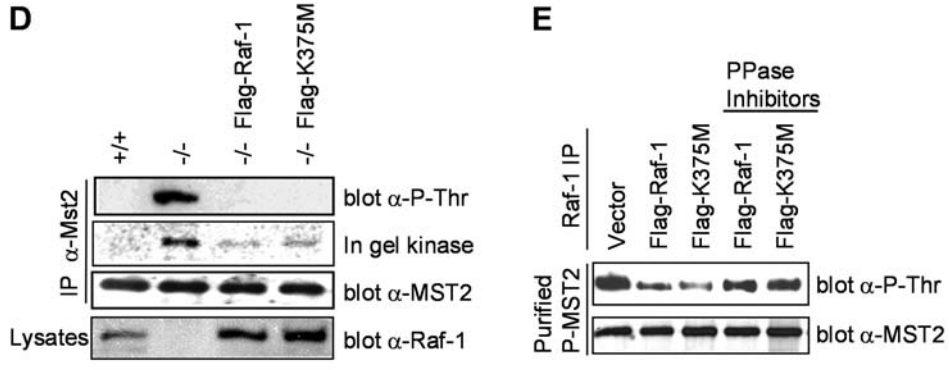

2E). These results indicate that Raf-1 restricts MST2 activity by preventing dimerization and recruiting a phosphatase to dephosphorylate the activation site of MST2.

MST2 was constitutively activated in Raf-1$^{-/-}$ cells, and this activity was enhanced by Fas ligation. In contrast, Fas ligation was inefficient in activating MST2 in Raf-1$^{+/+}$ cells (Fig. 3A). Staurosporine activated MST2 in Raf-1$^{-/-}$ cells better than in Raf-1$^{+/+}$ cells (Fig. 3B). Furthermore, Raf-1$^{-/-}$ cells succumb to apoptosis more rapidly than Raf-1$^{+/+}$ cells in response to Fas or staurosporine (Fig. 4A), but not tumor necrosis factor–α (TNF-α) (*8*). TNF-α failed to stimulate MST2 activity in Raf-1$^{-/-}$ cells (Fig. 3C). Thus, the pattern of MST2 activation reflects the pattern of apoptosis sensitivity of Raf-1$^{-/-}$ cells (*7*), suggesting that MST2 could be a critical apoptosis effector controlled by Raf-1.

Therefore, decreasing the levels of MST2 protein should reduce the sensitivity of Raf-1$^{-/-}$ cells to Fas ligation and serum withdrawal. Decreasing MST2 expression in Raf-1$^{-/-}$ cells using two different small interferening RNAs (siRNAs) (Fig. 4B) completely protected Raf-1$^{-/-}$ cells against apoptosis induced by serum withdrawal or Fas ligation (Fig. 4C). Conversely, the overexpression of MST2 increased the percentage of Raf-1$^{-/-}$ cells that underwent apoptosis when deprived of serum. A catalytically inactive MST2 mutant had no effect on apoptosis (Fig. 4D). Increasing MST2 expression enhanced apoptosis in the Raf-1$^{-/-}$ cells in a dose-dependent manner, whereas Raf-1$^{+/+}$ cells were unaffected except at the highest dose tested (fig. S3). We propose that Raf-1 may control MST2 by sequestering it into an inactive complex, which can be abolished by overexpression of MST2 or by disruption of the complex through stress signals. Decreasing Raf-1 expression in Raf-1$^{+/+}$ parental cells by siRNA also led to MST2 activation and apoptosis (Fig. 4E). We also explored MST2 regulation in Lovo (a colon cancer cell line) and MCF7 cells (a mammary cell line). Both MST2 activity and apoptosis increased upon down-regulation of Raf-1 expression by siRNA (fig S4). Fas stimulated both MST2 activity and apoptosis, and both activities were further increased upon Raf-1 down-regulation. The concomitant down-regulation of MST2 and Raf-1 completely prevented Fas-induced apoptosis in Lovo and MCF-7 cells (Fig. 4F).

These results provide evidence for Raf-1 as a physiological regulator of MST2 in anti-apoptotic signaling. This role is independent of MEK activation because kinase-negative Raf-1 also could inhibit MST2 activation (Fig. 2D) and apoptosis (fig. S5). Immunodepletion experiments showed that MST2 was quantitatively associated with Raf-1 (fig. S6), which suggests that Raf-1 sequesters MST2 in an inactive state. Raf-1 can counteract apoptosis by different mechanisms, which may be cell type–dependent (*1*). For instance, heart dilatation and cardiomyocyte apoptosis caused by cardiac-specific Raf-1 ablation is prevented by ablation of the proapoptotic kinase ASK1 (*17*). Raf-1 also can regulate Fas membrane expression, and the heterozygous inactivation of Fas rescues both the embryonic lethality

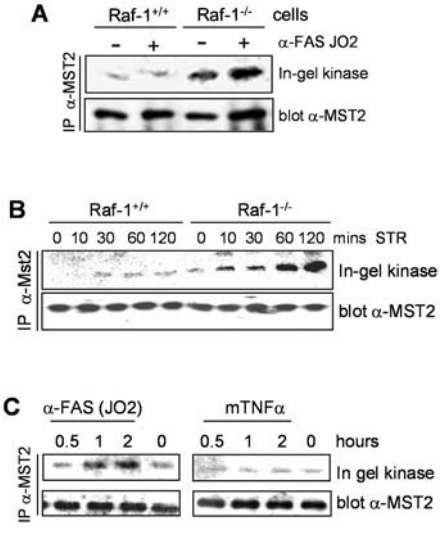

Fig. 3. Inhibition of threonine phosphorylation and activation of MST2 by Raf-1. (**A**) Raf-1$^{+/+}$ and Raf-1$^{-/-}$ cells were treated with mouse-specific antibody to Fas (JO2, 50 nM) plus cycloheximide (CHX, 5 μg/ml) for 1 hour, and MST2 activity was measured in an in-gel kinase assay. (**B**) Serum-starved Raf-1$^{+/+}$ and Raf-1$^{-/-}$ fibroblasts were treated with 100 nM STR for the indicated time points. MST2 was immunoprecipitated and its activity was determined in an in-gel kinase assay (*11*). (**C**) Serum-starved Raf-1$^{-/-}$ cells were stimulated with murine TNF-α (10 ng/ml) or antibody to Fas JO2 (50 nM) for the indicated times. MST2 immunoprecipitates were examined in an in-gel kinase assay, and portions were immunoblotted with antibody to MST2.

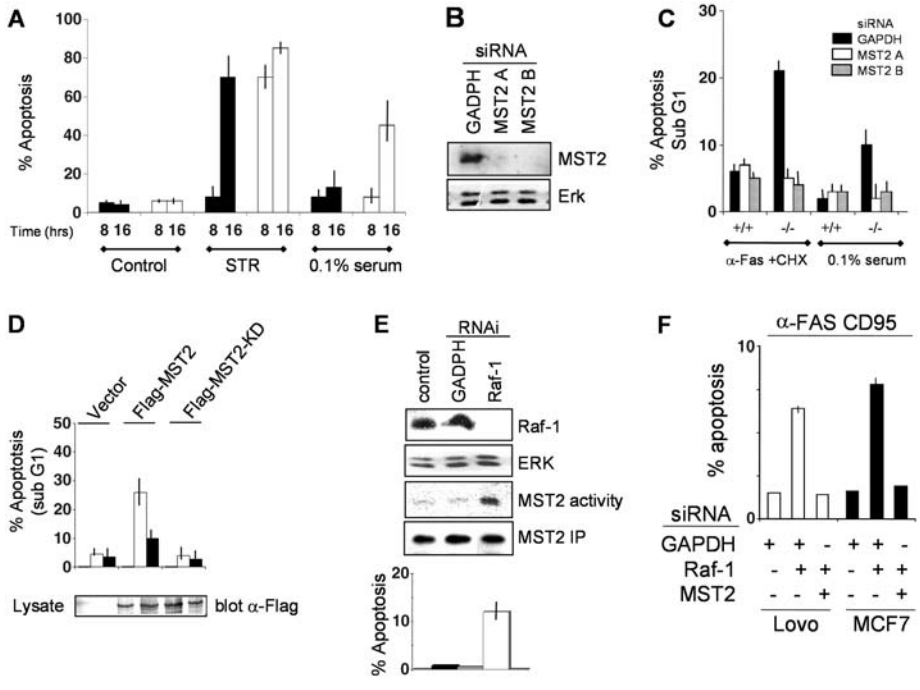

Fig. 4. Depletion of MST2 prevents enhanced apoptosis in cells lacking Raf-1. (**A**) Apoptosis in Raf-1$^{+/+}$ (solid bars) and Raf-1$^{-/-}$ (open bars) fibroblasts grown in 10% serum (control) were treated with 100 nM STR or placed in 0.1% serum. Apoptosis was measured 8 and 16 hours after treatment. (**B**) Absence of MST2 in Raf-1$^{+/+}$ and Raf-1$^{-/-}$ fibroblasts transfected with one of two siRNA nucleotides directed against MST2 (MST2A or MST2B). Control siRNA was to glyceraldehyde-3-phosphate dehydrogenase (GAPDH). Western blots show MST2 protein in total cell extracts. (**C**) Raf-1$^{+/+}$ and Raf-1$^{-/-}$ fibroblasts were transfected with the indicated siRNAs, and treated with 50 nM antibody to Fas JO2 and CHX (5 μg/ml) or placed in 0.1% serum. After 16 hours, apoptosis was quantified by measuring DNA fragmentation by fluorescence-activated cell sorting. (**D**) Raf-1$^{+/+}$ (solid bars) and Raf-1$^{-/-}$ (open bars) fibroblasts were transfected with Flag-MST2 or kinase-dead Flag-MST2-KD, and assayed for apoptosis as in (C). Overexpressed MST2 was detected by immunoblotting with antibody to Flag. (**E**) Raf-1$^{+/+}$ fibroblasts were transfected with siRNA directed against Raf-1 (open bars)or GADPH (hatched bars) or left untreated (solid bars). Cells were placed in 0.1% serum and assayed 16 hours later. Raf-1, ERK, or MST2 was detected by Western blotting of cell lysates. MST2 activity of MST2 immunoprecipitates was detected in an in-gel kinase assay. Apoptosis was determined by measuring DNA fragmentation. (**F**) Lovo and MCF7 cells were transfected with siRNA oligos against Raf-1(50 nM; Ambion), MST2 (50 nM; Ambion), or GAPDH as control, and apoptosis in response to antibody to Fas was measured as above.

of Raf-1$^{-/-}$ mice and the hypersensitivity of fibroblasts to Fas-induced apoptosis (*18*). In the fruit fly *Drosophila melanogaster*, mutations in the MST2 homolog Hippo cause excessive proliferation and survival of cells in imaginal discs (*19–23*). Hippo forms a complex with Warts and Salvador, whose respective mammalian orthologs, Lats and hWW45, are candidate tumor suppressor genes (*24*). The existence of similar complexes in mammalian cells has yet to be verified, but would link Raf-1 through MST2 with an important tumor suppressor pathway.

References and Notes

1. M. Baccarini, *Cell Death Differ.* **9**, 783 (2002).
2. J. Avruch *et al.*, *Recent Prog. Horm. Res.* **56**, 127 (2001).
3. W. Kolch, *Biochem. J.* **351**, 289 (2000).
4. M. Malumbres, M. Barbacid, *Nature Rev. Cancer* **3**, 459 (2003).
5. K. E. Mercer, C. A. Pritchard, *Biochim. Biophys. Acta* **1653**, 25 (2003).
6. E. O'Neill, W. Kolch, *Br. J. Cancer* **90**, 283 (2004).
7. M. Huser *et al.*, *EMBO J.* **20**, 1940 (2001).
8. M. Mikula *et al.*, *EMBO J.* **20**, 1952 (2001).
9. A. Yuryev, L. P. Wennogle, *Genomics* **81**, 112 (2003).
10. L. K. Taylor, H. C. Wang, R. L. Erikson, *Proc. Natl. Acad. Sci. U.S.A.* **93**, 10099 (1996).
11. K. K. Lee, T. Ohyama, N. Yajima, S. Tsubuki, S. Yonehara, *J. Biol. Chem.* **276**, 19276 (2001).
12. A. D. Cox, C. J. Der, *Oncogene* **22**, 8999 (2003).
13. E. O'Neill, W. Kolch, data not shown.
14. M. Praskova, A. Khoklatchev, S. Ortiz-Vega, J. Avruch, *Biochem. J.* **381**, 453 (2004).
15. D. Abraham *et al.*, *J. Biol. Chem.* **275**, 22300 (2000).
16. M. Jaumot, J. F. Hancock, *Oncogene* **20**, 3949 (2001).
17. O. Yamaguchi *et al.*, *J. Clin. Invest.* **114**, 937 (2004).
18. D. Piazzolla, K. Meissl, L. Kucerova, M. Baccarini, in preparation.
19. J. Jia, W. Zhang, B. Wang, R. Trinko, J. Jiang, *Genes Dev.* **17**, 2514 (2003).
20. S. Wu, J. Huang, J. Dong, D. Pan, *Cell* **114**, 445 (2003).
21. K. F. Harvey, C. M. Pfleger, I. K. Hariharan, *Cell* **114**, 457 (2003).
22. R. S. Udan, M. Kango-Singh, R. Nolo, C. Tao, G. Halder, *Nature Cell Biol.* **5**, 914 (2003).
23. S. Pantalacci, N. Tapon, P. Leopold, *Nature Cell Biol.* **5**, 921 (2003).
24. N. Tapon *et al.*, *Cell* **110**, 467 (2002).
25. Y. Deng, A. Pang, J. H. Wang, *J. Biol. Chem.* **278**, 11760 (2003).
26. H. Glantschnig, G. A. Rodan, A. A. Reszka, *J. Biol. Chem.* **277**, 42987 (2002).
27. Molecular interaction data have been deposited in the Biomolecular Interaction Network Database (BIND) with accession codes 182817, 182818, and 182819. We thank D. Piazzolla for help with Raf-1$^{-/-}$ cells; J. Chernoff, K. K. Lee, S. Yonehara, and D. Morrison for expression constructs; A. Pitt for help with mass spectrometry; and A. Dhillon and K. Hughes for helpful discussions. Supported by the European Union, a Biotechnology and Biochemical Sciences Research Council/Celltech Cooperative Award in Science and Engineering studentship, and Cancer Research UK.

Supporting Online Material

www.sciencemag.org/cgi/content/full/306/5705/2267/DC1
Materials and Methods
Figs. S1 to S6
References

26 July 2004; accepted 29 October 2004
10.1126/science.1103233

Enterococcus faecalis Senses Target Cells and in Response Expresses Cytolysin

Phillip S. Coburn,[1] Christopher M. Pillar,[2]* Bradley D. Jett,[2]† Wolfgang Haas,[2]‡ Michael S. Gilmore[1,2]*§

Many virulent strains of *Enterococcus faecalis* produce a two-subunit toxin, termed cytolysin. Cytolysin expression is regulated by one of the subunits (CylL$_S$″) through a quorum-sensing autoinduction mechanism. We found that when target cells are absent, the other subunit (CylL$_L$″) forms a complex with CylL$_S$″, blocking it from autoinducing the operon. When target cells are present, however, CylL$_L$″ binds preferentially to the target, allowing free CylL$_S$″ to accumulate above the induction threshold. Thus, enterococci use CylL$_L$″ to actively probe the environment for target cells, and when target cells are detected, allows the organism to express high levels of cytolysin in response.

Enterococcal cytolysin is a toxin distantly related to lantibiotic bacteriocins elaborated by Gram-positive bacteria. The active cytolysin consists of two small peptides. In concert they are toxic or lytic for a broad range of eukaryotic and prokaryotic cell types (*1*). The enterococcal cytolysin contributes to virulence in infection models (*2–7*) and is associated with acute mortality in humans (*8*). The cytolysin is encoded either by pheromone-responsive plasmids or within a pathogenicity island (*9*).

In addition to possessing toxin and bacteriocin activity, the extracellular, activated form of CylL$_S$ (CylL$_S$″) induces high-level expression of the cytolysin structural genes by a quorum-sensing mechanism (*10*). Cytolysin operon-encoded regulatory proteins, CylR1 and CylR2, cooperatively repress toxin expression (*10*), and derepression is affected by external accumulations of CylL$_S$″ through an as yet unknown signaling mechanism (*10*).

Although colonies of some strains of *E. faecalis* are capable of generating zones of hemolysis on blood agar, hemolytic activity is not detected in the culture fluid of broth cultures (*11*). One difference between growth in liquid laboratory media versus growth on blood agar made from the same broth base is the presence of target cells. However, when cytolytic *E. faecalis* is cultured in broth with added erythrocytes, the erythrocytes are lysed, whereas those added to a parallel culture of an isogenic strain defective in cytolysin production remain intact (*12*). Thus, *E. faecalis* appears somehow to be capable of sensing the presence of target cells and expressing the cytolysin in response.

Strains harboring mutations in *cylL$_L$* have been shown to express increased levels of CylL$_S$″ (*10*). Here, using real-time polymerase chain reaction, we found that transcripts of *cylL$_L$* and *cylL$_S$* were present at levels that were ~100-fold (103- and 105-fold, respectively) higher than in mid-log phase cells of an isogenic mutant that expresses an inactive, truncated form of CylL$_L$, compared to wild-type cells. This indicated that native CylL$_L$″ somehow interferes with the ability of CylL$_S$″ to feed back to the cell and induce high-level expression of the cytolysin operon.

To assess how a variety of environmental conditions affect cytolysin expression, we constructed a strain in which the *Escherichia coli* β-galactosidase (β-Gal) gene is fused to the cytolysin promoter P$_{lys}$, under the control of the cytolysin regulatory gene products, CylR1 and CylR2 (*10*). This strain expresses β-Gal in response to induction by exogenous CylL$_S$″ (Fig. 1A) (*10*). To determine directly whether CylL$_L$″ interferes with CylL$_S$″ induction of the cytolysin operon, we tested purified CylL$_L$″ for its ability to inhibit induction of β-Gal from this reporter strain (Fig. 1B). Complete inhibition of β-Gal expression was achieved with molar ratios of CylL$_L$″ to CylL$_S$″ above 1:1 (Fig. 1B).

To determine whether this CylL$_L$″ inhibition of CylL$_S$″-mediated autoinduction results from formation of a complex between CylL$_L$″ with CylL$_S$,″ we mixed similar quantities of CylL$_L$″ and CylL$_S$″ and analyzed them by tricine SDS–polyacrylamide gel electropho-

[1]Department of Microbiology and Immunology, [2]Department of Ophthalmology, University of Oklahoma Health Sciences Center, Stanton L. Young Biomedical Research Center, Room 356, Post Office Box 26901, Oklahoma City, OK 73190, USA.

*Present address: Department of Ophthalmology, Harvard Medical School, and The Schepens Eye Research Institute, 20 Staniford Street, Boston, MA 02114, USA.

†Present address: Department of Biology, Oklahoma Baptist University, Shawnee, OK 74804, USA.

‡Present address: Center for Oral Biology, University of Rochester, School of Medicine and Dentistry, Rochester, NY 14642, USA.

§To whom correspondence should be addressed. E-mail: mgilmore@vision.eri.harvard.edu

resis (PAGE). Mixing the mature subunits in solution resulted in very stable multimers of high apparent molecular mass (132 to > 216 kD), which were resistant to boiling in the presence of 0.5% SDS (Fig. 2). Thus, the observed lack of $CylL_S''$-mediated quorum induction in liquid culture, under conditions where $CylL_L''$ is also expressed or otherwise present, appeared to result from formation of a $CylL_S''$:$CylL_L''$ complex that was inactive for induction. This suggests that $CylL_L''$ plays a role in regulating cytolysin expression by titrating the level of free $CylL_S''$.

We hypothesized that the ability of $CylL_L''$ to modulate the concentration of free $CylL_S''$ could be influenced by the presence of a target cell if $CylL_L''$ were differentially adsorbed to its surface. Routine hemolysis assays of cytolysin activity are performed by adding 0.16 nmol of $CylL_L''$ to erythrocytes, immediately followed by the addition of about sevenfold molar excess (1.1 nmol) of $CylL_S''$ (hereafter termed 1X $CylL_L''$ and 1X $CylL_S''$, respectively). These represent the minimum quantities of each cytolysin subunit necessary to reach a plateau in erythrocyte lysis by 45 min. To determine whether one or the other cytolysin subunit preferentially bound target cells, we manipulated the order and timing of addition of cytolysin subunits as follows. To permit binding, we incubated one subunit with erythrocytes for 1 hour at 37°C, washed the erythrocytes three times in phosphate-buffered saline (PBS) to remove any unbound material, and then added the complementary subunit to initiate hemolysis (Fig. 3). Incubation of erythrocytes with 1X $CylL_L''$ for 1 hour followed by washing and the addition of 1X $CylL_S''$ resulted in a plateau of hemoglobin release being reached ~90 min after addition of the second subunit. Reversing the order of addition—incubation of erythrocytes with 1X $CylL_S''$ for 1 hour followed by washing and the addition of 1X $CylL_L''$—delayed the plateau of hemolysis by an additional 60 to 150 min. Preincubation of erythrocytes with 3X $CylL_L''$ for 1 hour followed by the addition of 1X $CylL_S''$ increased the rate of hemolysis ~ twofold compared to incubation with 1X $CylL_L''$. Conversely, preincubation of erythrocytes with 3X $CylL_S''$ for 1 hour followed by the addition of 1X $CylL_L''$ only slightly increased the rate of hemolysis compared to incubation with 1X $CylL_S''$. Moreover, incubating 1X $CylL_L''$ and 1X $CylL_S''$ together for 1 hour before the addition of erythrocytes completely eliminated hemolytic activity (Fig. 3). Thus, $CylL_L''$ has a higher affinity for erythrocytes than $CylL_S''$ and, in addition to being inactive for induction, the $CylL_L''$/$CylL_S''$ complex does not retain hemolytic activity.

Surface plasmon resonance was used to quantify the difference between $CylL_L''$ and $CylL_S''$ affinity using a model membrane system. Small unilamellar vesicles (SUVs), composed of 45 mol% 1-palmitoyl-2-oleoyl-*sn*-glycero-3-phosphocholine (POPC) and 55 mol% cholesterol, were used to coat a Biacore L1 chip (*13*). The binding of both $CylL_L''$ and $CylL_S''$ to the lipid bilayer was determined separately over a range of subunit concentrations (20 to 100 μM for $CylL_L''$; 100 to 800 μM for $CylL_S''$) (fig. S1, A and B). The mean dissociation constant (K_D) of $CylL_L''$ for POPC:cholesterol bilayers was 5.9 μM and for $CylL_S''$ it was 38.1 μM (P = 0.0006, Student's t test). Thus, the $CylL_L''$ subunit binds to phosphatidylcholine:cholesterol lipid bilayers with an affinity that is 6.5-fold greater than that of $CylL_S''$.

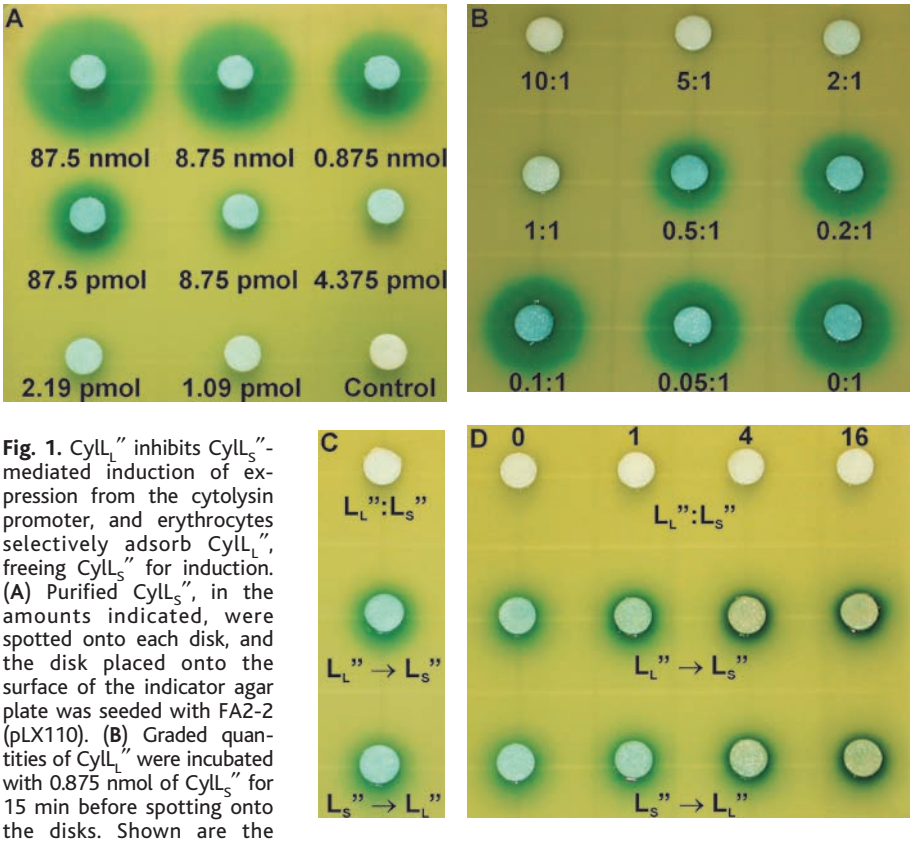

Fig. 1. $CylL_L''$ inhibits $CylL_S''$-mediated induction of expression from the cytolysin promoter, and erythrocytes selectively adsorb $CylL_L''$, freeing $CylL_S''$ for induction. (**A**) Purified $CylL_S''$, in the amounts indicated, were spotted onto each disk, and the disk placed onto the surface of the indicator agar plate was seeded with FA2-2 (pLX110). (**B**) Graded quantities of $CylL_L''$ were incubated with 0.875 nmol of $CylL_S''$ for 15 min before spotting onto the disks. Shown are the molar ratios of $CylL_L''$ to $CylL_S''$. (**C**) Equimolar amounts of $CylL_L''$ and $CylL_S''$ (0.875 nmol each) were mixed and immediately spotted onto the disk labeled $CylL_L''$:$CylL_S''$. For the middle disk, 0.875 nmol of $CylL_L''$ was added to human erythrocytes, immediately followed by the addition of 0.875 nmol of $CylL_S''$; the mixture was then centrifuged, and the supernatant was spotted onto the disk labeled $CylL_L'' \rightarrow CylL_S''$. For the bottom disk labeled $CylL_S'' \rightarrow CylL_L''$, the experiment was identical to that shown for the middle disk except that the order of addition of cytolysin components was reversed. (**D**) In the top panel of disks, equimolar amounts of $CylL_L''$ were mixed with $CylL_S''$ (0.875 nmol), and after 0, 1, 4, and 16 min, the mixtures were centrifuged and applied to the disks. For the middle panel of disks, 0.875 nmol of $CylL_L''$ was added to human erythrocytes, immediately followed by the addition of 0.875 nmol of $CylL_S''$. After 0, 1, 4, and 16 min, the mixtures were centrifuged, and the supernatants were spotted onto the disks labeled $CylL_L'' \rightarrow CylL_S''$. For the bottom panel of disks labeled $CylL_S'' \rightarrow CylL_L''$, the experiment was identical to that shown for the middle panel except that the order of addition of cytolysin components was reversed.

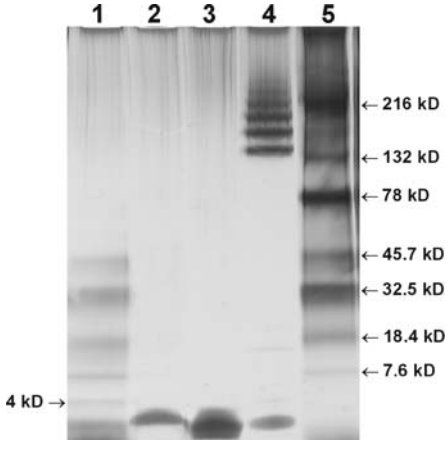

Fig. 2. A multimeric complex is formed by mixing $CylL_L''$ and $CylL_S''$. Tricine SDS-PAGE of $CylL_L''$, $CylL_S''$, and an equimolar mixture of the two subunits. Lanes 1 and 5 contain low and high molecular size markers, respectively (Bio-rad kaleidoscope polypeptide and prestained standards). Lanes 2 and 3 contain 1 nmol of $CylL_L''$ alone and 1 nmol of $CylL_S''$ alone, respectively. Lane 4 contains 500 pmol of $CylL_L''$ and 500 pmol of $CylL_S''$ preincubated together for 5 min before electrophoresis.

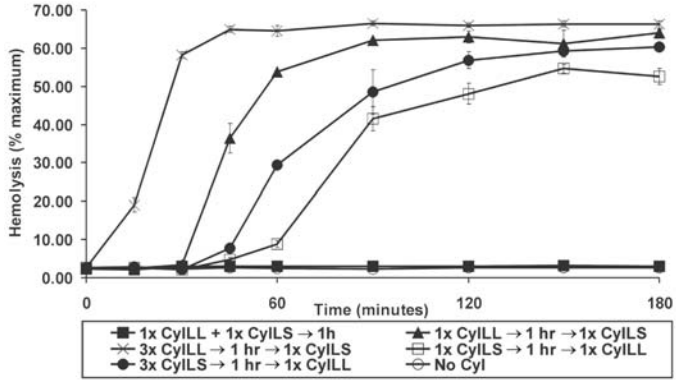

Fig. 3. $CylL_L''$ has a greater affinity "for human erythrocytes than $CylL_S''$. (▲) Erythrocytes were preincubated with 0.16 nmol (1x) of $CylL_L''$ for 1 hour and washed three times with PBS, and 1.1 nmol (1x) of $CylL_S''$ was added. (□) Erythrocytes were preincubated with 1.1 nmol (1x) of $CylL_S''$ for 1 hour and washed three times with PBS, and 0.16 nmol (1x) of $CylL_L''$ was added. (×) Erythrocytes were preincubated with 0.48 nmol (3x) $CylL_L''$ for 1 hour and washed three times with PBS, and 1.1 nmol (1x) of $CylL_S''$ was added. (●) Erythrocytes were preincubated with 3.3 nmol (3x) $CylL_S''$ for 1 hour and washed three times with PBS, and 0.16 nmol (1x) of $CylL_L''$ was added. (■) Preincubation of 0.16 nmol (1x) of $CylL_L''$ with 1.1 nmol (1x) of $CylL_S''$ for 1 hour before the addition of erythrocytes. (○) Neither cytolysin component was added to erythrocytes. For all reactions, hemoglobin release was quantified in triplicate at regular time intervals of 15, 30, 45, 60, 90, 120, 150, and 180 min. At each time point, reactions were centrifuged to pellet intact erythrocytes, and the supernatant was read at 562 nm. Data are plotted relative to maximum hemoglobin release after SDS lysis of 5% erythrocytes. Error bars represent the mean ± SD.

To determine whether the observed higher affinity of $CylL_L''$ for target cell membranes resulted in differential adsorption to the surface of target cells, leaving free $CylL_S''$ in solution to effect autoinduction, we tested the ability of target cells to differentially adsorb $CylL_L''$ and leave behind inducing levels of $CylL_S''$. The middle of the linear response range for $CylL_S''$-mediated induction of β-Gal expression from FA2-2 (pLX110), as observed using the disk test, occurred at about 0.875 nmol of $CylL_S''$ (Fig. 1A). When an equimolar quantity (0.875 nmol) of purified $CylL_L''$ was added to $CylL_S''$ before application to the FA2-2 (pLX110) lawn, no induction was observed owing to formation of the inactive $CylL_L''$:$CylL_S''$ complex (Fig. 1C). This complex forms nearly instantaneously (Fig. 1D). However, when 0.875 nmol of $CylL_L''$ was added first, followed by 5% (v/v) erythrocytes and then 0.875 nmol of $CylL_S''$, sufficient free $CylL_S''$ to cause readily detectable induction of β-Gal expression by FA2-2 (pLX110) remained in solution for at least 16 min (Fig. 1, C and D). Identical results were obtained even when the order of additions was reversed.

On the basis of these findings, we propose a model for the regulation of a toxin in a manner that is responsive to the presence of target cells. In the absence of a target cell, $CylL_L''$ and $CylL_S''$ are expressed at basal levels, and the subunits interact to form an inactive, oligomeric complex that is devoid of either cytolytic activity or the ability to induce high-level expression of the cytolysin operon (fig. S2). In the absence of a target cell, $CylL_L''$ acts to titrate the level of free $CylL_S''$ in solution, holding it below the threshold necessary to trigger high-level cytolysin production. However, in the presence of a target cell, $CylL_L''$ binds it preferentially, allowing free $CylL_S''$ to accumulate and induce high-level cytolysin expression (fig. S2). This mechanism effectively provides enterococci with the ability to actively probe the environment for cytolysin targets.

References and Notes

1. P. S. Coburn, M. S. Gilmore, *Cell. Microbiol.* **5**, 661 (2003).
2. Y. Ike, H. Hashimoto, D. B. Clewell, *Infect. Immun.* **45**, 528 (1984).
3. K. V. Singh, X. Qin, G. M. Weinstock, B. E. Murray, *J. Infect. Dis.* **178**, 1416 (1998).
4. J. W. Chow *et al.*, *Antimicrob. Agents Chemother.* **37**, 2474 (1993).
5. B. D. Jett, H. G. Jensen, R. E. Nordquist, M. S. Gilmore, *Infect. Immun.* **60**, 2445 (1992).
6. S. X. Stevens, H. G. Jensen, B. D. Jett, M. S. Gilmore, *Investig. Ophthalmol. Vis. Sci.* **33**, 1650 (1992).
7. D. A. Garsin *et al.*, *Proc. Natl. Acad. Sci. U.S.A.* **98**, 10892 (2001).
8. M. M. Huycke, C. A. Spiegel, M. S. Gilmore, *Antimicrob. Agents Chemother.* **35**, 1626 (1991).
9. N. Shankar, A. S. Baghdayan, M. S. Gilmore, *Nature* **417**, 746 (2002).
10. W. Haas, B. D. Shepard, M. S. Gilmore, *Nature* **415**, 84 (2002).
11. E. W. Todd, *J. Pathol. Bacteriol.* **39**, 299 (1934).
12. M. S. Gilmore, unpublished observations.
13. N. Papo, Y. Shai, *Biochemistry* **42**, 458 (2003).
14. We thank B. D. Novosad and J. Hunt for technical assistance, and A. Marpoe for providing liposomes. This work was supported by NIH grants AI041108 and EY08289, by a Senior Investigator Grant from Research to Prevent Blindness, and by those who inspired us: D.W.G., J.D.J., G.L.C., W.J.P., and D.B.R.

Supporting Online Material
www.sciencemag.org/cgi/content/full/306/5705/2270/DC1
Materials and Methods
Figs. S1 and S2

12 August 2004; accepted 27 October 2004
10.1126/science.1103996

New Products

http://science.labvelocity.com

Mouse Ig Blocking Reagent

Three M.O.M. (Mouse-on-Mouse) kits to localize mouse primary antibodies on mouse tissue sections offer the advantage of the ability to allow mouse primary antibodies to be stained while avoiding interfering background due to the detection reagents binding endogenous mouse antibody. A key component of the M.O.M. kits is the reagent used to block endogenous mouse antibody in the tissue section. The Mouse IgG Blocking Reagent is optimally effective when used in conjunction with the special biotinylated anti-mouse immunoglobulin in the M.O.M. kits.

Vector Laboratories For more information 650-697-3600 www.vectorlabs.com

Stereotaxic Instrument

The Just for Mice Stereotaxic Instrument was developed for the expanding research being done using knockout and transgenic mice. It allows the user to perform surgical procedures on two mice, neonatal rats, or other small rodents. This model features several advantages over stereotaxic instruments intended for rats. Two ear bar slots are located on each side of the base, and both are accessible by a single manipulator arm. The ear bars can be independently adjusted in height. Movement can be measured either manually or digitally. The digital system features a large LED display module accurate to 10 μm in all three directions.

Stoelting For information 630-860-9700 www.stoeltingco.com

Freeze Dryers

Genesis freeze dryers offer the versatility needed for pilot, research, or small-scale production applications. Part of the Virtis product line and developed with an extensive choice of options and add-ons, the Genesis line allows users to design the freeze dryer to meet specific application needs, including a design for clean-room installations, and allows for easy scale-up from research to full-scale production. Genesis chamber shelves and condenser chambers are made of chemical-resistant stainless steel and come with a standard 4-in diameter vapor port with an optional 8-in diameter port available.

SP Industries For information 800-431-8232 www.virtis.com

Improved Filtration

An enhanced bioburden reduction filter combines three novel technologies to provide more economical filtration of a broad range of biopharmaceutical fillers and buffers. The Supor UEAV 0.2 micron filter increases filter life and protects sterilizing grade filters and other sensitive downstream processing equipment such as tangential flow filtration and chromatography systems. It achieves this by incorporating three advanced technologies into a single filter: an assymetric Supor mach V membrane structure with controlled pores from 3 to 0.2 μm, which provides high solids capacity; the new deep-pleat Ultipleat construction, which provides enhanced surface area, resulting in high flow rates and extending solids capacity; and the Pall polyethersulfone membrane, which ensures excellent chemical compatibility and low nonspecific binding to extend service life. The new filter's particle removal capability works with a diverse range of biopharmaceutical fluids, including buffers, biologicals, tissue culture media, opththalmics, and cell-culture supernatants.

Pall For information 800-717-7255 www.pall.com

Dialysis Cassettes

The new 30-ml capacity Slide-A-Lyzer Dialysis Cassettes are available with 3.5 K and 10 K molecular weight cut-off (MWCO) membranes for efficient and easy dialysis of 12–30 ml samples. The 30-ml cassette has a built-in buoy and frame that is color-coded to show the MWCO of the membrane and transparent so the user can view needle placement during sample injection. The dialysis cassettes provide >95% sample recovery and the convenient cassette format eliminates the hassles of knots, caps, lids, and clamps associated with traditional dialysis methods. The cassettes are also available in capacities of 0.1–.05 ml, 0.5–3 ml, and 3–12 ml with 3.5 K, 7 K, and 10K MWCO membranes. The 10 K membrane cassettes are available in gamma-irradiated format.

Pierce For information 800-874-3723 www.piercenet.com

Protein Purification Scale-Up

The Pellicon XL tangential flow device incorporates tangential flow filtration technology to purify and concentrate from 300 mL to 2L of solution down to a final volume of 20 mL. The Pellicon XL device is self-contained with luer connections for easy set-up. It can beoperated with either a peristaltic pump or with Millipore's Labscale TFF System. The devices are easy to clean and can be re-used up to five times. An optional graduated 100-mL reservoir is also available for small-volume separations. Applications for the device include cell harvesting and clarification, preparation of material for clinical trials, concentration and desalting of proteins, buffer exchange, and depyrogenation.

Millipore For information 800-MILLIPORE www.millipore.com/proteinresearch

Sample Holders for Solvent Evaporator

A new line of sample holders is available for the EZ-2 solvent evaporator. The new holders are designed to take a variety of round bottom flasks ranging from 25 ml to 500 ml. Ingenious sample holder design has allowed the compact, benchtop EZ-2 to accommodate up to six 100-ml flasks simultaneously. With larger flasks, a total capacity of 1 liter is possible, for example 4 × 250 ml or 2 × 500 ml.

Genevac For information +44-1473-240000 www.genevac.co.uk

Newly offered instrumentation, apparatus, and laboratory materials of interest to researchers in all disciplines in academic, industrial, and government organizations are featured in this space. Emphasis is given to purpose, chief characteristics, and availability of products and materials. Endorsement by *Science* or AAAS of any products or materials mentioned is not implied. Additional information may be obtained from the manufacturer or supplier by visiting www.science.labvelocity.com on the Web, where you can request that the information be sent to you by e-mail, fax, mail, or telephone.